Atomic Layer Deposition of Low-Dimensional Transition Metal Di- and Tri-Chalcogenides and their Heterostructures

PROEFSCHRIFT

ter verkrijging van de graad van doctor aan de Technische Universiteit Eindhoven, op gezag van de rector magnificus prof.dr.ir. F.P.T. Baaijens, voor een commissie aangewezen door het College voor Promoties, in het openbaar te verdedigen op donderdag 12 november 2020 om 16:00 uur

door

Saravana Balaji Basuvalingam

geboren te Salem, India

Dit proefschrift is goedgekeurd door de promotoren en de samenstelling van de promotiecommissie is als volgt:

voorzitter:	prof.dr.ir. G.M.W. Kroesen
1e promotor:	prof.dr. A.A. Bol
2e promotor:	prof.dr.ir. W.M.M. Kessels
leden:	prof.dr. T. Banerjee (Rijksuniversiteit Groningen)
	prof.dr.ir. J.M.J. den Toonder
	prof.dr. P.G. Steeneken (Technische Universiteit Delft)
	prof. S. Lodha (Indian Institute of Technology Bombay)
	prof.dr.ir. R. Tuinier

Het onderzoek of ontwerp dat in dit proefschrift wordt beschreven is uitgevoerd in overeenstemming met de TU/e Gedragscode Wetenschapsbeoefening.

Funding Information

This research has been supported by European Research Council (Grant Agreement No. 648787- ALDof2DTMDs).

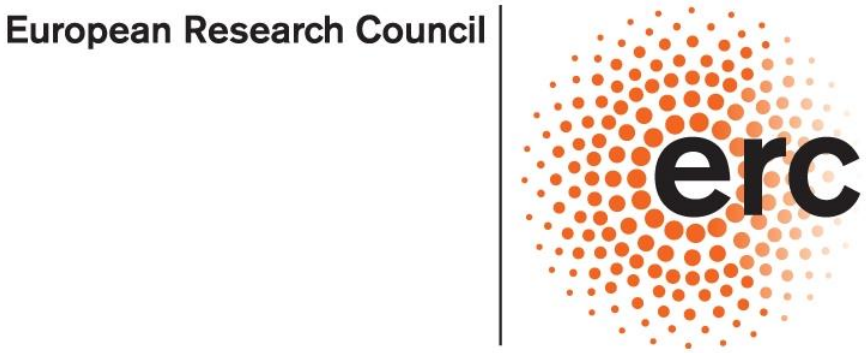

Front cover design by Saravana Balaji Basuvalingam & Komala Sundaram.

Printed and bound by: Ipskamp Printing

A catalogue record is available from the Eindhoven University of Technology Library
ISBN: 978-90-386-5155-2

List of Abbreviations

0D	- zero-dimensional
1D	- one-dimensional
2D	- two-dimensional
3D	- three-dimensional
ALD	- atomic layer deposition
APC	- automated pressure controller
BE	- binding energy
BEOL	- back-end of the line
C_{dl}	- double-layer capacitance
CDW	- charge density wave
C_s	- specific capacitance
CVD	- chemical vapor deposition
CVT	- chemical vapor transport
DFT	- density functional theory
DRAM	- dynamic random-access memory
EBID	- electron-beam induced deposition
ECSA	- electrochemical surface area
EDX	- energy-dispersive X-ray spectroscopy
E_F	- Fermi level
EIS	- electrochemical impedance spectroscopy
ERD	- elastic recoil detection
E_{VB}	- valence band maximum
FET	- field-effect transistor

FIB	- focused ion beam
FOEL	- front-end-of-line
FWHM	- full width half maximum
GAAFET	- gate-all-around transistor
geo	- geometric area
GI	- grazing-incidence
GPC	- growth per cycle
HAADF	- high-angle annular dark-field
HER	- hydrogen evolution reaction
ICP	- inductively coupled plasma
LSV	- linear sweep voltammetry
NIR	- near-infrared
OCP	- open circuit potential
OES	- optical emission spectroscopy
OoPO	- out-of-plane-orientation
PA-ALD	- plasma-assisted atomic layer deposition
PAW	- projector-augmented wave
PBE	- Perdew, Burke, and Ernzerhof
PE-ALD	- plasma enhanced atomic layer deposition
PL	- photoluminescence
PLD	- pulsed laser deposition
RBS	- Rutherford backscattering spectrometry
ReRAM	- resistive switching random access memory
RF	- radio frequency
RHE	- reversible hydrogen electrode
rpm	- rounds per minutes

SAED	- selected area electron diffraction
SCE	- saturated calomel electrode
SE	- spectroscopic ellipsometry
SEM	- scanning electron microscopy
SSR	- solid state reaction
STEM	- scanning transmission electron microscopy
TBTDEN	- (tert-butylimido)-tris-(diethylamino)-niobium
TDMAT	- tetrakis (dimethylamido) titanium
TEM	- transition electron microscopy
TMC	- transition metal chalcogenide
TMDC	- transition metal dichalcogenide
TMTC	- transition metal trichalcogenide
UPS	- ultraviolet photoelectron spectroscopy
VASP	- Vienna Ab initio Simulation Package
VB	- valence band
vdW	- van der Waals
V_O	- oxygen vacancy
XPS	- X-ray photoelectron spectroscopy
XRD	- X-ray diffraction

Table of Contents

General Introduction

1

In this introduction chapter, first a short overview of various layered nanomaterials is provided. The chapter then discusses some background of transition metal chalcogenides (TMCs): transition metal dichalcogenide (TMDCs) and transition metal trichalcogenides (TMTCs). The chapter also introduces atomic layer deposition, which forms the basis deposition method for the work described in this dissertation. The chapter then addresses three aspects of TMDC/TMTC related research that form the core of this thesis. Two of the three aspects addressed deals with the challenges associated with TMCs synthesis: phase-engineering and heterostructures, and the last one attends to the application of TMCs: hydrogen evolution reaction (HER). The chapter concludes by providing context for the research goals and the rest of the chapters in this dissertation.

1.1 Layered Nanomaterials

Nanoscience has emerged as a separate field of study since the concept was first introduced in 1959 during a lecture entitled “There’s Plenty of Room at the Bottom” at the annual meeting of American Physical Society by Richard P. Feynman. During this talk, Feynman contemplated miniaturization down to the atomic level would be ‘an invitation to enter a new field of physics´[1]. Even though he never coined the word nanoscience or nanotechnology, he is broadly credited for introducing the concept by bringing attention to this new area of science, which has emerged as one of the most widely studied areas of materials science.

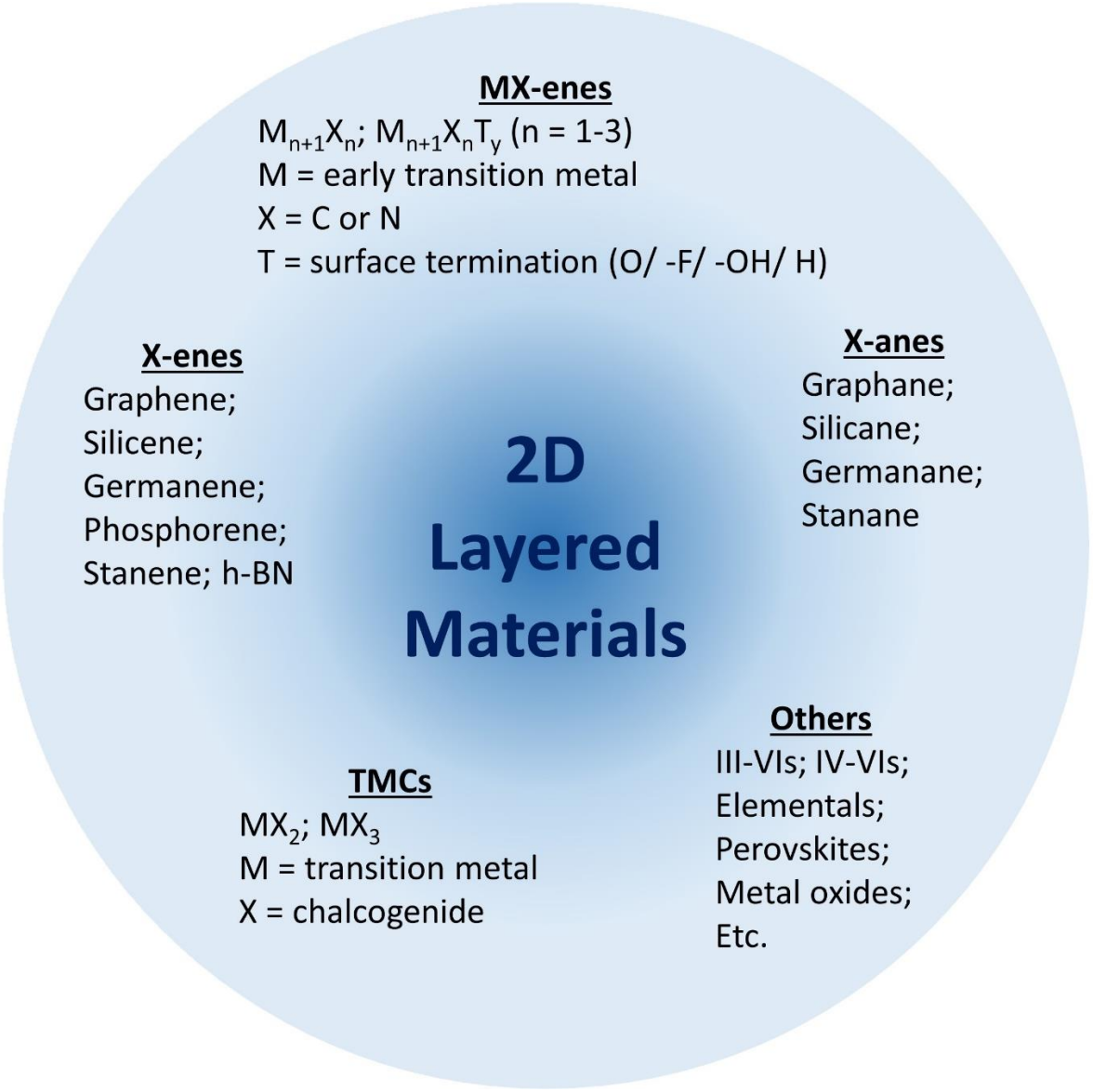

Figure 1.1 Family of 2D layered materials.

Any material with at least one of its dimensions smaller than 100 nm (1 nm = 10^{-9} m) is regarded as nanomaterial[2]. In general, nanomaterials can be classified into three groups depending on their dimensionality: two-dimensional (2D) layers, one-dimensional (1D) wires, and zero-dimensional (0D) particles[2]. Interestingly, in comparison to the 3D bulk counterpart, nanomaterials offer size-dependent properties such as quantum confinement, surface plasmon resonance, etc.[3,4,5]. Due to their large surface to bulk ratio, the chemically inert bulk materials can become extremely reactive in their nano form, leading to applications in fields such as catalysis[6]. The expansion of nanomaterials and their development into a major field of research can be traced back to the discovery of the carbon nanotube (1D) in 1991[7] subsequent to the fullerene (0D) discovery in 1985[8]. However, 2D layered materials emerged into a leading research area only after discovering graphene (2D) in 2004, which was soon recognized with the Physics Nobel prize in 2010[9]. The layered materials are a class of nanomaterials with strong in-plane chemical bonds (such as covalent bonding) and weak coupling (such as van der Waals and/or electrostatic interactions) between the individual layers in the out-of-plane direction.

Since the successful isolation of graphene (monolayer) from the bulk graphite using simple scotch tape, there has been a surge in discovery and identification of new layered materials, which is continuously expanding the family of 2D layered materials as illustrated in Figure 1.1. This family of layered materials include X-enes (mono-elemental 2D form of X = C, Si, Ge, Sn etc.), X-anes (ligand functionalized derivatives of X-enes), transition metal chalcogenides (TMCs) (*e.g.* MoS_2, TiS_3, etc.), MXenes (discovered in 2011, by selective etching of A-group elements in the MAX phase `*e.g.* $Ti_3AlC_2$´ to result in MX `*e.g.* Ti_3C_2OH´ with 2D morphology[10]), perovskites, metal oxides, metal halides etc.[11,12,13,14]. Note that this list is by no means complete and is extending almost on a daily basis. Among this huge pool of layered materials, TMCs have attracted considerable attention. Due to their outstanding electrical and optical properties, TMCs have emerged as promising materials for electronics and optoelectronic device-based applications such as field-effect transistors (FETs)[15,16,17], photodetectors[18,19], light-emitting diodes[20,21], solar cells[22–24] and lasers[21]. This dissertation focuses on synthesizing TMCs with a layered structure such as two-dimensional (2D) transition metal dichalcogenide (MX_2; TMDCs) and quasi-one-dimensional transition metal trichalcogenides (MX_3; TMTCs), where M and X correspond to transition metals and chalcogens, respectively.

1.2 Background on 2D Transition Metal Chalcogenides

TMCs have gained significant research interests in the past decade due to their layered structure with thickness dependent properties. TMCs in their bulk form are not new to the materials science community, as they have been synthesized and studied extensively over the last 60 years. TMCs are a class of materials consisting of a transition metal from the d-block and chalcogens, specifically S, Se, or Te, from group XVI of the periodic table. They have been found to exist in various transition metal to chalcogenide ratios, especially TMCs with transition metal to chalcogenide ratio of 2 (TMDC) and 3 (TMTC) have been of interest lately. Among the two popular classes of TMCs, TMDCs were the first to be studied using naturally occurring MoS_2 crystals back in 1923[25]. From the 1940s, there were serious efforts to study and synthesize various TMDCs. Subsequently, by the late 1960s, almost 60 types of TMDCs (MX_2) were identified, with more than two-thirds of them being layered materials. Their structure and properties will be discussed in detail in Chapter 2. These materials are widely used as dry lubricants and were also extensively studied as cathode materials in batteries. On the other hand, TMTCs were synthesized in the late 1940s, but their structure was eventually understood only in the 1960s. By the end of the 1970s, most of the known TMTCs were synthesized in their bulk form. These materials were initially used to study electrical conductivity in one-dimensional and as cathode material (similar to TMDCs) in batteries. The TMTC structure and properties will also be discussed in Chapter 2.

Recently, especially layered *semiconducting* TMDCs like MoS_2 and WS_2 gained renewed attention for having a natural direct band gap in the monolayer regime, contrary to graphene, which lacks a band gap and is semi-metallic in nature[26]. The first report on using adhesive tape for producing the ultrathin MoS_2 layer was way back in 1963[27], and the first exfoliation of a monolayer using an intercalation method was reported later in 1986[28]. Following the successful isolation of graphene in 2004, interests in the TMDCs class of material reemerged, which led to an array of research efforts uncovering unusual properties such as bandgap transition from indirect to direct by decreasing the thickness from bulk to monolayer[29,30], valley polarization (the process of selectively populating one of the momentum valleys at the first Brillouin zone)[31,32], etc. In terms of device applications, the field took off in 2011, when Kis *et al.* showed the first TMDC based FET using exfoliated monolayer MoS_2 as the channel material[33]. Since then, a plethora of device applications using various exfoliated semiconducting TMDCs were demonstrated, such as photodetectors[34,35], photoemitters[36–38], etc. As a result, it initiated significant efforts towards the scalable synthesis of TMDCs over a large area using various thin-film synthesis

techniques. Now, semiconductor foundries and leading-edge research organizations such as TSMC, IMEC, etc. have turned their efforts towards semiconducting TMDCs[15,16,17], as an alternative channel material to replace Si and to keep continuing the trend of Moore´s law while maintaining the device performance.

So far, especially semiconducting TMDCs from group VI have gained importance for their excellent electrical and optical properties. However, there are also equal and considerable demands for less explored *metallic* TMDCs in group IV and V for (opto)electronic device and electrochemical applications. In terms of (opto)electronics, there is a need for TMDCs with metallic behavior to act as a contact material for 2D semiconducting channels. According to experimental studies, 2D metals offer better device performance with low contact resistance over their 3D metal counterparts[39]. Furthermore, metallic TMDCs have also gained interest in electrochemical applications for HER, as they show better catalytic activity over their semiconducting counterparts[40].

In addition to the TMDCs (both metallic and semiconducting) in their primitive forms, several derivatives of TMDCs have emerged, which include alloys and van der Waals heterostructures, which widens the already broad range of TMDC properties and application potential in fields such as (opto)electronics[41], electrochemistry[42], photovoltaics[43], quantum computing[44], etc. Among them, van der Waals heterostructures have gained interest in (opto)electronic devices for band engineering, 2D-2D metal-semiconductor contacts, etc. for constructing a next-generation ultra-thin device as illustrated in Figure 1.2.

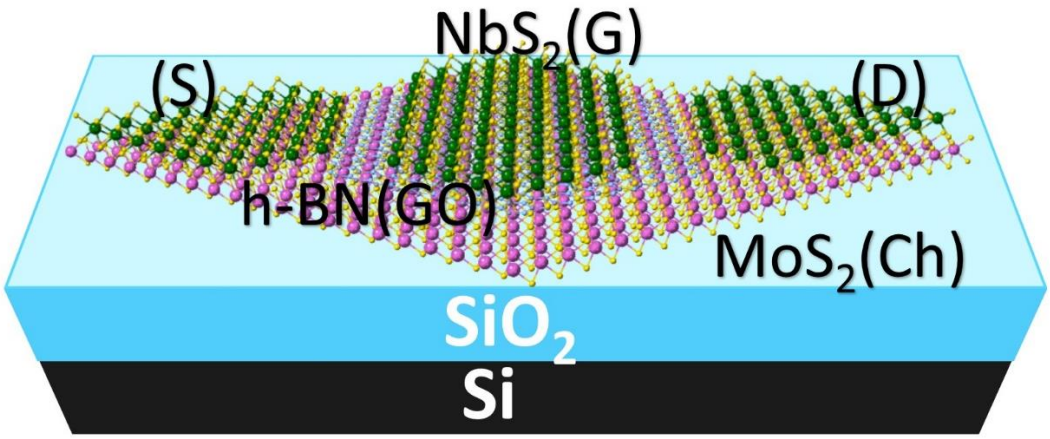

Figure 1.2 Schematic illustration of 2D transistor containing various layered materials acting as metal (source (S), gate (G), and drain (D)), semiconductor (channel: Ch) and insulator (gate oxide: GO).

In comparison to TMDCs, TMTCs are a less studied class of materials in terms of both synthesis and device applications. The first reports on a photodetector and a FET based on exfoliated TMTC were in 2014[45] and 2015[46], respectively. Since then, there have been a decent number of reports on using TMTCs in both (opto)electronic[47,19,48,49] and electrochemical[50] applications. However, almost all the reports on TMTCs were based on exfoliated material, indicating a need to synthesize them in the thin-film form over a large area, so their potential could be explored further[51].

From the discussion above, it follows that there is a need for synthesizing metallic TMDCs, TMTCs, and their heterostructures using a scalable (large area) technique. This dissertation focuses on synthesizing them using a thin-film technique known as atomic layer deposition (ALD).

1.3 Atomic Layer Deposition

ALD is a variant of chemical vapor deposition (CVD), which involves self-limiting and saturated growth of ultra-thin films with nanoscale control. This surface chemistry driven thin-film synthesis technique provides various advantages over other techniques such as precise thickness control, large area uniformity (scalability), and excellent conformality over complex 3D structures at low deposition temperatures, as illustrated in Figure 1.3. One of the first reports on ALD was in 1974 by Finnish inventors Suntola and Antson. Nevertheless, there were also reports from the researchers in USSR even before the 1970s[52]. Significant interests in ALD from industry emerged in the 1990s, as the need for control over the conformal growth of new materials on high aspect ratio structures arose. Resultantly, in 1998, ALD was reported to be used in the production of DRAM[52]. In 2007, Intel reported the introduction of ALD grown HfO_2 as the high-K gate oxide material in field-effect transistors[53]. Since then, with the drive for continuous downscaling of device dimensions and moving from 2D planar FETs to 3D *fin*FETs, ALD has increasingly played a crucial role in the front-end-of-line (FEOL) of the semiconductor device fabrication process. Besides the semiconductor industry, ALD has also been implemented in other industries, one of them being the solar cell industry for depositing passivation layers[54]. A more detailed description of the ALD technique itself will follow in Chapter 2.

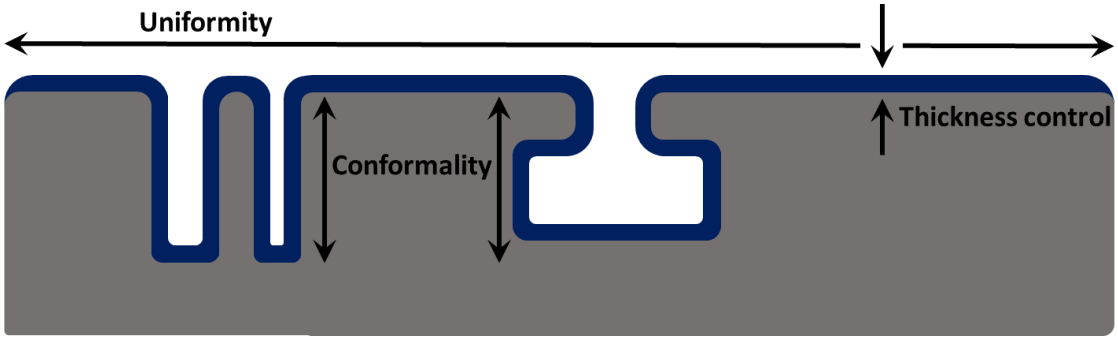

Figure 1.3 Schematic illustrating the key merits of ALD such as thickness control, uniformity over a large area, and conformality over the complex 3D structure.

Although ALD of oxides and nitrides is heavily studied, lately, ALD of 2D materials, particularly TMDCs, have gained momentum because of the benefits ALD offers with respect to uniformity, scalability, conformality, and precision thickness control. However, thus far, it is mostly restricted to the direct ALD of semiconducting and group VI TMDCs in general. In the direct ALD approach, both the transition metal and chalcogenide precursors are exposed to the growth substrate in a step by step cyclic manner to deposit the targeted TMDC, as will be described in Chapter 2. Besides, ALD has also been used to grow TMDCs by the indirect approach known as chalcogenization. In this approach, the targeted transition metal is first grown in the form of a transition metal oxide (*e.g.,* WO_3) by ALD. Then the transition metal is followed by the final step of chalcogenization treatment at high temperature in a targeted chalcogen environment (*e.g.,* S or H_2S) to form the final TMDC (*e.g.,* WS_2) film[55]. Like direct ALD, this indirect method has been reported only to synthesize semiconducting group VI TMDCs. On the other hand, ALD could also be suitable for the synthesis of TMTCs, as in comparison to TMDC growth, low temperature is ideal for TMTC formation, as will be discussed in Chapter 2. However, the growth of TMTCs has not been investigated using ALD.

It is apparent from the above discussion that ALD processes for the growth of metallic TMDCs, both by direct and indirect methods, are unexplored. In this dissertation, the focus is on extending the ALD toolbox with the deposition of conducting group IV and V TMDCs with metallic/ semi-metallic properties, and TMTCs through phase-engineering. Additionally, the stacking of TMDC and TMTC on top of one other to form vertical heterostructures using ALD will also be explored.

1.4 Phase-engineering

As mentioned in previous sections, to fabricate FETs (for example), all sorts of materials exhibiting various properties such as metal, semiconductor and insulator are required. Beneficially, layered TMCs, which exist in multiple phases, polymorphs and polytypes, can offer a wide range of electronic properties while containing analogous elements. For example, MoS_2 can exhibit both semiconducting and metallic properties, depending on its phase ((2*H* or 1*T*). Therefore, by acquiring control over the materials' phase, 2*H*-MoS_2 can be implemented as channel material while 1*T*-MoS_2 can act as a source, drain and gate in the transistor device[39]. Duly, phase-engineering has gained much consideration to achieve control over both phases and properties of TMCs[56]. Nevertheless, some of these material phases/polytypes (*say* metallic 1*T* phases of MoS_2 and WS_2) are metastable, and synthesizing these metastable phases is a persisting challenge[57].

There are plenty of phase-engineering strategies proposed and reported to modulate the TMCs phase and properties, and they can be classified into two types: phase transition and phase-controlled synthesis[58]. Phase transition involves the transformation process in which a stable phase of a TMC is converted into the metastable phase (Figure 1.4) or *vice versa* either by chemical or physical methods[59], which includes intercalation (with alkali metals and alkaline earth metals)[60], alloying, charge transfer, irradiation, thermal treatment[61], and stress induction. Even if the targeted phase can be efficiently obtained in a controlled way by the aforementioned methods, it might come at a cost such as unexpected doping or defects that sacrifices the intrinsic properties of the material. Also, there are other shortcomings like phase reversibility once the external factors inducing phase transformation are retracted.

Alternatively, the phase-controlled synthesis focuses on the direct fabrication of the targeted phase (also including the metastable phase) from the starting precursors (both transition metal and chalcogenide), see Figure 1.4. For example, phase-controlled synthesis between 2*H*- and 1´*T*- phases of $MoTe_2$ can be obtained by controlling the synthesis temperature between 670 and 710 °C while using the MoO_3 and Te as starting precursor[62]. Similarly, the control over the phase can also be obtained by optimizing the different reaction conditions such as precursor, pressure, temperature, etc[63].

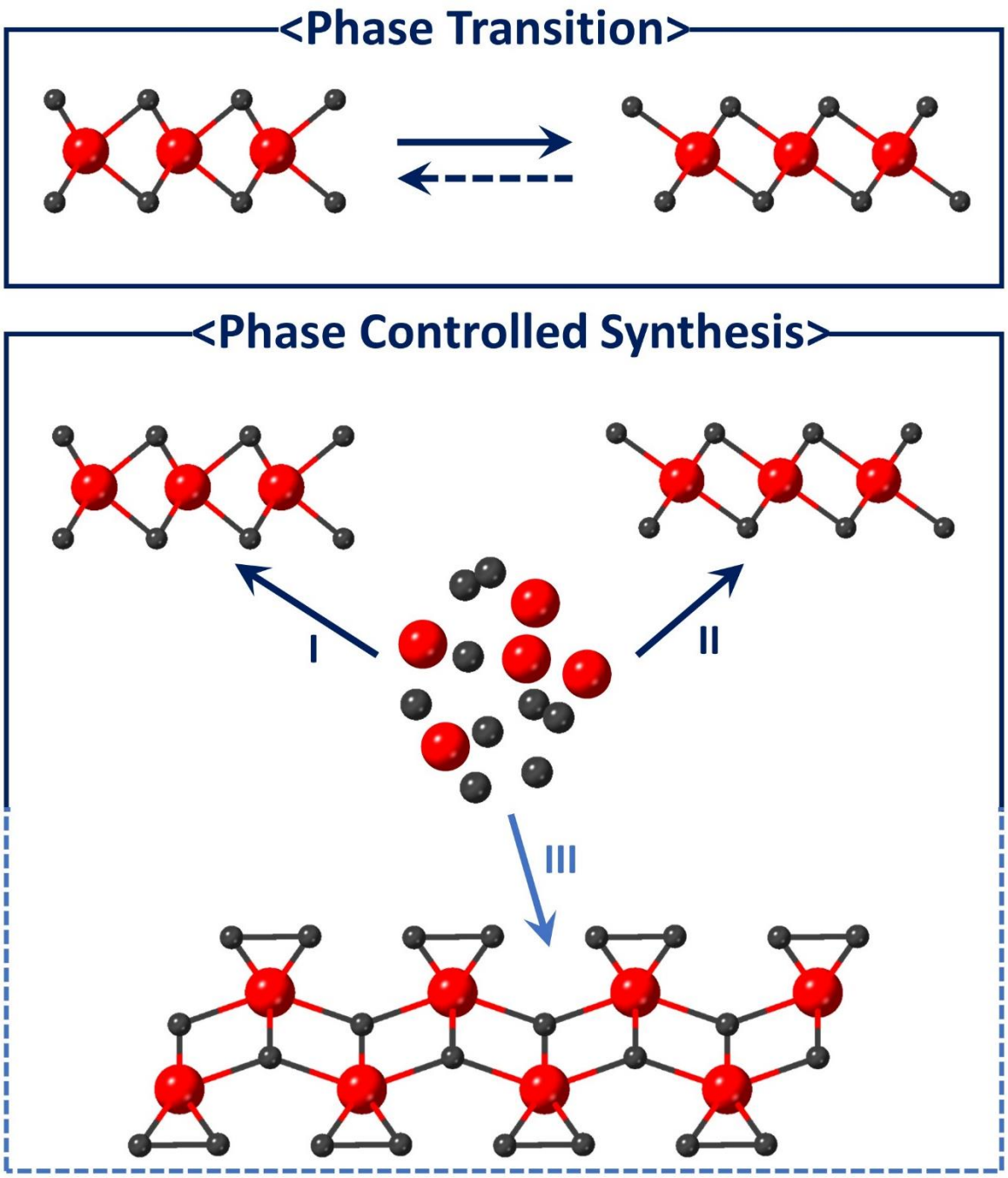

Figure 1.4 Schematic illustration of two phase-engineering types. Phase transition involves a transformation process, while phase-controlled synthesis involves direct fabrication of the targeted materials' phase.

Thus far, most reports on the phase-engineering focused on achieving phase control between metal and semiconducting polytypes of TMDCs such as 1*T*-MoS_2 Vs. 2*H*-MoS_2, 1*T*-WS_2 Vs. 2*H*-WS_2, 1*T*-VSe_2 Vs. 1´*T*-VSe_2, 1´*T*-$MoTe_2$ Vs. 2*H*-$MoTe_2$, etc. In addition to these, there are also many other unexplored layered TMCs offering similar combinations.

Interestingly, some of the TMDC counterparts in the TMTC class of materials with analogous elements exhibit complementing properties. For example, group IV TMDC 1*T*-TiS_2 is a metal/semi-metal, while its TMTC counterpart TiS_3 is a semiconductor with a direct band gap, independent of its thickness. Phase-engineering between TMDCs and TMTCs with complementing material properties has not yet gained much attention. Similar to the controlled synthesis between two TMDC phases, the phase-controlled synthesis between TMDCs and TMTCs can be obtained by carefully tuning the temperature and precursor pressure, as will be addressed in Chapter 3 and 5. Consequently, phase-controlled synthesis could be extended to an extra dimension by synthesizing TMDCs and TMTCs in a controlled manner, as illustrated in Figure 1.4.

1.5 Heterostructures

Dissimilar layered materials with strong in-plane covalent bonds and weak out-of-plane van der Waals interactions can be stacked on top of each other, forming a new composite[64,65,66]. In traditional 3D heterostructures like III-Vs on Si, there are challenges such as lattice mismatch and dangling bonds that result in defects and strain at the interface, restricting the viability of these kinds of heterostructures in (opto)electronic device applications[67]. However, in the case of layered materials, the heterostructures can be potentially fabricated without the constraints of lattice crystal structure mismatch and the creation of defects at the interface, due to the weak van der Waals interaction between the material layers[68,65,69]. To that end, these layered materials could be very suitable for next-generation (opto)electronic device fabrication and integration[64,70]. Furthermore, flexibility in stacking various layered materials on top of each other opens up new possibilities in terms of both unexplored properties and applications[69].

An example is the coupling of charge carriers (holes and electrons) from different material layers in the heterostructure under electrical or optical excitation, emitting indirect excitons at lower energy than those from the respective individual materials in the heterostructures[71,72,73]. The interlayer excitons generated at the interface of the dissimilar layers (heterostructure) create opportunities to construct tunable (opto)electronics devices such as photoemitters, photodetectors, photovoltaics, etc. with a thickness of bilayer and more.

In terms of device performance, for example, in 2D TMDC FETs, recent reports have shown that metal-semiconductor heterostructures consisting of a 2D-2D layered material

architecture offer advantageous over a 3D-2D architecture[74,75,76]. 2D-2D TMDC heterostructures offer, for example, low contact resistance as the result of low Schottky barrier height[77,41]. However, synthesizing such 2D-2D heterostructures over a large area is a persisting challenge which restricts their prospects for large scale device fabrication and implementation[69,78]. Additionally, devices made of only layered materials are worth exploring for improved and efficient device performance[69,79].

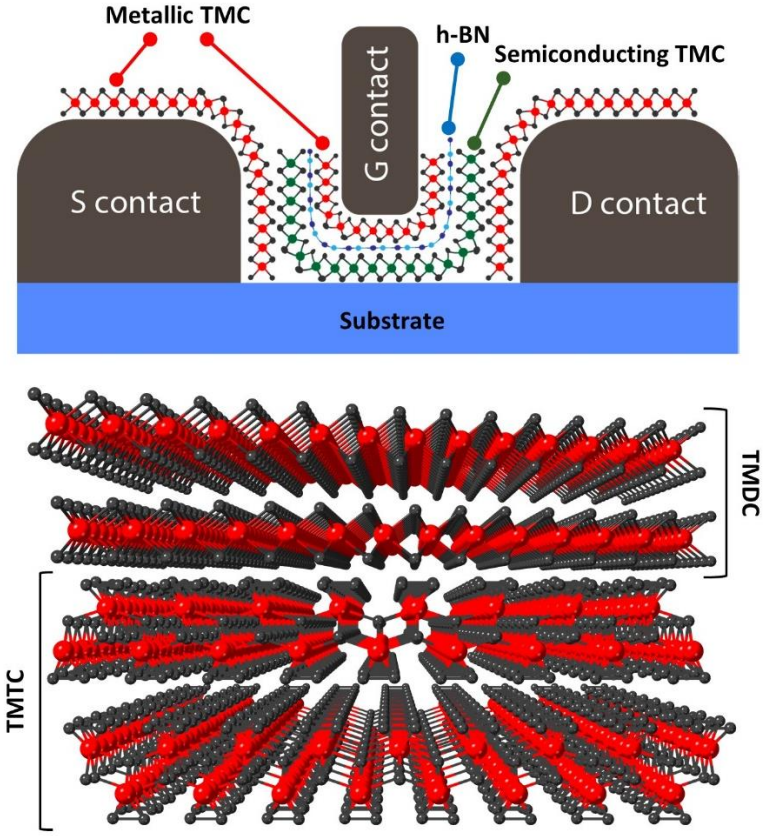

Figure 1.5 Schematic illustration of conformal coverage of TMDC based heterostructures in a 2D FETs with a complex structure (top) and a TMDC-TMTC heterostructure (bottom). The S, D, and G contacts correspond to the source, drain, and gate in the FET.

The methods commonly used to fabricate 2D-2D TMDC heterostructures are top-down mechanical exfoliation and transfer, and bottom-up CVD[20,80]. While the former method provides flexibility to stack almost any 2D material on one another, it has limitations such as contamination, poor scalability, and reproducibility[80,69]. The latter bottom-up CVD method can overcome the above limitations by directly synthesizing the target 2D material on another 2D material[75]. However, this method also suffers from limitations such as poor uniformity and thickness control along with the requirement of higher processing

temperatures (> 450 °C), restricting its integration with the semiconductor device processing steps[78]. In addition to the aforementioned limitations, there is also a need for fabricating such 2D-2D TMDC heterostructure conformally (see Figure 1.5 (top)) over complex 3D structures (which will be discussed in Chapter 4), as device architectures continue to become increasingly complex with the continuous trend in downscaling of device dimensions. Hence, there is a necessity to explore alternative methods to overcome all or most of these limitations.

On the other hand, to the best of our knowledge, experimentally integrating TMTCs in the heterostructure configuration is yet to be reported, as the primary research focus has been on TMDC-TMDC heterostructures configurations. In literature, low contact resistivity has been reported for metal-semiconductor heterostructures synthesized using analogous elements[39,65]. As mentioned in the previous section, TMDCs and TMTCs with analogous elements in both groups, IV and V, have complementing electrical properties exhibiting both semiconducting and metallic behavior, respectively. Therefore, for high-performance device applications, it is worth exploring the fabrication of metal-semiconductor heterostructures based on TMDC-TMTC configuration with analogous elements (see Chapter 5), as shown in Figure 1.5 (bottom).

1.6 Application of TMCs

As discussed, TMCs have been investigated for a broad range of applications. However, within the scope of this dissertation, we focus on implementing ALD-prepared TMCs for electrochemical applications, specifically the hydrogen evolution reaction (HER).

1.6.1 Hydrogen Evolution Reaction (HER)

Renewable green energy sources are gaining significant interests because of the expected depletion of traditional energy sources such as fossil fuels and coal, and increasing levels of global warming due to the use of fossil fuels[81]. Hydrogen is an important candidate as a renewable energy source due to its abundance, clean, and renewable nature. Electrochemical water splitting is a well-known method to generate hydrogen and oxygen. A catalyst is the key component for the electrochemical HER. Noble metals like Pt have been considered the most effective electrocatalysts for HER, but their high cost and low abundancy make the scalable use expensive and unsustainable. Thus, there is a quest to find low cost, abundant alternative catalysts offering equal or better HER efficiency. In

recent times, 2D TMDCs have emerged as promising alternative electrocatalysts[40,81]. Among them, semiconducting group VI TMDCs such as MoS_2, WS_2, etc. have been studied extensively. Such semiconducting TMDCs are HER active only at the edges of their basal planes, while the top of the basal planes (holding the significant share of surface area) are HER inert[40]. So, to harvest from the active edge sites with high efficiency, there is a requirement to synthesize edge enriched semiconducting TMDC films[82].

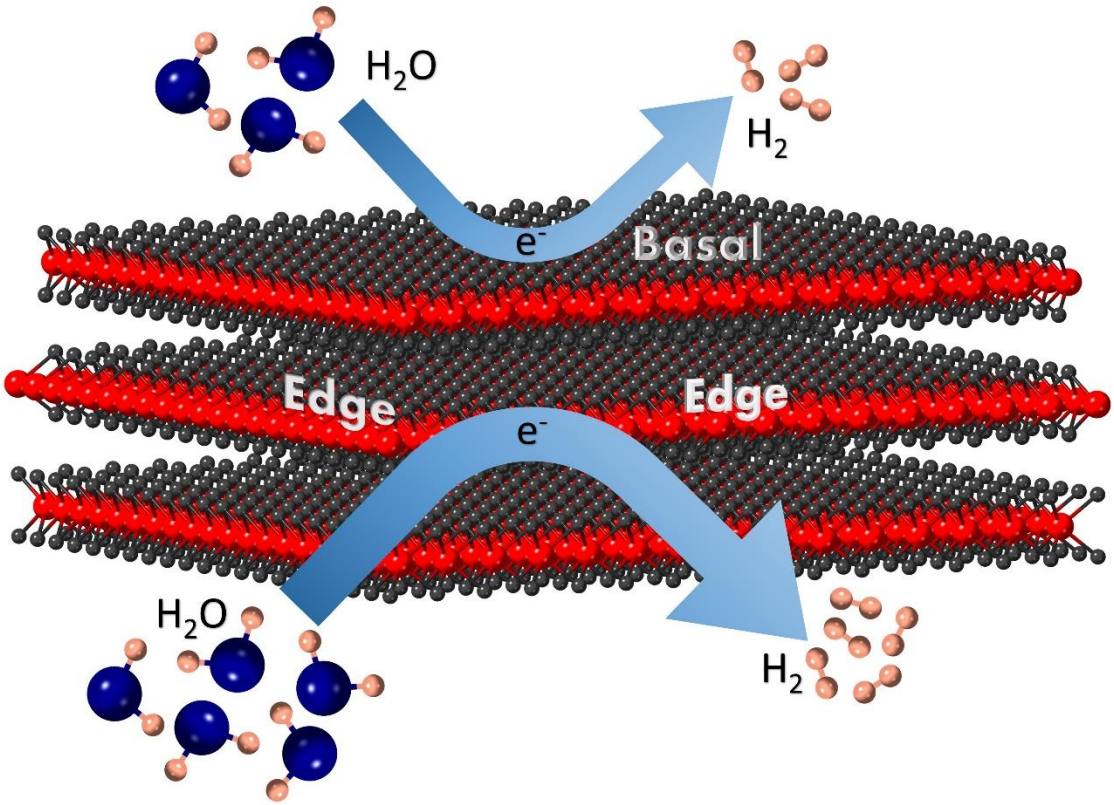

Figure 1.6 Schematic illustration of two forms of electrocatalytically active sites in TMDC class of materials: basal plane and edge sites.

On the contrary, based on theoretical predictions, metallic TMDCs of group V have emerged as an alternative option, as they have HER active sites both on the edges and basal planes[40], as shown in Figure 1.6. Theoretical calculations predict close to thermoneutral Gibbs free energy for hydrogen adsorption on the basal plane of group V TMDCs[83]. Correspondingly, experimental studies have shown excellent HER performance for NbS_2 and TaS_2[84–89]. Nevertheless, such superior HER performance was observed as a result of a self-optimizing depletion/ delamination process over an extensive number of reaction cycles. Meaning, the HER activity improvement was at the cost of the catalyst stability. It is detrimental since both activity and stability are essential for a good catalyst. Thus, casting

doubt over the use of metallic TMDCs for catalytic applications. This depletion problem was reported for catalysts synthesized by solid state reactions or CVD with inadequate area coverage and/or with weak interaction with the substrate. Therefore, there is a quest for an alternate synthesis technique that provides TMDCs layers with a stronger adhesion to the substrate and better substrate coverage (as will be discussed in Chapter 6).

1.7 Aim of this Research

The research interests in the thin-film synthesis of layered TMCs are continuing to grow. Among various thin-film synthesis methods, lately, ALD has gained significant interest for the synthesis of TMCs. As mentioned in the previous section, most of the ALD research interests have been primarily focused on group VI semiconducting TMDCs such as MoS_2, WS_2, etc. As discussed, in addition to semiconducting TMDCs, there is also a need to explore other layered group IV and V TMCs with exciting properties, which include metallic TMDCs and their semiconducting TMTCs counterparts. Although other thin-film techniques have been utilized to synthesize metallic TMDCs, the quest to achieve precise thickness control over a large area with uniform coverage persists, to successfully and efficiently implement them in the device and catalytic applications. As evident from the above discussions, for implementation of TMTCs in device fabrication and applications, thus far, a multi-step top-down approach are required to thin the bulk crystals. Hence, there is a clear need for scalable synthesis of TMTC thin films over a large area with precise thickness control and excellent uniformity and conformality. As discussed in the previous section, ALD is expected to be able to fulfill most of the abovementioned synthesis requirements at low processing temperatures.

ALD for TMC (TMDC and TMTC) Synthesis

The first objective of this research is to expand the ALD toolbox to synthesize both TMDCs and TMTCs of group IV and V by direct ALD and indirect ALD (*e.g.,* by chalcogenization of transition metal oxides) approaches. To do so, we choose Ti and Nb based sulfide and oxide systems, respectively, because TMDC and TMTC of TiS_x and NbS_x systems were identified to offer complementing material properties (metal and semiconductor). The following objectives are addressed in this research:

- Develop new direct ALD processes to synthesize both TiS_x and NbS_x material systems with precise thickness control over a large area at low temperatures (Chapter 3, 4 and 5).

- Assess if ALD can be a viable technique to achieve phase-engineering between TMDC and TMTC of the TiS_x and NbS_x material systems (Chapter 3 and 5).

Next, as discussed before, in addition to the direct ALD growth, there is an alternative high temperature approach to synthesize TMDCs. However, thus far, this indirect ALD based approach has been reported only to synthesize semiconducting group VI TMDCs. Therefore, the following objective is addressed in this research:

- Develop an indirect ALD based process for the growth of a metallic TMDC (NbS_2) by chalcogenization of ALD grown transition metal oxide film at high temperature and compare its material and film properties with the NbS_2 synthesized by direct ALD (Chapter 6, 7).

ALD for Heterostructure Formation

As mentioned in previous sections, there is a prevailing challenge to fabricate TMC-TMC based heterostructures over a large area with good thickness control, uniformity, and conformality. This challenge could be tackled by using ALD at low processing temperatures. However, this has yet to be explored experimentally. Also, experimental studies on integrating TMTCs with TMDCs in a heterostructure configuration have yet to be explored. Therefore, the following objectives are addressed in this research work:

- Fabricate TMDC-TMDC (*e.g.,* TiS_2-NbS_2) heterostructures over a large area at low temperatures using ALD, and to achieve excellent uniformity and precise thickness control of the individual material layers within the heterostructure (Chapter 4).

- Explore the capability of ALD to grow heterostructures conformally over a 3D substrate with good thickness control and uniformity (Chapter 4).

- Explore whether the TMTC synthesized by phase-engineering can be integrated with the corresponding TMDC to synthesize TMDC-TMTC (*e.g.,* NbS_2-NbS_3) heterostructures directly using ALD (Chapter 5).

ALD of TMDCs for Electrochemical Applications

In terms of application, as discussed in the previous section, metallic group V TMDCs (*e.g.,* NbS_2) have gained interests as an alternative electrocatalytic material for HER. However, the observed superior catalytic performance of NbS_2 was a result of depletion/ delamination of poorly covered electrodes, which raises serious doubts about the stability and reliability of these metallic TMDCs. ALD might offer a better adhesion of the TMDC to the electrode because of the ALD process's chemical nature and provide uniform coverage over a large area. Hence, the following objective involving uniformly covered metallic TMDCs formed by various ALD processes will be covered in this thesis:

- Investigate and compare the catalytic HER activity and stability of direct and indirect ALD grown metallic TMDC electrodes (*e.g.,* NbS_2) with uniform coverage over a large area (Chapter 6).

1.8 Outline of the Thesis

An overview of the crystal structures and properties of both TMDCs and TMTCs is provided in Chapter 2. The chapter also includes a brief discussion on various structural polytypes of TMDCs and TMTCs. The wide range of properties observed for various combinations of transition metals and chalcogenides are described. The chapter also illustrates various synthesis methods for the fabrication of both TMDCs and TMTCs, including the ALD technique.

Chapter 3 presents a new ALD process developed for TiS_x using a metal organic precursor and H_2S (gas or plasma) as coreactant. The chapter deals with the role of deposition temperature and coreactant (H_2S gas or H_2S plasma) in the phase-controlled synthesis of TiS_2 (TMDC) and TiS_3 (TMTC) by ALD. This work is the first to report on the synthesis of TMTCs by ALD.

Chapter 4 describes ALD´s capability to grow TMDC-TMDC heterostructures in the form of TiS_x-NbS_x on both planar and 3D substrates. This chapter also presents a new ALD process developed for the deposition of NbS_x by thermal ALD. This work also demonstrates the efficacy of ALD to precisely control the thickness of the individual material layer in a heterostructure. It then presents the ability of ALD to deposit multilayer TiS_x-NbS_x heterostructures conformally over a nanowire array.

Chapter 5 introduces a new plasma enhanced ALD (PE-ALD) process for the phase-controlled synthesis of NbS_2 and NbS_3. This chapter also discusses the role of the coreactant plasma composition in obtaining phase-control between TMDC and TMTC, in addition to achieving control by deposition temperature. This work includes the deposition of NbS_2-NbS_3 heterostructures by PE-ALD at a constant deposition temperature.

Chapter 6 addresses the HER performance of ALD-derived NbS_2. Various ALD synthesis routes for NbS_2, including direct ALD-grown NbS_2 and sulfurized ALD-grown Nb_2O_5 (indirect), are compared in terms of HER activity and stability.

The development of a new ALD process for the synthesis of Nb_2O_5 films is presented in Chapter 7. Both thermal ALD and PE-ALD processes are developed using H_2O and O_2 plasma as coreactant, respectively. The role of coreactant and temperature on material properties and composition are compared.

Chapter 8 concludes this thesis by summarizing the contents of this dissertation and providing an outline for future research on low-dimensional TMCs using the ALD toolbox.

References

[1] Richard P. Feynman, Eng. Sci. **23**, 22 (1960).

[2] Andreas Öchsner, L.F.M. da Silva, and H. Altenbach, *Advanced Structured Materials EMR/ESR/EPR Spectroscopy for Characterization of Nanomaterials* (2017).

[3] D.E. Mainwaring, A.L. Let, C. Rix, and P. Murugaraj, Solid State Commun. **140**, 355 (2006).

[4] M.G. Stanford, P.D. Rack, and D. Jariwala, Npj 2D Mater. Appl. **2**, 20 (2018).

[5] A.B. Evlyukhin, C. Reinhardt, U. Zywietz, and B.N. Chichkov, Phys. Rev. B **85**, 245411 (2012).

[6] M.H. Rashid and T.K. Mandal, J. Phys. Chem. C **111**, 16750 (2007).

[7] S. Iijima, Nature **354**, 56 (1991).

[8] H.W. Kroto, J.R. Heath, S.C. O'Brien, R.F. Curl, and R.E. Smalley, Nature **318**, 162 (1985).

[9] K.S. Novoselov, Science (80-.). **306**, 666 (2004).

[10] M. Naguib, M. Kurtoglu, V. Presser, J. Lu, J. Niu, M. Heon, L. Hultman, Y. Gogotsi, and M.W. Barsoum, Adv. Mater. **23**, 4248 (2011).

[11] C. Tan, X. Cao, X.J. Wu, Q. He, J. Yang, X. Zhang, J. Chen, W. Zhao, S. Han, G.H. Nam, M. Sindoro, and H. Zhang, Chem. Rev. **117**, 6225 (2017).

[12] K. Khan, A.K. Tareen, M. Aslam, R. Wang, Y. Zhang, A. Mahmood, Z. Ouyang, H. Zhang, and Z. Guo, *Recent Developments in Emerging Two-Dimensional Materials and Their Applications* (Royal Society of Chemistry, 2020).

[13] T. Gould, S. Lebègue, T. Björkman, and J.F. Dobson, Semicond. Semimetals **95**, 1 (2016).

[14] K. Khan, A.K. Tareen, M. Aslam, R. Wang, Y. Zhang, A. Mahmood, Z. Ouyang, H. Zhang, and Z. Guo, J. Mater. Chem. C **8**, 387 (2020).

[15] C.-C. Cheng, Y.-Y. Chung, U.-Y. Li, C.-T. Lin, C.-F. Li, J.-H. Chen, T.-Y. Lai, K.-S. Li, J.-M. Shieh, S.-K. Su, H.-L. Chiang, T.-C. Chen, L.-J. Li, H.-S.P. Wong, and C.-H. Chien, in *2019 Symp. VLSI Technol.* (IEEE, 2019), pp. T244–T245.

[16] T. Agarwal, A. Szabo, M.G. Bardon, B. Soree, I. Radu, P. Raghavan, M. Luisier, W. Dehaene, and M. Heyns, in *2017 IEEE Int. Electron Devices Meet.* (IEEE, 2017), pp. 5.7.1-5.7.4.

[17] Q. Smets, B. Groven, M. Caymax, I. Radu, G. Arutchelvan, J. Jussot, D. Verreck, I. Asselberghs, A.N. Mehta, A. Gaur, D. Lin, and S. El Kazzi, in *2019 IEEE Int. Electron Devices Meet.* (IEEE, 2019), pp. 23.2.1-23.2.4.

[18] T. Dai, Y. Liu, X. Liu, D. Xie, and Y. Li, J. Alloys Compd. **785**, 951 (2019).

[19] S. Liu, W. Xiao, M. Zhong, L. Pan, X. Wang, H.-X. Deng, J. Liu, J. Li, and Z. Wei, Nanotechnology **29**, 184002 (2018).

[20] H. Tian, M.L. Chin, S. Najmaei, Q. Guo, F. Xia, H. Wang, and M. Dubey, Nano Res. **9**, 1543 (2016).

[21] M. Ye, D. Zhang, and Y.K. Yap, Electronics **6**, 43 (2017).

[22] P. Huang, L. Yuan, K. Zhang, Q. Chen, Y. Zhou, B. Song, and Y. Li, ACS Appl. Mater. Interfaces **10**, 14796 (2018).

[23] P. Huang, Q. Chen, K. Zhang, L. Yuan, Y. Zhou, B. Song, and Y. Li, J. Mater. Chem. A (2019).

[24] T. Jeong, S.Y. Ham, B. Koo, P. Lee, Y.S. Min, J.Y. Kim, and M.J. Ko, J. Ind. Eng. Chem. **80**, 106 (2019).

[25] R.G. Dickinson and L. Pauling, J. Am. Chem. Soc. **45**, 1466 (1923).

[26] G. Lu, K. Yu, Z. Wen, and J. Chen, Nanoscale **5**, 1353 (2013).

[27] R. F. Frindt and A. D. Yoffe, Proc. R. Soc. London. Ser. A. Math. Phys. Sci. **273**, 69 (1963).

[28] P. Joensen, R.F. Frindt, and S.R. Morrison, Mater. Res. Bull. **21**, 457 (1986).

[29] K.F. Mak, C. Lee, J. Hone, J. Shan, and T.F. Heinz, Phys. Rev. Lett. **105**, 136805 (2010).

[30] A. Splendiani, L. Sun, Y. Zhang, T. Li, J. Kim, C.-Y. Chim, G. Galli, and F. Wang, Nano Lett. **10**, 1271 (2010).

[31] H. Zeng, J. Dai, W. Yao, D. Xiao, and X. Cui, Nat. Nanotechnol. **7**, 490 (2012).

[32] K.F. Mak, K. He, J. Shan, and T.F. Heinz, Nat. Nanotechnol. **7**, 494 (2012).

[33] B. Radisavljevic, A. Radenovic, J. Brivio, V. Giacometti, and A. Kis, Nat. Nanotechnol. **6**, 147 (2011).

[34] W. Choi, M.Y. Cho, A. Konar, J.H. Lee, G.-B. Cha, S.C. Hong, S. Kim, J. Kim, D. Jena, J. Joo, and S. Kim, Adv. Mater. **24**, 5832 (2012).

[35] O. Lopez-Sanchez, D. Lembke, M. Kayci, A. Radenovic, and A. Kis, Nat. Nanotechnol. **8**, 497 (2013).

[36] C. Chakraborty, L. Kinnischtzke, K.M. Goodfellow, R. Beams, and A.N. Vamivakas, Nat. Nanotechnol. **10**, 507 (2015).

[37] M. Koperski, K. Nogajewski, A. Arora, V. Cherkez, P. Mallet, J.-Y. Veuillen, J. Marcus, P. Kossacki, and M. Potemski, Nat. Nanotechnol. **10**, 503 (2015).

[38] Y.M. He, G. Clark, J.R. Schaibley, Y. He, M.C. Chen, Y.J. Wei, X. Ding, Q. Zhang, W. Yao, X. Xu, C.Y. Lu, and J.W. Pan, Nat. Nanotechnol. **10**, 497 (2015).

[39] R. Kappera, D. Voiry, S.E. Yalcin, B. Branch, G. Gupta, A.D. Mohite, and M. Chhowalla, Nat. Mater. **13**, 1128 (2014).

[40] X. Chia, A. Ambrosi, P. Lazar, Z. Sofer, and M. Pumera, J. Mater. Chem. A **4**, 14241 (2016).

[41] S. Kim, Y.C. Kim, Y.J. Choi, H.J. Woo, Y.J. Song, M.S. Kang, C. Lee, and J.H. Cho, ACS Appl.

Mater. Interfaces **11**, 35444 (2019).

[42] K. Yang, X. Wang, H. Li, B. Chen, X. Zhang, S. Li, N. Wang, H. Zhang, X. Huang, and W. Huang, Nanoscale **9**, 5102 (2017).

[43] M.M. Furchi, F. Höller, L. Dobusch, D.K. Polyushkin, S. Schuler, and T. Mueller, Npj 2D Mater. Appl. **2**, 3 (2018).

[44] X. Liu and M.C. Hersam, Nat. Rev. Mater. **4**, 669 (2019).

[45] J.O. Island, M. Buscema, M. Barawi, J.M. Clamagirand, J.R. Ares, C. Sánchez, I.J. Ferrer, G.A. Steele, H.S.J. van der Zant, and A. Castellanos-Gomez, Adv. Opt. Mater. **2**, 641 (2014).

[46] A. Lipatov, P.M. Wilson, M. Shekhirev, J.D. Teeter, R. Netusil, and A. Sinitskii, Nanoscale **7**, 12291 (2015).

[47] Y. Niu, R. Frisenda, E. Flores, J.R. Ares, W. Jiao, D. Perez de Lara, C. Sánchez, R. Wang, I.J. Ferrer, and A. Castellanos-Gomez, Adv. Opt. Mater. **6**, 1800351 (2018).

[48] A.J. Molina-Mendoza, J.O. Island, W.S. Paz, J.M. Clamagirand, J.R. Ares, E. Flores, F. Leardini, C. Sánchez, N. Agraït, G. Rubio-Bollinger, H.S.J. van der Zant, I.J. Ferrer, J.J. Palacios, and A. Castellanos-Gomez, Adv. Funct. Mater. **27**, 1605647 (2017).

[49] R. Frisenda, E. Giovanelli, P. Mishra, P. Gant, E. Flores, C. Sánchez, J.R. Ares, D. Perez de Lara, I.J. Ferrer, E.M. Pérez, and A. Castellanos-Gomez, Chem. Commun. **53**, 6164 (2017).

[50] E. Flores, J.R. Ares, C. Sánchez, and I.J. Ferrer, Catal. Today **321–322**, 107 (2019).

[51] J.O. Island, A.J. Molina-Mendoza, M. Barawi, R. Biele, E. Flores, J.M. Clamagirand, J.R. Ares, C. Sánchez, H.S.J. van der Zant, R. D'Agosta, I.J. Ferrer, and A. Castellanos-Gomez, 2D Mater. **4**, 022003 (2017).

[52] G.N. Parsons, J.W. Elam, S.M. George, S. Haukka, H. Jeon, W.M.M. (Erwin) Kessels, M. Leskelä, P. Poodt, M. Ritala, and S.M. Rossnagel, J. Vac. Sci. Technol. A Vacuum, Surfaces, Film. **31**, 050818 (2013).

[53] K. Mistry, R. Chau, C.-H. Choi, G. Ding, K. Fischer, T. Ghani, R. Grover, W. Han, D. Hanken, M. Hattendorf, J. He, C. Allen, J. Hicks, R. Huessner, D. Ingerly, P. Jain, R. James, L. Jong, S. Joshi, C. Kenyon, K. Kuhn, K. Lee, C. Auth, H. Liu, J. Maiz, B. McIntyre, P. Moon, J. Neirynck, S. Pae, C. Parker, D. Parsons, C. Prasad, L. Pipes, B. Beattie, M. Prince, P. Ranade, T. Reynolds, J. Sandford, L. Shifren, J. Sebastian, J. Seiple, D. Simon, S. Sivakumar, P. Smith, D. Bergstrom, C. Thomas, T. Troeger, P. Vandervoorn, S. Williams, K. Zawadzki, M. Bost, M. Brazier, M. Buehler, and A. Cappellani, in *2007 IEEE Int. Electron Devices Meet.* (IEEE, 2007), pp. 247–250.

[54] M.A. Hossain, K.T. Khoo, X. Cui, G.K. Poduval, T. Zhang, X. Li, W.M. Li, and B. Hoex, Nano Mater. Sci. (2019).

[55] J. Song, J. Park, W. Lee, T. Choi, H. Jung, C.W. Lee, S. Hwang, J.M. Myoung, J. Jung, S.-H. Kim, C. Lansalot-Matras, and H. Kim, ACS Nano **7**, 11333 (2013).

[56] J. Wang, Y. Wei, H. Li, X. Huang, and H. Zhang, Sci. China Chem. **61**, 1227 (2018).

[57] D. Voiry, A. Mohite, and M. Chhowalla, Chem. Soc. Rev. **44**, 2702 (2015).

[58] Y. Xiao, M. Zhou, J. Liu, J. Xu, and L. Fu, Sci. China Mater. **62**, 759 (2019).

[59] Z. Qian, L. Jiao, and L. Xie, Chinese J. Chem. cjoc. 202000064 (2020).

[60] X. Wang, X. Shen, Z. Wang, R. Yu, and L. Chen, ACS Nano **8**, 11394 (2014).

[61] D. Li, X. Wang, C. Kan, D. He, Z. Li, Q. Hao, H. Zhao, C. Wu, C. Jin, and X. Cui, ACS Appl. Mater. Interfaces acsami.0c04449 (2020).

[62] J.H. Sung, H. Heo, S. Si, Y.H. Kim, H.R. Noh, K. Song, J. Kim, C.-S. Lee, S.-Y. Seo, D.-H. Kim, H.K. Kim, H.W. Yeom, T.-H. Kim, S.-Y. Choi, J.S. Kim, and M.-H. Jo, Nat. Nanotechnol. **12**, 1064 (2017).

[63] S. Cheng, L. Yang, J. Li, Z. Liu, W. Zhang, and H. Chang, CrystEngComm **19**, 1045 (2017).

[64] A.K. Geim and I. V Grigorieva, Nature **499**, 419 (2013).

[65] Y. Liu, N.O. Weiss, X. Duan, H.-C. Cheng, Y. Huang, and X. Duan, Nat. Rev. Mater. **1**, 16042 (2016).

[66] W. Liao, Y. Huang, H. Wang, and H. Zhang, Appl. Mater. Today **16**, 435 (2019).

[67] L.A. Walsh and C.L. Hinkle, Appl. Mater. Today **9**, 504 (2017).

[68] D.S. Koda, F. Bechstedt, M. Marques, and L.K. Teles, J. Phys. Chem. C **120**, 10895 (2016).

[69] D.M. Hamann, E.C. Hadland, and D.C. Johnson, Semicond. Sci. Technol. **32**, 093004 (2017).

[70] K.S. Novoselov, A. Mishchenko, A. Carvalho, and A.H. Castro Neto, Science (80-.). **353**, aac9439 (2016).

[71] S. Lukman, L. Ding, L. Xu, Y. Tao, A.C. Riis-Jensen, G. Zhang, Q.Y.S. Wu, M. Yang, S. Luo, C. Hsu, L. Yao, G. Liang, H. Lin, Y.W. Zhang, K.S. Thygesen, Q.J. Wang, Y. Feng, and J. Teng, Nat. Nanotechnol. (2020).

[72] Y. Gong, J. Lin, X. Wang, G. Shi, S. Lei, Z. Lin, X. Zou, G. Ye, R. Vajtai, B.I. Yakobson, H. Terrones, M. Terrones, B.K. Tay, J. Lou, S.T. Pantelides, Z. Liu, W. Zhou, and P.M. Ajayan, Nat. Mater. **13**, 1135 (2014).

[73] K. Koåmider and J. Fernández-Rossier, Phys. Rev. B - Condens. Matter Mater. Phys. **87**, 2 (2013).

[74] A. Di Bartolomeo, Phys. Rep. **606**, 1 (2016).

[75] Y. Liu, S. Zhang, J. He, Z.M. Wang, and Z. Liu, Nano-Micro Lett. **11**, (2019).

[76] Y. Wang, J.C. Kim, R.J. Wu, J. Martinez, X. Song, J. Yang, F. Zhao, A. Mkhoyan, H.Y. Jeong, and M. Chhowalla, Nature **568**, 70 (2019).

[77] Y. Liu, P. Stradins, and S.-H. Wei, Sci. Adv. **2**, e1600069 (2016).

[78] R. Dong and I. Kuljanishvili, J. Vac. Sci. Technol. B, Nanotechnol. Microelectron. Mater. Process. Meas. Phenom. **35**, 030803 (2017).

[79] T. Roy, M. Tosun, J.S. Kang, A.B. Sachid, S.B. Desai, M. Hettick, C.C. Hu, A. Javey, and

R.O.Y.E.T. Al, ACS Nano **8**, 6259 (2014).

[80] D. Chu and E.K. Kim, J. Korean Phys. Soc. **73**, 805 (2018).

[81] H. Pan, Sci. Rep. **4**, 5348 (2015).

[82] D. Kong, H. Wang, J.J. Cha, M. Pasta, K.J. Koski, J. Yao, and Y. Cui, Nano Lett. **13**, 1341 (2013).

[83] C. Tsai, K. Chan, J.K. Nørskov, and F. Abild-Pedersen, Surf. Sci. **640**, 133 (2015).

[84] J. Si, Q. Zheng, H. Chen, C. Lei, Y. Suo, B. Yang, Z. Zhang, Z. Li, L. Lei, Y. Hou, and K. (Ken) Ostrikov, ACS Appl. Mater. Interfaces **11**, 13205 (2019).

[85] P. Gnanasekar, D. Periyanagounder, P. Varadhan, J.-H. He, and J. Kulandaivel, ACS Appl. Mater. Interfaces **11**, 44179 (2019).

[86] L. Najafi, S. Bellani, R. Oropesa-Nuñez, B. Martín-García, M. Prato, V. Mazánek, D. Debellis, S. Lauciello, R. Brescia, Z. Sofer, and F. Bonaccorso, J. Mater. Chem. A **7**, 25593 (2019).

[87] J. Yang, A.R. Mohmad, Y. Wang, R. Fullon, X. Song, F. Zhao, I. Bozkurt, M. Augustin, E.J.G. Santos, H.S. Shin, W. Zhang, D. Voiry, H.Y. Jeong, and M. Chhowalla, Nat. Mater. (2019).

[88] J. Zhang, J. Wu, X. Zou, K. Hackenberg, W. Zhou, W. Chen, J. Yuan, K. Keyshar, G. Gupta, A. Mohite, P.M. Ajayan, and J. Lou, Mater. Today **25**, 28 (2019).

[89] C. Huang, X. Wang, D. Wang, W. Zhao, K. Bu, J. Xu, X. Huang, Q. Bi, J. Huang, and F. Huang, Chem. Mater. **31**, 4726 (2019).

Transition Metal Di- and Tri-Chalcogenides: Structure, Properties, and Synthesis

2

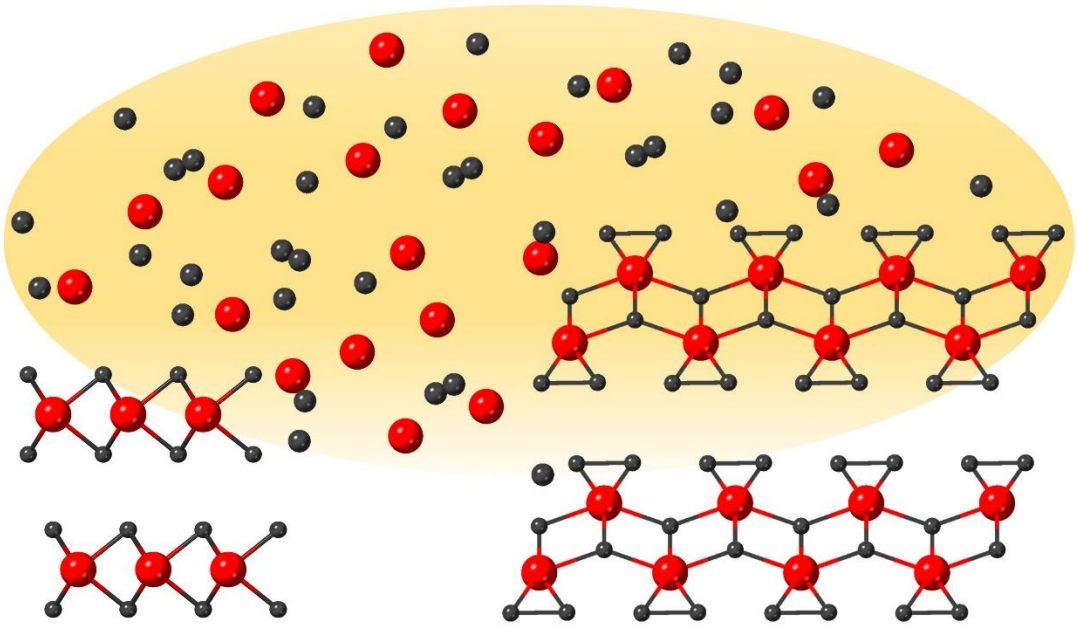

This chapter provides an overview of the structure, properties and synthesis of transition metal di- and tri-chalcogenides. First, the crystal structure and polymorphism of transition metal di- (TMDCs) and tri-chalcogenides (TMTCs) are discussed. The associated relation between the structural polytype and composition with their functional properties is briefly described. Finally, various synthesis techniques to fabricate both TMDCs and TMTCs are reviewed.

2.1 Structure and Properties

Transition metals and chalcogenides are highly reactive with each other, constructing a number of transition metal chalcogenide (TMC) combinations with various structural polymorphs and stoichiometric ratios. Among the various TMCs, TMDCs (transition metal dichalcogenides) have multiple structural polymorphs (polytypes), determining their functional properties. For example: octahedral (2*H*) MoS_2 is a semiconductor, while trigonal prismatic (1*T*) MoS_2 is a metal[1]. Similarly, transition metal dichalcogenides and transition metal trichalcogenides (TMTCs) containing analogous elements but with different stoichiometry have distinct properties. For example, TiS_2 is a metal/semi-metal, while TiS_3 is a direct band gap semiconductor[2]. Therefore, for effective control over material properties during synthesis, it is imperative to know the TMC's crystal structures and associated structural polymorphs. In the next section, we will discuss the crystal structure and various phases (structural polymorphs) observed for TMDCs, which will be followed by a discussion on the crystal structure of TMTCs.

2.1.1 Transition Metal Dichalcogenides (TMDCs)

In recent times, TMDCs (MX_2) have become one of the most studied classes of layered two-dimensional materials. These materials have a transition metal to chalcogenide ratio of 1:2, and each layer consists of three sub-layers of atoms packed hexagonally where the middle sub-layer consisting of transition metal atoms are sandwiched between two sub-layers of chalcogenide atoms, see Figure 2.1a. Within a layer (in-plane direction), all the atoms are covalently bonded to each other, while weak van der Waals forces bond one layer to another (out-of-plane direction)[3]. Therefore, there is an anisotropy in the material´s properties, i.e., between in-plane and out-of-plane orientations. The transition metal atoms in TMDCs are in the +4 oxidation state, while the chalcogenide atoms are in the -2 oxidation state, sharing two electrons each in the structural formula $(M)^{+4}((X)^{-2})_2^4$. Each TMDC can exist in various polymorphs, which determine their electronic properties.

To describe the possible polymorphs, first, the stacking options within a monolayer will be discussed, after which the permutations of stacking the two types of layers will be presented.

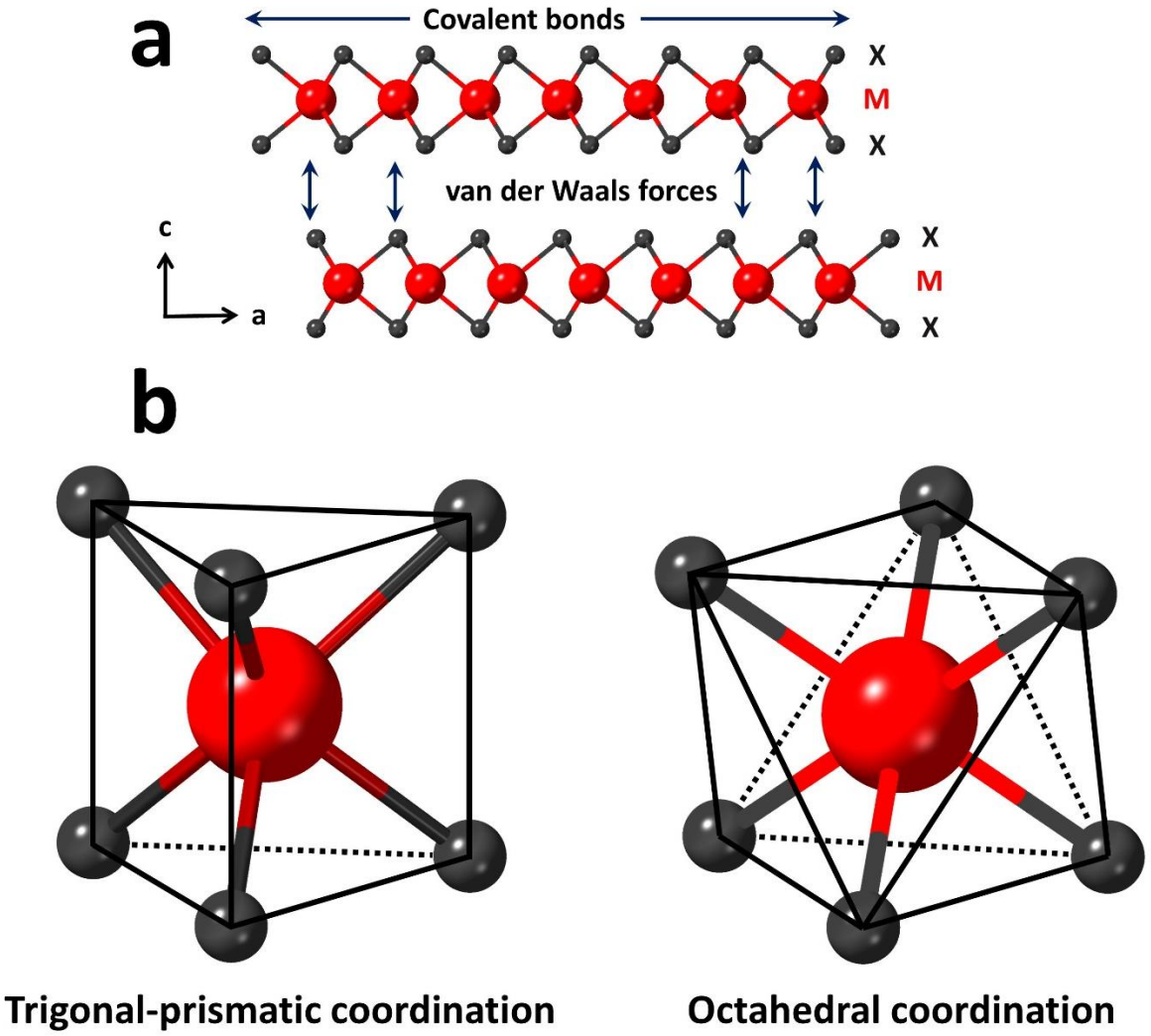

Figure 2.1 (a) Schematic illustration of 2D TMDC down the b-axis using two monolayers. The red and dark grey spheres correspond to transition metal and chalcogenide atoms, respectively. (b) The two local coordination's of the transition metal in TMDCs are: trigonal-prismatic (left) and octahedral coordination (right).

In TMDCs, each transition metal is coordinated to six chalcogenide atoms forming MX_6 units. Within one 2D monolayer, the transition metal atoms can be found in two possible coordination geometries: trigonal-prismatic and octahedral, as illustrated in Figure 2.1[5]. As TMDCs have a hexagonal lattice structure, the coordination geometries can be described using a close-packed stacking of spheres arrangement, where the stacking sequence is expressed using A, B, and C, indicating the position of the sphere. Note, the upper-case letters represent the row of chalcogenide atoms while the lower-case represents the middle row containing the transition metal atoms. In the trigonal-prismatic arrangement, the chalcogenide atoms are stacked directly above each other with a stacking sequence of AbA,

while in the octahedral arrangement, the upper chalcogenide plane is rotated 180° with respect to the lower one, leading to a stacking sequence of AbC. In general, most of the TMDCs crystal structures have naturally only one of these coordination geometries, but there are also few instances like polytype 4*H*, 6*R*, etc. (see Table 2.1 and Figure 2.2), where both the geometries are found in a single crystal structure as alternative layers[6].

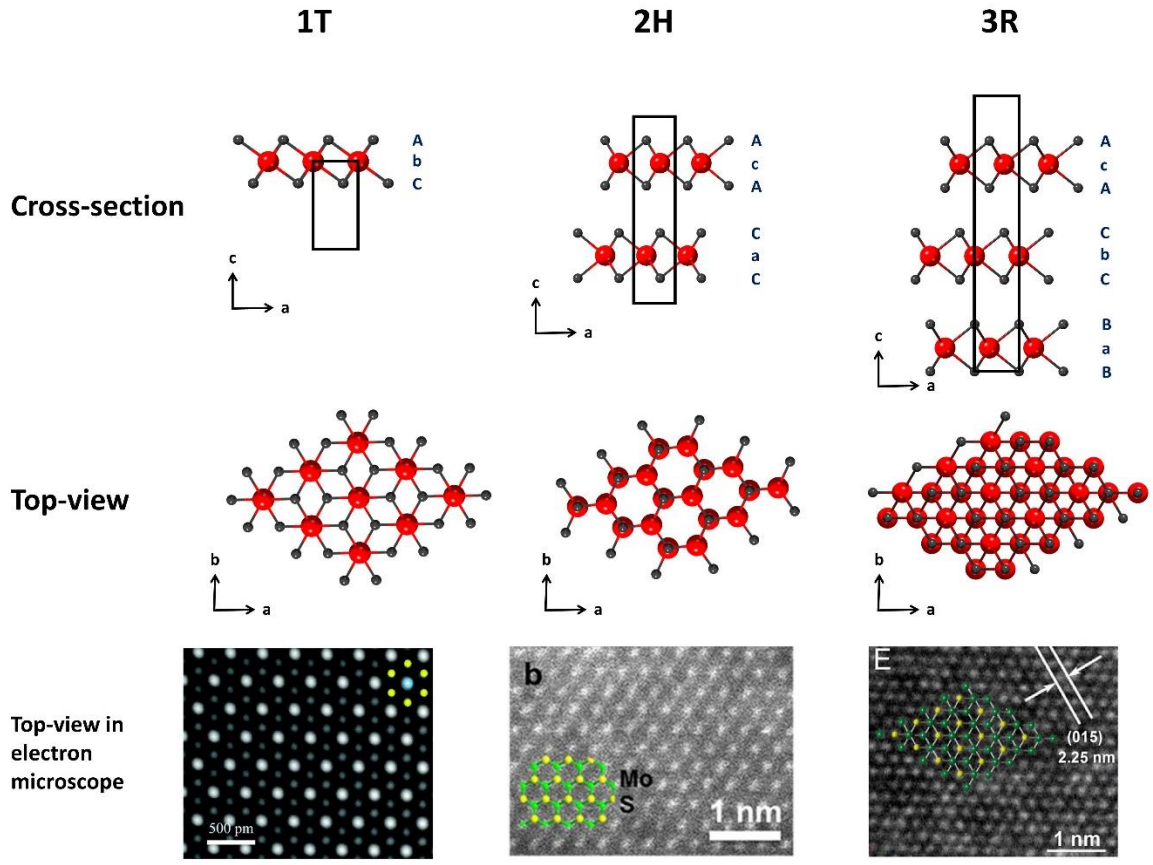

Figure 2.2 The three most common polytype structures for TMDCs are 1*T* (with trigonal symmetry, one layer per unit cell and has octahedral metal coordination), 2*H* (with hexagonal symmetry, two layers per unit cell and has trigonal-prismatic metal coordination), and 3*R* (with rhombohedral symmetry, three layers per unit cell and has trigonal-prismatic metal coordination). The upper row displays views parallel to the 2D layers of all three polytype crystal structures, each with a unit cell (in black rectangular box) is shown (view down b-axis). The central row shows the atomic arrangement when looking orthogonal to the 2D layers (view down c-axis). The corresponding top-view scanning transmission electron microscopy (STEM) images of 1*T*-TiS_2[7], 2*H*-MoS_2[8], and 3*R*-NbS_2[9] are displayed in the bottom row.

The layers with the above-mentioned coordination geometries can be stacked on top of each other in various ways forming several distinct structures known as polytypes, see Table 2.1. Most of the TMDC polytypes can be categorized into three symmetries called *T*, *H* and

R, and a significant amount of TMDCs are usually found in at least one of the three polytypes called 1*T*, 2*H* and 3*R*, as shown in Figure 2.2. In the literature, polytypes of TMDCs are generally expressed according to the Ramsdell notation, for example, 2*H*, where the number (2 in this case) represents the number of MX_2 layers (each with the formula unit MX_2) within a unit cell (represented as Z in Table 2.1), and it is followed by a letter representing the observed symmetry[10]. The notation *T*, *H* and *R* correspond to trigonal, hexagonal and rhombohedral symmetry, respectively. Both *H* and *R* symmetries have trigonal-prismatic transition metal coordination while *T* has the octahedral metal coordination[11]. While 1*T*, 2*H* and 3*R* being the most common polytypes, other polytypes such as 4*H* and 6*R* also exist, see Table 2.1 and Figure 2.3[12]. Among the polytypes mentioned above, both 2*H* and 4*H* have an added level of stacking variation within the individual unit cell of 2 and 4 MX_2 layers, and this is commonly represented in the literature by adding a lower-case letter *a*, *b*, *c*,.. etc. to the Ramsdell notation like 2*Ha*[12]. This letter indicates differences in stacking arrangement; for example, 2*Ha* and 2*Hc* have stacking sequences of AbA CbC and AcA CaC, respectively. There are also other stacking sequences like 2*Hb*, which are observed for TMDCs crystals with excess intercalated transition metal atoms, *e.g.,* $Ta_{1+x}Se_2$[11]. Note that these notations *a*, *b* and *c* are not followed uniformly in the literature, which might lead to confusion. Thus, there are more than 11 experimentally known polytypes for TMDCs, see Table 2.1[12]. Additionally, there are also TMDCs with distorted (1´*T*) structures (see Figure 2.3). They develop a periodic distortion of the crystal lattice leading to the formation of metal-metal pairs[11]. These distorted TMDCs have been observed in various structural symmetries such as monoclinic, orthorhombic and triclinic depending on the material[11]. In the literature, all of them are commonly represented as 1´*T*, and seldom they are represented in various notations such as T_d, 1*T*´ etc. Apart from the above mentioned layered TMDCs, there are other non-layered TMDCs which are mostly observed for transition metals of Group 8 and beyond, and they are not discussed here[13].

As mentioned earlier, structural variation related to polymorphism in TMDCs has a significant effect on material properties. Likewise, the chemical composition of the TMDCs also influences the properties, see Table 2.2. The electrical properties of a TMDC are primarily dependent on the valence *d* electron count of the transition metal, which varies from d^0 for group IV to d^6 for group X[4]. When the number of valence electrons in the transition metal is even (fully occupied orbitals), the material is semiconducting [4,14]. On the other hand, materials with an odd number of valence electrons (partially occupied orbitals) are metallic[4,14]. In comparison, the effect of chalcogenide atoms (six valence electrons in *s* and *p* orbitals) on the TMDC band structure is minor[4,14]. Although, a trend in band structure

in terms of band gap can be observed with the increasing atomic number of the chalcogen atom from S to Te. For example: the band gap decreases from 1.3 eV for 2*H*-MoS_2 to 1 eV for 2*H*-$MoTe_2$[13]. Below, the properties of the TMDCs will be discussed separately for each group of transition metals.

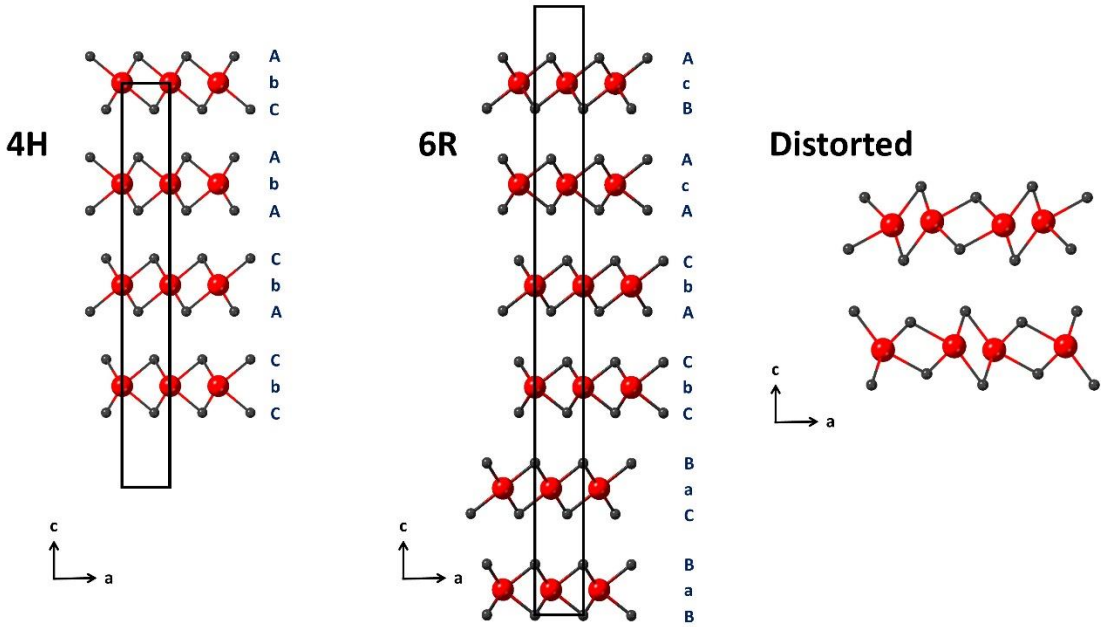

Figure 2.3 The cross-section view (down b-axis) of less common polytypes of TMDCs such as 4H, 6R, and distorted (1'*T*).

The TMDCs containing *group IV* transition metals such as Ti, Zr and Hf most commonly exists in 1*T* as the stable phase. They likely exhibit semiconducting properties, as the number of valence electron is even (d^0). Veritably, ZrS_2, $ZrSe_2$, HfS_2 and $HfSe_2$ are semiconductors except for TiX_2 and all three Te based materials. The electronic structure of TiS_2 is under debate both by experimentalists and theorists for many decades between being a metal/ semi-metal/ semiconductor[15,16]. While $TiSe_2$ and all three MTe_2 are semimetals due to overlap between the conduction and valence band states[17].

The TMDCs formed by *group V* transition metals such as V, Nb and Ta are predominantly metallic, as an odd number (d^1) of valence electrons are present. The VX_2 has 1*T* as the stable phase, while both NbX_2 and TaX_2 have 2*H* as the stable phase. In addition to 2*H*, NbS_2 and $NbSe_2$ also exist in the 1*T* and 3*R* phases, while the latter also displays a 4*H* phase. TaS_2 and $TaSe_2$ are excellent examples of TMDCs with a rich polymorphic system with more than five polytypes, including 2*H*, 1*T*, 3*R*, 4*H* and 6*R* phases[17,13].

Table 2.1 Overview of the various TMDCs polytypes. The polytypes with corresponding space group and stacking sequences are mentioned.

Z	Symmetry	Polytype	Space group	Stacking sequence
1	T	1T	$P\bar{3}m1$	AbC
2	H	2Ha	$P6_3/mmc$	AbA CbC
		2Hb	$P6_3/mmc$	AcA CaC
		2Hc	$P\bar{6}m2$	AbA BcB
3	R	3R	R3m	AcA CbC BaB
4	H	4Ha	$P\bar{6}m2$	AcA BcB CaC BcB
		4Hb	$P6_3/mmc$	AbC AbA CbA CbC
		4Hc	$P6_3mc$	AcA BcB CaC BaB
		4HdI	P3m1	AbC AbA CaB CbC
		4HdII	$P\bar{6}m2$	AbC AcA CbA CbC
6	R	6R	R3m	AcB AcA CbA CbC BaC BaB

"Z" number of MX_2 layers with the formula unit MX_2 within a unit cell

The *group VI* TMDCs with transition metals such as Mo and W have 2*H* as the stable phase except for WTe_2 and $MoTe_2$, which exist in the distorted 1´*T* phase. It is also important to note, that of all TMDCs, MoS_2 existing in 2*H* and 3*R* phases are the only naturally occurring crystal[13]. As expected for group VI transition metals with an even number of valence electrons (d^2): MoS_2, $MoSe_2$, WS_2, WSe_2, $MoTe_2$ exhibit semiconducting behavior. Nevertheless, there are also exceptions such as 1*T*-MoS_2, 1*T*-WS_2 (metastable phase) having metallic behavior, while both WTe_2 and $MoTe_2$ exhibit semi-metal properties[13].

The *group VII* TMDCs such as TcS_2, $TcSe_2$, ReS_2 and $ReSe_2$ are semiconductors with distorted 1´*T* phase[13]. Even though they have an odd number (d^3) of valence electrons, they exhibit semiconducting behavior instead of metallic. This change in property is due to the distorted 1´*T* structure of the materials, where the short distance between transition metal atoms creates clusters consisting of four atoms. This strong distortion causes splitting of bands resulting in semiconducting behavior[13].

TMDCs of *group IX*, such as Co, Rh and Ir, have layered structures only with Te and have 1*T* as the stable phase. As expected, for the transition metal with an odd number of valence electrons (d^5), all of them are metals. Similarly, all the Te based TMDCs in *group X*, such as $NiTe_2$, $PdTe_2$, and $PtTe_2$, are metallic with 1*T* as the stable phase. Like PtS_2 and $PtSe_2$, semiconducting behavior was expected for all group X Te-based TMDCs as it contains even

Table 2.2 Overview of the TMDCs. The TMDCs are classified into transition metal groups and chalcogenides. Their corresponding polytypes and material properties (for TMDC with more than one polytypes, the properties are not categorized per polytype) are mentioned.

Group	Transition metal	Chalcogenide					
		S		Se		Te	
IV	Ti	1*T*[22]	Semi-C[22], M[22], SM[22]	1*T*[22]	Semi-C[22], M[22], SM[22], CDW[22]	1*T*[22]	M[23], SM[22], CDW[22]
	Zr	1*T*[22]	Semi-C[22]	1*T*[22]	Semi-C[22]	1*T*[22]	SM[22]
	Hf	1*T*[22]	Semi-C[22]	1*T*[22]	Semi-C[22]	1*T*[22]	SM[22]
V	V	1*T*[24]	Semi-C[21], M[21], CDW[21], FM[21], MR[21]	1*T*[25], 2*H*[25], 1´*T*[26]	Semi-C[25], M[27], CDW[27], FM[27]	1*T*[28], 1'*T*[28]	M[28], CDW[28]
	Nb	1*T*[29], 2*Ha*[17], 3*R*[17]	M[13], SC[13], CDW[19]	1*T*[17], 2*Ha*[17], 4*Ha*[17], 4*Hd1*[17], 4*Hd1*[17], 3*R*[17]	M[13], SC[13], CDW[19]	1*T*[30], 1´*T*[13]	M [13], SC[13]
	Ta	1*T*[17], 2*Ha*[17], 4*Hb*[17], 3*R*[17], 6*R*[17]	M[13], SC[13], CDW[19]	1*T*[13], 2*Ha*[13], 4*Ha*[13], 4*Hb*[13], 4*Hc*[13], 3*R*[13], 6*R*[13]	M[13], SC[13], CDW[19]	1´*T*[13]	M[13]
VI	Mo	1*T*[1], 1'*T*[31], 2*Hb*[17], 3*R*[17]	Semi-C[32], M[1]	1*T*[31], 1'*T*[31], 2*Hb*[17], 3*R*[17]	Semi-C[32]	2*Hb*[17], 1'*T*[13]	Semi-C[32], M[33], SM[13]
	W	1*T*[34], 2*Hb*[17], 3*R*[17]	Semi-C[32], M[34]	1*T*[35], 2*Hb*[17]	Semi-C[32], M[35]	1'*T*[36]	SM[36], TI[36], MR[20]
VII	Tc	1´*T*[13]	Semi-C[37]	1´*T*[13]	Semi-C[37]		
	Re	1´*T*[13]	Semi-C[32]	1´*T*[13]	Semi-C[32]		
IX	Co					1*T*[17]	M[13]
	Rh					1*T*[17]	M[13]
	Ir					1*T*[17]	M[13]
X	Ni					1*T*[17]	M[13]
	Pd					1*T*[17]	M[13], SC[13]
	Pt	1*T*[17]	Semi-C[13]	1*T*[17]	Semi-C[13]	1*T*[17]	M[13], SM[38]

Semi-C: semiconductor, **M**: metal, **SM**: semimetal, **SC**: superconductor, **CDW**: charge density wave, **TI**: topological insulator, **FM**: ferromagnetic, **MR**: magneto resistant

number (d^6) of valence electrons in its unit cell. The observed metallic nature of MTe_2 is due to overlap in the band states, like Te in group IV[13].

In addition to metal, semiconductor and semi-metal properties, some TMDCs also exhibit superconducting, charge density wave (CDW), and magnetic properties depending on the elements and phase. For example, both 2*H*-NbS_2 and 3*R*-NbS_2 are metallic and have CDW, but only the former has superconducting behavior[18], while, on the other hand, the only stable phase 1*T* of $PdTe_2$ is superconducting and does not exhibit CDW. CDW is a phenomenon observed in metallic layered 2D and quasi-1D materials (discussed in the upcoming section), such as TMDCs (also in TMTCs). It is a periodic modulation of electrons, which creates a standing wave of charge within a material. Usually, CDW is accompanied by the periodic distortion of the atomic lattice, also known as Peierls distortion, which can influence the electric properties like opening an energy band gap at the Fermi level[19]. Some of the more unique TMDCs are VS_2, VSe_2 and WTe_2, as the former two being 2D ferromagnetic materials. At the same time, a recent discovery shows the latter to exhibit extremely positive magnetoresistance (i.e., resistivity increases under external magnetic field) at low temperature (<4.2 K) using low magnetic field[20]. In addition to ferromagnetic properties, VS_2 has been observed to exhibit negative magnetoresistance (i.e., resistivity decreases under external magnetic field)[21].

In addition, within a single phase of the material, say in 2*H*-MoS_2 and 2*H*-WS_2, the semiconducting nature with an indirect band gap in its bulk form can be changed to the direct band gap semiconductor by thinning of the layers to a single monolayer[39]. This change in band structure with reducing layer thickness is caused primarily by the increasing indirect band gap near the Γ point of the Brillouin zone, while the direct band gap near the K point remains unaffected[40]. On the contrary, ReX_2 systems: 1´*T*-ReS_2 and 1´*T*-$ReSe_2$ are direct band gap semiconductors, independent of their layer thickness[41,42].

Summarizing, TMDCs provide significant variation in functional properties depending on the material phase, elements and thickness, offering wide options in terms of application.

2.1.2 Transition Metal Trichalcogenides (TMTCs)

The TMTCs (MX_3) are layered, quasi-one-dimensional (quasi-1D) materials, with a transition metal to chalcogenide ratio of 1:3[43,44]. Similar to TMDCs, these TMTCs exhibit a wide range of properties such as semiconductor, metal, CDW, etc. On the other hand, such similarity does not pertain when it comes to crystal structures and dimensionality. It is also

important to note that TMTCs, compared to TMDCs, are little explored in terms of synthesis, implementation, and applications.

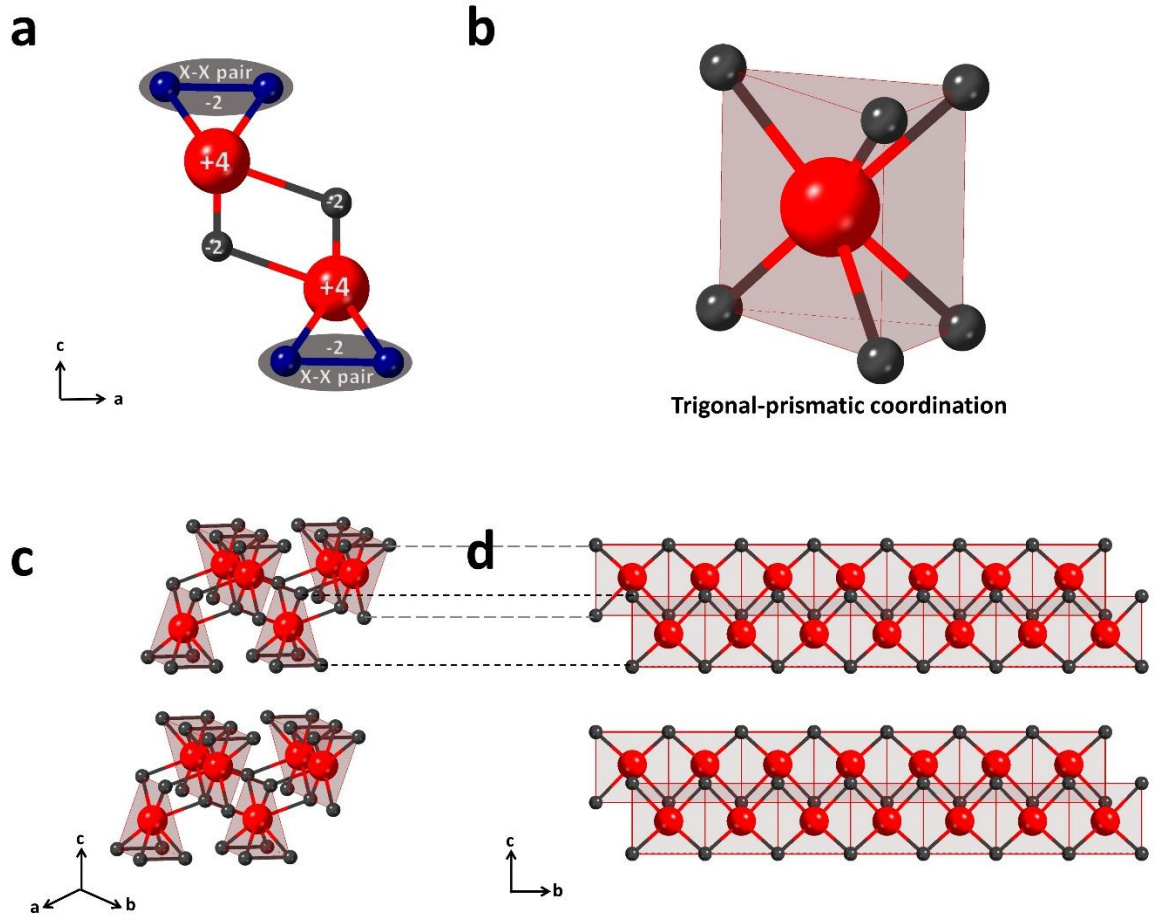

Figure 2.4 (a) Shows the two types of chalcogenide atoms, one chalcogenide atom (black) share 2 electrons with the transition metal atom, while the other two chalcogenides (blue) share 2 electrons amongst them (view down b-axis). (b) The image shows one block of the trigonal-prismatic metal coordination in TMTCs. (c) Cross-section view of the two-layer TMTCs structure with a van der Waals gap in between. (d) Stacking of trigonal-prismatic blocks on each other forming quasi-1D chains along the b axis.

One of the primary differences between TMDCs and TMTCs is the number of chalcogenide atom types. The TMDC structures have only one type of chalcogenide atoms, each sharing 2 electrons, TMTCs have two types of chalcogenide atoms. One chalcogenide atom shares 2 electrons (like in TMDCs) while the other two chalcogenides atoms (chalcogenide-chalcogenide [X-X] pair) share 2 electrons among them, see Figure 2.4a. Comparable to TMDCs, the oxidation state of transition metal in TMTCs is +4 with the structural formula $(M)^{+4}X^{-2}(X_2)^{-2}$ [44]. The two oxidation states of chalcogenide atoms can be differentiated using XPS studies, where each X species type separately exhibit two doublets.

For a stoichiometric material, the integrated peak area ratio between X^{-2}:$(X_2)^{-2}$ species is 1:2, and the latter ($(X_2)^{-2}$ species) has the higher binding energy[45].

The TMTCs, similar to TMDCs, are composed of MX_6 units but with only one metal coordination geometry: trigonal-prismatic, as illustrated in Figure 2.4b and c[46]. This arrangement consists of a non-equivalent triangular base of three chalcogenide atoms with one side (chalcogenide-chalcogenide pair) much shorter than the other two[43,44]. The coordination number of the transition metal atoms occupying the center of the trigonal-prismatic prism is 8 rather than 6, as they bond with two chalcogenides of the neighboring chains (see Figure 2.4c) within a monolayer[47,17].

These trigonal-prismatic MX_6 units, when stacked on top of each other, form infinite metal-metal chains, which usually run along the b axis, as shown in Figure 2.4d. These transition metal chains along the b axis are responsible for the quasi-one-dimensional character of TMTCs. A monolayer of TMTC consists of two such 1D transition metal chains, as the second chain is translated by b/2, as illustrated in Figure 2.4d[43,44]. Such 1D metal chains create an added anisotropy between a and b axes in terms of material properties and growth[48,49,50,51,52].

In general, TMTCs exist in three crystal structures types known as $ZrSe_3$, $TaSe_3$, and $NbSe_3$ types[43,44]. They are classified into three types based on the complexity of the structures such as one, two, and three different chains within a unit cell, where each chain is repeated twice, as shown in Figure 2.5[43,44]. The different chain type is defined by the bond length of the X-X atoms (chalcogenide-chalcogenide pair), as illustrated by different colors. The $ZrSe_3$ structure contains one chain type (with light grey X-X atoms in Figure 2.5) and is the most common TMTCs structure observed in all group IV transition metals and in NbS_3, see Table 2.3. The $TaSe_3$ structure contains two chain types (chains are differentiated by light grey and light green X-X atoms in Figure 2.5) and observed only by itself. The $NbSe_3$ structure consists of three chain types (chains are differentiated by light grey, light green and light blue X-X atoms in Figure 2.5), and this structure is observed by itself and TaS_3.

All TMTCs exist in monoclinic (space group: $P2_1/m$) structural symmetry, except for NbS_3 and TaS_3. NbS_3 and TaS_3 have been reported to also exists in triclinic (space group: $P\bar{1}$) and orthorhombic (space group: Cmcm) structural symmetry, respectively. Therefore, contradictory to TMDCs, except for TaS_3 and NbS_3, all the other TMTCs do not exhibit polymorphism, see Table 2.3. NbS_3 has been reported to be the only TMTCs existing in more than two stable phases, as two of these phases were reported very recently[53]. Alike TMDCs,

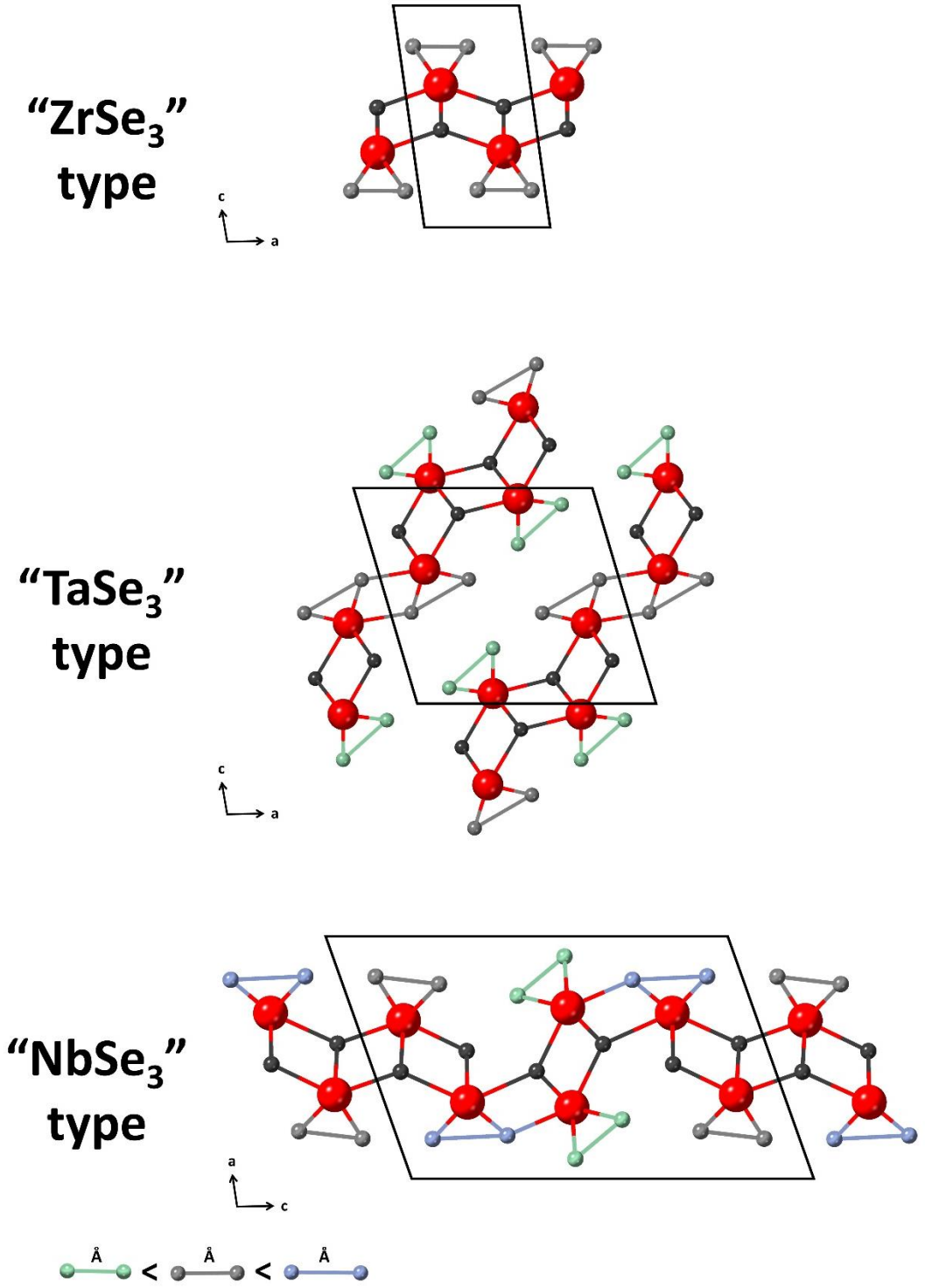

Figure 2.5 The cross-section view of the three types of TMTC crystal structures along with a unit cell of each: $ZrSe_3$, $TaSe_3$, and $NbSe_3$. The image also shows the three chain types. The three chain types are represented by three different colors for the X-X (chalcogenide-chalcogenide) bond. The key difference between the three chain types is the X-X bond length (shown in the bottom).

Table 2.3 Overview of the TMTCs. The TMTCs are classified into transition metal groups and chalcogenides. Their corresponding crystal symmetry, structure type, and material properties (for TMDC with more than one polytypes/phase, the properties are not categorized per polytype/phase) are mentioned in the table.

Group	Transition metal	Chalcogenide					
		S		Se		Te	
IV	Ti	Mono[61] ($ZrSe_3$ type)	Semi-C[43]				
	Zr	Mono[61] ($ZrSe_3$ type)	Semi-C[43]	Mono[61] ($ZrSe_3$ type)	Semi-C[43]	Mono[61] ($ZrSe_3$ type)	Semi-C[55], M[55], SM[62], SC[58], CDW[56]
	Hf	Mono[61] ($ZrSe_3$ type)	Semi-C[48]	Mono[61] ($ZrSe_3$ type)	Semi-C[48]	Mono[22] ($ZrSe_3$ type)	M[57], CDW[57], SC[57]
V	Nb	Mono[53] Tri[63] ($ZrSe_3$ type)	Semi-C[54], M[54], CDW[56], SC[43]	Mono[64] ($NbSe_3$ type)	M[43], CDW[56]		
	Ta	Mono[65] Ortho[66] ($NbSe_3$ type)	Semi-C[46], M[46], CDW[56]	Mono[66] ($TaSe_3$ type)	M[43], SC[43]		

Mono: Monoclinic, **Tri**: Triclinic, **Ortho**: Orthorhombic

Semi-C: semiconductor, **M**: metal, **SM**: semimetal, **TI**: topological insulator
CDW: charge density wave, **SC**: superconductor, **FM**: ferromagnetic
MR: magneto resistant

the electrical properties of NbS_3 change with different phases as NbS_3-I is semiconducting, while NbS_3-II is metallic[54].

Except for $ZrTe_3$ and $HfTe_3$, all the TMTCs in group IV (d^0), containing transition metal Ti, Zr and Hf, are semiconductors. For $ZrTe_3$, there is no consensus on whether the material is a metal, semiconductor or semi-metal[55]. Interestingly, TiS_3 is unique in the sense that its direct band gap is independent of the thickness[52]. All group V (d^1) TMTCs with Nb and Ta are metallic, with the exception of certain polymorphs of TaS_3 and NbS_3. Additionally, like TMDCs, several TMTCs also exhibit CDW: $ZrTe_3$[56], $HfTe_3$[57], $NbSe_3$[56], etc. and superconductor properties: $ZrTe_3$[58], $TaSe_3$[43], etc. While TMTCs exist for group IV and V transition metals,

there are also reports on synthesizing TMTCs with group VI transition metals such as MoS_3 and WS_3 but not yet in crystalline form[46,59,60].

Interestingly, some of the TMTCs (TiS_3 and NbS_3) counterparts of TMDCs (TiS_2 and NbS_2) containing analogous elements have complementing properties, as one being a conductor while the other is a semiconductor.

From a characterization point of view, TMTCs can be differentiated from TMDCs by various methods such as XPS (as mentioned earlier), Raman, XRD and TEM analysis, as will be discussed in Chapter 3 and 5. Unlike TMDCs, for TMTCs, a change in properties due to thinning from bulk to monolayer has not been reported, indicating there is a lot to be explored about TMTCs in terms of properties.

2.2 Synthesis Techniques

The TMCs synthesis methods can be generally categorized into two approaches, known as top-down and bottom-up. The top-down approach includes methods such as exfoliation, intercalation, etc., where the bulk material (found in nature or synthesized by bottom-up methods) is trimmed or carved down to few or monolayers. The bottom-up approaches consist of direct synthesis methods such as chemical vapor transport (CVT), chemical vapor deposition (CVD), etc. which can be further subcategorized into bulk and thin film growth methods. In this section, we discuss three bottom-up methods for synthesizing both TMDCs and TMTCs. First, CVT is discussed, which is a bulk growth method. This is followed by thin film growth methods such as CVD and atomic layer deposition (ALD). Many other methods like molecular beam epitaxy have been reported in the literature but mostly for TMDCs synthesis. The three methods to be discussed have also been utilized for the synthesis of TMTCs along with TMDCs.

2.2.1 Chemical Vapor Transport (CVT)

Chemical vapor transport is a bottom-up bulk synthesis technique where both transition metal and chalcogenide precursors in their elemental form are vacuum sealed inside an ampoule (quartz) with or without a transport agent, and to which a temperature gradient is applied[67]. The sealed ampoule is placed in a furnace and can be split into two zones (ends). A simple illustration of the CVT method is shown in Figure 2.6. The high temperature zone contains both the precursor (such as transition metal and chalcogenide) and a transport

agent (such as halogens, hydrogen halides, mercury halides, etc.), while the low temperature zone is where the crystal growth occurs. In general, the CVT process is reported to proceed in three stages[67]. First, in the high temperature zone, one or more solid precursors/ agents evaporate and volatilize other precursors. Second, transport of the volatile precursors happens, as these newly formed volatile species are transported from the high to the low temperature zone through diffusion in the temperature gradient. Third, the volatile precursors condense to form the final product. In the low temperature zone, the condensed precursors react to result in the crystal growth of the intended transition metal chalcogenide. This method results in high quality crystals (in terms of crystallinity) of up to a few cms in size[5].

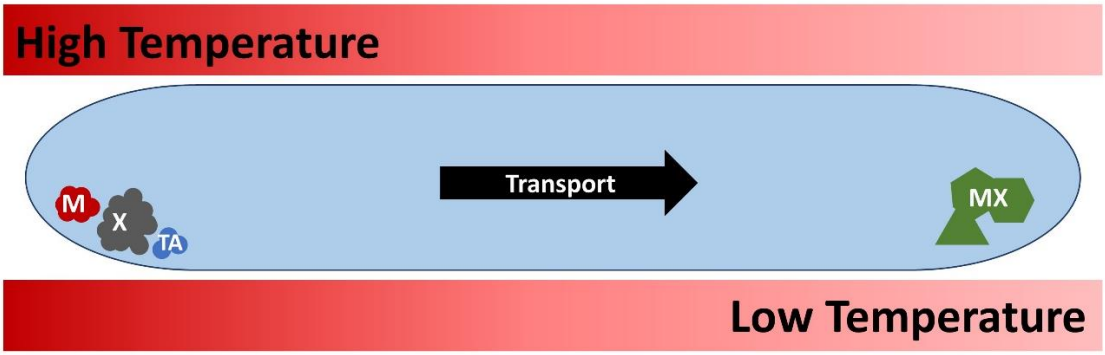

Figure 2.6 Schematic illustration of the chemical vapor transport method. The starting transition metal (M) and chalcogenide (X) precursor in their elemental form are on the high temperature zone (left side) along with the transport agent (TA). The resulting TMC crystals are formed on the low temperature zone (right side).

Using this synthesis method, TMDCs can be grown, and the control between various phases (e.g., 5 phases of $TaSe_2$) can be achieved by controlling various parameters such as synthesis temperature, reaction time, and heating and cooling rate[5,14]. Additionally, this method is suitable for synthesizing TMTCs, and it is essential to note that thus far (in the literature), this has been the primary method to synthesize TMTCs[46]. When TMTCs are heated to higher temperatures, they decompose to TMDCs due to pyrolysis[2]. Therefore, key parameters such as temperature and chalcogenide partial pressure (or chalcogenide to transition metal ratio) must be optimized and controlled to achieve a phase-controlled stable synthesis between TMDC and TMTC[68,69]. Figure 2.7 simply illustrates the relation between processing temperature and chalcogenide partial pressure for the phase-controlled synthesis of TMDCs and TMTCs by CVT. The TMTCs can only be synthesized at low temperatures and with high chalcogenide-to-transition metal precursor ratio (or high chalcogenide partial pressure); otherwise, TMDCs would be formed[68]. The typical

temperature to grow TMCs by CVT is highly dependent on the targeted material, composition and phase, and it can vary between 300 to 1200 °C.

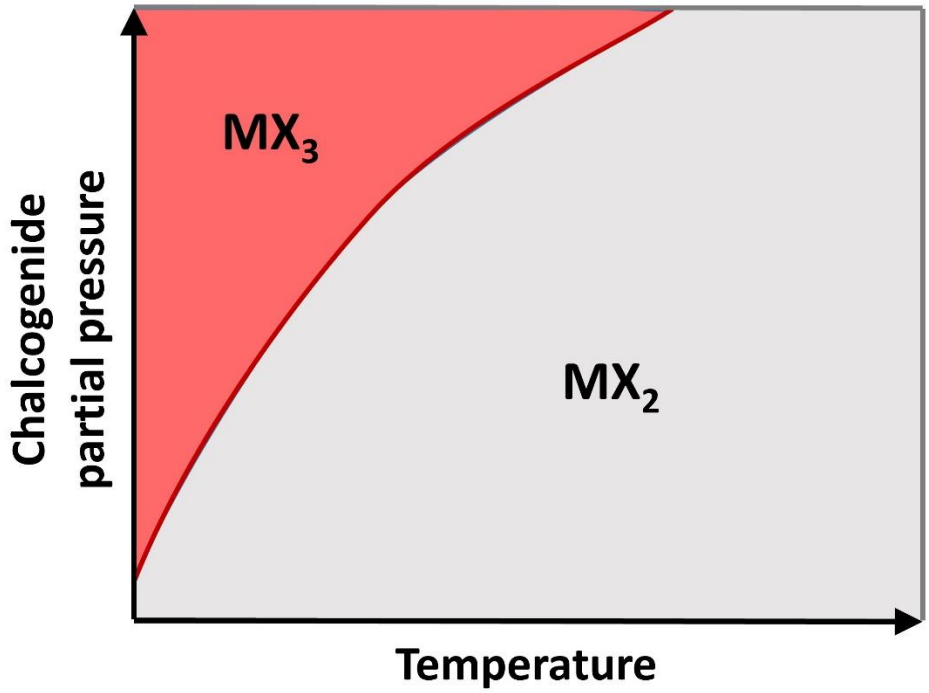

Figure 2.7 The importance of the two parameters: temperature and chalcogenide partial pressure on achieving phase-control between TMDC (MX_2) and TMTC (MX_3) is illustrated.

CVT-grown TMCs crystals are the most commonly used material source for the commonly employed top-down mechanical exfoliation method to isolate mono to a few layers of TMC from their bulk form[70]. Following the successful isolation of graphene, similar isolation of monolayer TMDCs received considerable interest as their electrical properties change from indirect-band gap semiconductors in bulk to direct-band gap semiconductors in their monolayer form (e.g., both in MoS_2 and WS_2). Besides, this method (CVT + mechanical exfoliation) has also been used to fabricate vertical heterostructures consisting of various 2D TMDC materials[71]. This gives new flexibility and possibilities to synthesize novel materials with novel properties, which provides new application opportunities for these materials[72,73]. Nevertheless, this top-down method has limitations such as low scalability (wafer scale), poor reproducibility, low-yield, and residue/contamination issues[74].

2.2.2 Chemical Vapor Deposition (CVD)

Chemical vapor deposition is a bottom-up thin film synthesis method commonly used to deposit mono to a few layers of TMCs directly on a preferred substrate. The transition metal and the chalcogenide precursors are evaporated and carried within a reaction chamber by inert carrier gases (such as Ar, N_2, etc.). The transition metal precursor used is in elemental or metal-halide or metal-oxide or metal-organic form, while the chalcogenide precursor is in elemental or metal-organic or gaseous form. Within the reaction chamber (hot zone), these precursors react to grow the final product on a target substrate. Also, note that CVD reactions can occur when creating a plasma consisting of the precursor species using a plasma source[75]. A simple illustration of a CVD process is shown in Figure 2.8. In general, the CVD process to grow TMCs proceeds in four stages[75]. First, both the precursors are heated and evaporated (vapor phase) into the carrier gas. Second, the reaction between the precursors takes place in the gas phase to produce the TMC compound. Third, the diffusion of the TMC compound from the carrier gas onto the target substrate occurs. Fourth, the TMC compound migrates over the surface and reacts with the surface to initiate nucleation and growth of the TMC layer. Hence, parameters such as flow rate of the carrier gas, concentration of the individual precursors, and their ratio along with growth temperature and target substrate govern the quality of the resulting film over a large area[75].

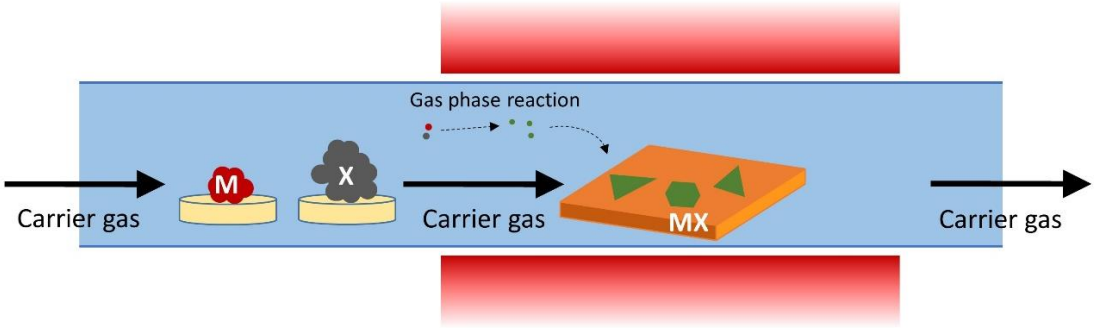

Figure 2.8 Schematic illustration of the chemical vapor deposition method. The starting transition metal (M) and chalcogenide (X) precursors in their elemental and/or (in-)organic compound form are placed up-stream. The reaction between the two precursors occurs in the gas phase to form the targeted TMC material (MX). The resulting TMC film growth occurs on the growth surface present down-stream within the high-temperature furnace zone (red).

This method is primarily used for the synthesis of TMDCs (successfully growing most of them)[14]. This method also provides good phase control between different phases of a TMDC. For example, phase-controlled growth between 2*H* and 1´*T* phase of $MoTe_2$ by CVD

has been demonstrated[76]. The control over the various phases was achieved by carefully optimizing the previously mentioned process parameters such as temperature, flow, etc. On the other hand, this method has rarely been reported for the synthesis of TMTCs. For example, TiS_3 growth by CVD has been reported in a few instances while primarily investigating TiS_2 (TMDC) growth[77,78,79]. This method also provides advantages over the mechanical transfer method with improved yield and reproducibility along with low residues/ contamination issues. Hence, this method has advantages for direct fabrication of vertical as well as lateral 2D heterostructures[71]. Thus far, two main strategies are reported in the literature for heterostructure formation known as one-step and two-step CVD[71]. In the one-step method, the growth between two TMC (*e.g.,* TiS_2 *Vs.* NbS_2) is controlled by varying the process temperature and flow as the function of time. In the two-step method, which is also the most commonly used approach among both, the second TMC (*e.g.,* NbS_2) film growth is carried out on a substrate containing previously CVD grown TMC (*e.g.,* TiS_2). It is important to note that CVD also has limitations in individual film growth and in 2D heterostructure formations, such as relatively poor uniformity and thickness control, as the reaction between the precursors takes place in the vapor phase before reaching the target substrate[80]. Additionally, the requirement of a high processing temperature (> 450 °C) is also not ideal for the direct implementation of CVD for TMC synthesis in (opto)electronics device processing flows on an industrial scale.

2.2.3 Atomic Layer Deposition (ALD)

Atomic layer deposition is a surface-controlled thin film synthesis method. The growth occurs in a saturated self-limiting cyclic way on the desired substrate, as both transition metal and chalcogenide precursors are introduced into the reaction chamber in a step by step manner separated by a purge step. A simple illustration of an ALD process is shown in Figure 2.9, which consists of two half-cycles: each has a precursor exposure step followed by a purge step[81]. In the first half-cycle A, the transition metal precursor in metal-halide/ metal-organic form is exposed to react with the surface functional groups and gets adsorbed on the starting surface. In the following step, the reaction by-products, along with the excess of unreacted precursor molecules, are purged away from the reaction chamber using an inert gas. In the second half-cycle B, the chalcogenide precursor in the form of metal-organic/ gaseous/ plasma species is exposed to react with the adsorbed transition metal precursor to produce the final intended TMC film. This is followed by a purge step to remove the reaction by-products and the remaining precursor species. Due to the step by step exposure of the precursors, the reaction between the precursors occurs only on the

target surface with no vapor/ gas phase reaction, avoiding CVD reactions. In both half-cycles, adsorption of the precursor molecules/ species reach saturation once most (due to the steric hindrance effect, not all surface sites are occupied with precursor molecules) of the surface functional groups are occupied. Therefore, due to its self-limiting nature, ALD provides excellent uniformity over a large area (wafer scale) along with conformality over complex 3D substrates[82]. As a result of the cyclic nature, it provides ultimate control over the thickness down to the Ångström level. In general, ALD requires low-processing temperature (< 450 °C), which is an advantage for the integration of ALD into industrial process flows and therefore provides an edge over the other thin film synthesis techniques[82]. However, thus far, in terms of TMC film quality, ALD produces amorphous or polycrystalline films with grain size in the range of 10-300 nm depending on the process parameters such as deposition temperature and transition metal/ chalcogenide precursors.

Based on the coreactant used, ALD processes can be grouped into two methods: thermal ALD and plasma-enhanced ALD (PE-ALD)[83,84]. Note that in the literature, the latter method is also known as plasma-assisted ALD (PA-ALD)[85,86–89]. In the thermal ALD case, the co-reactant utilized in the process is a gas or vapor such as H_2S gas, O_2, O_3 or H_2O, etc., while in the latter cases, plasma such as H_2S or O_2 plasma, etc. containing ions, radicals, photons, and electrons is used as co-reactant[89]. In relation to thermal ALD, PE-ALD provides benefits such as broader precursor choice (therefore, depositing more materials are feasible) along with high growth rates and better film quality at low synthesis temperature, due to additional plasma species[90]. PE-ALD also offer tunability of material properties such as composition and phase, as discussed in Chapter 3 and 5.

As a direct synthesis method for TMCs, ALD has gained interests lately, as it provides precise thickness control over a large area. This method has reportedly synthesized a wide range of materials such as MoS_2[91–131], $MoSe_2$[132,133], WS_2[134–149], WSe_2[150,151], ReS_2[152], TiS_2[153–155,138], HfS_2[156] and ZrS_2[156] successfully using both metal-halide and metal-organic as the transition metal precursors. The most common chalcogenide coreactant being H_2S and H_2Se gas, in addition to these, other coreactant such as H_2S plasma, $S(SiMe_3)_2$, MeSSMe, $Se(SiMe_3)_2$, etc. have also been reported. Thermal ALD of TMDCs has been the most common approach, as all the above-mentioned TMDCs have been synthesized using this process, with the exceptions of MoS_2 and WS_2, where the PE-ALD process using H_2S plasma have also been reported.

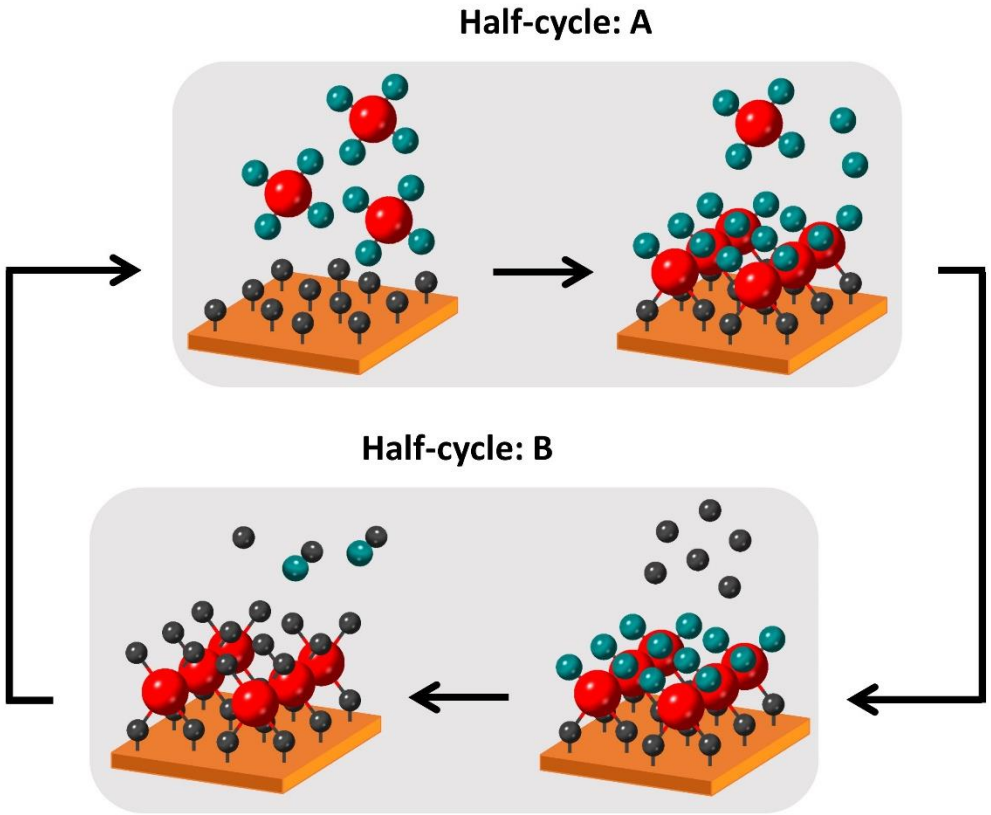

Figure 2.9 Schematic illustration of the atomic layer deposition method. The reaction consists of the two half-cycles A and B. In the first half-cycle (A), the transition metal precursor is dosed into the reactor chamber. The transition metal atoms and surrounding ligands are represented in red and green spheres, respectively. The transition metal precursor reacts with the surface groups on the starting surface and gets adsorbed. The remaining precursors, along with the reaction products, are purged away in the following step. In the second half-cycle (B), the chalcogenide precursor is dosed to react with the adsorbed transition metal precursor and form the TMC material. The chalcogenide atoms/precursors are represented in the dark grey sphere. This is followed by a second purge step to remove the excess chalcogenide precursor along with the reaction products. This AB half-cycles can be repeated to continue to deposition of TMC.

Similar to the deposition of other materials by ALD, the growth rate or growth per ALD cycle (GPC) for TMDC depositions are lower than a monolayer thickness. For TMDCs, this is typically one to two orders of magnitude lower than a TMDC monolayer thickness (~6-7 Å). Therefore, depending on the GPC, it might take around 10-100 ALD cycles to reach one monolayer thickness, while it requires more than that to achieve a completely closed layer. Morphology and film quality of the ALD grown TMDCs are highly selective to the processing conditions. In some cases, rough film morphology has been reported with growth orthogonal to the substrate, known in the literature as fins or out-of-plane-orientation growth (see chapter 3 and 4). However, the origin of fin formation is yet to be understood.

These rough fin structures are preferred for catalytic applications, especially in semiconducting group VI TMDCs where only edge sites are catalytically active.

Thus far, almost all ALD processes are for synthesizing semiconducting TMDCs with few reports on synthesizing metallic TMDCs (TiS_2). On the other hand, prior to this work in chapter 3 and 5 syntheses of TMTCs by ALD has not been reported to the best of our knowledge. Here similar to the CVT method (Figure 7), the phase-controlled synthesis between TMDCs and TMTCs was obtained by both controlling the temperature and chalcogenide (coreactant mixture/ composition) using metal-organic precursor and both H_2S gas (thermal ALD) as well as H_2S plasma (PE-ALD) as coreactant. Additionally, as lower processing temperatures are favorable for TMTC formation, ALD known for its low deposition temperatures would be suitable for TMTC deposition, as will be discussed in chapter 3 and 5.

ALD can also be used to fabricate 2D heterostructures as it would provide advantages such as precise thickness control of individual layers independently at a low-processing temperature over a large area along with good conformality on a 3D substrate. While ALD has been studied to directly grow 2D vertical heterostructures consisting of 2D non-TMDCs layered materials[157–159], chapter 4 discusses that ALD can also be used to grow 2D TMDC vertical heterostructures with precise control of individual material layer thickness at low deposition temperatures. Conformal growth of 2D TMDC vertical heterostructures over a 3D structure is also shown in chapter 4. Additionally, 2D heterostructures consisting of TMDC-TMTC has not yet been explored experimentally to the best of our knowledge. Chapter 5 shows that the ALD toolbox can be extended to synthesize 2D vertical heterostructures consisting of both TMDC and TMTC at a constant processing temperature.

An alternative indirect approach for the synthesis of TMCs using ALD (also includes other methods such as CVD, evaporation, etc.) is known as chalcogenization in which transition metal/ transition metal oxide films are annealed and chalcogenized at higher temperatures. For example, an ALD grown WO_x film is sulfurized using H_2S gas at 800 °C to form WS_2[160]. Similar to direct ALD of TMDCs, this indirect approach has been primarily reported for synthesizing semiconducting TMDCs based on Mo and W[160–173,174,131,175]. It is important to note that in this approach, ALD acts as the primary method to control the thickness, uniformity, and conformality of the final TMDC material formed by chalcogenization of the ALD grown transition metal oxide at a high temperature (> 450 °C). In chapter 6, this approach has been extended to metallic TMDC for the first time to the best of our

knowledge, to form NbS_2 by sulfurization of ALD grown Nb_2O_5 (chapter 7) within a tube furnace using H_2S gas at high temperature.

References

[1] R. Kappera, D. Voiry, S.E. Yalcin, B. Branch, G. Gupta, A.D. Mohite, and M. Chhowalla, Nat. Mater. **13**, 1128 (2014).

[2] X.C. Wu, Y.R. Tao, and Q.X. Gao, Nano Res. **2**, 558 (2009).

[3] S.-H. Cai and C.-W. Liu, J. Mol. Struct. THEOCHEM **362**, 379 (1996).

[4] M. Chhowalla, H.S. Shin, G. Eda, L. Li, K.P. Loh, and H. Zhang, Nat. Chem. **5**, 263 (2013).

[5] R.M.A. Lieth and J.C.J.M. Terhell, in *Prep. Cryst. Growth Mater. with Layer. Struct.* (Springer Netherlands, Dordrecht, 1977), pp. 141–223.

[6] I. Ekvall and J.J. Kim, Phys. Rev. B - Condens. Matter Mater. Phys. **55**, 6758 (1997).

[7] B. Han, S. Chen, J. Zou, R. Shao, Z. Dou, C. Yang, X. Ma, J. Lu, K. Liu, D. Yu, L. Wang, H. Wang, and P. Gao, Nanoscale **11**, 7474 (2019).

[8] Y. Yu, C. Li, Y. Liu, L. Su, Y. Zhang, and L. Cao, Sci. Rep. **3**, 1866 (2013).

[9] X. Ou, X. Xiong, F. Zheng, C. Yang, Z. Lin, R. Hu, C. Jin, Y. Chen, and M. Liu, J. Power Sources **325**, 410 (2016).

[10] L.S. Ramsdell, Am. Mineral. J. Earth Planet. Mater. **32**, 64 (1947).

[11] A. V. Kolobov and J. Tominaga, *Two-Dimensional Transition-Metal Dichalcogenides* (Springer International Publishing, Cham, 2016).

[12] H. Katzke, P. Tolédano, and W. Depmeier, Phys. Rev. B **69**, 134111 (2004).

[13] J.A. Wilson and A.D. Yoffe, Adv. Phys. **18**, 193 (1969).

[14] G.H. Han, D.L. Duong, D.H. Keum, S.J. Yun, and Y.H. Lee, Chem. Rev. **118**, 6297 (2018).

[15] Z.Y. Wu, F. Lemoigno, P. Gressier, G. Ouvrard, P. Moreau, J. Rouxel, and C.R. Natoli, Phys. Rev. B **54**, R11009 (1996).

[16] C.S. Cucinotta, K. Dolui, H. Pettersson, Q.M. Ramasse, E. Long, S.E. O'Brian, V. Nicolosi, and S. Sanvito, J. Phys. Chem. C **119**, 15707 (2015).

[17] F. Hulliger, *Structural Chemistry of Layer-Type Phases* (Springer Netherlands, Dordrecht, 1976).

[18] C. Schlenker, J. Dumas, M. Greenblatt, and S. van Smaalen, *Physics and Chemistry of Low-Dimensional Inorganic Conductors* (Springer US, 2012).

[19] M. Hossain, Z. Zhao, W. Wen, X. Wang, J. Wu, and L. Xie, Crystals **7**, 1 (2017).

[20] M.N. Ali, J. Xiong, S. Flynn, J. Tao, Q.D. Gibson, L.M. Schoop, T. Liang, N. Haldolaarachchige, M. Hirschberger, N.P. Ong, and R.J. Cava, Nature **514**, 205 (2014).

[21] Y. Guo, H. Deng, X. Sun, X. Li, J. Zhao, J. Wu, W. Chu, S. Zhang, H. Pan, X. Zheng, X. Wu, C. Jin, C. Wu, and Y. Xie, Adv. Mater. **29**, 1700715 (2017).

[22] C. Yan, C. Gong, P. Wangyang, J. Chu, K. Hu, C. Li, X. Wang, X. Du, T. Zhai, Y. Li, and J. Xiong, Adv. Funct. Mater. **28**, 1803305 (2018).

[23] P. Chen, W.W. Pai, Y.-H. Chan, A. Takayama, C.-Z. Xu, A. Karn, S. Hasegawa, M.Y. Chou, S.-K. Mo, A.-V. Fedorov, and T.-C. Chiang, Nat. Commun. **8**, 516 (2017).

[24] F. Arnold, R.-M. Stan, S.K. Mahatha, H.E. Lund, D. Curcio, M. Dendzik, H. Bana, E. Travaglia, L. Bignardi, P. Lacovig, D. Lizzit, Z. Li, M. Bianchi, J.A. Miwa, M. Bremholm, S. Lizzit, P. Hofmann, and C.E. Sanders, 2D Mater. **5**, 045009 (2018).

[25] D. Li, X. Wang, C. Kan, D. He, Z. Li, Q. Hao, H. Zhao, C. Wu, C. Jin, and X. Cui, ACS Appl. Mater. Interfaces acsami.0c04449 (2020).

[26] Y. Sun, T. Dai, Z. He, W. Zhou, P. Hu, S. Li, and S. Wu, Appl. Phys. Lett. **116**, 033101 (2020).

[27] M. Bonilla, S. Kolekar, Y. Ma, H.C. Diaz, V. Kalappattil, R. Das, T. Eggers, H.R. Gutierrez, M.-H. Phan, and M. Batzill, Nat. Nanotechnol. **13**, 289 (2018).

[28] P.M. Coelho, K. Lasek, K. Nguyen Cong, J. Li, W. Niu, W. Liu, I.I. Oleynik, and M. Batzill, J. Phys. Chem. Lett. **10**, 4987 (2019).

[29] Z.-L. Liu, L.-C. Cai, and X.-L. Zhang, J. Alloys Compd. **610**, 472 (2014).

[30] J. Li, B. Zhao, P. Chen, R. Wu, B. Li, Q. Xia, G. Guo, J. Luo, K. Zang, Z. Zhang, H. Ma, G. Sun, X. Duan, and X. Duan, Adv. Mater. **30**, 1801043 (2018).

[31] Y. Yu, G.-H. Nam, Q. He, X.-J. Wu, K. Zhang, Z. Yang, J. Chen, Q. Ma, M. Zhao, Z. Liu, F.-R. Ran, X. Wang, H. Li, X. Huang, B. Li, Q. Xiong, Q. Zhang, Z. Liu, L. Gu, Y. Du, W. Huang, and H. Zhang, Nat. Chem. **10**, 638 (2018).

[32] M. Ye, D. Zhang, and Y.K. Yap, Electronics **6**, 43 (2017).

[33] Q. Zhang, Y. Xiao, T. Zhang, Z. Weng, M. Zeng, S. Yue, R.G. Mendes, L. Wang, S. Chen, M.H. Rümmeli, L. Peng, and L. Fu, Chem. Mater. **29**, 4641 (2017).

[34] D. Voiry, H. Yamaguchi, J. Li, R. Silva, D.C.B. Alves, T. Fujita, M. Chen, T. Asefa, V.B. Shenoy, G. Eda, and M. Chhowalla, Nat. Mater. **12**, 850 (2013).

[35] Y. Ma, B. Liu, A. Zhang, L. Chen, M. Fathi, C. Shen, A.N. Abbas, M. Ge, M. Mecklenburg, and C. Zhou, ACS Nano **9**, 7383 (2015).

[36] Z. Fei, T. Palomaki, S. Wu, W. Zhao, X. Cai, B. Sun, P. Nguyen, J. Finney, X. Xu, and D.H. Cobden, Nat. Phys. **13**, 677 (2017).

[37] P.F. Weck, E. Kim, and K.R. Czerwinski, Dalt. Trans. **42**, 15288 (2013).

[38] L. Fu, D. Hu, R.G. Mendes, M.H. Rümmeli, Q. Dai, B. Wu, L. Fu, and Y. Liu, ACS Nano **12**, 9405 (2018).

[39] K.F. Mak, C. Lee, J. Hone, J. Shan, and T.F. Heinz, Phys. Rev. Lett. **105**, 136805 (2010).

[40] S. Das, J.A. Robinson, M. Dubey, H. Terrones, and M. Terrones, Annu. Rev. Mater. Res. **45**, 1 (2015).

[41] S. Tongay, H. Sahin, C. Ko, A. Luce, W. Fan, K. Liu, J. Zhou, Y.-S. Huang, C.-H. Ho, J. Yan, D.F. Ogletree, S. Aloni, J. Ji, S. Li, J. Li, F.M. Peeters, and J. Wu, Nat. Commun. **5**, 3252 (2014).

[42] B. Jariwala, D. Voiry, A. Jindal, B.A. Chalke, R. Bapat, A. Thamizhavel, M. Chhowalla, M. Deshmukh, and A. Bhattacharya, Chem. Mater. **28**, 3352 (2016).

[43] J. Rouxel, *Crystal Chemistry and Properties of Materials with Quasi-One-Dimensional Structures* (Springer Netherlands, Dordrecht, 1986).

[44] G.G. L.P. Gor'kov, *Charge Density Waves in Solids* (Springer Netherlands, Amsterdam, 1989).

[45] K. Endo, H. Ihara, K. Watanabe, and S. Gonda, J. Solid State Chem. **44**, 268 (1982).

[46] F. Lévy and H. Berger, J. Cryst. Growth **61**, 61 (1983).

[47] E. Bjerkelund, A. Kjekshus, G. Widmark, P.H. Nielsen, B. Sjöberg, and E. Larsen, Acta Chem. Scand. **19**, 701 (1965).

[48] H. Jin, D. Cheng, J. Li, X. Cao, B. Li, X. Wang, X. Liu, and X. Zhao, Solid State Sci. **13**, 1166 (2011).

[49] W. Kong, C. Bacaksiz, B. Chen, K. Wu, M. Blei, X. Fan, Y. Shen, H. Sahin, D. Wright, D.S. Narang, and S. Tongay, Nanoscale **9**, 4175 (2017).

[50] A. Pant, E. Torun, B. Chen, S. Bhat, X. Fan, K. Wu, D.P. Wright, F.M. Peeters, E. Soignard, H. Sahin, and S. Tongay, Nanoscale **8**, 16259 (2016).

[51] J.O. Island, R. Biele, M. Barawi, J.M. Clamagirand, J.R. Ares, C. Sánchez, H.S.J. van der Zant, I.J. Ferrer, R. D'Agosta, and A. Castellanos-Gomez, Sci. Rep. **6**, 22214 (2016).

[52] A. Khatibi, R.H. Godiksen, S.B. Basuvalingam, D. Pellegrino, A.A. Bol, B. Shokri, and A.G. Curto, 2D Mater. **7**, 015022 (2019).

[53] M.A. Bloodgood, P. Wei, E. Aytan, K.N. Bozhilov, A.A. Balandin, and T.T. Salguero, APL Mater. **6**, 026602 (2018).

[54] S.G. Zybtsev, V.Y. Pokrovskii, V.F. Nasretdinova, S. V. Zaitsev-Zotov, V. V. Pavlovskiy, A.B. Odobesco, W.W. Pai, M.-W. Chu, Y.G. Lin, E. Zupanič, H.J.P. van Midden, S. Šturm, E. Tchernychova, A. Prodan, J.C. Bennett, I.R. Mukhamedshin, O. V. Chernysheva, A.P. Menushenkov, V.B. Loginov, B.A. Loginov, A.N. Titov, and M. Abdel-Hafiez, Phys. Rev. B **95**, 035110 (2017).

[55] K. Stöwe and F.R. Wagner, J. Solid State Chem. **138**, 160 (1998).

[56] V.Y. Pokrovskii, S.G. Zybtsev, M. V. Nikitin, I.G. Gorlova, V.F. Nasretdinova, and S. V. Zaitsev-Zotov, Uspekhi Fiz. Nauk **183**, 33 (2013).

[57] S.J. Denholme, A. Yukawa, K. Tsumura, M. Nagao, R. Tamura, S. Watauchi, I. Tanaka, H. Takayanagi, and N. Miyakawa, Sci. Rep. **7**, 45217 (2017).

[58] C.S. Yadav and P.L. Paulose, J. Phys. Condens. Matter **24**, 235702 (2012).

[59] E. Diemann, Zeitschrift Für Anorg. Und Allg. Chemie **432**, 127 (1977).

[60] T. Matsuyama, M. Deguchi, K. Mitsuhara, T. Ohta, T. Mori, Y. Orikasa, Y. Uchimoto, Y. Kowada, A. Hayashi, and M. Tatsumisago, J. Power Sources **313**, 104 (2016).

[61] S. Furuseth, L. Brattås, A. Kjekshus, A.F. Andresen, and P. Fischer, Acta Chem. Scand. **29a**, 623 (1975).

[62] X. Yu, X. Wen, W. Zhang, L. Yang, H. Wu, X. Lou, Z. Xie, Y. Liu, and H. Chang, CrystEngComm **21**, 5586 (2019).

[63] J. Rijnsdorp and F. Jellinek, J. Solid State Chem. **25**, 325 (1978).

[64] A. Meerschaut and J. Rouxel, J. Less Common Met. **39**, 197 (1975).

[65] A. Meerschaut, J. Rouxel, P. Haen, P. Monceau, and M. Núñez-Regueiro, J. Phys. Lettres **40**, 157 (1979).

[66] E. Bjerkelund and A. Kjekshus, Zeitschrift Für Anorg. Und Allg. Chemie **328**, 235 (1964).

[67] S.J. Denholme, (2011).

[68] M. Talib, R. Tabassum, S.S. Islam, and P. Mishra, RSC Adv. **9**, 645 (2019).

[69] S.J. Denholme, P.S. Dobson, J.M.R. Weaver, I. MacLaren, and D.H. Gregory, Int. J. Nanotechnol. **9**, 23 (2012).

[70] D. Hu, G. Xu, L. Xing, X. Yan, J. Wang, J. Zheng, Z. Lu, P. Wang, X. Pan, and L. Jiao, Angew. Chemie Int. Ed. **56**, 3611 (2017).

[71] R. Dong and I. Kuljanishvili, J. Vac. Sci. Technol. B, Nanotechnol. Microelectron. Mater. Process. Meas. Phenom. **35**, 030803 (2017).

[72] S.J. Haigh, A. Gholinia, R. Jalil, S. Romani, L. Britnell, D.C. Elias, K.S. Novoselov, L.A. Ponomarenko, A.K. Geim, and R. Gorbachev, Nat. Mater. **11**, 764 (2012).

[73] Y. Liu, N.O. Weiss, X. Duan, H.-C. Cheng, Y. Huang, and X. Duan, Nat. Rev. Mater. **1**, 16042 (2016).

[74] Y. Liu, S. Zhang, J. He, Z.M. Wang, and Z. Liu, Nano-Micro Lett. **11**, (2019).

[75] H.O. Pierson, *Handbook of Chemical Vapor Deposition: Principles, Technology and Applications*, 2nd ed. (William Andrew, Norwich, 1999).

[76] S. Cheng, L. Yang, J. Li, Z. Liu, W. Zhang, and H. Chang, CrystEngComm **19**, 1045 (2017).

[77] C.J. Carmalt, I.P. Parkin, and E.S. Peters, Polyhedron **22**, 1263 (2003).

[78] R. Shimanouchi, T. Yamamoto, S. Kikkawa, and M. Koizumi, Chem. Lett. **14**, 1323 (1985).

[79] S. Kikkawa, Ceram. Int. **8842**, 7 (1996).

[80] W. Liao, Y. Huang, H. Wang, and H. Zhang, Appl. Mater. Today **16**, 435 (2019).

[81] R.L. Puurunen, J. Appl. Phys. **97**, (2005).

[82] H.C.M. Knoops, S.E. Potts, A.A. Bol, and W.M.M. Kessels, in *Handb. Cryst. Growth*, Second Edi (Elsevier, Amsterdam, 2015), pp. 1101–1134.

[83] S.E. Potts, G. Dingemans, C. Lachaud, and W.M.M. Kessels, J. Vac. Sci. Technol. A Vacuum, Surfaces, Film. **30**, 021505 (2012).

[84] S.B. Basuvalingam, B. Macco, H.C.M. Knoops, J. Melskens, W.M.M. (Erwin) Kessels, and A.A. Bol, J. Vac. Sci. Technol. A **36**, 041503 (2018).

[85] V.R. Rai, V. Vandalon, and S. Agarwal, Langmuir **26**, 13732 (2010).

[86] K.B. Jinesh, J.L. van Hemmen, M.C.M. van de Sanden, F. Roozeboom, J.H. Klootwijk, W.F.A. Besling, and W.M.M. Kessels, J. Electrochem. Soc. **158**, G21 (2011).

[87] G. Dingemans, C. Van Helvoirt, M.C.M. Van de Sanden, and W.M. Kessels, in *ECS Trans.* (2011), pp. 191–204.

[88] V. Longo, N. Leick, F. Roozeboom, and W.M.M. Kessels, in *ECS Trans.* (2011), pp. 63–72.

[89] H.B. Profijt, S.E. Potts, M.C.M. van de Sanden, and W.M.M. Kessels, J. Vac. Sci. Technol. A Vacuum, Surfaces, Film. **29**, 050801 (2011).

[90] P.O. Oviroh, R. Akbarzadeh, D. Pan, R.A.M. Coetzee, and T.-C. Jen, Sci. Technol. Adv. Mater. **20**, 465 (2019).

[91] A.J. Mughal, T.N. Walter, K.A. Cooley, A. Bertuch, and S.E. Mohney, J. Vac. Sci. Technol. A **37**, 010907 (2019).

[92] W. Jeon, Y. Cho, S. Jo, J.H. Ahn, and S.J. Jeong, Adv. Mater. **29**, 1 (2017).

[93] Y. Kim, D. Choi, W.J. Woo, J.B. Lee, G.H. Ryu, J.H. Lim, S. Lee, Z. Lee, S. Im, J.H. Ahn, W.H. Kim, J. Park, and H. Kim, Appl. Surf. Sci. **494**, 591 (2019).

[94] L.K. Tan, B. Liu, J.H. Teng, S. Guo, H.Y. Low, and K.P. Loh, Nanoscale **6**, 10584 (2014).

[95] R. Browning, P. Padigi, R. Solanki, D.J. Tweet, P. Schuele, and D. Evans, Mater. Res. Express **2**, (2015).

[96] A. Valdivia, D.J. Tweet, and J.F. Conley, J. Vac. Sci. Technol. A Vacuum, Surfaces, Film. **34**, 021515 (2016).

[97] L. Liu, Y. Huang, J. Sha, and Y. Chen, Nanotechnology **28**, (2017).

[98] Y. Huang, L. Liu, W. Zhao, and Y. Chen, Thin Solid Films **624**, 101 (2017).

[99] Y. Huang, L. Liu, J. Sha, and Y. Chen, Appl. Phys. Lett. **111**, 1 (2017).

[100] Y. Huang, L. Liu, J. Lv, J. Yang, J. Sha, and Y. Chen, AIP Adv. **8**, (2018).

[101] Y. Huang, L. Liu, J. Yang, and Y. Chen, Langmuir **35**, 3651 (2019).

[102] Y. Huang, L. Liu, and X. Liu, Nanotechnology **30**, (2019).

[103] Y. Jang, S. Yeo, H.B.R. Lee, H. Kim, and S.H. Kim, Appl. Surf. Sci. **365**, 160 (2016).

[104] T.A. Ho, C. Bae, S. Lee, M. Kim, J.M. Montero-Moreno, J.H. Park, and H. Shin, Chem. Mater. **29**, 7604 (2017).

[105] M.B. Sreedhara, S. Gope, B. Vishal, R. Datta, A.J. Bhattacharyya, and C.N.R. Rao, J.

Mater. Chem. A **6**, 2302 (2018).

[106] J. Joe, C. Bae, E. Kim, T.A. Ho, H. Yang, J.H. Park, and H. Shin, Catalysts **8**, 1 (2018).

[107] M. Alqahtani, S. Sathasivam, F. Cui, L. Steier, X. Xia, C. Blackman, E. Kim, H. Shin, M. Benamara, Y.I. Mazur, G.J. Salamo, I.P. Parkin, H. Liu, and J. Wu, J. Mater. Chem. A **7**, 8550 (2019).

[108] A.U. Mane, S. Letourneau, D.J. Mandia, J. Liu, J.A. Libera, Y. Lei, Q. Peng, E. Graugnard, and J.W. Elam, J. Vac. Sci. Technol. A Vacuum, Surfaces, Film. **36**, 01A125 (2018).

[109] S. Letourneau, M.J. Young, N.M. Bedford, Y. Ren, A. Yanguas-Gil, A.U. Mane, J.W. Elam, and E. Graugnard, ACS Appl. Nano Mater. **1**, 4028 (2018).

[110] D.K. Nandi, U.K. Sen, D. Choudhury, S. Mitra, and S.K. Sarkar, Electrochim. Acta **146**, 706 (2014).

[111] J.J. Pyeon, S.H. Kim, D.S. Jeong, S.H. Baek, C.Y. Kang, J.S. Kim, and S.K. Kim, Nanoscale **8**, 10792 (2016).

[112] D. Xiong, Q. Zhang, W. Li, J. Li, X. Fu, M.F. Cerqueira, P. Alpuim, and L. Liu, Nanoscale **9**, 2711 (2017).

[113] D.K. Nandi, S. Sahoo, S. Sinha, S. Yeo, H. Kim, R.N. Bulakhe, J. Heo, J.J. Shim, and S.H. Kim, ACS Appl. Mater. Interfaces **9**, 40252 (2017).

[114] B. Kalanyan, R. Beams, M.B. Katz, A. V. Davydov, J.E. Maslar, and R.K. Kanjolia, J. Vac. Sci. Technol. A **37**, 010901 (2019).

[115] S. Oh, J.B. Kim, J.T. Song, J. Oh, and S.H. Kim, J. Mater. Chem. A **5**, 3304 (2017).

[116] S. Shin, Z. Jin, D.H. Kwon, R. Bose, and Y.S. Min, Langmuir **31**, 1196 (2015).

[117] D.H. Kwon, Z. Jin, S. Shin, W.S. Lee, and Y.S. Min, Nanoscale **8**, 7180 (2016).

[118] X. Li, M. Puttaswamy, Z. Wang, C. Kei Tan, A.C. Grimsdale, N.P. Kherani, and A.I.Y. Tok, Appl. Surf. Sci. **422**, 536 (2017).

[119] M. Song, H. Tan, X. Li, A.I.Y. Tok, P. Liang, D. Chao, and H.J. Fan, Small Methods **1900274**, 1900274 (2019).

[120] H. Sopha, A.T. Tesfaye, R. Zazpe, J. Michalicka, F. Dvorak, L. Hromadko, M. Krbal, J. Prikryl, T. Djenizian, and J.M. Macak, FlatChem **17**, (2019).

[121] T. Jurca, M.J. Moody, A. Henning, J.D. Emery, B. Wang, J.M. Tan, T.L. Lohr, L.J. Lauhon, and T.J. Marks, Angew. Chemie - Int. Ed. **56**, 4991 (2017).

[122] Y. Cao, Y. Wu, C. Badie, S. Cadot, C. Camp, E.A. Quadrelli, and J. Bachmann, ACS Omega **4**, 8816 (2019).

[123] A. Sharma, M.A. Verheijen, L. Wu, S. Karwal, V. Vandalon, H.C.M. Knoops, R.S. Sundaram, J.P. Hofmann, W.M.M. (Erwin) Kessels, and A.A. Bol, Nanoscale **10**, 8615 (2018).

[124] Z. Jin, S. Shin, D.H. Kwon, S.-J. Han, and Y.-S. Min, Nanoscale **6**, 14453 (2014).

[125] S. Cadot, O. Renault, M. Frégnaux, D. Rouchon, E. Nolot, K. Szeto, C. Thieuleux, L. Veyre, H. Okuno, F. Martin, and E.A. Quadrelli, Nanoscale **9**, 538 (2017).

[126] Y. Kim, J.-G. Song, Y.J. Park, G.H. Ryu, S.J. Lee, J.S. Kim, P.J. Jeon, C.W. Lee, W.J. Woo, T. Choi, H. Jung, H.-B.-R. Lee, J.-M. Myoung, S. Im, Z. Lee, J.-H. Ahn, J. Park, and H. Kim, Sci. Rep. **6**, 18754 (2016).

[127] C. MacIsaac, J.R. Schneider, R.G. Closser, T.R. Hellstern, D.S. Bergsman, J. Park, Y. Liu, R. Sinclair, and S.F. Bent, Adv. Funct. Mater. **28**, 1 (2018).

[128] T. Zhang, H. Liu, Y. Wang, H. Zhu, L. Chen, Q. Sun, and D.W. Zhang, Phys. Status Solidi - Rapid Res. Lett. **13**, 1 (2019).

[129] Y. Wang, Z.-H. Gu, H. Liu, L. Chen, X. Liu, L. Min, Z. Li, H. Zhu, and Q.-Q. Sun, ACS Appl. Electron. Mater. **1**, 1418 (2019).

[130] T. Zhang, Y. Wang, J. Xu, L. Chen, H. Zhu, Q. Sun, S. Ding, and D.W. Zhang, 2D Mater. **5**, (2018).

[131] Y. Wang, T. Chen, T. Zhang, H. Zhu, L. Chen, Q. Sun, and D.W. Zhang, J. Mater. Sci. Mater. Electron. **30**, 4085 (2019).

[132] M. Krbal, J. Prikryl, R. Zazpe, F. Dvorak, F. Bures, and J.M. Macak, Phys. Status Solidi - Rapid Res. Lett. **12**, 1800023 (2018).

[133] S. Ng, M. Krbal, R. Zazpe, J. Prikryl, J. Charvot, F. Dvořák, L. Strizik, S. Slang, H. Sopha, Y. Kosto, V. Matolin, F.K. Yam, F. Bures, and J.M. Macak, Adv. Mater. Interfaces **5**, 1701146 (2018).

[134] S. Balasubramanyam, M. Shirazi, M.A. Bloodgood, L. Wu, M.A. Verheijen, V. Vandalon, W.M.M. Kessels, J.P. Hofmann, and A.A. Bol, Chem. Mater. **31**, 5104 (2019).

[135] S. Yeo, D.K. Nandi, R. Rahul, T.H. Kim, B. Shong, Y. Jang, J.S. Bae, J.W. Han, S.H. Kim, and H. Kim, Appl. Surf. Sci. **459**, 596 (2018).

[136] D.K. Nandi, S. Yeo, M.Z. Ansari, S. Sinha, T. Cheon, J. Kwon, H. Kim, J. Heo, T. Song, and S.H. Kim, Electrochim. Acta **322**, 134766 (2019).

[137] Y. Wu, M.H. Raza, Y.C. Chen, P. Amsalem, S. Wahl, K. Skrodczky, X. Xu, K.S. Lokare, M. Zhukush, P. Gaval, N. Koch, E.A. Quadrelli, and N. Pinna, Chem. Mater. **31**, 1881 (2019).

[138] F.N. Sayed, M.B. Sreedhara, A. Soni, U. Bhat, R. Datta, A.J.J. Bhattacharyya, and C.N.R. Rao, Mater. Res. Express **6**, (2019).

[139] R. Browning, P. Plachinda, P. Padigi, R. Solanki, and S. Rouvimov, Nanoscale **8**, 2143 (2016).

[140] B. Groven, A. Nalin Mehta, H. Bender, J. Meersschaut, T. Nuytten, P. Verdonck, T. Conard, Q. Smets, T. Schram, B. Schoenaers, A. Stesmans, V. Afanas'ev, W. Vandervorst, M. Heyns, M. Caymax, I. Radu, and A. Delabie, Chem. Mater. **30**, 7648 (2018).

[141] B. Groven, A.N. Mehta, H. Bender, Q. Smets, J. Meersschaut, A. Franquet, T. Conard, T. Nuytten, P. Verdonck, W. Vandervorst, M. Heyns, I. Radu, M. Caymax, and A. Delabie, J. Vac. Sci. Technol. A Vacuum, Surfaces, Film. **36**, 01A105 (2018).

[142] T.W. Scharf, S. V. Prasad, M.T. Dugger, P.G. Kotula, R.S. Goeke, and R.K. Grubbs, Acta Mater. **54**, 4731 (2006).

[143] T.W. Scharf, D.R. Diercks, B.P. Gorman, S. V. Prasad, and M.T. Dugger, Tribol. Trans. **52**, 284 (2009).

[144] A. Delabie, M. Caymax, B. Groven, M. Heyne, K. Haesevoets, J. Meersschaut, T. Nuytten, H. Bender, T. Conard, P. Verdonck, S. Van Elshocht, S. De Gendt, M. Heyns, K. Barla, I. Radu, and A. Thean, Chem. Commun. **51**, 15692 (2015).

[145] B. Groven, M. Heyne, A. Nalin Mehta, H. Bender, T. Nuytten, J. Meersschaut, T. Conard, P. Verdonck, S. Van Elshocht, W. Vandervorst, S. De Gendt, M. Heyns, I. Radu, M. Caymax, and A. Delabie, Chem. Mater. **29**, 2927 (2017).

[146] T. Schram, Q. Smets, B. Groven, M.H. Heyne, E. Kunnen, A. Thiam, K. Devriendt, A. Delabie, D. Lin, M. Lux, D. Chiappe, I. Asselberghs, S. Brus, C. Huyghebaert, S. Sayan, A. Juncker, M. Caymax, and I.P. Radu, Eur. Solid-State Device Res. Conf. 212 (2017).

[147] D.K. Nandi, U.K. Sen, A. Dhara, S. Mitra, and S.K. Sarkar, RSC Adv. **6**, 38024 (2016).

[148] Y. Sun, Z. Chai, X. Lu, and J. Lu, Tribol. Int. **114**, 478 (2017).

[149] Y.F. Sun, Z.M. Chai, X.C. Lu, and D.N. He, Sci. China Technol. Sci. **60**, 51 (2017).

[150] R. Browning, N. Kuperman, R. Solanki, V. Kanzyuba, and S. Rouvimov, Semicond. Sci. Technol. **31**, 095002 (2016).

[151] K. Park, Y. Kim, J.-G. Song, S. Jin Kim, C. Wan Lee, G. Hee Ryu, Z. Lee, J. Park, and H. Kim, 2D Mater. **3**, 014004 (2016).

[152] J. Hämäläinen, M. Mattinen, K. Mizohata, K. Meinander, M. Vehkamäki, J. Räisänen, M. Ritala, and M. Leskelä, Adv. Mater. **30**, 1703622 (2018).

[153] V. Pore, M. Ritala, and M. Leskela, Chem. Vap. Depos. **13**, 163 (2007).

[154] N. Mahuli and S.K. Sarkar, J. Vac. Sci. Technol. A Vacuum, Surfaces, Film. **33**, 01A150 (2015).

[155] H. Nam, H. Yang, E. Kim, C. Bae, and H. Shin, J. Vac. Sci. Technol. A **37**, 020916 (2019).

[156] M. Mattinen, G. Popov, M. Vehkamäki, P.J. King, K. Mizohata, P. Jalkanen, J. Räisänen, M. Leskelä, and M. Ritala, Chem. Mater. **31**, 5713 (2019).

[157] D. Nminibapiel, K. Zhang, M. Tangirala, H. Baumgart, V.S.K. Chakravadhanula, C. Kübel, and V. Kochergin, ECS J. Solid State Sci. Technol. **3**, P95 (2014).

[158] R. Browning, N. Kuperman, B. Moon, and R. Solanki, Electronics **6**, 27 (2017).

[159] K. Zhang, D. Nminibapiel, M. Tangirala, H. Baumgart, and V. Kochergin, ECS Trans. **50**, 3 (2013).

[160] J.G. Song, J. Park, W. Lee, T. Choi, H. Jung, C.W. Lee, S.H. Hwang, J.M. Myoung, J.H. Jung, S.H. Kim, C. Lansalot-Matras, and H. Kim, ACS Nano **7**, 11333 (2013).

[161] H. Wang, Z. Lu, S. Xu, D. Kong, J.J. Cha, G. Zheng, P.C. Hsu, K. Yan, D. Bradshaw, F.B.

Prinz, and Y. Cui, Proc. Natl. Acad. Sci. U. S. A. **110**, 19701 (2013).

[162] K.Y. Ko, J.G. Song, Y. Kim, T. Choi, S. Shin, C.W. Lee, K. Lee, J. Koo, H. Lee, J. Kim, T. Lee, J. Park, and H. Kim, ACS Nano **10**, 9287 (2016).

[163] W. Zeng, L.P. Feng, J. Su, H. xi Pan, and Z.T. Liu, J. Alloys Compd. **745**, 834 (2018).

[164] N. Li, L.P. Feng, J. Su, W. Zeng, and Z.T. Liu, RSC Adv. **6**, 64879 (2016).

[165] C.T. Chen, J. Pedrini, E.A. Gaulding, C. Kastl, G. Calafiore, S. Dhuey, T.R. Kuykendall, S. Cabrini, F.M. Toma, S. Aloni, and A.M. Schwartzberg, Sci. Rep. **9**, 1 (2019).

[166] C. Martella, P. Melloni, E. Cinquanta, E. Cianci, M. Alia, M. Longo, A. Lamperti, S. Vangelista, M. Fanciulli, and A. Molle, Adv. Electron. Mater. **2**, 3 (2016).

[167] J.G. Song, G.H. Ryu, S.J. Lee, S. Sim, C.W. Lee, T. Choi, H. Jung, Y. Kim, Z. Lee, J.M. Myoung, C. Dussarrat, C. Lansalot-Matras, J. Park, H. Choi, and H. Kim, Nat. Commun. **6**, 1 (2015).

[168] M.L. Shi, L. Chen, T.B. Zhang, J. Xu, H. Zhu, Q.Q. Sun, and D.W. Zhang, Small **13**, 1 (2017).

[169] B.D. Keller, A. Bertuch, J. Provine, G. Sundaram, N. Ferralis, and J.C. Grossman, Chem. Mater. **29**, 2024 (2017).

[170] T.R. Hellstern, D.W. Palm, J. Carter, A.D. Deangelis, K. Horsley, L. Weinhardt, W. Yang, M. Blum, N. Gaillard, C. Heske, and T.F. Jaramillo, ACS Appl. Energy Mater. **2**, 1060 (2019).

[171] T.J. Dai, X.D. Fan, Y.X. Ren, S. Hou, Y.Y. Zhang, L.X. Qian, Y.R. Li, and X.Z. Liu, J. Mater. Sci. **53**, 8436 (2018).

[172] T. Dai, Y. Liu, X. Liu, D. Xie, and Y. Li, J. Alloys Compd. **785**, 951 (2019).

[173] T.J. Dai, Y.C. Liu, X.D. Fan, X.Z. Liu, D. Xie, and Y.R. Li, Nanophotonics **7**, 1959 (2018).

[174] C. Martella, L. Ortolani, E. Cianci, A. Lamperti, V. Morandi, and A. Molle, Nano Res. **12**, 1851 (2019).

[175] A. Sharma, R. Mahlouji, L. Wu, M.A. Verheijen, V. Vandalon, S. Balasubramanyam, J.P. Hofmann, W.M.M. Erwin Kessels, and A.A. Bol, Nanotechnology **31**, 255603 (2020).

Low-Temperature Phase-Controlled Synthesis of Titanium Di- and Tri-sulfide by Atomic Layer Deposition

3

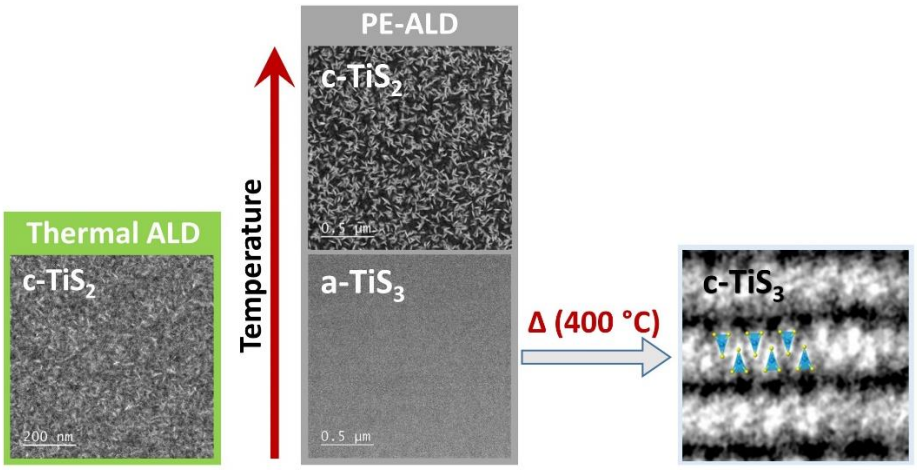

Phase-controlled synthesis of two-dimensional (2D) transition metal chalcogenides (TMCs) at low temperatures with a precise thickness control has to date been rarely reported. Here, we report on a process for the phase-controlled synthesis of TiS_2 (metallic) and TiS_3 (semiconducting) nano-layers by atomic layer deposition (ALD) with precise thickness control. The phase-control has been obtained by carefully tuning the deposition temperature and coreactant composition during ALD. In all cases, characteristic self-limiting ALD growth behavior with a growth per cycle (GPC) of ~0.16 nm per cycle was observed. TiS_2 was prepared at 100 °C using H_2S gas as coreactant and was also observed using H_2S plasma as a coreactant at growth temperatures between 150 and 200 °C. TiS_3 was synthesized only at 100 °C using H_2S plasma as the coreactant. The S_2 species in the H_2S plasma, as observed by optical emission spectroscopy, has been speculated to lead to the formation of the TiS_3 phase at low temperatures. The control between the synthesis of TiS_2 and TiS_3 was elucidated by Raman spectroscopy, X-ray photoelectron spectroscopy, high-resolution electron microscopy, and Rutherford back scattering studies. Electrical transport measurements showed the low resistive nature of ALD grown 2D-TiS_2 (*1T*-phase). Postdeposition annealing of the TiS_3 layers at 400 °C in a sulfur-rich atmosphere improved the crystallinity of the film and yielded photoluminescence at ~0.9 eV, indicating the semiconducting (direct band gap) nature of TiS_3. The current study opens up a new ALD-based synthesis route for controlled, scalable growth of transition metal di- and tri-chalcogenides at low temperatures.

Saravana Balaji Basuvalingam, Yue Zhang, Matthew A. Bloodgood, Rasmus H. Godiksen, Alberto G. Curto, Jan P. Hofmann, Marcel A. Verheijen, Wilhelmus M. M. Kessels, and Ageeth A. Bol, Chem. Mater. **31**, 22 (2019)

3.1 Introduction

Since the isolation of monolayer graphene, two-dimensional (2D) materials such as the transition metal *di*-chalcogenides (TMDCs) have shown interesting electrical and optical properties[1]. TMDCs consist of a transition metal (such as Mo, W, Ti, Nb, etc.) paired with a chalcogenide (S, Se and Te) forming a layered structure in which the layers are held together by weak van der Waals forces. Besides TMDCs there is an alternative class of low-dimensional materials that consist of similar elements as TMDCs. This class of materials is known as the transition metal *tri*-chalcogenides (TMTCs) and consists of quasi-1D materials possessing an added degree of freedom that results in a strong electrical and optical in-plane anisotropy[2,3]. The TMTCs are known for the groups IV, V and VI transition metals (such as Ti, Hf, Nb, etc.) and are predominantly semiconducting in nature[2–6]. The electrical properties vary between *di*- and *tri*-chalcogenide systems containing analogous elements. For example, TiS_2 and NbS_2 are considered a semi-metal and metal, respectively, whereas TiS_3 and NbS_3 are both semiconductors. Therefore, controlling phase transitions between TMDCs and TMTCs during synthesis allows for direct tailoring of the electrical characteristics of these low-dimensional materials. This phase-control could offer new possibilities for device fabrication.

Titanium sulfide (TiS_x) is one of the systems that could provide an excellent framework for phase control during synthesis. TiS_2 has been studied extensively for batteries[7], optics[8], and thermoelectric material[9] applications and has been synthesized by various techniques such as chemical vapor transport (CVT)[10], chemical vapor deposition (CVD)[11–15], atomic layer deposition (ALD)[16–18], and wet chemical synthesis[19]. Interestingly, the electrical properties of TiS_2 have been under debate for the last few decades, with hypotheses from both theory and experimental results splitting between a semiconducting, metallic or semi-metallic nature[20,21]. Recently, TiS_2 has been considered as a degenerate, small-gap semiconductor or a semi-metal owing to its high conductivity and optical absorption properties[22]. Conversely, TiS_3 has a direct band gap in the infrared region (0.9-1 eV) irrespective of its thickness and is the only known TMTC possessing a direct band gap[3]. This makes TiS_3 an ideal candidate for (opto)electronics applications[23,24]. It is known from the literature that TiS_3 is much more difficult to synthesize, with reports predominantly using CVT methods[3] with a few instances of CVD[13,25, 26]. CVT is a technique where elemental Ti and S are sealed inside a quartz ampoule and placed inside a furnace for synthesis making this a non-scalable (*i.e.*, not wafer-scale), relatively high temperature, and are time-consuming technique[3–5,27].

In TiS_x CVT synthesis,[10] phase-control can be attained by carefully modulating both the S to Ti ratio and the process temperature. TiS_2 is obtained with an initial S to Ti ratio of 2, whereas TiS_3 is obtained by maintaining a S to Ti ratio above 3. Temperature is also important due to pyrolysis of S from TiS_3 above 550 °C. Thus, TiS_3 must be synthesized at or below 550 °C. A significant drawback of the CVT technique is that it requires days to weeks at high temperatures (> 450 °C) for growing large crystals (> 1 cm), which can be subsequently used to mechanically exfoliate 2D flakes of only several microns in size. Thus, a technique to rapidly synthesize both TiS_2 and TiS_3 over a large area (wafer-scale) with high uniformity and controlled thickness would be very beneficial for nanoelectronic applications.

In this work, using atomic layer deposition (ALD) as a synthesis technique, we address the challenges associated with other synthesis methods. The ALD method has advantages such as precise thickness control and conformal growth over a large area[28,29]. In addition, most ALD processes are performed at low temperatures (<450 °C) which are favorable for device manufacturing schemes[29–31]. Recently, interest in controlling the phase as well as the composition of metal-oxide based materials has been made viable by ALD[32–34]. Therefore, ALD could serve as the ideal technique for synthesizing both TMDCs and TMTCs over a large area at low temperatures with precise thickness control. Previously, TiS_2 has been reported to be synthesized by ALD using $TiCl_4$ and H_2S with a growth per cycle (GPC) between 0.15 and 0.5 Å depending on deposition temperature[16,17]. Recently, ALD of amorphous TiS_2 has been reported by Nam *et al.*[18] using tetrakis (dimethylamido) titanium and H_2S at a deposition temperature between 120 and 180 °C with a GPC of ~0.5 Å. They also reported the surface oxidation of TiS_2 after exposure to the ambient conditions. On the other hand, so far to the best of our knowledge TiS_3 has not been synthesized by ALD.

This work describes a scalable, low temperature ALD synthesis route with control over the phase of titanium sulfide (TiS_x). The effect of varying the sulfur coreactant and the deposition temperature on the phase of the deposited material is studied using an extensive array of characterization techniques (Raman spectroscopy, transition electron microscopy (TEM), X-ray photoelectron spectroscopy, and Rutherford backscattering spectrometry (RBS)). Our work shows that ALD is well suited for obtaining both metallic TiS_2 and semiconducting TiS_3 in a temperature range of 100 to 200 °C. By tuning the temperature and the sulfur coreactant in this temperature range, we demonstrate control over the phase.

3.2 Experimental Details

3.2.1 Film Growth

The TiS_x thin films were deposited by ALD using an Oxford Instruments Plasma Technology FlexAL ALD reactor. The base pressure of the system was 10^{-6} Torr and the reactor was equipped with a remote inductively coupled plasma source (ICP, 13.56 MHz). The deposition temperature was varied between 100 and 200 °C. The reactor was a warm wall reactor where the wall temperature can be varied from room temperature to a maximum of 150 °C, independently of table temperature. For depositions below 150 °C, both the table and wall temperatures were maintained at equal temperatures, whereas for depositions above 150 °C, only the table temperature was varied while the wall temperature remained at 150 °C (maximum wall temperature). The metal-organic precursor tetrakis (dimethylamido) titanium (TDMAT) (Sigma-Aldrich Chemie BV, 99.999 % pure) was kept in a stainless steel bubbler at 50 °C, and was bubbled using Ar as the carrier gas. In the first half-cycle, the precursor was dosed into the reactor using Ar as the carrier gas and the pressure was maintained at 80 mTorr. During the second half-cycle, a gas mixture of Ar and H_2S (both >99.98 % pure) with 10 and 40 sccm, respectively was used as co-reactant in the case of thermal ALD. In the case of plasma-enhanced ALD (PE-ALD), H_2S:Ar plasma with the aforementioned gas ratio was used as coreactant and an ICP power of 200 W was applied to ignite the plasma. Ar (300 sccm) was used as the purge gas after the precursor as well as the coreactant dose steps in both the ALD processes. The thin films were deposited on Si substrates covered with approximately 450 nm thermally grown SiO_2.

In some cases, post-deposition annealing of the ALD grown film was conducted in a sulfur atmosphere in a tube furnace. The sample was placed at the center of a quartz tube. After loading sulfur powder on a quartz boat (500 mg, 99.98 %, Aldrich), which was situated upstream, the tube was sealed and Ar (50 sccm) was flown downstream as the carrier gas. The furnace was heated up to the target temperature (400 °C) with a heating rate of 10 °C/min. Meanwhile, the sulfur powder situated upstream of the tube was heated to 170 °C by heating tape. The sample was annealed at 400 °C for 3 h and then cooled down naturally in Ar to room temperature.

3.2.2 Analysis Techniques

Spectroscopic ellipsometry (SE) was used to investigate the film growth *in-situ* where the film thickness was measured as a function of the number of ALD cycles. A J.A. Woollam Co., Inc., M2000U with a rotating compensator having a photon energy range of 0.7-5 eV was used. The film thickness was modeled using a B-spline oscillator (the film thickness was verified using cross-section scanning electron microscopy (SEM)). Raman spectroscopy was performed on a Renishaw inVia system using a 514 nm excitation laser in the ambient environment. X-ray photoelectron spectroscopy (XPS) was used to determine both the elemental composition and valence band spectra of synthesized thin films. A Thermo Scientific KA1066 spectrometer with monochromatic Al Kα (hν = 1486.6 eV) X-ray radiation was employed. The crystallinity of the thin films was studied by X-ray diffraction (XRD) with a PANalytical X´Pert Pro MRD analyzer, using a Cu Kα (λ = 1.54 Å) X-ray source. The surface morphology of the films was investigated by scanning electron microscopy (SEM) using a Zeiss Sigma with an in-lens detector and operating at an acceleration voltage of 3 kV. The thin film microstructure was studied using transition electron microscopy (TEM) and scanning transmission electron microscopy (STEM) with a JEOL ARM 200F operated at 200 kV. For TEM/STEM studies, the films were grown on Si_3N_4 TEM windows coated with ~5 nm ALD SiO_2. The selected area electron diffraction (SAED) patterns were acquired from a 1.3 µm diameter area on each sample. For cross-section TEM/STEM, a thin lamella (~100 nm) was prepared by a focused ion beam (FIB) using the lift-out preparation procedure. To protect the post-deposition annealed TiS_3 film during lamella preparation, a SiO_2 layer was deposited on the top by electron-beam induced deposition. High-angle annular dark-field STEM (HAADF-STEM) combined with energy-dispersive X-ray spectroscopy (EDX) was used to study the chemical composition of the post-deposition annealed TiS_3 films. Rutherford backscattering spectrometry (RBS) and elastic recoil detection (ERD) measurements were used to determine the composition and purity of the thin films. The measurements were conducted by Detect 99 B.V. Eindhoven, The Netherlands with a 2 MeV He^+ beam source containing two detectors at scattering angles of 105° and 170°. Optical emission spectroscopy (OES) of the H_2S:Ar plasma was performed using a USB4000 spectrometer from Ocean Optics with a wavelength range of 180-1100 nm mounted vertically on top of the plasma source. Resistivity measurements were performed *ex-situ* and at room temperature using a Signatone four-point probe in combination with a Keithley 2400 sourcemeter acting both as a current source and as a voltage meter. The resistivity of the thin films was determined from the slope of the *I-V* curve. The near-infrared (NIR) photoluminescence (PL) measurements were conducted using an inverted microscope in an

epi-illumination geometry with an objective lens (50X Mitutoyo M Plan NIR Infinity Corrected, NA = 0.42) and a 2.040 eV excitation continuous wave laser. The PL spectra were recorded using an Andor Shamrock 163 spectrometer and an Andor iDus 1.7 µm InGaAs camera.

3.3 Results and Discussion

Phase-control between TiS_2 and TiS_3 during CVT has previously been observed to obey the following empirical relationship[35]:

$$\log P_{(\mathrm{Torr})} = 10.42\ (\pm 0.42) - 6850 / T_{(\mathrm{K})}\ (\pm 340),$$

where P corresponds to the partial pressure of sulfur and T corresponds to the synthesis/system temperature. This relationship indicates the sulfur partial pressure at which the pyrolysis of TiS_3 to TiS_2 is favored at a given temperature and therefore illustrates the minimum partial pressure of S required at a given temperature to synthesize TiS_3. Thus, these two variables can be modulated accordingly to achieve phase-control between TiS_2 and TiS_3. This forms the basis for studying the effects of H_2S as a coreactant and the deposition temperature during the ALD process.

The effect of the coreactant sulfur species was studied by comparing H_2S plasma (PE-ALD) and H_2S gas (thermal ALD) as the coreactant at a deposition temperature of 100 °C for ~30 nm thick TiS_x thin films. The schematic representation of one complete ALD cycle as a function of time is shown in Figure 3.1(a). In the case of PE-ALD, power was applied to the ICP source to ignite the plasma during the H_2S:Ar coreactant step as shown in Figure 3.1(a), whereas in the case of thermal ALD the ICP source was turned off. The film thickness as a function of the number of ALD cycles as measured by *in-situ* SE is shown in Figure 3.1(b). The growth per cycle (GPC) was calculated by taking the slope of the curve in the linear part. Both the PE-ALD and the thermal ALD processes have a GPC of ~1.6 Å, and exhibit typical ALD linear growth behavior with precise thickness control from monolayer to bulk. The self-limiting saturated growth behavior was observed for both ALD processes at a deposition temperature of 100 °C (appendix 3 Figure A3.1). In the first half-cycle, the TDMAT precursor dose reached saturation around 4 s for both ALD processes. In the second half-cycle, in the case of PE-ALD, the H_2S: Ar plasma exposure reached saturation around 25 s. Although plasma exposure reached saturation around 25 s, a plasma exposure of 30 s was used during the film deposition to ensure uniform growth over a large area. In the case of thermal ALD,

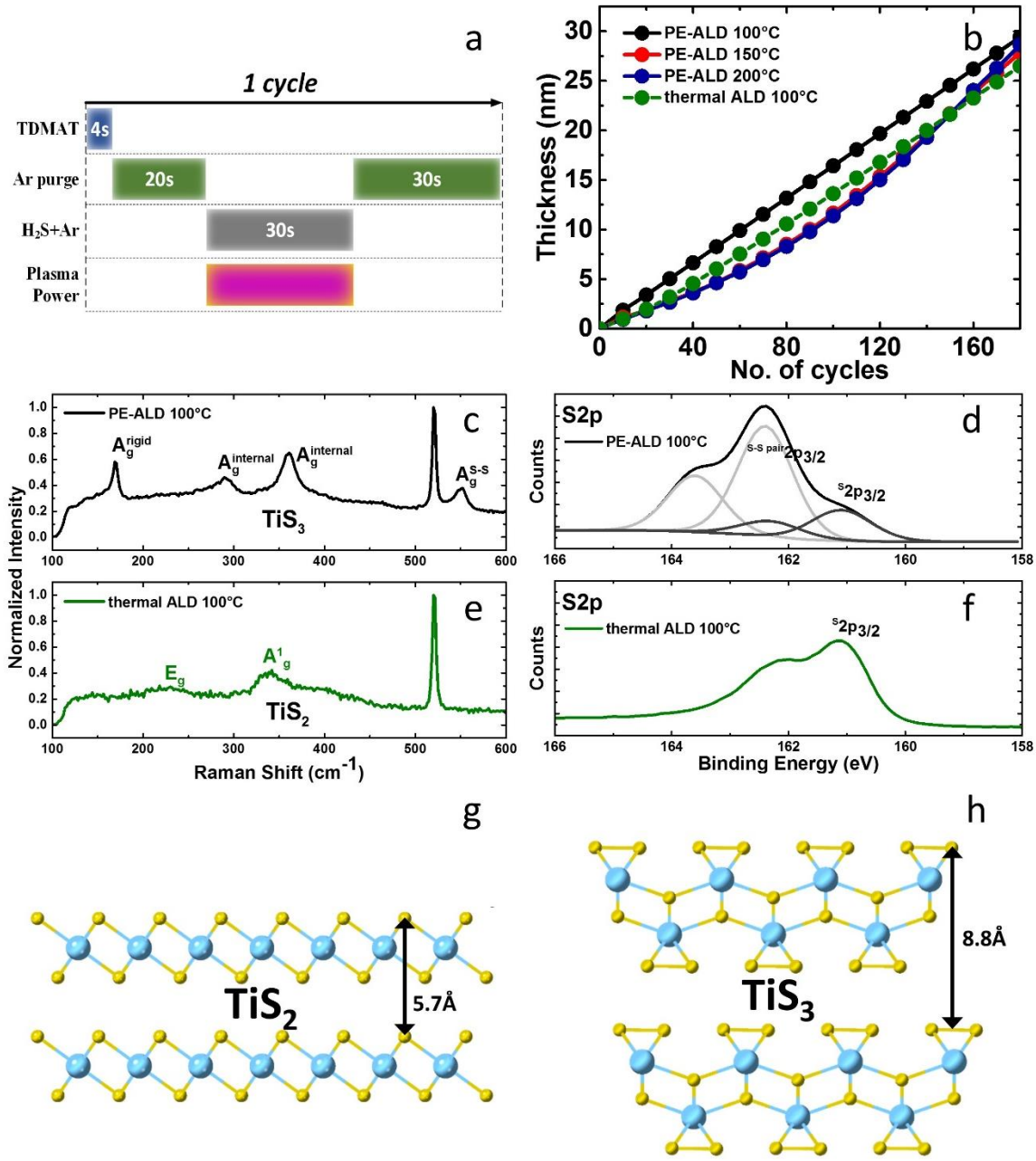

Figure 3.1 (a) Schematic of one complete ALD process cycle implemented at all investigated temperatures. Plasma power was ON for PE-ALD, while it was OFF for thermal ALD. (b) Film thickness as a function of the number of ALD cycles measured using *in-situ* SE for PE-ALD grown films at deposition temperatures between 100 and 200 °C, and also for a thermal ALD film grown at 100 °C. Raman spectra of (c) PE-ALD and (e) thermal ALD grown films at 100 °C deposition temperature and also the corresponding TiS_3 and TiS_2 vibration peaks. The peak at 520 cm^{-1} is of the Si substrate. S2p XPS spectra of (d) PE-ALD and (f) thermal ALD grown films at 100 °C deposition temperature. In (d) the (dark grey) doublet peaks correspond to S^{2-} atoms and the (light grey) doublet peaks at higher energy correspond to $(S_2)^{2-}$ atoms of TiS_3 ($Ti^{4+}(S_2)^{2-}S^{2-}$). (g, h) Crystal structures of two TiS_2 and TiS_3 monolayers, where the respective thickness of one monolayer is indicated.

a 30 s dose time of H_2S: Ar gas was chosen to have a fair comparison with the PE-ALD process and the chosen dose time was observed to be in the saturation regime as well.

Raman spectroscopy studies were conducted on the TiS_x films deposited by both ALD processes at 100 °C. For the film deposited by PE-ALD, four vibrational peaks at 170, 295, 360 and 550 cm^{-1} were observed. These four vibrational peaks correspond to the four A^1_g-type (Figure 3.1(c)) Raman modes of TiS_3[36]. Interestingly, the Raman spectrum for the film deposited by thermal ALD had only two vibrational peaks at ~230 and ~330 cm^{-1} with a shoulder peak at ~380 cm^{-1}. The two vibrational peaks at 230 cm^{-1} and 330 cm^{-1} observed for thermal ALD (Figure 3.1(e)) film correspond to the E_g and A^1_g Raman modes of 1*T*-TiS_2, respectively[37]. These findings indicate that phase-controlled synthesis of TiS_2 and TiS_3 can be attained with ALD by switching between H_2S gas and H_2S plasma in the coreactant step at 100 °C.

The chemical composition and binding environments in the deposited films were then investigated using XPS analysis. The as-deposited films had some C and O contamination at the surface due to exposure of the films to ambient conditions after deposition. However, the bulk of the films was free from C and O impurities. The XPS spectra obtained were calibrated by setting the C–C peak to 248.8 eV in the C1s spectrum. The S2p spectrum of the PE-ALD grown film at 100 °C contains two doublets (Figure 3.1(d)): one at 161.1 eV and 162.3 eV (dark grey), and the other at 162.4 and 163.6 eV (light grey). In comparison to the literature, the lower energy doublet at 161.1 eV and 162.3 eV corresponds to the $S2p_{3/2}$ and $S2p_{1/2}$ spin-orbit doublet of an isolated S^{2-} species, and the second doublet at 162.4 and 163.6 eV corresponds to the spin-orbit doublet of $(S_2)^{2-}$ (also known as a S–S pair). This is consistent with the TiS_3 formula written as $Ti^{4+}(S_2)^{2-}S^{2-}$ [38]. The presence of both doublets could also be due to the presence of a mixed phase of both TiS_2 and TiS_3, but the Raman spectrum from Figure 3.1(c) showed vibration modes of only TiS_3, indicating a lack of TiS_2 in the film. Additionally, the fitted peak area ratio of $(S_2)^{2-}$:S^{2-} was calculated to be 2.5:1 which indicated the presence of excess $(S_2)^{2-}$ species in the film. From the XPS S2p peaks, it was determined that the excess S present in the film does not match the binding energy of any elementary S species such as S_8, S_4 etc. The S to Ti atomic ratio calculated from RBS measurements for a PE-ALD grown film at 100 °C further confirms the synthesis of TiS_3 (see Table 3.1) with the incorporation of excess S (S/Ti ratio above 3). In contrast to the PE-ALD film, the films deposited by thermal ALD (Figure 3.1(f)) at 100 °C exhibited only one S2p doublet at 161.1 and 162.3eV (spin-orbit doublet of S^{2-}) indicating the deposition of TiS_2. The S to Ti atomic ratio calculated from RBS measurements also confirms that the TiS_2 film obtained by thermal ALD is slightly S deficient (S/Ti ratio less than 2). The RBS and XPS

results confirm that we can obtain phase control during ALD by tuning the gas composition in the coreactant step.

To better understand the conditions contributing to the phase-controlled synthesis of TiS_2 and TiS_3, OES was performed (Figure 3.2) to obtain insight into the chemistry of the H_2S:Ar plasma. In the H_2S:Ar plasma, S-containing species, including SH^+ (at around 337 nm) and S_2 (peaks between 280 and 610 nm) species, were detected along with the Ar and H species[39,40]. The contribution of S_2 species in the OES spectrum (between 280 and 610 nm) is significant (see appendix 3 Figure A3.2, where Figure 3.2 is compared with the OES spectrum of H_2:Ar plasma without S species). In the case of thermal ALD, the H_2S:Ar gas (no optical emission in the gas phase) would most likely decompose into Ar and reactive H, SH and S species at the reaction surface[41,42]. By comparing both the cases, we hypothesize that the generation of S_2 species in the H_2S:Ar plasma could lead to the synthesis of TiS_3 [$Ti^{4+}(S_2)^{2-}S^{2-}$] where mojority of the sulfur exists as S–S pairs. A similar observation was made by Carmalt *et al* using CVD[13], where TiS_3 was synthesized only when a coreactant containing S_2 species was used. These S_2 species, however, are not present in the case of H_2S:Ar gas utilized during thermal ALD, which yielded only TiS_2.

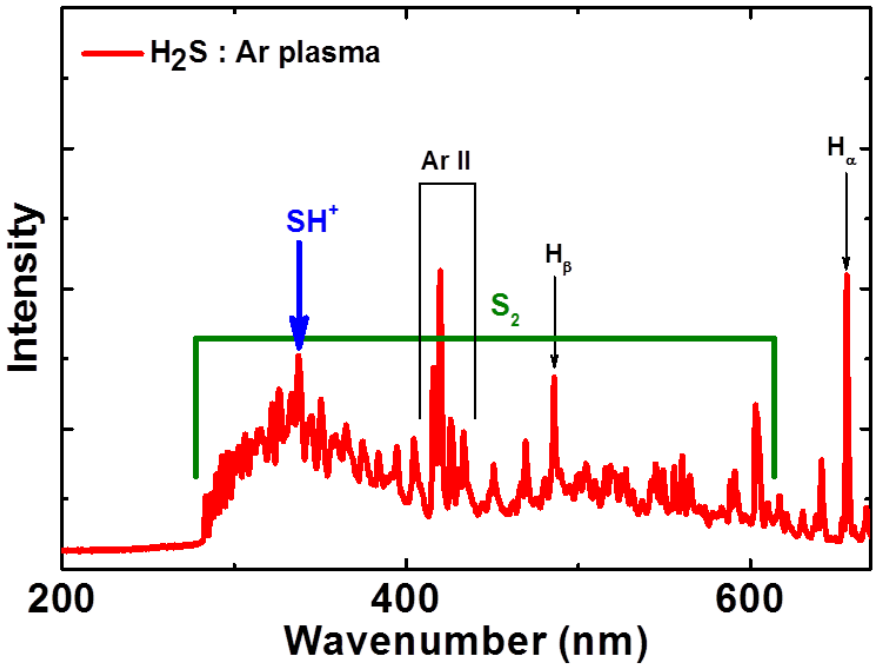

Figure 3.2 Optical emission spectrum of the H_2S:Ar plasma from PE-ALD with a gas flow of 10:40 sccm. It shows the corresponding peak for SH^+ (blue) and the range of peaks for S_2 (green) species along with H and Ar species (black).

Following the synthesis of TiS_3 by PE-ALD at 100 °C, the effect of the synthesis temperature (second variable in the earlier mentioned empirical relationship) on the material´s phase/composition was studied by varying the deposition temperature in PE-ALD between 100 and 200 °C. In Figure 3.1(b), the film thickness as a function of the number of ALD cycles is shown for the investigated deposition temperatures. Linear growth was observed for deposition at 100 °C without any nucleation delay, whereas, for depositions at 150 °C and 200 °C non-linear growth was observed. This non-linear growth can be ascribed to both the change in morphology of the film and the change in material phase (as will be discussed later). The GPC of the PE-ALD films increased from 1.6 Å at 100 °C to >2.0 Å at the higher temperatures, see Table 3.1. In comparison to the 100 °C film, the increase in GPC at higher temperatures is due to fin-like, out-of-plane oriented (OoPO) growth as will be discussed later (in Figure 3.4). Similar growth behavior and increased GPC with OoPO growth have been previously observed for PE-ALD grown MoS_2[29].

Raman spectra of the films grown at higher temperatures were compared to the previously studied, TiS_3 film grown at 100 °C. Figure 3.3(a) shows the Raman spectra of the films deposited at 150 and 200 °C containing two vibrational peaks at 230 and 330 cm^{-1} along with a shoulder at 380 cm^{-1} analogous to the Raman spectrum obtained for the TiS_2 film grown at 100 °C by thermal ALD (Figure 3.1(e)). These results demonstrate that phase control within the PE-ALD process was achieved between TiS_2 and TiS_3 by increasing the growth temperature, similar to that in CVT. In the PE-ALD process, the transition temperature of ~100 °C for TiS_3 to TiS_2 synthesis is very low in comparison to CVT (550 °C). Additionally, the XPS S2p spectra for the 150 and 200 °C films corroborate this result with the Figure 3.1(f). The S2p spectra of both films display only one doublet at 161.1 and 162.3 eV (similar to thermal ALD grown films at 100 °C) corresponding to the spin-orbit doublet of S^{2-} species indicating the deposition of TiS_2.

The valence band spectra of the films deposited by PE-ALD were also investigated using XPS analysis. The Fermi level (BE = 0 eV) was calibrated by measuring the Fermi edge of gold. At 100 °C four broad peaks (see Figure 3.3(b), black) at around 1.6, 4.5, 10.7 and 15.3 eV binding energies (BE) were observed. Due to the hybridization by excess S–S pairs in TiS_3, the two valence band peaks of TiS_2 split to form four broad peaks[38]. The XPS valence band spectra for films deposited at 150 and 200 °C differed from the spectrum obtained at 100 °C showing only two broad peaks at around 3.5 and 13 eV (Figure 3.3(b)). In comparison to the literature, the spectra for the films deposited at 150 and 200 °C correspond to the valence band spectrum of TiS_2[38]. These results further confirm that the phase-controlled synthesis of TiS_2/TiS_3 can be obtained by tuning the deposition temperature.

The composition and purity of the material were further determined using RBS measurements, see Table 3.1. The S/Ti ratio was measured to be 3.48 for the film deposited at 100 °C, whereas the S/Ti ratio for the films deposited at 150 and 200 °C was around 2 with a small S deficiency (or excess Ti). Additionally, contaminants such as C and O were detected within the error limit (Table 3.1), confirming the high purity of the films similar to the XPS measurements. Interestingly, ERD revealed a significant amount of H impurities (~10 at.%) for the 150 and 200 °C films. The H may have most likely been incorporated from the plasma coreactant and/or precursor ligands. It could be possible to reduce the H impurities in the film by further optimizing the H_2S:Ar plasma coreactant exposure time during the ALD cycle.

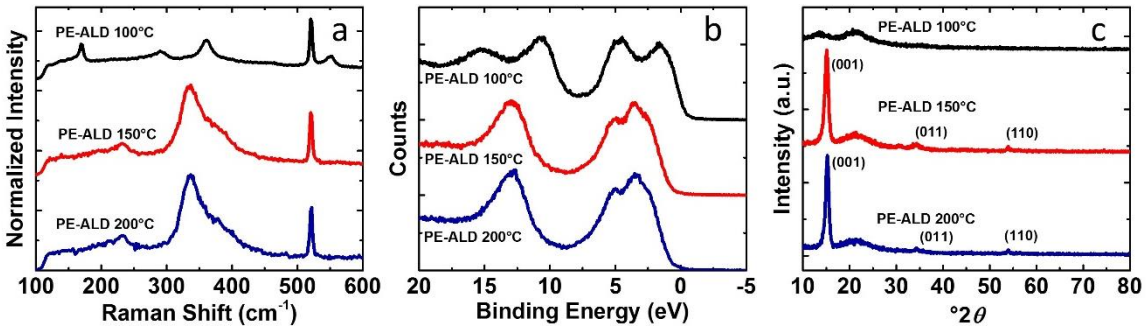

Figure 3.3 (a) Raman spectra showing the vibration mode peaks and (b) XPS valence band spectra of PE-ALD grown films between 100 and 200 °C deposition temperature. (c) Grazing-incidence X-ray diffraction (GI-XRD) patterns of the films deposited at various temperatures where the peaks corresponding to (001), (011), and (110) planes are mentioned.

The crystallinity of the PE-ALD grown TiS_3 and TiS_2 films was investigated using grazing-incidence (GI)-XRD. The GI-XRD pattern of the film deposited at 100 °C (TiS_3) does not show well-defined peaks, indicating the formation of an amorphous film (Figure 3.3(c)). The films deposited at 150 and 200 °C, however, confirm the synthesis of crystalline 1*T*-TiS_2[19]. The strong peak around 2θ of 15° corresponds to the (001) plane of 1*T*-TiS_2 and reveals a significant orientation effect. This orientation effect can be explained by a crystalline layer in which a strong majority of crystals have their basal planes of 1*T*-TiS_2 oriented parallel to the substrate. This implies that below the OoPO structures visible in the SEM and TEM images (Figure 3.4), a continuous film of the aforementioned basal plane texture is present. The contribution of OoPO structures to the XRD pattern ((011) and (110) peaks) is small because of their limited volume fraction and random orientation with respect to the XRD detection geometry.

Additionally, the SAED pattern also shows the amorphous nature of the film synthesized at 100 °C (Figure 3.4(g)). Complementary to GI-XRD, the SAED patterns of the 150 and 200 °C films display reflections of lattice planes oriented perpendicular to the substrates. As a result, for both 150 and 200 °C films (Figure 3.4(h&i)) high intensity (011), (110) and (010) rings are visible. The continuous nature of the rings confirms the polycrystalline nature of PE-ALD grown TiS_2 films. The discontinuous (001) ring reflects the presence of only a few OoPO structures per probed area having their c-axis parallel to the film surface.

Table 3.1 *in-situ* SE, RBS, ERD and Four-Point Probe measurements of PE-ALD deposited titanium sulfide thin film between 100 and 200 °C deposition temperatures. All films were ~30 nm thick and the GPC was calculated by taking the slope of the linear region above 140 cycles, see Figure 3.1(b). The atomic concentrations of O, C, and the S/Ti ratio were determined by RBS. The H content was determined by ERD. The resistivity was measured using the four-point probe method.

	GPC Å	S/Ti Ratio	O at.%	C at.%	H at.%	Resistivity 10^3 µΩcm
100 °C	1.6	3.48 ± 0.02	1.4 ± 0.6	3.7 ± 0.9	1.3 ± 0.1	-
150 °C	2.1	1.94 ± 0.01	1.7 ± 0.1	1.0 ± 0.1	10.1 ± 0.8	9
200 °C	2.3	1.93 ± 0.01	0.6 ± 0.1	0.6 ± 0.1	9.8 ± 0.8	3.5

Top-view SEM images (Figure 3.4(a-c)) display the morphology of the PE-ALD grown films deposited at all three temperatures. For the film deposited at 100 °C, no surface texture was observed. Similar to SEM, top-view TEM (Figure 3.4(d)) shows no lateral variation in the morphology (*i.e.*, crystallinity and density) of the film. On the other hand, for the films deposited at 150 and 200 °C, top-view SEM images show OoPO structures, which can explain the high growth rate observed in the *in-situ* SE measurements. Analogous OoPO structures have been observed previously for other TMDCs like MoS_2[29] and ReS_2[43]. A similar relation between the OoPO film morphology and increased GPC has been previously observed for MoS_2[29]. The top-view TEM images of films grown at 150 and 200 °C (Figure 3.4(e&f)) confirm the OoPO morphology of the TiS_2 film. The average distance between the 2D layers was measured to be ~5.7 Å (Figure 3.4(e&f)), equivalent to the distance between two 1*T*-TiS_2 layers (Figure 3.1(g))[44].

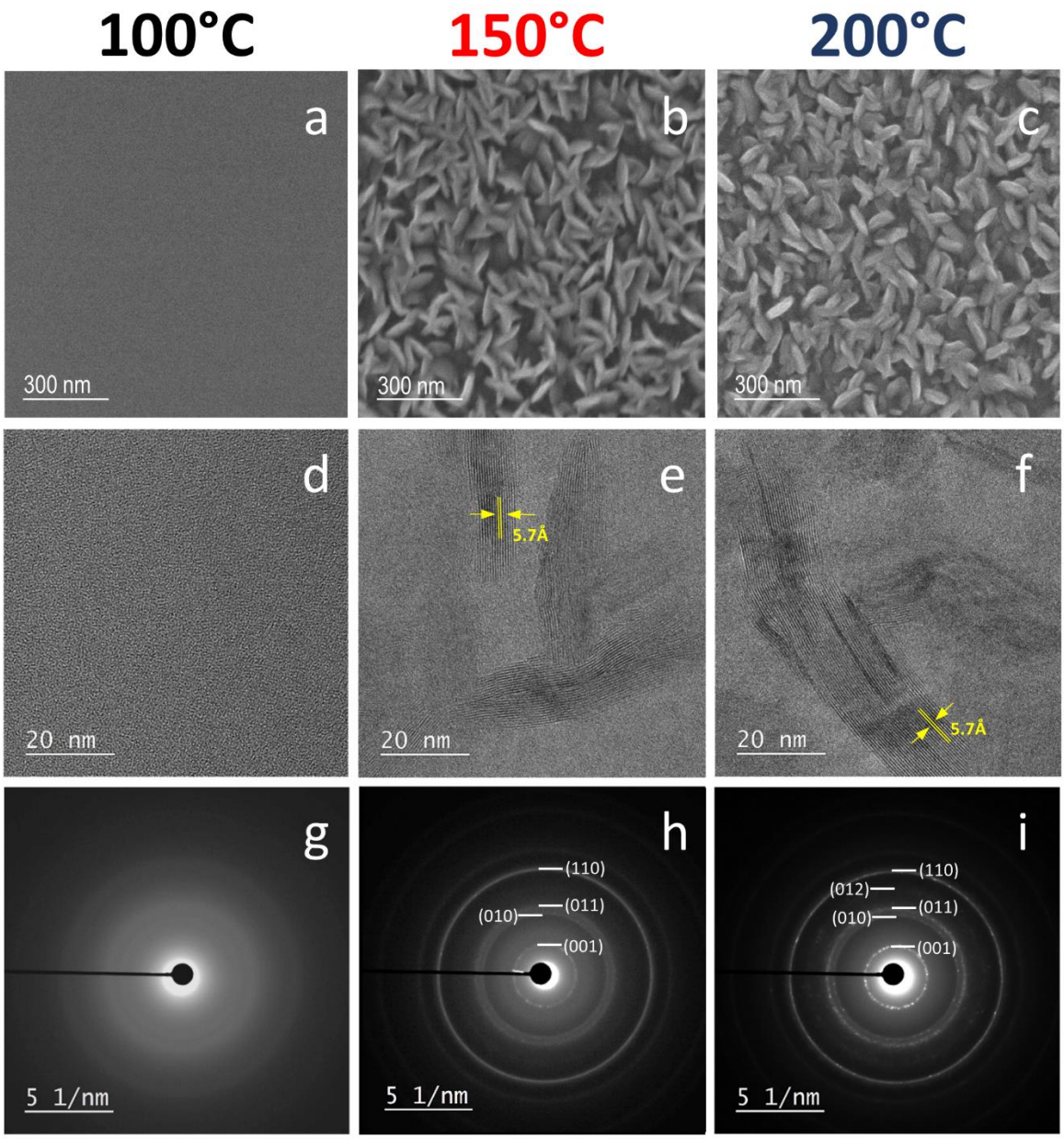

Figure 3.4 Electron microscopy studies of the structure of PE-ALD films. The images (a,d,g), (b,e,h), and (c,f,i) correspond to films deposited by PE-ALD at 100, 150, and 200 °C, respectively. (a-c) Top-view SEM images showing the change in film morphology for various deposition temperatures. (d-f) Top-view TEM images showing the microstructure of the films, in (e) and (f) the layered structure of the OoPO structure in TiS_2 film can be seen. The average measured distance between two layers is highlighted. (g) SAED patterns showing the amorphous nature of the film deposited at 100 °C. (h) and (i) SAED patterns showing the polycrystalline nature of the films deposited at 150 and 200 °C.

The electrical resistivity of the PE-ALD deposited TiS_x films was measured using a four-point probe method. The resistivity of the TiS_3 film deposited at 100 °C could not be measured due to its primarily amorphous nature, which could have yielded a high resistivity

value that was beyond the measurement detection limit. Table 3.1 shows the measured resistivity of the other films. The deposited TiS_2 films exhibit a decrease in resistivity from 9000 to 3500 μΩcm with the increase in temperature from 150 to 200 °C. From an application perspective, these low resistivity *1T*-TiS_2 films could be used as 2D contact materials with 2D semiconductors in device fabrication. (Note that the crystalline (by GI-XRD) TiS_2 film synthesized by thermal ALD at 100 °C has a resistivity of 2000 μΩcm). In summary, the effect of temperature on material composition, phase, morphology, and resistivity was studied in detail. All of the discussed characterization techniques confirm the synthesis of TiS_3 at 100 °C and a transition to TiS_2 at temperatures above 100 °C by PE-ALD. We also investigated the effect of deposition temperature by thermal ALD and observed no change in phase from TiS_2 at all investigated temperatures. These studies, however, will be discussed in detail in Chapter 4.

The crystallinity of the PE-ALD grown amorphous TiS_3 film at 100 °C deposition temperature was improved by a post-deposition annealing step. To avoid oxidation to TiO_2 and pyrolysis to TiS_2 during annealing, a sulfur-rich atmosphere was chosen for the annealing treatment of 3 h at 400 °C. The Raman spectra of TiS_3 before and after annealing are compared in Figure 3.5(a). The four vibration peaks observed for the annealed film confirm that the TiS_3 phase was preserved. Additionally, the red shift of the vibration peaks along with the reduced width of the peaks, indicated improved crystallinity of the film. Some surface oxidation to anatase TiO_2 (~143 cm^{-1}) was observed, probably due to the transfer of the sample through the air from the ALD chamber after deposition to the annealing furnace. The GI-XRD pattern (Figure 3.5(b)) of the annealed film also confirmed improved crystallinity and preservation of the TiS_3 phase of the film, along with TiO_2 (*) due to surface oxidation. Similar to the PE-ALD grown 1*T*-TiS_2 crystalline films, a strong peak around 2θ of 10° corresponds to the (001) plane of TiS_3 and indicates that basal planes of TiS_3 are orientated parallel to the substrate. An average (vertical) crystal size of ~16 nm was calculated using the Scherrer equation[45].

A cross-sectional TEM image of the post-deposition annealed TiS_3 film displays the layered crystalline nature of the post-deposition annealed TiS_3 film (Figure 3.5(c)). Similar to the results from GI-XRD, the basal planes of TiS_3 are oriented parallel to the substrate. An average (lateral) crystal size of ~50nm was measured from the cross-sectional TEM images. The corresponding EDX elemental mapping of the S, Ti and O are shown in Figure 3.5(d-f), respectively. EDX mapping also further confirms the surface oxidation (to TiO_2) of the film, and also shows the presence of a pure titanium sulfide phase below the oxidized surface. Figure 3.5(g) shows a high-resolution HAADF-STEM image of a cross-sectional

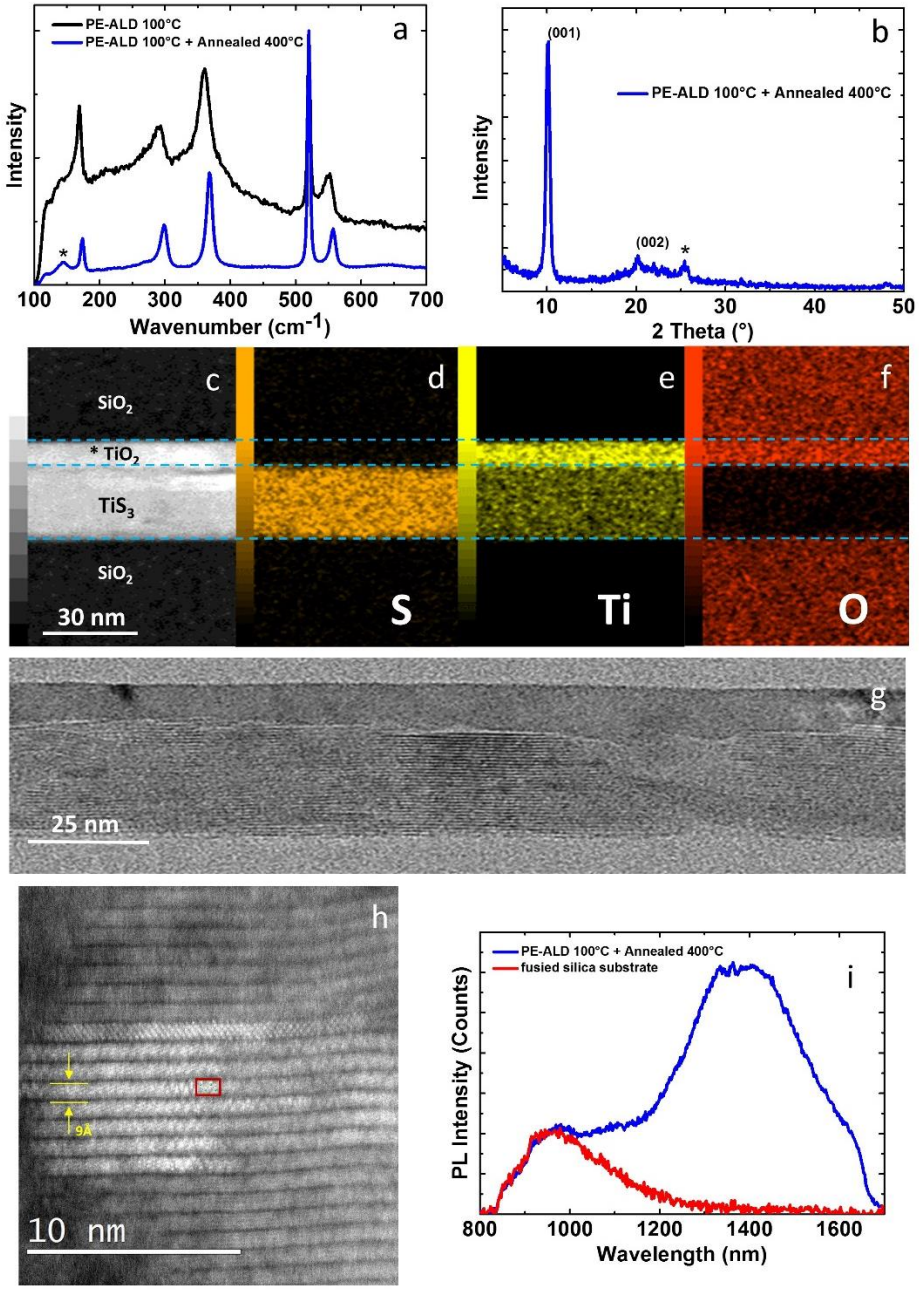

Figure 3.5 (a) Comparison of the Raman spectra of PE-ALD grown TiS_3 before (red, amorphous) and after annealing at 400 °C (blue). (b) GI-XRD pattern of the post-deposition annealed TiS_3 film showing its crystalline nature with peaks corresponding to TiS_3 (00*l*) planes. (c-f) TEM image showing a cross-section of the post-deposition annealed TiS_3 film with corresponding EDX elemental mapping of Ti, S and O. The red (*) in (a), (b and (c) indicates the presence of anatase TiO_2 due to surface oxidation. The white dashed line in (c) highlights the interface between TiO_2 and TiS_3. (g) High-resolution HAADF-STEM image shows the cross-section of post-deposition annealed TiS_3 with atomic resolution. The average measured distance between two layers is highlighted. (h) Zoomed-in area (red box) from (g) with an atomic model of the TiS_3 crystal structure overlaid on the STEM image. (i) PL spectrum demonstrating the semiconductor nature of the annealed film with an optical bandgap ~0.9 eV, compared with PL (red) of the fused silica substrate.

region in the post-deposition annealed crystalline TiS_3 film. The average distance between the monolayers was measured to be 8.9 Å which is equivalent to the distance between two TiS_3 layers reported in the literature[46]. In the zoomed-in inset (Figure 3.5(h)), an overlay of the TiS_3 crystal structure viewed along the [010] zone axis is shown in the HAADF-STEM image.

Finally, the semiconducting nature of the TiS_3 after annealing was confirmed using NIR PL spectroscopy. Photoluminescence was observed to be centred around ~1400 nm (~0.9 eV) after annealing (Figure 3.5 (i)), whereas it was not detectable before annealing. The position of the PL peak is close to the band gap of TiS_3[47]. Thus, the post-deposition annealing treatment of the PE-ALD grown amorphous TiS_3 at 400 °C improves the quality and crystallinity of the TiS_3 film.

3.4 Conclusions

We report on a low temperature ALD process with which the phase of titanium sulfide films can be precisely tuned between TiS_2 and TiS_3. The key to successful phase-control was to carefully tune the coreactant composition and deposition temperature. The generation of S_2 species in the H_2S plasma has been speculated to lead to the formation of amorphous TiS_3 by PE-ALD at a deposition temperature of 100 °C. Above 100 °C, a transition to the formation of TiS_2 occurs by PE-ALD. Electrical measurements show the low resistive nature of the TiS_2 films. The crystallinity of PE-ALD grown TiS_3 films was improved by adding a post-deposition annealing step of 400 °C for 3 h. After annealing, NIR photoluminescence was observed at ~1400 nm, confirming the direct optical band gap of TiS_3 at ~0.9 eV. This approach can potentially be extended to other transition metal *di*- and *tri*-chalcogenides, opening up new avenues for implementation of both transition metal *di*- and *tri*-chalcogenides in nano- and optoelectronic device fabrication schemes.

Acknowledgments

The authors acknowledge Jeroen van Gerwen and Christian van Helvoirt for their technical assistance and Dr. Bora Karasulu, and Dr. Tahsin Faraz for the valuable suggestions. This work was supported by the European Research Council (grant agreement No. 648787) and the Netherlands Organisation for Scientific Research (NWO) through Gravitation grant “Research Centre for Integrated Nanophotonics”. Dr. Beatriz Barcones is

acknowledged for the FIB preparation of the TEM sample. Solliance and the Dutch province of Noord-Brabant are acknowledged for funding the TEM facility.

References

[1] M. Chhowalla, H.S. Shin, G. Eda, L. Li, K.P. Loh, and H. Zhang, Nat. Chem. **5**, 263 (2013).

[2] J. Dai, M. Li, and X.C. Zeng, Wiley Interdiscip. Rev. Comput. Mol. Sci. **6**, 211 (2016).

[3] J.O. Island, A.J. Molina-Mendoza, M. Barawi, R. Biele, E. Flores, J.M. Clamagirand, J.R. Ares, C. Sánchez, H.S.J. van der Zant, R. D'Agosta, I.J. Ferrer, and A. Castellanos-Gomez, 2D Mater. **4**, 022003 (2017).

[4] F. Lévy and H. Berger, J. Cryst. Growth **61**, 61 (1983).

[5] S.K. Srivastava and B.N. Avasthi, J. Mater. Sci. **27**, 3693 (1992).

[6] Y. Jin, X. Li, and J. Yang, Phys. Chem. Chem. Phys. **17**, 18665 (2015).

[7] E.J. Frazer and S. Phang, J. Power Sources **6**, 307 (1981).

[8] X. Zhu, S. Chen, M. Zhang, L. Chen, Q. Wu, J. Zhao, Q. Jiang, Z. Zheng, and H. Zhang, Photonics Res. **6**, C44 (2018).

[9] R. Zhang, C. Wan, Y. Wang, and K. Koumoto, Phys. Chem. Chem. Phys. **14**, 15641 (2012).

[10] S.J. Denholme, P.S. Dobson, J.M.R. Weaver, I. MacLaren, and D.H. Gregory, Int. J. Nanotechnol. **9**, 23 (2012).

[11] E.S. Peters, C.J. Carmalt, and I.P. Parkin, J. Mater. Chem. **14**, 3474 (2004).

[12] R.G. Palgrave and I.P. Parkin, New J. Chem. **30**, 505 (2006).

[13] C.J. Carmalt, I.P. Parkin, and E.S. Peters, Polyhedron **22**, 1263 (2003).

[14] C.J. Carmalt, S. a. O. Neill, I.P. Parkin, and E.S. Peters, J. Mater. Chem. **14**, 830 (2004).

[15] K. Kanehori, Y. Ito, F. Kirino, K. Miyauchi, and T. Kudo, Solid State Ionics **18–19**, 818 (1986).

[16] V. Pore, M. Ritala, and M. Leskela, Chem. Vap. Depos. **13**, 163 (2007).

[17] N. Mahuli and S.K. Sarkar, J. Vac. Sci. Technol. A Vacuum, Surfaces, Film. **33**, 01A150 (2015).

[18] H. Nam, H. Yang, E. Kim, C. Bae, and H. Shin, J. Vac. Sci. Technol. A **37**, 020916 (2019).

[19] V. V. Plashnitsa, F. Vietmeyer, N. Petchsang, P. Tongying, T.H. Kosel, and M. Kuno, J. Phys. Chem. Lett. **3**, 1554 (2012).

[20] Z.Y. Wu, F. Lemoigno, P. Gressier, G. Ouvrard, P. Moreau, J. Rouxel, and C.R. Natoli, Phys. Rev. B **54**, R11009 (1996).

[21] C.S. Cucinotta, K. Dolui, H. Pettersson, Q.M. Ramasse, E. Long, S.E. O'Brian, V. Nicolosi, and S. Sanvito, J. Phys. Chem. C **119**, 15707 (2015).

[22] E. Amzallag, I. Baraille, H. Martinez, M. Rérat, M. Loudet, and D. Gonbeau, J. Chem. Phys. **126**, 074703 (2007).

[23] R. Frisenda, E. Giovanelli, P. Mishra, P. Gant, E. Flores, C. Sánchez, J.R. Ares, D. Perez de Lara, I.J. Ferrer, E.M. Pérez, and A. Castellanos-Gomez, Chem. Commun. **53**, 6164 (2017).

[24] J.O. Island, M. Barawi, R. Biele, A. Almazán, J.M. Clamagirand, J.R. Ares, C. Sánchez, H.S.J. van der Zant, J. V Álvarez, R. D'Agosta, I.J. Ferrer, and A. Castellanos-Gomez, Adv. Mater. **27**, 2595 (2015).

[25] R. Shimanouchi, T. Yamamoto, S. Kikkawa, and M. Koizumi, Chem. Lett. **14**, 1323 (1985).

[26] S. Kikkawa, Ceram. Int. **8842**, 7 (1996).

[27] H. Jin, D. Cheng, J. Li, X. Cao, B. Li, X. Wang, X. Liu, and X. Zhao, Solid State Sci. **13**, 1166 (2011).

[28] W. Hao, C. Marichy, and C. Journet, 2D Mater. **6**, 012001 (2018).

[29] A. Sharma, M.A. Verheijen, L. Wu, S. Karwal, V. Vandalon, H.C.M. Knoops, R.S. Sundaram, J.P. Hofmann, W.M.M. (Erwin) Kessels, and A.A. Bol, Nanoscale **10**, 8615 (2018).

[30] S.B. Basuvalingam, B. Macco, H.C.M. Knoops, J. Melskens, W.M.M. (Erwin) Kessels, and A.A. Bol, J. Vac. Sci. Technol. A **36**, 041503 (2018).

[31] H.C.M. Knoops, S.E. Potts, A.A. Bol, and W.M.M. Kessels, in *Handb. Cryst. Growth*, Second Edi (Elsevier, Amsterdam, 2015), pp. 1101–1134.

[32] J.R. Avila, S.B. Qadri, J.A. Freitas, N. Nepal, D.R. Boris, S.G. Walton, C.R. Eddy, and V.D. Wheeler, Chem. Mater. **31**, 3900 (2019).

[33] T. Faraz, H.C.M. Knoops, M.A. Verheijen, C.A.A. van Helvoirt, S. Karwal, A. Sharma, V. Beladiya, A. Szeghalmi, D.M. Hausmann, J. Henri, M. Creatore, and W.M.M. Kessels, ACS Appl. Mater. Interfaces **10**, 13158 (2018).

[34] S. Oh, S. Jung, Y.H. Lee, J.T. Song, T.H. Kim, D.K. Nandi, S.-H. Kim, and J. Oh, ACS Catal. **8**, 9755 (2018).

[35] E. TRONG and M. Huber, COMPTES RENDUS Hebd. DES SEANCES L Acad. DES Sci. Ser. C **268**, 1771 (1969).

[36] W. Kong, C. Bacaksiz, B. Chen, K. Wu, M. Blei, X. Fan, Y. Shen, H. Sahin, D. Wright, D.S. Narang, and S. Tongay, Nanoscale **9**, 4175 (2017).

[37] S.J. Sandoval, X.K. Chen, and J.C. Irwin, Phys. Rev. B **45**, 14347 (1992).

[38] K. Endo, H. Ihara, K. Watanabe, and S. Gonda, J. Solid State Chem. **44**, 268 (1982).

[39] R.W.B. Pearse and A.G. Gaydon, *The Identification of Molecular Spectra*, 4th editio (Chapman and Hall, London, 1976).

[40] A. Vesel, J. Kovac, G. Primc, I. Junkar, and M. Mozetic, Materials (Basel). **9**, 95 (2016).

[41] E. Linga Reddy, V.M. Biju, and C. Subrahmanyam, Appl. Energy **95**, 87 (2012).

[42] H. Bashiri and S. Mohamadi, Appl. Catal. A Gen. **509**, 105 (2016).

[43] J. Hämäläinen, M. Mattinen, K. Mizohata, K. Meinander, M. Vehkamäki, J. Räisänen, M. Ritala, and M. Leskelä, Adv. Mater. **30**, 1703622 (2018).

[44] S.J. Hazarika, D. Mohanta, A. Tripathi, and D. Kanjilal, J. Phys. Conf. Ser. **765**, 012007 (2016).

[45] A.L. Patterson, Phys. Rev. **56**, 978 (1939).

[46] E. Guilmeau, D. Berthebaud, P.R.N. Misse, S. Hébert, O.I. Lebedev, D. Chateigner, C. Martin, and A. Maignan, Chem. Mater. **26**, 5585 (2014).

[47] I.J. Ferrer, J.R. Ares, J.M. Clamagirand, M. Barawi, and C. Sánchez, Thin Solid Films **535**, 398 (2013).

Appendix 3

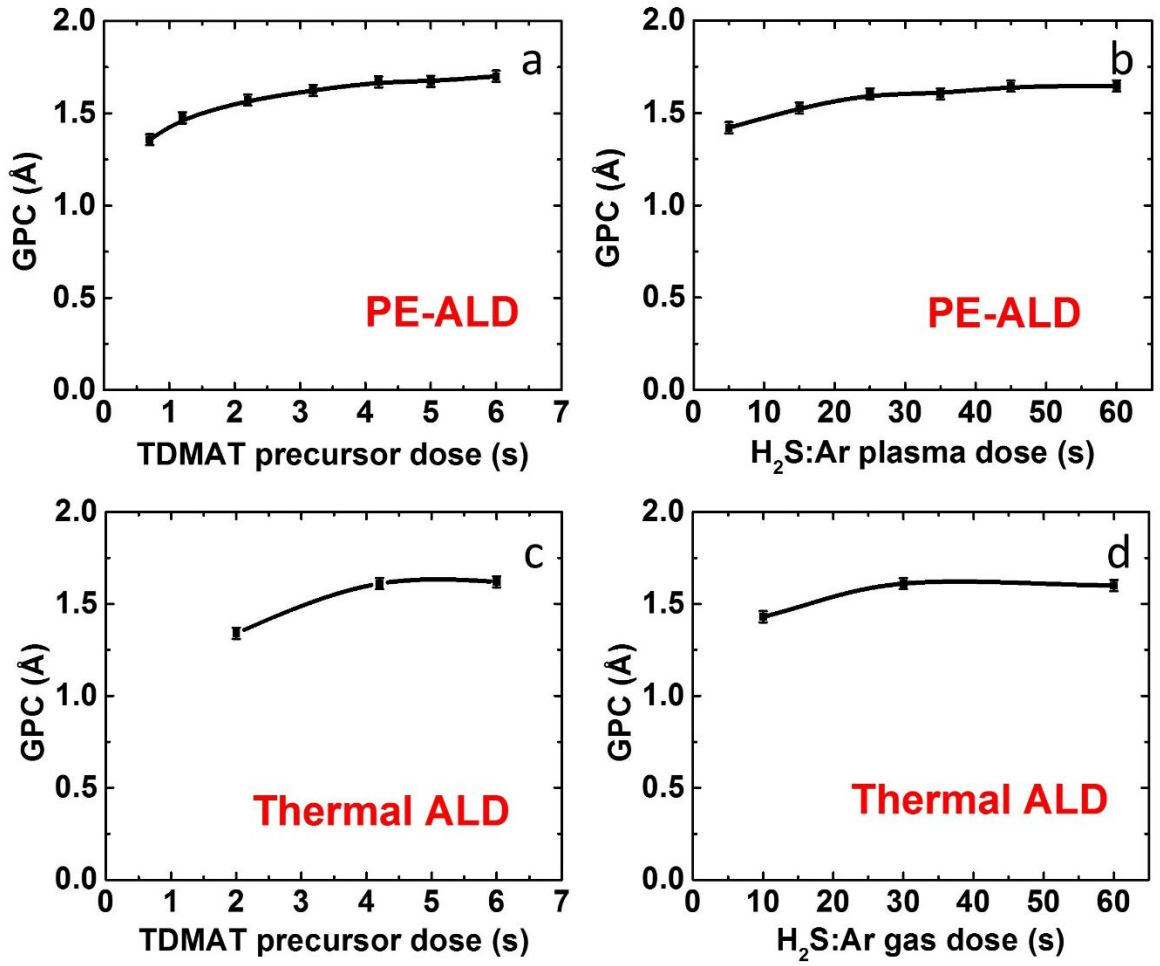

Figure A3.1 Saturation curves for self-limiting PE-ALD (a&b) as well as thermal ALD (c&d) processes at 100 °C is shown in GPC as a function of (a&c) precursor (TDMAT as Ti precursor), (b) coreactant (H_2S:Ar plasma) flow time & (d) coreactant (H_2S:Ar gas) flow time, respectively.

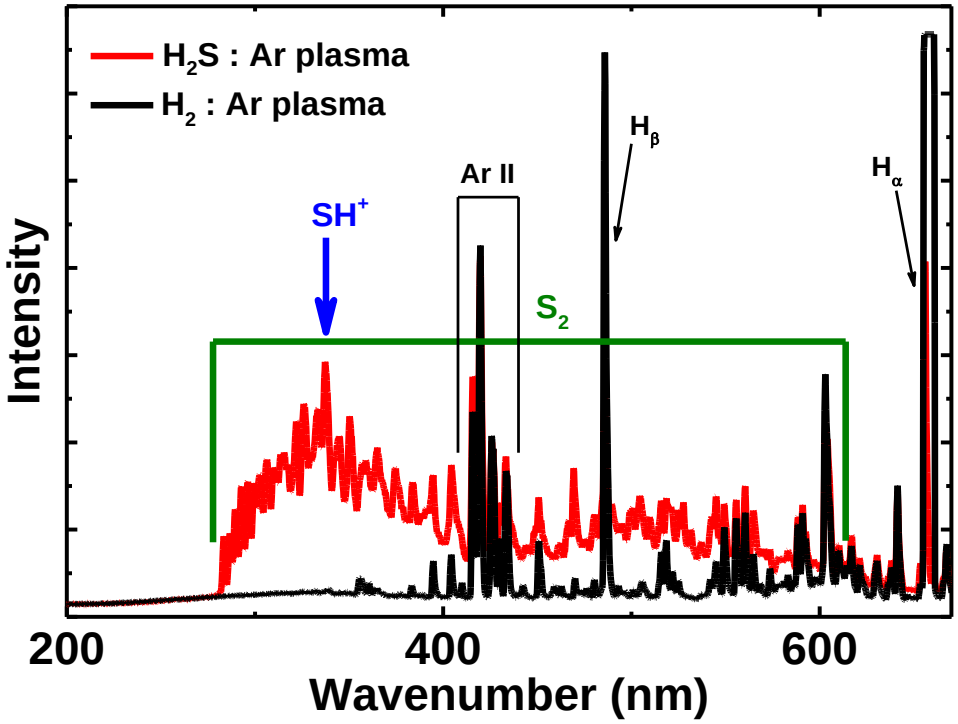

Figure A3.2 The optical emission spectrum of the H_2S:Ar (red curve) and H_2:Ar (black curve) plasma from PE-ALD with both having a gas flow of 10:40 sccm. It shows the corresponding peak for SH^+ (blue) and the range of peaks for S_2 (green) species along with H and Ar species (black).

Conformal Growth of Transition Metal Dichalcogenide TiS_x-NbS_x Heterostructures over 3D substrates by Atomic Layer Deposition

4

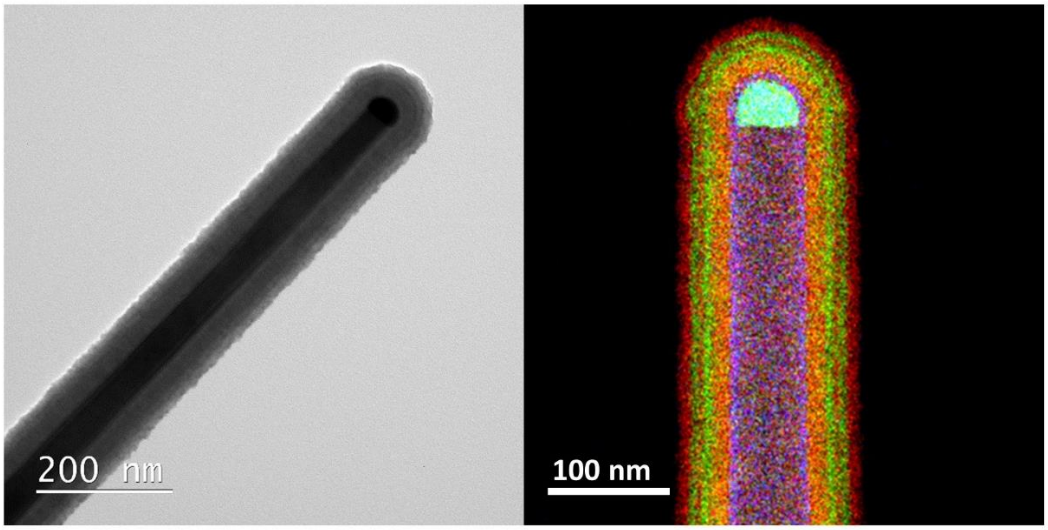

The scalable and conformal synthesis of two-dimensional (2D) transition metal dichalcogenide (TMDC) heterostructures is a persisting challenge for their implementation in next-generation devices. In this work, we report on the synthesis of 2D TMDC heterostructures consisting of TiS_x-NbS_x on both planar and 3D structures using atomic layer deposition (ALD) at low temperatures (200-300 °C). To this end, a new process was developed for the growth of 2D NbS_x by thermal ALD using (tert-butylimido)-tris-(diethylamino)-niobium (TBTDEN) and H_2S gas. This process complemented the TiS_x thermal ALD process for the growth of 2D TiS_x-NbS_x heterostructures. Precise thickness control of the individual TMDC material layers was demonstrated by fabricating multilayer (5-layer) TiS_x-NbS_x heterostructures with independently varied layer thicknesses. The heterostructures were successfully deposited on large area planar substrates as well as over a 3D nanowire array for demonstrating the scalability and conformality of the heterostructure growth process. The current study demonstrates the advantages of ALD for the scalable synthesis of 2D heterostructures conformally over a 3D substrate with precise thickness control at low temperatures.

Saravana Balaji Basuvalingam, Matthew A. Bloodgood, Marcel A. Verheijen, Wilhelmus M. M. Kessels, and Ageeth A. Bol (to be submitted)

4.1 Introduction

Layered two-dimensional (2D) transition metal dichalcogenides (TMDCs) such as MoS_2, NbS_2, etc., have attracted much interest for their unique electrical, optical, and mechanical properties[1,2]. Lately, fabrication of vertical heterostructures based on 2D TMDCs (*e.g.,* WS_2-NbS_2) has gained significance over the formation of heterostructures based on 3D materials due to advantages such as absence of dangling bonds and lattice mismatch at the layers' interface. Additionally, stacking different 2D materials on top of each other continues to open up unique functionalities, which in turn leads to prospects for new applications in various fields[3–5]. For example: in 2D material based FETs (field-effect transistors), 2D-2D heterostructures provide superior device performance due to weak Fermi level pinning at the metal-semiconductor interface along with reduced Schottky barrier height compared to 2D-3D heterostructures[6,7]. While 2D-2D TMDC vertical heterostructures exhibit enormous potential, the ability to fabricate them on the wafer-scale (over a large area) is a persisting challenge.

The most common fabrication technique for 2D heterostructures is a top-down approach known as the mechanical transfer method. In this method, the scotch tape technique is used to exfoliate 2D TMDC layers before aligning and placing them on top of another 2D TMDC layer to form the heterostructure. This approach provides significant flexibility to create various 2D heterostructure combinations[8,9]. However, it is not an industrially scalable method, and it has some critical issues such as reproducibility, yield, and residue/ contamination[4]. Recently, chemical vapor deposition (CVD) has been explored as an alternative approach as a direct, bottom-up heterostructure synthesis method. In this method, a CVD grown 2D TMDC is used as a substrate for the CVD growth of a second 2D TMDC material. While this method overcomes most of the limitations mentioned above for 2D heterostructure synthesis[10,11], limitations such as large area uniformity (due to island growth leading to discontinuous films), thickness control, and high synthesis temperatures persist[12].

On top of the aforementioned constraints, the capability to grow 2D TMDCs heterostructures conformally on a 3D structure (including high aspect ratio) have yet to be explored using above mentioned methods. However, incompetency to grow conformally could be an additional bottleneck for implementation as the down-scaling of device dimensions continues with an increasing level of structural complexity. Conformal growth means having complete coverage with uniform thickness over a 3D structure. Control in the

growth of 2D TMDCs over complex 3D structures could also open new unique application potentials. For example: conformal growth of 2D TMDCs as a copper metal-dielectric barrier layer in the back-end of the line (BEOL)[13]. Furthermore, in the front-end of the line (FEOL), the ability to grow gate oxide and gate metal conformally around the channel in gate-all-around transistors (GAAFETs) makes continuous down-scaling of device dimensions below 5nm feasible[14]. For further down-scaling the technology node below 5 nm or so, 2D TMDCs have emerged as strong contenders to overcome device performance limitations accompanied with down-scaling[15]. Similar to GAAFETs, the conformal growth of TMDCs and their heterostructures could thus be an added benefit in the fabrication of 2D based transistors (vdWFETs)[16]. Therefore, conformality could be a valuable addition to the toolbox for 2D vertical heterostructure formation to fast track the implementation of 2D materials in device process flows.

Lately, atomic layer deposition (ALD) has become of significance for synthesizing various 2D TMDCs[17,18–20]. It is a method that is based on self-limiting, saturated surface reactions where precursors are dosed in a cyclic manner, separated by purge steps to avoid parasitic CVD reactions[21,22]. Due to its self-limiting nature, ALD provides precise thickness control over a large area along with uniformity and conformality on complex 3D substrates at low processing temperatures. These attributes of ALD would be favorable for the fabrication of 2D TMDC heterostructures, as they can overcome the limitations observed in the aforementioned synthesis methods. Thus far, direct ALD of vertical heterostructures (*i.e.,* layers of different materials stacked on top of each other) based on non-TMDC based layered materials such as Sb_2Se_3, Sb_2Te_3, etc. have been successfully demonstrated over a large planar substrate[23–25]. With reference to layered TMDC based heterostructure formation using ALD, there have been reports only on growing TMDCs on an exfoliated or CVD-grown TMDC substrate[26,27]. On that account, to the best of our knowledge, direct synthesis of 2D heterostructures based on layered TMDCs by ALD has not been demonstrated.

In this work, we report on a newly developed ALD process for niobium sulfide (NbS_x) growth, in addition to the previously reported process for titanium sulfide (TiS_x) film growth[29]. Using these ALD processes, we synthesize TMDC-TMDC vertical heterostructures in the form of TiS_x-NbS_x heterostructures at low deposition temperatures ($\leq$ 300 °C). Through the deposition of multilayer (5 layers), TiS_x-NbS_x heterostructures composed of TiS_x and NbS_x as the alternating layers with the varying number of ALD cycles per individual layer, we demonstrate thickness control of the individual material layers in the

heterostructure. In addition to TMDC heterostructure formation on a planar substrate, we also demonstrate the conformal growth of multilayer TiS_x-NbS_x heterostructures on a 3D substrate consisting of a nanowire array. Our work shows that ALD is an excellent method to grow TMDC-TMDC vertical heterostructures over a large area with precise thickness control and conformality at low deposition temperatures.

4.2 Experimental Details

4.2.1 Atomic Layer Deposition

The TiS_x and NbS_x thin films were deposited by atomic layer deposition (ALD) using an Oxford Instruments Plasma Technology FlexAL ALD reactor. The base pressure of the system was 10^{-6} Torr. The reactor acted as a hot wall reactor for depositions up to and including 150 °C. However, the reactor acted as a warm wall reactor for depositions above 150 °C as the wall temperature was maintained at 150 °C while the table temperature was varied between 150 °C and 450 °C. The metal-organic precursors tetrakis-(dimethylamido)-titanium (TDMAT) (Sigma-Aldrich Chemie BV, 99.999 %) and (tert-butylimido)-tris-(diethylamino)-niobium (TBTDEN) (STREM Chemical, Inc., 98%) were used for TiS_x and NbS_x growth, respectively. The TDMAT and TBTDEN precursors were kept in stainless steel bubblers at 50 °C and 65 °C, respectively, and were bubbled using Ar as the carrier gas. In both ALD processes, the pressure was maintained at 80 mTorr during both the precursor and coreactant exposure steps. In both the processes, the coreactant gas mixture consisted of 10 sccm of H_2S gas (>99.98 %) and 40 sccm of Ar gas (>99.999 %), respectively.

The TiS_x process consists of the TDMAT precursor and the coreactant gas exposure for 4 s and 30 s, respectively. In the case of the NbS_x process, the TBTDEN precursor exposure was 10 s, while the coreactant was dosed for 20 s. More details on ALD process optimization and saturation data for both processes are provided in appendix 4 Figure A4.1. In all cases, the precursor and coreactant exposure steps were separated by Ar purge steps. The details about the TiS_x-NbS_x heterostructure formation, such as deposition temperature and growth will be addressed in the results and discussion section. The thin films were deposited on Si substrates covered with approximately 450 nm thick thermally grown SiO_2 (planar substrate). The conformal growth studies were performed by growing the TiS_x-NbS_x heterostructures on an ALD SiO_2 coated regular array (pitch: 2 µm) of 2 µm long GaAs nanowires with a diameter of 60 nm thick (3D substrate).

4.2.2 Characterization Techniques

Scanning electron microscopy (SEM) was employed to investigate the surface morphology of the films. A Zeiss Sigma SEM with an in-lens detector and operating at an accelerating voltage of 3 kV was used for SEM studies. The microstructures of the thin film and the heterostructures were studied using (scanning) transmission electron microscopy [(S)TEM] with a JEOL ARM 200F microscope operated at 200 kV. For cross-section (S)TEM studies on planar Si substrates, a lamella (~100 nm) was prepared in an FEI Nova600i NanoLab SEM/FIB using the lift-out preparation procedure after a protective SiO_2 layer was deposited on the top of the film by electron-beam induced deposition (EBID). High-angle annular dark-field STEM (HAADF-STEM) combined with energy-dispersive X-ray spectroscopy (EDX) was used to study the chemical composition of the TiS_x-NbS_x heterostructures on both the planar Si and 3D nanowire substrates. The growth of the TiS_x and NbS_x thin films was investigated using *in-situ* spectroscopic ellipsometry (SE), where the film thickness was measured as a function of the number of ALD cycles. Data were collected every 10 ALD cycles by a J.A. Woollam Co., Inc., M2000U spectroscopic ellipsometer with a photon energy range of 0.7-5 eV. The dielectric function of the films was modeled using a B-spline model. The crystallinity of the thin films was studied by Gonio and grazing-incident X-ray diffraction (XRD) with a PANalytical X´Pert Pro MRD analyzer using a Cu Kα (λ = 1.54 Å) X-ray source operated at 40 mA and 45kV. The scan range was 5 to 80° 2θ with a scan rate and step size of 0.2 s/step and 0.01, respectively. The composition and purity of the thin films were determined using Rutherford backscattering spectrometry (RBS) and elastic recoil detection (ERD) by Detect 99 B.V. Eindhoven, The Netherlands using a 2 MeV He^+ beam source and with the detectors at scattering angles of 105° and 170° for RBS, and 25° for ERD. X-ray photoelectron spectroscopy (XPS) data were collected on a Thermo Scientific KA1066 spectrometer with monochromatic Al Kα (*h*ν = 1486.6 eV) X-ray radiation to determine the binding environment and valence band spectra for the deposited thin films. Resistivity measurements were performed *ex-situ* at ambient conditions using a Signatone Four-Point Probe method in combination with a Keithley 2400 sourcemeter acting both as the current source and voltmeter. The resistivity of the thin films was determined from the slope of the obtained *I-V* curves.

4.3 Results and Discussion

The film growth of both TiS_x and NbS_x by ALD was investigated independently before the synthesis of the TMDC-TMDC heterostructures based on TiS_x-NbS_x was attempted. Thermal ALD processes for TiS_x and NbS_x were preferred over plasma-enhanced ALD, as plasma could cause interface mixing or damage during heterostructure formation[28]. In addition, thermal ALD processes could provide better conformal growth than plasma-enhanced ALD processes[28]. We previously reported a thermal ALD process for TiS_x films using TDMAT as the precursor and H_2S gas as the coreactant[29]. A thermal ALD process for NbS_x films was developed in this work, using TBTDEN as the precursor and H_2S gas as the coreactant for deposition temperatures between 150 and 300 °C. More details on the NbS_x ALD process optimization and film properties as a function of the deposition temperature can be found in appendix 4 (Figure A4.1 and A4.2).

Next, to achieve high quality TiS_x-NbS_x heterostructures, we investigated the properties of the individual TMDCs as a function of the deposition temperatures to determine the optimal deposition temperature. In the case of TiS_x, the film deposited at 200 °C had the best crystallinity (see Figure 4.1a and A4.3). Cross-section HAADF-STEM analysis of TiS_x deposited at 200 °C shows (Figure 4.1b) the layered 2D nature of the TiS_x film. All van der Waals layers are oriented parallel to the substrate without any out-of-plane oriented (OoPO) growth. The average distance between the two layers was measured to be ~5.7 Å, which is in good agreement with the distance between two layers of 1*T*-TiS_2[30]. Likewise, the top-view SEM and cross-section STEM in Figure 4.1(a and c), respectively of the TiS_x film deposited at 200 °C shows a smooth surface morphology with the absence of OoPO structures. The resistivity of the TiS_x prepared at 200° C was measured to be below 0.8 Ω-cm (see Table A4.1). This resistivity value is similar to the reported bulk resistivity of TiS_2[31].

NbS_x films deposited at the highest temperature (at 300 °C) were observed to have the best crystallinity (see Figure A4.3). Yet, the crystallinity of the TiS_x film grown at 200 °C is more pronounced than that of the NbS_x film synthesized at 300 °C (see Figure 4.1g). The cross-section HAADF-STEM image of NbS_x (Figure 4.1f) confirms these XRD results. The layer is polycrystalline, exhibiting a grain size of only a few nm's and random grain orientation. As a result, the layered 2D nature was only visible in selected regions. The average distance between two van der Waals layers was measured to be ~5.9 Å, which is in accordance with the interlayer spacing value reported in the literature for NbS_2[32]. The top-view SEM of the NbS_x film (see Figure 4.1e and A4.4) shows that irrespective of deposition temperatures

OoPO structures were present on the film surface. The density of OoPO structures decreased with increasing deposition temperature which led to relatively smooth surfaces for films deposited at 300 °C. A few of these OoPO structures were marked by white dotted circles in Figure 4.1e. Likewise, the cross-section HAADF-STEM image of the top part of the NbS_x film in Figure 4.1d confirms the relatively smooth surface with few vertically tapered OoPO structures as highlighted by white dotted lines. The resistivity value of the NbS_x deposited at 300°C was 4.8 Ω-cm and is close to the reported bulk resistivity of NbS_2[33].

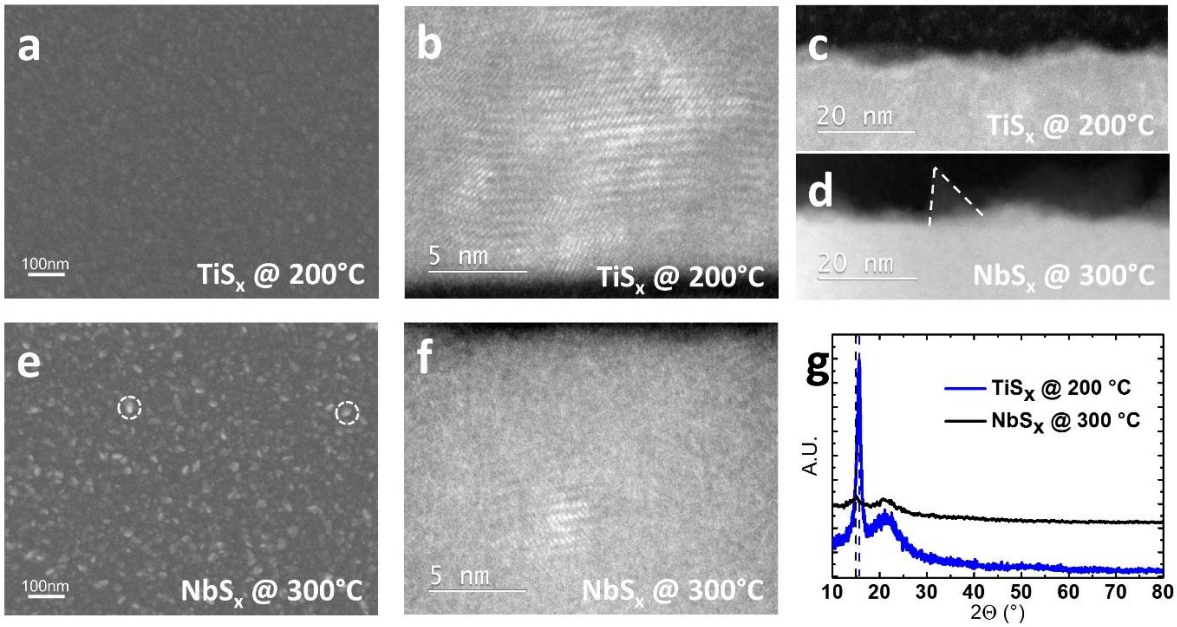

Figure 4.1 Top-view SEM images of ~30 nm thick TiS_x (a) and NbS_x (e) films deposited at 200 °C and 300 °C, respectively, on SiO_2/Si substrate. Cross-section HAADF-STEM image of the TiS_x (b, c) and NbS_x (d, f) films deposited at 200 °C and 300 °C, respectively. Note: (b, f) show cross-section views of the central part of the films while (c, d) show cross-section views of the surface of the films. (g) GI-XRD pattern of TiS_x and NbS_x films deposited at 200 °C and 300 °C, respectively. The dotted lines indicate the peak position corresponding to (001) and (003) planes of TiS_x (blue) and NbS_x (black), respectively.

4.3.1 Heterostructure Growth on a Planar Substrate

As ALD is a self-limiting cyclic process, the thickness of the film/layer can be controlled precisely by the number of ALD cycles. Linear growth in terms of film thickness as a function of the number of ALD cycles was observed for the TiS_x and NbS_x thermal ALD processes at 200 °C and 300 °C, respectively (see Figure A4.1c). The corresponding growth per cycle (GPC) values were measured (by taking the slope over the linear region of the curve) to be ~0.6 Å and ~1.17 Å, using *in-situ* SE measurements (Figure A4.1). It is important to note that TiS_x could not be deposited above 200 °C due to the decomposition of the TDMAT precursor

above 200 °C. Therefore, as schematically illustrated in Figure 4.2, two different deposition temperatures were used to grow TiS_x (200 °C) and NbS_x (300 °C) layers, and the table temperature was increased and decreased accordingly for the TiS_x-NbS_x heterostructure formation to acquire the best individual layer quality.

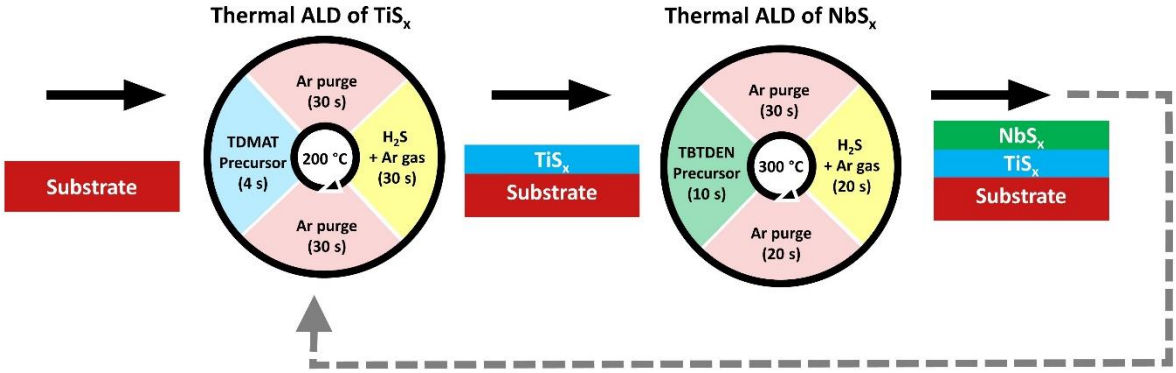

Figure 4.2 Schematic illustration of the synthesis of the TiS_x-NbS_x heterostructure by thermal ALD. The TDMAT and TBTDEN correspond to Ti and Nb precursors, respectively.

In addition, to demonstrate thickness controllability by ALD, a 5-layer TiS_x-NbS_x heterostructure with varying individual layer thickness was fabricated (employing a process indicated by the grey dotted line in Figure 4.2). At 200 °C, ~15.0 nm of TiS_x was deposited as the first layer in the heterostructure using 260 cycles of the TiS_x thermal ALD process. On top of this TiS_x layer, an NbS_x layer was deposited for 60 cycles at 300 °C. The 60 ALD cycles of NbS_x would lead to a nominal thickness of ~5.8 nm (measured using *in-situ* SE) on a SiO_2 as the starting surface, see Figure A4.1. However, the thickness of 60 cycles of NbS_x ALD on TiS_x as the starting surface might deviate from 5.8 nm due to possible differences in nucleation behavior. Therefore, from now on, the term nominal thickness was used to refer to the thickness of the material (for both TiS_x and NbS_x) when deposited for an N number of ALD cycles on SiO_2 as the starting surface. The buildup of the heterostructure continued with the deposition of layers comprised of TiS_x (90 cycles), NbS_x (60 cycles), and TiS_x (180 cycles) with nominal thicknesses of ~5.1, ~5.8 nm, and ~10.7 nm, respectively. Both NbS_x layers were limited to 60 ALD cycles to minimize the appearance of OoPO structures (marked by white circles in Figure 4.1c) at the interface. Additionally, during heating and cooling of the substrate table between 200 °C and 300 °C for the growth of TiS_x and NbS_x layers, respectively, the sample was transferred to the load lock chamber from the ALD chamber to reduce annealing effects at the elevated temperatures. While the number of layers in the heterostructure was restricted to five in this work, this process can be easily

repeated by any number of times to grow multilayer heterostructures with varied individual layer thicknesses.

The microstructure of the synthesized 5-layer TiS_x-NbS_x heterostructure was then studied by cross-section (S)TEM imaging, as shown in Figure 4.3. A clear difference in contrast can be observed between the TiS_x and NbS_x layers in bright-field TEM (Figure 4.3a), due to the difference in mass density between the materials: the TiS_x layers appear bright, while the NbS_x layers are dark. Furthermore, considering the width of the lamella being ~100 nm, the sharp transition in layer contrast between the TiS_x (light) and NbS_x (dark) layers in the TEM image indicates a sharp interface between the layers, with a low degree of mixing. The average vertical thickness of each individual layer was measured by taking an average of thickness measurements from several cross-section HAADF-STEM images. The measured layer thickness of the three TiS_x layers (layer 1, 3 and 5) were ~14.4±0.9, 4.9±0.5 and 10.2±0.6 nm, respectively, and that of the two NbS_x layers (layer 2 and 4) were ~4.2±0.6 and 4.5±0.4 nm, respectively.

The measured thickness of both the TiS_x (layer 3 and 5) layers grown on the NbS_x surface was comparable to the expected nominal thickness of 5.1 and 10.7 nm, respectively. On the contrary, the measured thickness of both NbS_x (layer 2 and 4) layers grown on TiS_x as the starting surface was lower than the nominal thickness of 5.8 nm. This reduced thickness in the case of NbS_x could be due to nucleation delay on the TiS_x starting surface in comparison to a SiO_2 starting surface. This change in growth indicates the higher sensitivity of the NbS_x thermal ALD process to the starting surface chemistry over the TiS_x thermal ALD process. Similar nucleation delays have also been observed for several other ALD processes, as ALD critically depends on the starting surface chemistry[34,35].

Differences in crystallinity between the TiS_x and NbS_x layers can also be observed in Figure 4.3a. Here the TiS_x layers display the expected layered structure with clearly visible van der Waals gaps, while the NbS_x layers lack significant ordering and appear much more amorphous. This agrees with the observations from GI-XRD and STEM in Figure 4.1 for the individual TiS_x and NbS_x films of 30 nm each. The intensity of the 15° 2θ peak (corresponding to the (00*1*) and (*003*) planes for both TiS_2 and NbS_2, respectively) in the XRD spectrum was observed to be much stronger for the TiS_x film than for the NbS_x film, indicating a higher crystallinity. This shows that the observed crystallinity differences between the TiS_x and NbS_x layers is intrinsic to the respective ALD processes and not due to growth in the heterostructure. Although the NbS_x is lower in crystallinity, there are regions where a continuous layered van der Waals formation is clearly visible through all five layers of the

heterostructure. Therefore, provided NbS_x layers were also synthesized with equally high crystallinity as TiS_x layers, this shows that ALD has the capability to synthesize high quality 2D van der Waals heterostructures with relatively sharp interfaces *in-situ* without exposing to ambient condition.

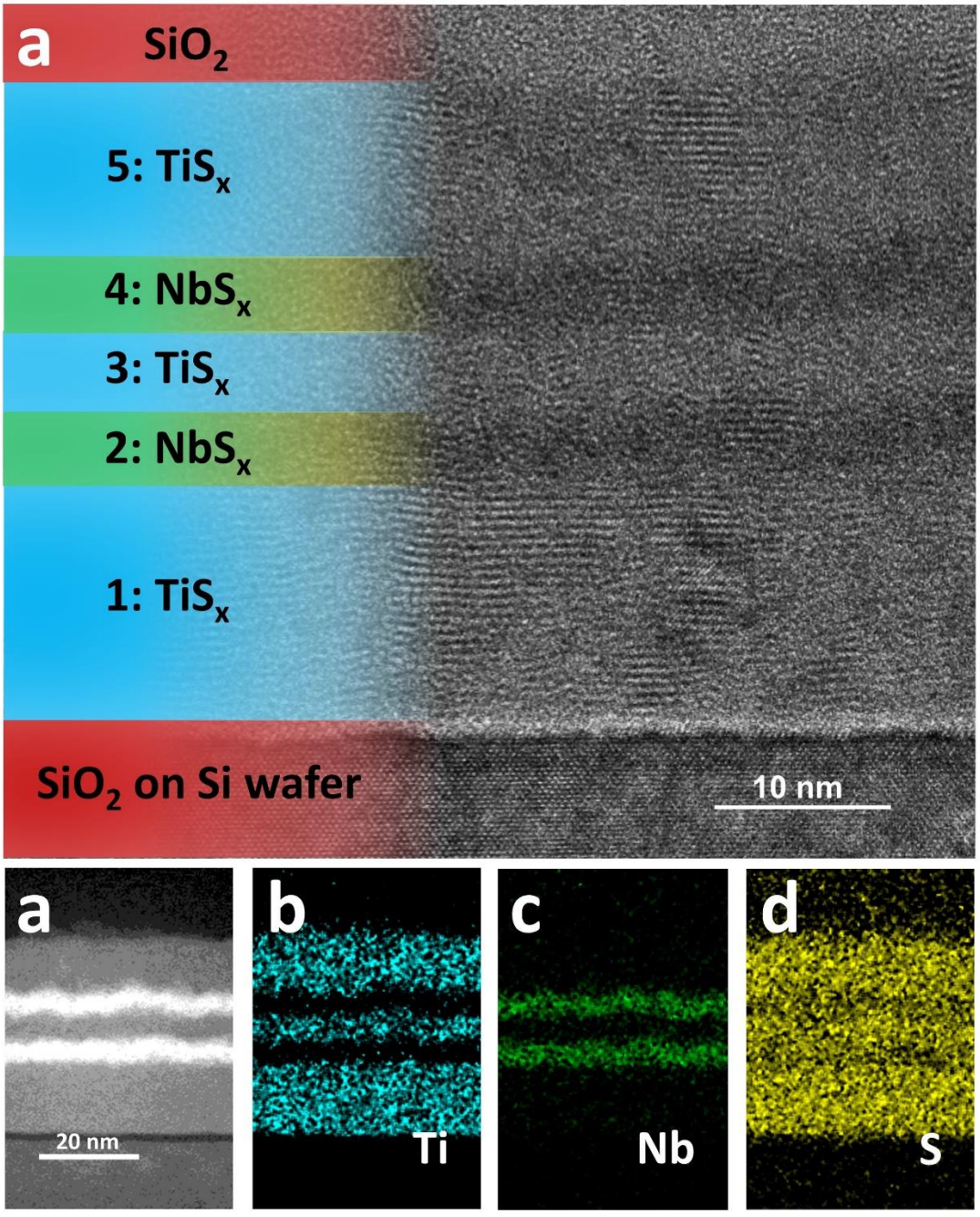

Figure 4.3 (a) Cross-section bright-field TEM image of the TiS_x-NbS_x heterostructure with 5 layers on the Si wafer with native SiO_2 on top. (b) Cross-section HAADF-STEM image of the TiS_x-NbS_x heterostructure layers. (c-e) Corresponding EDX elemental mapping of Ti, Nb and S, respectively.

A HAADF-STEM image of the heterostructure is shown in Figure 4.3b, and the corresponding EDX elemental mapping of Ti, Nb and S are shown in Figure 4.3c-d, respectively. The EDX maps of both Ti and Nb confirm the presence of two NbS_x layers of similar thickness, sandwiched between three TiS_x layers of different individual layer thicknesses. The EDX mapping also reveals the lack of inter-mixing between the two elements per layer, as no Ti was observed in the NbS_x layer within the detection limits of EDX. Likewise, no Nb counts were detected in the TiS_x layers. Therefore, the EDX mapping strongly indicates that ALD can fabricate TMDC heterostructures with little interlayer mixing.

On the other hand, the S mapping shows a difference in S content between TiS_x and NbS_x layers, as S counts were observed to be relatively low in the NbS_x layers. This could indicate differences in the chemical composition/stoichiometry between the TiS_x and NbS_x layers. Consequently, the chemical composition of both TiS_x and NbS_x films deposited at 200 °C and 300 °C, respectively were individually investigated using RBS, see Table A4.1. From the RBS measurements, the stoichiometry (sulfur to transition metal ratio) of both the films was calculated to be 1.41 and 1.25 for TiS_x and NbS_x, respectively. This confirms the difference in stoichiometry between the two films while also revealing relatively low S content, especially in the NbS_x film. This indicates the presence of S vacancies and/or excess metal in both layers. In addition, RBS revealed the presence of 6-9 at.% of H, 7 at.% of C and 1 at.% of O impurities in both TiS_x and NbS_x ALD grown films, see Table A4.1. The detected H and C in the films could be from precursor ligands and/or coreactant. The observed O impurities in the film could be due to the presences of residual O_2 and H_2O in the background of the ALD chamber during deposition.

4.3.2 Heterostructure growth on a 3D substrate

Finally, to demonstrate conformality, an analogous 5-layer TiS_x-NbS_x heterostructure was deposited on an array of wurtzite GaAs nanowires (3D substrates), which were coated with SiO_2 by ALD. The coverage of the 5-layer heterostructure on the nanowires was analyzed with side-view HAADF-STEM (Figure 4.4a) upon aligning the wurtzite GaAs nanowire to its <11-20> zone axis, allowing for imaging parallel to the {10-10} side facets. The HAADF-STEM image shows the complete coverage of the nanowire with the heterostructure over the length as well as the curvature (tip) of the nanowire (formed by the Au catalyst particle used for the nanowire growth), confirming conformal growth. Furthermore, the thickness of the heterostructure was measured on various spots along the length of the nanowire and was

observed to hardly vary, with a thickness variation of < 5%. Thus, this validates the uniform growth of the 5-layer heterostructure on a 3D structure.

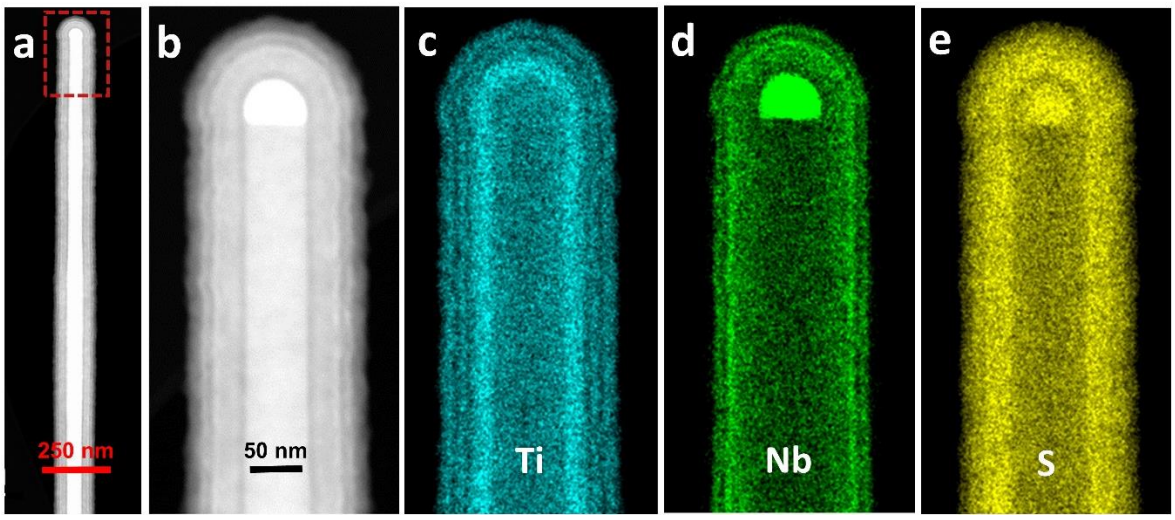

Figure 4.4 (a) Side-view HAADF-STEM image of the ALD SiO_2 coated GaAs nanowire, grown from an Au seed particle, covered with the TiS_x-NbS_x heterostructure. (b-e) Higher magnification (red box in (a)) HAADF-STEM image and the corresponding EDX elemental mapping of Ti, Nb and S, respectively.

Figure 4.4b shows the magnified STEM image of the nanowire (red box), and the corresponding EDX elemental mapping of Ti, Nb and S, respectively, are shown in Figure 4.4(c-e). The STEM image along with EDX maps confirms the synthesis of the 5-layer TiS_x-NbS_x heterostructure. The Ti mapping shows three TiS_x layers with different individual layer thickness as expected. The Nb mapping shows two NbS_x layers with comparable thickness sandwiched between TiS_x layers. The average individual layer thicknesses were measured on various spots on the STEM image (Figure 4.4(b)), and it was observed that the TiS_x layers grown on NbS_x layers were measured to be 4.9 and 10.4 nm, respectively (layer 3 and 5). The thicknesses of the NbS_x layers on top of the TiS_x layers were measured to be 4.4 and 4.7 nm (layer 2 and 4), respectively. These values are comparable to the individual layer thickness observed on a planar Si wafer. Thus, confirms the precise thickness control of all five individual layers in the TiS_x-NbS_x heterostructure over the nanowire and the absence of intermixing between the layers. Hence, this strongly establishes the capability of ALD for the scalable synthesis of 2D TMDC vertical heterostructures with sharp interfaces, excellent uniform coverage and conformally over a 3D structure at low temperature.

4.4 Conclusions

In this work, ALD has been successfully applied as a suitable technique to synthesize 2D TMDC vertical heterostructures. A TiS_x-NbS_x heterostructure consisting of 5-layers with different individual layer thickness was deposited on a planar Si wafer as well as on a 3D substrate. The thickness of the individual layers was controlled precisely by varying the number of ALD cycles of the corresponding thermal ALD process. We successfully demonstrated large area uniformity and conformality over a 3D substrate at low deposition temperatures. The ability to synthesize TMDC and their heterostructures by ALD with conformal growth over 3D structures at low temperatures could be beneficial to open new avenues such as fabricating complex 3D device structures (partly) consisting of 2D TMDCs both in BEOL and FEOL. Furthermore, the current work can be extended to synthesize other 2D TMDC based heterostructures such as metal-semiconductor heterostructures.

Acknowledgements

The authors acknowledge Jeroen van Gerwen, Martijn G. Dijstelbloem, and Christian van Helvoirt for their technical assistance and Dr. Vincent Vandalon for the valuable suggestions. The authors acknowledge Jeff J.P.M. Schulpen for the DFT calculations. Dr. Beatriz Barcones is acknowledged for the FIB preparation of the TEM sample. Solliance and the Dutch province of Noord-Brabant are acknowledged for funding the TEM facility. E.M.T. Fadaly and Prof. Dr. E.P.A.M. Bakkers are gratefully acknowledged for supplying the GaAs nanowire substrates. This work was supported by the European Research Council (Grant Agreement No. 648787).

References

[1] S. Das, J.A. Robinson, M. Dubey, H. Terrones, and M. Terrones, Annu. Rev. Mater. Res. **45**, 1 (2015).

[2] M. Chhowalla, H.S. Shin, G. Eda, L. Li, K.P. Loh, and H. Zhang, Nat. Chem. **5**, 263 (2013).

[3] A.K. Geim and I. V Grigorieva, Nature **499**, 419 (2013).

[4] Y. Liu, S. Zhang, J. He, Z.M. Wang, and Z. Liu, Nano-Micro Lett. **11**, (2019).

[5] H. Wang, F. Liu, W. Fu, Z. Fang, W. Zhou, and Z. Liu, Nanoscale **6**, 12250 (2014).

[6] R. Kappera, D. Voiry, S.E. Yalcin, B. Branch, G. Gupta, A.D. Mohite, and M. Chhowalla, Nat. Mater. **13**, 1128 (2014).

[7] Y. Liu, P. Stradins, and S.-H. Wei, Sci. Adv. **2**, e1600069 (2016).

[8] S.J. Haigh, A. Gholinia, R. Jalil, S. Romani, L. Britnell, D.C. Elias, K.S. Novoselov, L.A. Ponomarenko, A.K. Geim, and R. Gorbachev, Nat. Mater. **11**, 764 (2012).

[9] Y. Liu, N.O. Weiss, X. Duan, H.-C. Cheng, Y. Huang, and X. Duan, Nat. Rev. Mater. **1**, 16042 (2016).

[10] X. Gong, X. Zhao, M.E. Pam, H. Yao, Z. Li, D. Geng, S.J. Pennycook, Y. Shi, and H.Y. Yang, Nanoscale **11**, 4183 (2019).

[11] L. Samad, S.M. Bladow, Q. Ding, J. Zhuo, R.M. Jacobberger, M.S. Arnold, and S. Jin, ACS Nano **10**, 7039 (2016).

[12] W. Liao, Y. Huang, H. Wang, and H. Zhang, Appl. Mater. Today **16**, 435 (2019).

[13] C.L. Lo, M. Catalano, K.K.H. Smithe, L. Wang, S. Zhang, E. Pop, M.J. Kim, and Z. Chen, Npj 2D Mater. Appl. **1**, (2017).

[14] N. Loubet, T. Hook, P. Montanini, C.W. Yeung, S. Kanakasabapathy, M. Guillom, T. Yamashita, J. Zhang, X. Miao, J. Wang, A. Young, R. Chao, M. Kang, Z. Liu, S. Fan, B. Hamieh, S. Sieg, Y. Mignot, W. Xu, S.C. Seo, J. Yoo, S. Mochizuki, M. Sankarapandian, O. Kwon, A. Carr, A. Greene, Y. Park, J. Frougier, R. Galatage, R. Bao, J. Shearer, R. Conti, H. Song, D. Lee, D. Kong, Y. Xu, A. Arceo, Z. Bi, P. Xu, R. Muthinti, J. Li, R. Wong, D. Brown, P. Oldiges, R. Robison, J. Arnold, N. Felix, S. Skordas, J. Gaudiello, T. Standaert, H. Jagannathan, D. Corliss, M.H. Na, A. Knorr, T. Wu, D. Gupta, S. Lian, R. Divakaruni, T. Gow, C. Labelle, S. Lee, V. Paruchuri, H. Bu, and M. Khare, in *Dig. Tech. Pap. - Symp. VLSI Technol.* (IEEE, 2017), pp. T230–T231.

[15] C. Huyghebaert, T. Schram, Q. Smets, T. Kumar Agarwal, D. Verreck, S. Brems, A. Phommahaxay, D. Chiappe, S. El Kazzi, C. Lockhart De La Rosa, G. Arutchelvan, D. Cott, J.

Ludwig, A. Gaur, S. Sutar, A. Leonhardt, D. Marinov, D. Lin, M. Caymax, I. Asselberghs, G. Pourtois, and I.P. Radu, Tech. Dig. - Int. Electron Devices Meet. IEDM **2018**-**Decem**, 22.1.1 (2019).

[16] O. Sul, J. Bang, S.-O. Yeom, G. Ryu, H.-B. Joo, S.-J. Kim, H. Yang, J. Lee, G. Lee, E. Choi, and S.-B. Lee, Nanotechnology **30**, 405203 (2019).

[17] W. Hao, C. Marichy, and C. Journet, 2D Mater. **6**, 012001 (2018).

[18] B. Groven, M. Heyne, A. Nalin Mehta, H. Bender, T. Nuytten, J. Meersschaut, T. Conard, P. Verdonck, S. Van Elshocht, W. Vandervorst, S. De Gendt, M. Heyns, I. Radu, M. Caymax, and A. Delabie, Chem. Mater. **29**, 2927 (2017).

[19] A.U. Mane, S. Letourneau, D.J. Mandia, J. Liu, J.A. Libera, Y. Lei, Q. Peng, E. Graugnard, and J.W. Elam, J. Vac. Sci. Technol. A Vacuum, Surfaces, Film. **36**, 01A125 (2018).

[20] Y. Kim, D. Choi, W.J. Woo, J.B. Lee, G.H. Ryu, J.H. Lim, S. Lee, Z. Lee, S. Im, J.H. Ahn, W.H. Kim, J. Park, and H. Kim, Appl. Surf. Sci. **494**, 591 (2019).

[21] H.C.M. Knoops, S.E. Potts, A.A. Bol, and W.M.M. Kessels, in *Handb. Cryst. Growth*, Second Edi (Elsevier, Amsterdam, 2015), pp. 1101–1134.

[22] T. Kääriäinen, D. Cameron, M.-L. Kääriäinen, and A. Sherman, *Atomic Layer Deposition* (John Wiley & Sons, Inc., Hoboken, NJ, USA, 2013).

[23] D. Nminibapiel, K. Zhang, M. Tangirala, H. Baumgart, V.S.K. Chakravadhanula, C. Kübel, and V. Kochergin, ECS J. Solid State Sci. Technol. **3**, P95 (2014).

[24] R. Browning, N. Kuperman, B. Moon, and R. Solanki, Electronics **6**, 27 (2017).

[25] K. Zhang, D. Nminibapiel, M. Tangirala, H. Baumgart, and V. Kochergin, ECS Trans. **50**, 3 (2013).

[26] Y. Kim, D. Choi, W.J. Woo, J.B. Lee, G.H. Ryu, J.H. Lim, S. Lee, Z. Lee, S. Im, J.-H. Ahn, W.-H. Kim, J. Park, and H. Kim, Appl. Surf. Sci. **494**, 591 (2019).

[27] Y. Kim, J.-G. Song, Y.J. Park, G.H. Ryu, S.J. Lee, J.S. Kim, P.J. Jeon, C.W. Lee, W.J. Woo, T. Choi, H. Jung, H.-B.-R. Lee, J.-M. Myoung, S. Im, Z. Lee, J.-H. Ahn, J. Park, and H. Kim, Sci. Rep. **6**, 18754 (2016).

[28] H.B. Profijt, S.E. Potts, M.C.M. van de Sanden, and W.M.M. Kessels, J. Vac. Sci. Technol. A Vacuum, Surfaces, Film. **29**, 050801 (2011).

[29] S.B. Basuvalingam, Y. Zhang, M.A. Bloodgood, R.H. Godiksen, A.G. Curto, J.P. Hofmann, M.A. Verheijen, W.M.M. Kessels, and A.A. Bol, Chem. Mater. **31**, 9354 (2019).

[30] S.J. Hazarika, D. Mohanta, A. Tripathi, and D. Kanjilal, J. Phys. Conf. Ser. **765**, 012007 (2016).

[31] E. Guilmeau, A. Maignan, C. Wan, and K. Koumoto, Phys. Chem. Chem. Phys. **17**, 24541 (2015).

[32] C. Schuffenhauer, R. Popovitz-Biro, and R. Tenne, J. Mater. Chem. **12**, 1587 (2002).

[33] A. Niazi and A.K. Rastogi, J. Phys. Condens. Matter **13**, 6787 (2001).

[34] A.J.M. Mackus, A.A. Bol, and W.M.M. Kessels, Nanoscale **6**, 10941 (2014).

[35] A.J.M. Mackus, M.J.M. Merkx, and W.M.M. Kessels, Chem. Mater. **31**, 2 (2019).

[36] K. Endo, H. Ihara, K. Watanabe, and S. Gonda, J. Solid State Chem. **44**, 268 (1982).

[37] C.G. Hawkins and L. Whittaker-Brooks, ACS Appl. Nano Mater. **1**, 851 (2018).

[38] B. Morosin, Acta Crystallogr. Sect. B Struct. Crystallogr. Cryst. Chem. **30**, 551 (1974).

[39] A. Sharma, M.A. Verheijen, L. Wu, S. Karwal, V. Vandalon, H.C.M. Knoops, R.S. Sundaram, J.P. Hofmann, W.M.M. (Erwin) Kessels, and A.A. Bol, Nanoscale **10**, 8615 (2018).

[40] J. Hämäläinen, M. Mattinen, K. Mizohata, K. Meinander, M. Vehkamäki, J. Räisänen, M. Ritala, and M. Leskelä, Adv. Mater. **30**, 1703622 (2018).

[41] C. Lin, X. Zhu, J. Feng, C. Wu, S. Hu, J. Peng, Y. Guo, L. Peng, J. Zhao, J. Huang, J. Yang, and Y. Xie, J. Am. Chem. Soc. **135**, 5144 (2013).

Appendix 4

TiS_x and NbS_x Film Growth by ALD

In this work, thin films of TiS_x and NbS_x were deposited by ALD on a thermally grown 450 nm SiO_2/Si substrate. Unless otherwise mentioned, this was the standard starting substrate. The TiS_x thermal ALD process used in this work was reported previously[1]. For the NbS_x growth, a new process was developed by thermal ALD using (tert-butylimido)-tris-(diethylamino)-niobium (TBTDEN) and H_2S gas as coreactant. The self-limiting saturated growth behavior for the NbS_x ALD processes was investigated at 250 °C. All the growth-per-cycle (GPC) values were determined by measuring the thickness as a function of the ALD cycle measurement by *in-situ* Spectroscopic Ellipsometry (SE). Saturation of the GPC was observed when at least 10 s and 20 s of TBTDEN precursor and H_2S coreactant gas were pulsed, respectively, and when both were separated by a 30 s Ar purge steps to avoid parasitic CVD reactions (See Figures A4.1(a and b) (red)). The GPC value under saturated growth conditions was 1.65 Å.

For the TiS_x thermal ALD process, the growth and film properties at deposition temperatures above 100 °C were not discussed in the previous work. Therefore, the growth behavior as a function of the deposition temperature was investigated for both ALD processes. For various deposition temperatures in both ALD processes, the thickness as a function of the number of ALD cycles was determined by *in-situ* SE, as shown in Figure A4.1(c and d). The deposition temperatures were varied between 100 °C and 200 °C for the TiS_x process, and between 150 °C and 300 °C for the NbS_x process. Indicating a narrow temperature window for the combined processes, as TiS_x film could not be deposited above 200 °C due to the decomposition of TDMAT, while in the case of the NbS_x, film growth was not observed below 150 °C. In the case of TiS_x, linear ALD growth was observed without any delay at all deposition temperatures, see Figure A4.1c. The GPC was calculated by taking a slope over above 50 cycles, and it was observed that the GPC decreases from 1.6 to 0.6 Å with increasing deposition temperature, see Table A4.1. On the contrary, for the NbS_x case, below a deposition temperature of 300 °C, immediate nucleation up until 10 ALD cycles was observed. Following this initial nucleation, there is a growth delay between 10 and ~80 cycles, see Figure A4.1d. This indicates that the initial nucleation on the SiO_2 substrate was rapid, and the further growth on deposited/nucleated NbS_x layers was delayed significantly

at lower deposition temperature (150 °C). However, by increasing the deposition temperature from 150 to 250 °C, the delayed growth between 10 and ~80 cycles was observed to recover. Leading to an increasing trend in GPC along with deposition temperature from 1.52 Å at 150 °C to 1.65 Å at 250 °C. On the contrary, the growth behavior at 300 °C was different, as linear ALD growth was observed without any trend of delayed growth. The GPC at 300 °C was measured to be 1.17 Å, which is lower than the GPC at 250 °C. This drop in GPC at 300 °C could be ascribed to film morphology changes, as will be discussed later.

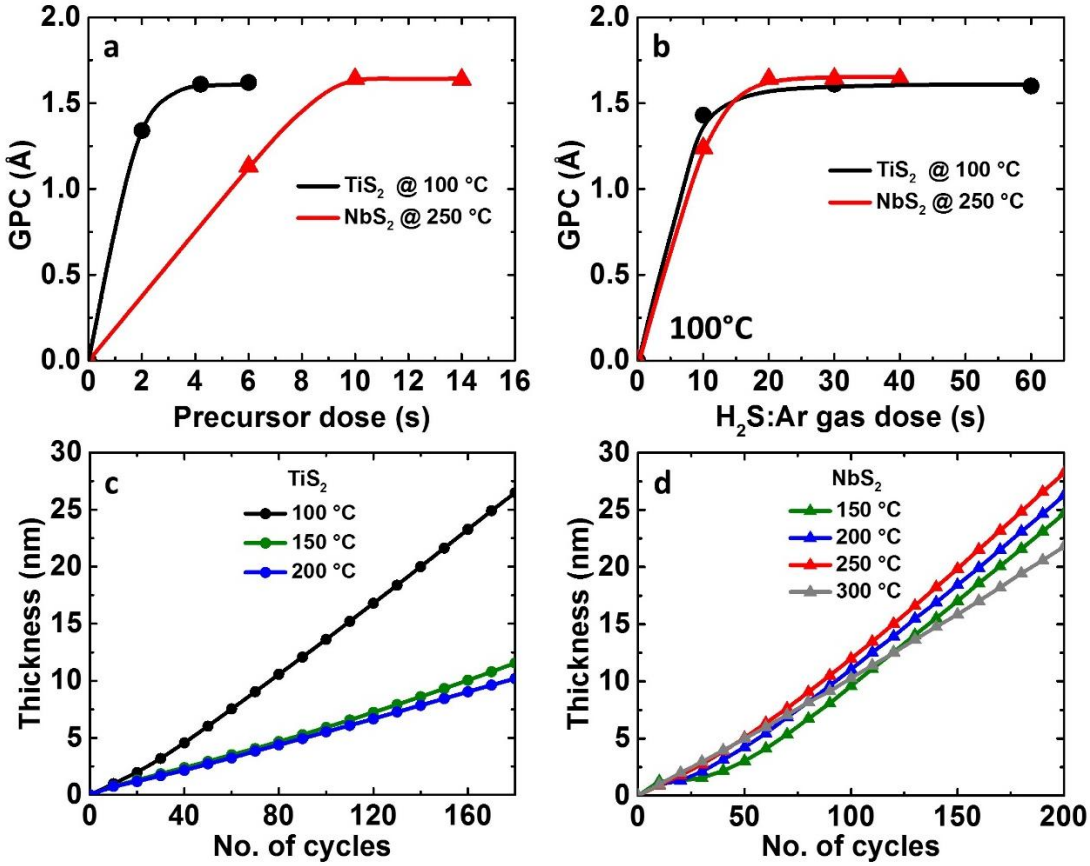

Figure A4.1 (a) and (b) Saturated curves for TiS_x and NbS_x as a function of precursor dose time and coreactant gas dose time, respectively. (c) and (d) Thickness as a function of the number of ALD cycles for both TiS_x and NbS_x processes, respectively for various deposition temperatures.

Composition Analysis

The TiS_x and NbS_x films deposited at various deposition temperatures were characterized in detail. The elemental composition of the deposited films was studied using XPS analysis. The S2p XPS spectra for both the TiS_x and NbS_x films deposited at various deposition temperatures are shown in Figure A4.2(a and b). All films were observed to have one doublet at ~161.1 and ~162.3 eV, corresponding to S $2p_{3/2}$ and S $2p_{1/2}$ spin-orbit doublets of S^{2-} species in MX_2 type materials, indicating the disulfide (TiS_2 and NbS_2) nature of the films. Depth profiling of the films by means of sputtering using Ar^+ ions was performed to study the purity of the films at the bulk by avoiding surface oxidation/ impurities due to exposure to ambient conditions. The depth profiling revealed the presence of C, O, and N impurities. Further, to avoid the influence of preferential sputtering on the qualitative composition of these impurities and to obtain the chemical composition of the film, RBS studies were performed on these films, as shown in Table A4.1.

To further confirm the synthesis of TiS_x and NbS_x, valence band spectra were measured using XPS, see Figure A4.2. The valence band spectra of the TiS_x films deposited at various temperatures are in good agreement with the TiS_2 valence band spectra reported in the literature[4]. Additionally, an evolution of a shoulder close to the Fermi level around ~-1 eV (marked with *) was observed, and the intensity of this peak increased with increasing deposition temperature. Similarly, in literature, Hawkins *et al.*, using UPS valence band spectra measurements, observed a peak around -1 eV, and they attribute this peak to Ti^{3+} defect states in TiS_2[5]. Following the literature, the observed peak around -1 eV was also attributed to Ti^{3+} (and/or Ti^{2+}) defect states indicating the presence of S vacancies and/or excess Ti in the TiS_x films[2]. In the case of NbS_x films, we could not find any literature for the NbS_2 valence band spectra. Therefore, the spectrum was simulated for the NbS_2 crystal structure[6] using density functional theory (DFT), see Figure A4.2e. This simulated spectrum was compared with the measured spectra and yielded a good match with the spectra, indicating the synthesis of NbS_2 films. Similar to the TiS_x case, the shoulder close to the Fermi level around ~-1 eV (an intrinsic NbS_2 valence band spectrum peak) in the valence band spectra of NbS_x film was observed to increase in peak intensity with increasing deposition temperatures. This peak could also be attributed to Nb^{3+} (and/or Nb^{2+}) defect states indicating the presence of S vacancies and/or excess Nb in the NbS_x films.

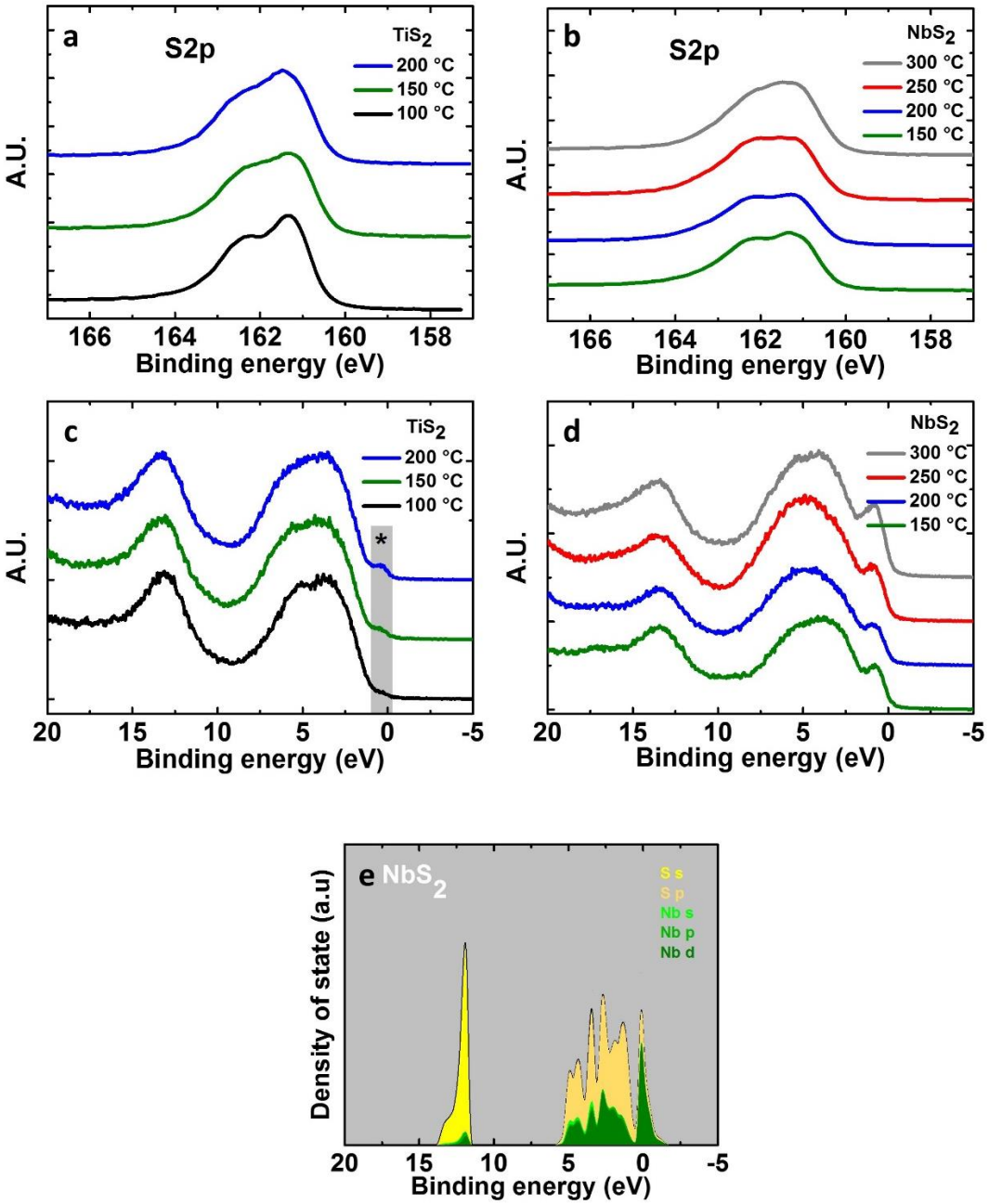

Figure A4.2 (a) and (b) XPS S2p spectra of TiS_x and NbS_x films, respectively, for various deposition temperatures. (c) and (d) shows the XPS valence band spectra of TiS_x and NbS_x films, respectively for various deposition temperatures. In (c) grey area marked with `*` indicates defect states in TiS_2. (e) DFT simulated valence band spectra using the crystal structure parameters of NbS_2.

To expand on XPS analysis and to obtain an in-depth understanding of the composition of both the TiS_x and NbS_x films as a function of deposition temperature RBS study was performed. For both TiS_x and NbS_x films, S to transition metal (Ti or Nb) ratio was calculated

from RBS measurements. RBS revealed sub-stoichiometry for both the material systems with a value less than 2, and the ratio was observed to decreases with increasing deposition temperatures. In the case of TiS_x film, the ratio decreased from 1.75 for 100 °C to 1.41 for 200 °C film. Whereas, in the case of NbS_x films, the ratio decreased from 1.47 for 200 °C to 1.25 for 300 °C film. This indicates the presence of S vacancies and/or excess metal in the films, similar to the observation made by XPS valence band measurement. In addition to the S to transition metal ratio, there were also other similarities in the case of impurities between TiS_x and NbS_x ALD grown films. The H content decreases in both cases (Table A4.1) with increasing deposition temperatures from ~18 to 6 at.% for TiS_x films, and from ~23 to 9 at.% for NbS_x films. The presence of H in the film could be from precursor ligands and/or coreactant. The C content for TiS_x films decreases from ~5 at.% at 100 °C to below the detection limit at 200 °C, while for NbS_x films, it was below the detection limit irrespective of deposition temperatures. The C content in the film could be from precursor ligands. Whereas, O content increases for both the processes with increasing deposition temperature from ~4 to 7 at.%, and could be due to residual O_2 and H_2O present in the ALD reactor during deposition.

Table A4.1 Growth and material properties of the TiS_x and NbS_x films, such as GPC, resistivity, H, C, and O content, and S/transition metal ratio for various deposition temperatures. The GPC was calculated using the *in-situ* SE measurement as a function of the number of ALD cycles. Resistivity was calculated using the Four-Point Probe measurements. The H, C, O at.% and S/transition metal ratio were obtained from RBS and ERD measurements.

TiS_x	GPC (Å)	Resistivity (10^3 μΩ-cm)	H (at.%)	C (at.%)	O (at.%)	S/Ti ratio
100 °C	1.60± 0.03	2.4± 0.1	18.8 ± 0.4	5.6 ± 1.2	4.2 ± 1.6	1.8 ± 0.1
150 °C	0.72± 0.03	1.2± 0.1	10.8 ± 0.7	1.1 ± 0.1	6.7 ± 0.1	1.5 ± 0.1
200 °C	0.60± 0.03	0.8± 0.1	6.3 ± 0.5	x	7.1 ± 0.1	1.4 ± 0.1

NbS_x	GPC (Å)	Resistivity (10^3 μΩ-cm)	H (at.%)	C (at.%)	O (at.%)	S/Nb ratio
150 °C	1.52± 0.03	16.4± 0.1	-	-	-	-
200 °C	1.54± 0.03	12.8± 0.1	23.7 ± 1.5	x	5.6 ± 0.2	1.5 ± 0.1
250 °C	1.65± 0.03	8.6± 0.1	-	-	-	-
300 °C	1.17± 0.03	4.8± 0.1	9.2 ± 0.7	x	7.5 ± 0.3	1.3 ± 0.1

"-" no data
"x" below the detection limit

Crystallinity and Morphology Analysis

The role of deposition temperature on the crystallinity and the film morphology of both films was investigated using XRD and SEM analysis, respectively. The XRD patterns of both the TiS_x and NbS_x films are shown in Figure A4.3, where the crystallinity of the films was observed to increase with increasing deposition temperature. Both the GI-XRD and gonio-XRD (shown in the inset of the Figure A4.3a) patterns of the TiS_x films indicate that the crystallinity increases significantly with increasing deposition temperature. The only peak visible in both the scan was around 15° 2θ , which corresponds to the (001) plane of the 1T phase of TiS_2. The gonio-XRD shows that the basal (001) plane growth of the TiS_x film increases with increasing temperature. Similarly, the crystallinity of the NbS_x films also increases with deposition temperature. The peak around 15° 2θ appears and increases in intensity for the films deposited at higher temperatures, and this peak corresponds to the (00*3*) plane of the NbS_2. The gonio XRD (data not shown here) did not show any peaks confirming the poor crystallinity of the NbS_x films. Therefore, note that the relative crystallinity of the 300 °C NbS_x film was poor in comparison to the TiS_x film deposited at 200 °C. The broad peak around 20° 2θ for the films at all deposition temperatures also indicates the amorphous content in the films.

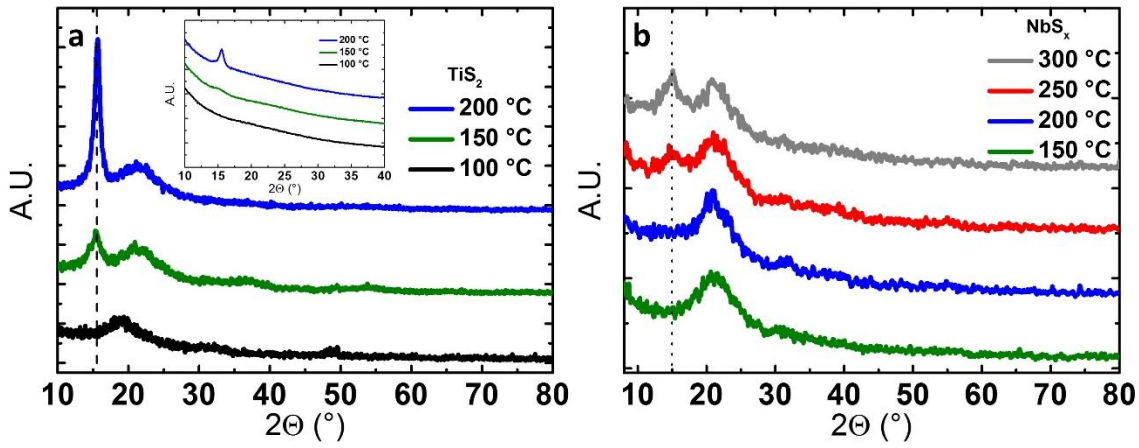

Figure A4.3 (a) and (b) GI-XRD patterns for TiS_x and NbS_x films, respectively, deposited at various deposition temperatures. Inset in (a) shows the Gonio XRD pattern for TiS_x films deposited at various deposition temperatures.

The top-view SEM image of TiS_x film deposited at 100°C (Figure A4.4a) shows out-of-plane orientation (OoPO) structures, also known as fins. Similar OoPO structures were also observed for TiS_2 films deposited by PE-ALD[1], and also for other TMDCs synthesized by ALD

such as MoS_2[7] and ReS_2[8]. The number of OoPO structures was observed to decrease with increasing deposition temperature. At 200 °C (see Figure A4.5c), OoPO structures were not observed. In the case of NbS_x films, the top-view SEM images show OoPO structures for all deposition temperatures, see Figure A4.4(e-f). For the films deposited between 150 and 250 °C, a high density of OoPO structures was observed, while at 300 °C, the OoPO structures were observed to be suppressed. This significant change in morphology from 250 °C to 300 °C, can also explain the change in growth behavior observed in Figure A4.1d. A similar effect of the OoPO structure on GPC has been observed previously for PE-ALD grown TiS_2[1] and MoS_2[7], where the GPC was observed to rise due to the OoPO structures of the film. Therefore, the suppression of the OoPO structures could explain the decreasing GPC at 300 °C for the NbS_x process.

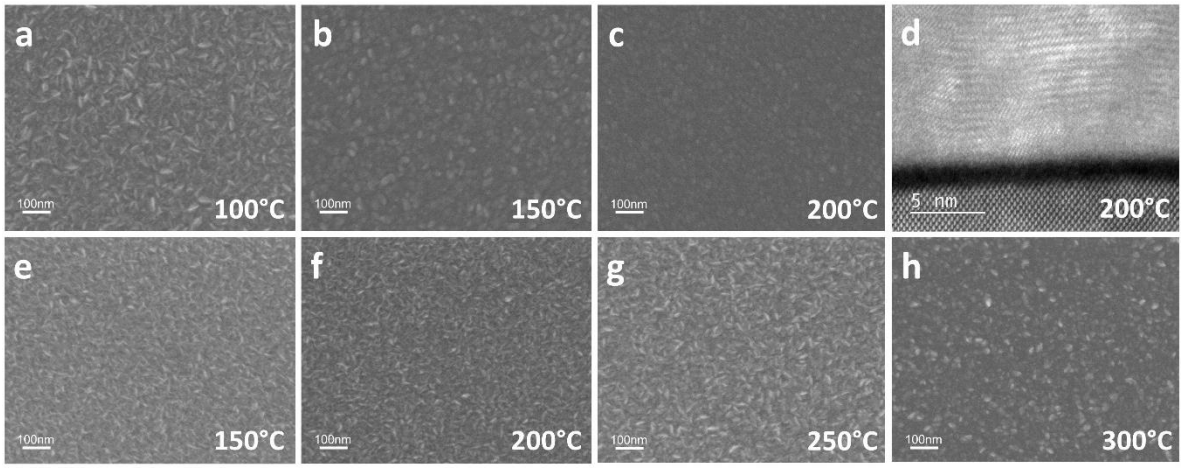

Figure A4.4 Top-view SEM image of deposited TiS_x (a-c) and NbS_x (e-h) films at various deposition temperatures. (d) shows the cross-section STEM image of the TiS_x film deposited at 200 °C.

Resistivity measurements

The resistivity of the films was calculated using Four-Point Probe measurements for both TiS_x and NbS_x films deposited at different deposition temperatures, see Table A4.1. It was observed that the resistivity of both films decreases with increasing deposition temperature. The resistivity of TiS_x films decreases from 2.4 $x10^3$ for 100 °C to 0.8 10^3μΩ-cm for 200 °C film. And that of NbS_x films decreases from 16.4 $x10^3$ for 150 °C to 4.8 10^3μΩ-cm for 300 °C film. Such a variation in resistivity of the films could be due to one or more factors such as morphology, decreasing stoichiometry and/or increasing crystallinity of the

films. In literature, the TiS_2 resistivity has been observed to decrease with the sub-stoichiometric of the films[9,5,2]. Such a trend of a decreasing resistivity was reported to be due to an increasing number of defect states near the Fermi level with an increasing level of sub-stoichiometry in the films. This could also explain the trend observed here for both TiS_x and NbS_x films as the presence of defect states near the Fermi level (XPS valence band spectra) increases with the sub-stoichiometry of the films, thus clearly indicating the role of stoichiometry in the films on resistivity. It is also important to note that in addition to film stoichiometry, film crystallinity plays an additional role in the resistivity of the film, as metallic NbS_x film with S/Nb ratio of 1.25 deposited at 300 °C has a higher resistivity than the TiS_x film with S/Ti ratio of 1.41 deposited at 200 °C, considering that the bulk resistivity of both the TiS_2 and NbS_2 are roughly similar[2,3].

References

[1] S.B. Basuvalingam, Y. Zhang, M.A. Bloodgood, R.H. Godiksen, A.G. Curto, J.P. Hofmann, M.A. Verheijen, W.M.M. Kessels, and A.A. Bol, Chem. Mater. **31**, 9354 (2019).

[2] E. Guilmeau, A. Maignan, C. Wan, and K. Koumoto, Phys. Chem. Chem. Phys. **17**, 24541 (2015).

[3] A. Niazi and A.K. Rastogi, J. Phys. Condens. Matter **13**, 6787 (2001).

[4] K. Endo, H. Ihara, K. Watanabe, and S. Gonda, J. Solid State Chem. **44**, 268 (1982).

[5] C.G. Hawkins and L. Whittaker-Brooks, ACS Appl. Nano Mater. **1**, 851 (2018).

[6] B. Morosin, Acta Crystallogr. Sect. B Struct. Crystallogr. Cryst. Chem. **30**, 551 (1974).

[7] A. Sharma, M.A. Verheijen, L. Wu, S. Karwal, V. Vandalon, H.C.M. Knoops, R.S. Sundaram, J.P. Hofmann, W.M.M. (Erwin) Kessels, and A.A. Bol, Nanoscale **10**, 8615 (2018).

[8] J. Hämäläinen, M. Mattinen, K. Mizohata, K. Meinander, M. Vehkamäki, J. Räisänen, M. Ritala, and M. Leskelä, Adv. Mater. **30**, 1703622 (2018).

[9] C. Lin, X. Zhu, J. Feng, C. Wu, S. Hu, J. Peng, Y. Guo, L. Peng, J. Zhao, J. Huang, J. Yang, and Y. Xie, J. Am. Chem. Soc. **135**, 5144 (2013).

Low-Temperature Phase-controlled Synthesis of NbS_2 and NbS_3 using Atomic Layer Deposition for Vertical Heterostructures

5

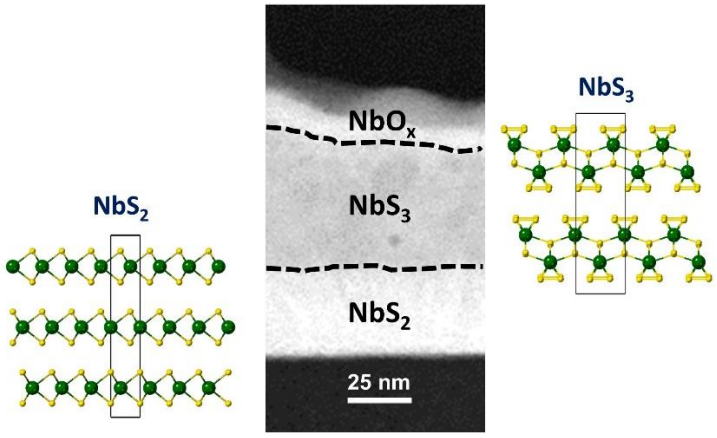

The prospects of combining metal-semiconductor transition metal chalcogenides (TMCs) to form heterostructures have gained momentum for future optoelectronic applications. While various transition metal dichalcogenides (TMDC) based heterostructures have been explored, metal-semiconductor heterostructures based on TMDC-TMTC (trichalcogenides) have yet to be demonstrated experimentally. However, there are many technical challenges associated with fabricating such heterostructures, such as phase-control between TMDC and TMTC, scalability, thickness control, and adequate processing temperatures. Here, we report on the phase-controlled synthesis of NbS_2 (metallic) and NbS_3 (semiconducting) by plasma-enhanced atomic layer deposition (PE-ALD) at low-temperature (300 °C) along with the fabrication of metal-semiconductor NbS_2-NbS_3 vertical heterostructures. The phase-control between NbS_2 and NbS_3 was achieved by tuning two parameters in the PE-ALD process: first by varying the deposition temperature and second by carefully optimizing the H_2S:H_2 flow mixture during the plasma coreactant step. In the former case, NbS_3 was synthesized below a deposition temperature of 350 °C, while at higher deposition temperatures, NbS_2 was obtained. In the latter case, increasing the H_2 flow with respect to the H_2S flow led to the deposition of NbS_2 at a deposition temperature of 300 °C. This phase-control between NbS_3 and NbS_2 by modulating the H_2S:H_2 flow mixture was exploited to form NbS_2-NbS_3 heterostructures at 300°C. Preparation of the heterostructure was confirmed using transmission electron microscopy and energy dispersive X-ray spectroscopy. This work could open new avenues for the synthesis and implementation of TMDCs, TMTCs, and their heterostructures for (opto)electronic applications.

Saravana Balaji Basuvalingam[1,], Matthew A. Bloodgood[1], Jeff J. P. M. Schulpen[1], Marcel A. Verheijen[1,3], Wilhelmus M. M. Kessels[1], and Ageeth A. Bol[1,*]* (to be submitted)

5.1 Introduction

Since the discovery of graphene, layered low-dimensional materials with weak interlayer (van der Waals) interactions such as transition metal di-chalcogenides (TMDCs) and black-phosphorus have gained a lot of interests because of their intriguing physical and chemical properties[1]. Among them, TMDCs are layered two-dimensional (2D) materials with formula MX_2, where M is a transition metal (such as Ti, Ta, Nb, Mo, W, etc.) and X is a chalcogenide (S, Se, and Te). In some TMDCs, both electrical and optical properties vary depending on their crystal phase (*e.g.,* 1T-MoS_2 is metallic, whereas 2H-MoS_2 is semiconducting) or on their thickness (*e.g.,* monolayer 2H-MoS_2 has a direct band gap, whereas bulk 2H-MoS_2 has an indirect band gap)[2]. In addition to TMDCs, there is a class of layered low-dimensional materials known as transition metal tri-chalcogenides (TMTCs) involving similar elements as TMDCs. The TMTCs are quasi-one-dimensional materials exhibiting a strong electrical and optical in-plane anisotropy[3,4]. TMTCs are layered materials with formula MX_3, where M is a transition metal (group IV, V, VI), and X is a chalcogenide. In TMTCs, chalcogenide atoms can be categorized into two types, as one of the chalcogenide atoms shares 2 electrons (like in TMDCs) while the remaining two chalcogenide atoms share 2 electrons between them[5]. So, the transition metal is in the +4 oxidation state (similar to TMDCs). In some cases, TMDCs and TMTCs containing analogous elements can also vary in electrical properties. For example, in both TiS_2/TiS_3 and NbS_2/NbS_3 systems, the TMDCs are considered semi-metal/ metal while their counterpart TMTCs are considered semiconductors.

Recently, van der Waals heterostructures with a 2D–2D metal-semiconductor architecture have gained significant interest due to improved device performance compared to a 3D-2D architecture[6]. This performance improvement is due to weak Fermi level pinning at the 2D–2D interface along with reduced Schottky barrier height resulting in low contact resistivity[7]. The most widely studied 2D metal-semiconductor heterostructure configurations are TMDC-TMDC and TMDC-graphene. Among them, phase-engineered TMDC-TMDC metal-semiconductor heterostructures synthesized with analogous elements (1T MoS_2 –2H MoS_2 heterostructure) were shown to improve the electronic device performance due to their record low contact resistivity[6,8]. On the other hand, the poor stability and lack of a scalable synthesis method for 1T-MoS_2 (converted from 2H-MoS_2 by various methods) are major issues. Therefore, it would be of interest to explore alternative metal-semiconductor heterostructures. This could potentially be addressed by synthesizing TMDC-TMTC heterostructures with analogous elements.

Van der Waals metal-semiconductor heterostructures involving both TMDCs and TMTCs have yet to be explored experimentally. Initial computational studies by Liu *et al.* have shown that in comparison to 3D metal-TMTC heterostructures, the Schottky barrier height is smaller for TMDCs-TMTCs based metal-semiconductor heterostructures[9]. Therefore, there are lots of potentials to experimentally investigate these 2D van der Waals metal-semiconductor heterostructures based on TMDC-TMTC combinations. Among various TMDC-TMTC systems, the niobium sulfide (NbS_x) system is a stable and rarely studied group V based system, which, as mentioned above, also exists both in a metallic (NbS_2) and semiconducting (NbS_3) form. For NbS_2, the most commonly reported phases are 3*R* and 2*H*, while there are also reports on its existence in the 1*T* phase[10]. Irrespective of the phase, NbS_2 is metallic and has gained much interest recently as contacts in electronic devices[11–13], and as an electrode in hydrogen evolution reaction[14–16] applications. NbS_2 has been synthesized by various techniques such as chemical vapor deposition (CVD)[13,17–23], chemical vapor transport (CVT)[24], and wet chemical[25,26] synthesis. On the contrary, NbS_3, depending on its phase, can be a semiconductor or a metal. The most common and straightforward phase to synthesize is the semiconducting phase[3,27]. Recently, the carrier mobility of ~1200-2400 $cm^2 V^{-1} S^{-1}$ was reported using an NbS_3 film as a channel material in a back-gated device configuration, indicating the potential of NbS_3 for device applications[28]. To date, NbS_3 has been synthesized principally using the CVT method[29–31].

While CVT is the most common synthesis technique for both NbS_2 and NbS_3, it is not suitable for direct heterostructure formation. However, CVT grown crystals are commonly used for a top-down mechanical transfer method to form 2D metal-semiconductor heterostructures. For example, a 2D metal (or semiconductor) synthesized by CVT can be exfoliated and stacked on an exfoliated or CVD-grown 2D semiconductor (or metal) using a polymer tape. Unfortunately, such a top-down method has limitations such as leftover residues at the interface, low yields, and poor scalability, which hinders the resulting device performance[11] and limits their implementation in industry. These limitations could be overcome by a direct bottom-up *in-situ* synthesis method. However, synthesizing both TMDC and TMTC directly on top of each other in a controlled manner would be challenging, as both synthesis temperature and chalcogenide partial pressure have to be controlled simultaneously to achieve phase-control between TMDC and TMTC[32]. Recently, we have reported on the phase-controlled synthesis of TiS_2 and TiS_3 at low-temperature by atomic layer deposition (ALD) (see Chapter 3)[33]. Therefore, ALD has the potential to be a suitable technique to grow TMDC-TMTC heterostructures with the phase-controlled preparation of TMDC and TMTC vertically on each other.

In this work, we develop a plasma-enhanced atomic layer deposition (PE-ALD) process to grow niobium sulfide (NbS_x). We study the control over the material phase between NbS_2 and NbS_3 by varying the deposition temperature (between 200 °C and 450 °C) and co-reactant plasma composition (H_2S/H_2 ratio), respectively. Control over the material phase is investigated using various characterization techniques and DFT simulation. Using the obtained phase control, we fabricate NbS_2–NbS_3 (metal-semiconductor) heterostructures. The heterostructure formation is investigated using cross-section high-resolution transmission electron microscopy (TEM). Our work shows that ALD enables control over the phase between TMDC and TMTC at low deposition temperatures, and also facilitates the fabrication of a TMDC-TMTC heterostructure over a large area.

5.2 Experimental Section

5.2.1 Atomic Layer Deposition of Niobium Sulfide

The NbS_x thin films were prepared by PE-ALD in an Oxford Instruments Plasma Technology FlexAL ALD reactor. The system´s base pressure was 10^{-6} Torr, and the reactor was equipped with a remote inductively coupled plasma source (ICP, 13.56 MHz). The table temperature was varied between 200 °C and 450 °C. For all the deposition temperatures, the wall was maintained at 150 °C. The metal-organic precursor (*tert*-butylimido)-tris(diethylamino)-niobium (TBTDEN) [STREM Chemical, Inc., 98% pure] was used as the niobium precursor without further purification. The precursor was held at 65 °C in a stainless-steel container and was bubbled using Ar as the carrier gas. The NbS_x PE-ALD reaction cycle consisted of two half-cycles separating the Nb and S reactants. In the first half-cycle, the niobium precursor was dosed using Ar as carrier gas into the reactor, while the pressure was maintained at 80 mTorr. During the second half-cycle, a plasma gas mixture consisting of H_2S, H_2, and Ar gas was used as coreactant. An ICP power of 200 W was applied to ignite the plasma while maintaining a pressure of 8 mTorr. Both half-cycles were separated by an Ar purge step.

Two NbS_x PE-ALD processes were developed; type 1: using a H_2S and Ar coreactant gas mixture with a flow of 10 and 40 sccm, respectively; and type 2: using a H_2S, H_2, and Ar coreactant gas mixture with varied H_2S and H_2 flow rates while Ar flow remained constant. In the second process, the Ar flow was maintained at 40 sccm, while the total flow of H_2S+H_2 was kept constant at 10 sccm with a varying H_2S:H_2 gas mixture ratio. The thin films were deposited on Si substrates covered with approximately 450 nm thick thermally grown SiO_2.

5.2.2 Analysis Techniques

The film thickness was investigated as a function of the number of ALD cycles by *in-situ* spectroscopic ellipsometry (SE). The SE spectra were recorded after every 10 ALD cycles. The SE employed was a J.A. Woollam Co., Inc., M2000U, with a rotating compensator, yielding a photon energy range of 0.7-5 eV. COMPLETEEASE software was used to model the optical constants of the deposited NbS_x film. The model consists of Si substrate, 450 nm SiO_2, and NbS_x film. The dielectric function of the NbS_x film was modeled using a B-spline function. The molecular structure and phase of the prepared films were examined by Raman spectroscopy using a confocal Renishaw inVia system with a 514 nm excitation laser in an ambient environment. The binding environment and valence band structure of the synthesized films were studied by X-ray photoelectron spectroscopy (XPS) with a Thermo Scientific KA1066 spectrometer with monochromatic Al Kα (hν = 1486.6 eV) X-ray radiation. The XPS spectra were calibrated by setting the C–C peak to 248.8 eV in the C1s spectrum. The crystallinity of the thin films was investigated by grazing-incident X-ray diffraction (GI-XRD). A PANalytical X´Pert Pro MRD analyzer using a Cu Kα (λ = 1.54 Å) X-ray source operated at 40mA, and 45kV was employed. The scan range was 5 to 80° 2θ with a scan rate and step size of 0.2 s/step and 0.01, respectively. The species in the H_2S:H_2:Ar plasma was studied using optical emission spectroscopy (OES). A USB4000 spectrometer from Ocean Optics with a wavelength range of 180−1100 nm was mounted vertically on top of the ICP plasma source. The thin film´s composition and purity were determined from Rutherford backscattering spectrometry (RBS) and elastic recoil detection (ERD) measurements. The measurements were conducted by Detect 99 B.V. Eindhoven, The Netherlands, with a 2 MeV He^+ beam source containing two detectors at scattering angles of 105° and 170°. The resistivity measurements were conducted *ex-situ* in ambient conditions using a Signatone four-point probe combined with a Keithley 2400 Sourcemeter acting both as a current source and a voltage meter. Resistivity was determined from the slope of the I-V curve. The carrier concentration and Hall mobility of the films were measured *ex-situ* using a LakeShore cryotronics 8400 Series set-up at room temperature. The microstructure of the NbS_2-NbS_3 heterostructure was investigated using scanning transmission electron microscopy (STEM) with a JEOL ARM 200F operated at 200 keV. For cross-section STEM studies, a lamella (~100 nm) was prepared in an FEI Nova600i NanoLab SEM/FIB using a lift-out preparation procedure after a protective SiO_2 layer was deposited on the top of the film by electron-beam induced deposition (EBID). The STEM combined with energy-dispersive X-ray spectroscopy (EDX) was used to study the chemical composition of the NbS_2-NbS_3 heterostructures. Scanning electron microscopy (SEM) was used to study the surface

morphology of the films. A Zeiss Sigma SEM with an in-lens detector and operating at an acceleration voltage of 3 keV was utilized.

5.2.3 Simulations Details

The *Ab-initio* calculations of the valence band density of states for NbS_2 and NbS_3 were carried out by density functional theory (DFT) in the projector-augmented wave (PAW) framework as implemented in the Vienna Ab initio Simulation Package (VASP) software. Electron exchange and correlation contributions were approximated using the Perdew, Burke, and Ernzerhof (PBE) functional[34]. The lattice parameters used in the DFT calculations were obtained from Bloodgood *et al.*[29] for NbS_3 (NbS_3-IV) and from Morosin *et al.*[35] for 3*R*-NbS_2. Plane-wave cutoff energy of 400 eV was employed for the density of states calculations, while van der Waals interactions were taken into account through the DFT-D3 method of Grimme[36]. Partial occupancies around the Fermi level were accounted for with the tetrahedron smearing method with Blöchl corrections[37]. The density of states was calculated with an energy resolution of 0.05 eV. After the calculation, any density of states above the Fermi level was discarded.

5.3 Results and Discussion

In this work, to form NbS_2-NbS_3 heterostructures, we first developed novel PE-ALD processes for NbS_2 and NbS_3 using the metal-organic TBTDEN precursor and an H_2S, H_2 and Ar gas mixture as the coreactant. For the development of the ALD process, we drew inspiration from the commonly used CVT method[38], where the control between TMDC and TMTC synthesis has been demonstrated in two ways. One, by varying the temperature, where the TMTC growth occurs at low temperature (*e.g.,* < 750 °C for NbS_3), while the TMDC grows at high temperature (*e.g.,* >750 °C for NbS_2). Second, by modulating the chalcogenide to transition metal precursor ratio at a constant temperature (< 450 °C). The TMTC growth then occurs when this ratio is above 3, while TMDCs were synthesized below a ratio of 3. Hence, we studied the effect of both temperature and sulfur coreactant composition on the phase-control of the NbS_x system during ALD. The saturated self-limiting ALD growth behavior was investigated at a deposition temperature of 250 °C (appendix 5 Figure A5.1) using H_2S/Ar plasma as the coreactant (*type 1 ALD process*, see above). In the first half-cycle, the niobium precursor dose reached saturation at 10 s of exposure when the H_2S:Ar plasma exposure was maintained at 30 s. Thus, a precursor exposure time of 10 s was fixed for film

growth. In the second half-cycle, the H_2S:Ar (10:40 sccm, without H_2 in the mixture) plasma exposure was observed to reach saturation at 30 s exposure time. Ar gas was used to purge away remaining precursor, coreactant and/or by-products after both the ALD half-cycles, to avoid parasitic CVD reactions. Both these purge steps were observed to saturate at 10 s. The final optimized recipe adopted for NbS_x film growth is schematically represented as a function of time in Figure 5.1a. The same recipe was also utilized for the *type 2 ALD process* with added H_2 to the gas mixture of the plasma coreactant step [H_2S+Ar(+H_2)].

5.3.1 Phase-control by Varying the Deposition Temperature

The effect of deposition temperature on the niobium sulfide (NbS_x) film growth was studied using the type 1 ALD process by varying the deposition temperature between 200 °C and 450 °C. The thickness as a function of the number of ALD cycles was measured using *in-situ* SE, see Figure 5.1b. A linear increase in thickness with the number of ALD cycles was observed for all the investigated temperatures indicating typical ALD growth. The growth per cycle (GPC) was calculated by taking a slope over the linear region between 50 and 100 cycles in Figure 5.1b. An increase in GPC was observed with deposition temperature changing from 1.38 Å at 200 °C to 3.17 Å at 450 °C, see also Table 5.1. A significant increase in GPC was observed with temperature from ~1.7 Å at 350 °C to ~2.5 Å at 400 °C. Such significant variation in GPC could be explained by the change in material phase (from NbS_3 to NbS_2) and/or film properties, such as morphology[33,39].

Raman spectroscopy revealed a change of vibration peaks for the films as a function of the deposition temperature, indicating a change in material phase, see Figure 5.1c. For the films deposited below 350 °C, three vibrational peaks around 195, 320, and 530 cm^{-1} were observed. These three vibrational peaks correspond to the ν(Nb-S_2), ν(Nb-S_1), and ν(S-S)[2] Raman modes of NbS_3[40]. However, increasing the deposition temperature to 350°C reveals two additional peaks: around 270 and 380 cm^{-1}. These belong to the E_1 and A_1 Raman vibration modes of 3*R*-NbS_2[41]. With a further increase in deposition temperature above 350 °C, the three peaks corresponding to NbS_3 disappeared. Thus, Raman spectroscopy confirms the preparation of NbS_3 below 350 °C, and 3*R*-NbS_2 above 350 °C, while at 350 °C mixed-phase containing both the NbS_3 and NbS_2 were obtained. This change in material phase from NbS_3 to NbS_2 could contribute to the observed increase in GPC between 350 °C and 400 °C, as shown in Figure 5.1b.

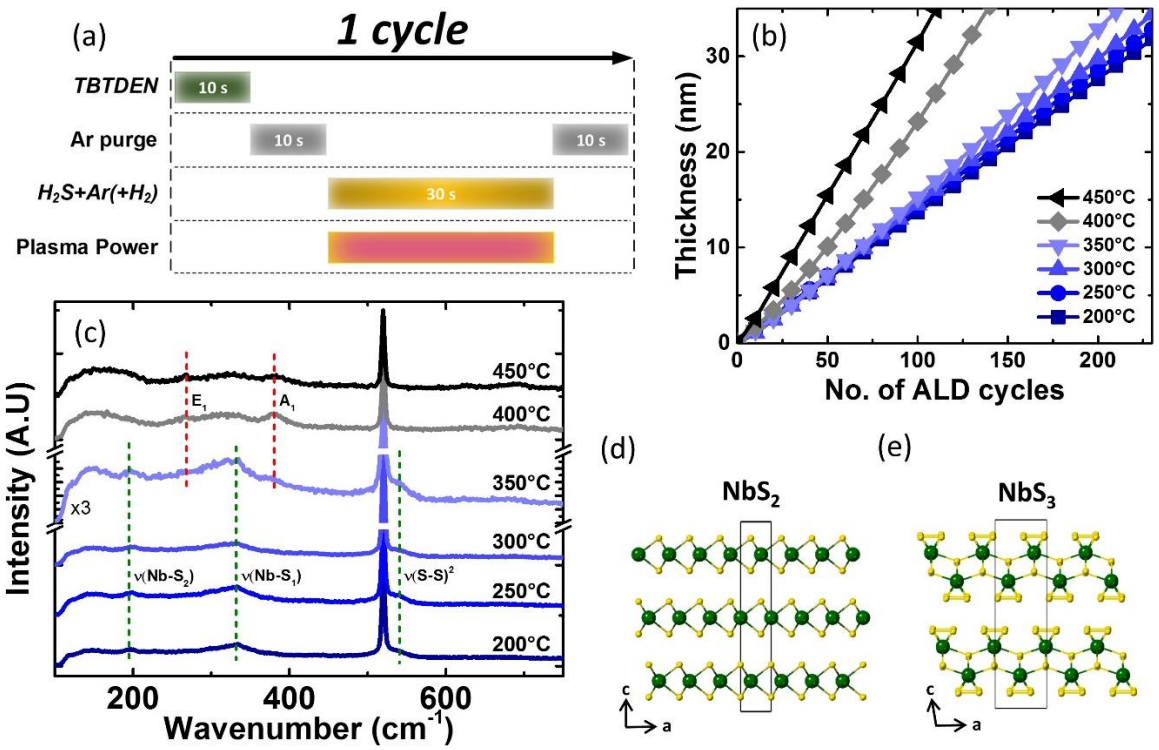

Figure 5.1 (a) Schematic of one complete PE-ALD cycle for the synthesis of NbS_x thin films. (b) Film thickness as a function of the number of ALD cycles for deposition temperatures between 200 °C and 450 °C (type 1 ALD process). (c) Raman spectra of the films deposited between 200 °C and 450 °C (the 350 °C spectrum has been magnified 3 times as indicated). The dashed lines correspond to the vibrational modes of both NbS_2 (green) and NbS_3 (red). (d) and (e) The NbS_2 and NbS_3 crystal structures, respectively, when viewed down the b-axis. The rectangles indicate the unit cells.

To further study the observed material variation as a function of the deposition temperature, we turned to XPS to explore the binding environments and valence band of the deposited films. The S2p spectra for the films deposited below 350 °C (see Figure 5.2a) contain two doublets: one at 161.3 / 162.4 eV, and the other at 162.6 / 163.8 eV (indicated with green dotted lines). As can be deduced from other TMTCs reported in the literature[42], the lower energy doublet corresponds to the $S2p_{3/2}$ and $S2p_{1/2}$ spin-orbit doublets of isolated S^{2-} species, while the higher energy doublet corresponds to the spin-orbit doublets of a $(S_2)^{2-}$ species (also known as S–S pair). For below 350 °C spectra, the fitted peak area ratio of $(S_2)^{2-}$:S^{2-} was calculated to be ~2.2:1. This nearly 2:1 ratio of $(S_2)^{2-}$:S^{2-} is consistent with the NbS_3 structure $[Nb^{4+}(S_2)^{2-}S^{2-}]$, where the $(S_2)^{2-}$ (S-S pair) to S^{2-} ratio is 2:1. The over-stoichiometric ratio 2.2:1 indicates the presence of some excess $(S_2)^{2-}$ species in the film. Contrary to the films deposited below 350 °C, only one doublet with peaks at 160.8 and 161.9 eV (indicated with red dotted lines) was observed for films deposited above 350 °C.

This doublet corresponds to the $S2p_{3/2}$ and $S2p_{1/2}$ spin-orbit doublets of an isolated S^{2-} species. The presence of only this type of S species indicates the deposition of NbS_2. The shoulder observed around ~162.8 eV could be due to excess S (as will be discussed using RBS data). The peaks of the S^{2-} species in NbS_2 were observed to be shifted by ~0.5 eV towards lower binding energy in comparison to that of NbS_3. Consistent with the Raman observation, for 350 °C film, a mixed-phase was observed, as it contains two S doublets indicating the presence of NbS_3 and also a peak shift of ~0.5 eV towards the lower binding energy as observed for NbS_2.

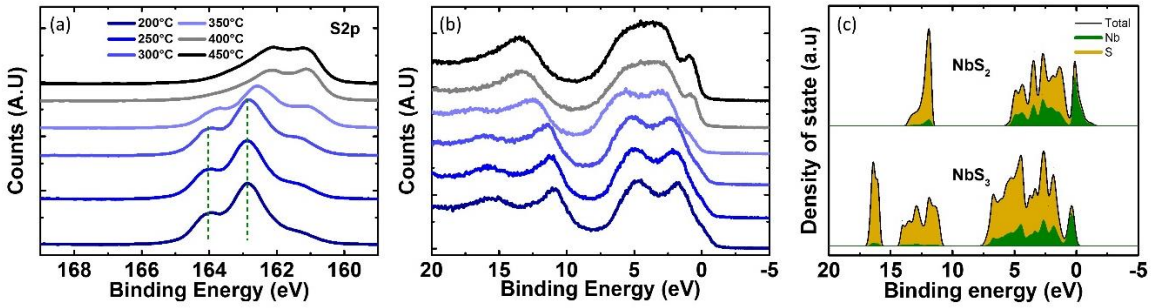

Figure 5.2 (a) S2p XPS spectra of the PE-ALD (type 1 ALD process) grown NbS_x films at deposition temperatures between 200 °C and 450 °C. Dotted lines indicate the fitted peak position of the doublets corresponding to S^{2-} and $(S_2)^{2-}$ species. (b XPS valence band spectra of the films grown at various deposition temperatures. (c) DFT simulated valence band spectra using the crystal structure parameters of NbS_2 and NbS_3.

Following the binding environment studies using XPS, valence band spectra of the deposited NbS_x films were also investigated, see Figure 5.2b. For films deposited below 350 °C, four broad peaks centered around 2, 5, 11, and 16 eV were observed, while for above 350 °C case, three broad peaks centered around 1, 4 and 13 eV were observed. To understand this difference, the valence band spectra (density of states below the Fermi level) of both NbS_2 and NbS_3 were calculated by DFT, see Figure 5.2c. The major difference between NbS_2 and NbS_3 based on DFT calculated valence band spectra is the split in the density of states between 10 and 17 eV for NbS_3 in comparison to NbS_2. A similar trend was observed in the experimental valence band spectra. As shown in Figure 5.2c, most of the density of states observed between 10 and 17 eV were contributions from S atoms. Similar phenomena have been observed previously for the TiS_2/TiS_3 system[42], where valence band spectra split in TiS_3 due to hybridization by excess S–S pairs. Similar to TiS_3, NbS_3 also has excess S-S pairs as compared to NbS_2. Therefore, such a split in NbS_3 spectra in comparison to NbS_2 can be associated with hybridization by excess S–S pairs.

Table 5.1 Results of the *In-situ* SE (GPC), RBS (S/Nb ratio), ERD (H concentration), four-point probe (resistivity), and Hall (mobility and carrier concentration) measurements for the obtained PE-ALD NbS_x films at deposition temperatures between 200 and 450 °C with various coreactant H_2S+Ar+H_2 plasma gas mixtures (in sccm). All films were ~30 nm thick, see Figure 5.1b and 5.3a.

Coreactant [H_2S+H_2+Ar] (sccm)*	T (°C)	GPC (Å)	S/Nb	H (at.%)	σ (μΩ-cm)	Hall mobility ($cm^2V^{-1}s^{-1}$)	Carrier-concentration (cm^{-3})
10+0+40	200	1.38	-	-	x	x	x
	250	1.42	-	-	1.6 E^{+9}	x	x
	300	1.51	3.4	5.9	3.6 E^{+8}	x	x
	350	1.71	-	-	5.6 E^{+6}	x	x
	400	2.47	-	-	1.3 E^{+3}	0.7	9.9 E^{+21}
	450	3.17	2.2	5.9	1.1 E^{+3}	1.4	5.3 E^{+21}
8+2+40	300	1.61	-	-	1.5 E^{+8}	x	x
5+5+40	300	2.51	2.3	3.6	2.5 E^{+3}	0.2	1.0 E^{+22}
Typical Error		±0.03	±0.1	±0.1			

"-" no data
"x" below the detection limit
"*" flow of individual gases in sccm

The composition and purity of the deposited NbS_x films were quantified using RBS measurements (Table 5.1). The S/Nb ratio was calculated to be 3.4 for the films deposited at 300 °C indicating NbS_3 growth with some excess S, while the S/Nb ratio of 2.2 for the film deposited at 450 °C indicates NbS_2 growth with some excess of S. A similar observation on excess S in both NbS_3 and NbS_2 preparation was also made by the XPS in the S2p spectrum, see Figure 5.2a. Contaminants such as C and O were detected only on the surface (similar to XPS) due to exposure of the films to ambient conditions, underlining a high quality of the synthesized films. Additionally, ERD measurements revealed 4–6 at.% of H, which could be from the plasma coreactant and/or precursor ligands.

Summarizing, in addition to our previous work on the phase-controlled synthesis of TiS_3 and TiS_2 by ALD[33] (see Chapter 3), the results presented above show that phase-control by ALD can be expanded to group V transition metal chalcogenides.

5.3.2 Phase-control by Varying the Coreactant Composition

As mentioned earlier, an alternative way to achieve phase-control between TMTC and TMDC at a constant synthesis temperature could be by varying the chalcogenide (sulfur precursor) concentration with respect to the transition metal (Niobium) precursor[32]. Above, in the temperature variation study, at a deposition temperature of 300 °C, NbS_3 was obtained using H_2S:Ar (type 1 ALD process) as a plasma coreactant. To achieve NbS_2 growth at 300 °C, the effect of plasma coreactant composition on the material phase/composition was studied by adding H_2 (type 2 ALD process) to the H_2S:Ar gas mixture. The H_2S:H_2 ratio was varied from 10:0 to 5:5 (in sccm) while maintaining a total flow of 10 sccm with respect to a constant Ar flow of 40 sccm. Three H_2S:H_2 flow ratios (10:0, 8:2, and 5:5 sccm) were chosen as plasma coreactant. In all cases, a film of ~30 nm of NbS_x was deposited. The film thickness as a function of the number of ALD cycles was again monitored with *in-situ* SE (see Figure 5.3a); above 70 ALD cycles, a linear growth trend was observed for all three gas mixture conditions. A substantial increase in GPC was observed from 1.51 to 2.51 Å when reducing the H_2S flow (and increasing the H_2 flow), see Table 5.1. The GPC increased significantly from 1.60 Å for the 8:2 gas mixture to 2.51 Å for the 5:5 gas mixture. Interestingly, this increase in GPC is similar to the increment observed during the temperature variation study, and such a change in GPC could be due to a change in material phase (between NbS_3 and NbS_2) and/or other film properties.

A change in material phase from NbS_3 to NbS_2 was observed upon a change in coreactant plasma composition, as revealed by Raman spectroscopy, see Figure 5.3b. Like the film with 10:0 ratio (300 °C in Figure 5.1c), the Raman spectrum of the film deposited with 8:2 gas ratio contained three vibrational peaks around 195, 320, and 530 cm^{-1} corresponding to the $\nu(Nb\text{-}S_2)$, $\nu(Nb\text{-}S_1)$, and $\nu(S\text{-}S)^2$ Raman modes of NbS_3. Contrarily, for the 5:5 ratio case, only two vibration peaks at ~270 and 380 cm^{-1} were observed, similar to the Raman spectrum obtained at high processing temperatures (400 and 450 °C in Figure 5.1c), which correspond to E_1 and A_1 Raman vibration modes of 3R-NbS_2. Thus, we have demonstrated that a significant change in H_2S:H_2 flow mixture enabled a phase-change from NbS_3 to NbS_2 by PE-ALD at a constant temperature.

Similar to the temperature variation study, using XPS, the effect of coreactant plasma composition on the deposited film´s binding environments and valence band of the deposited films was investigated. The S2p spectra of the 8:2 case (see Figure 5.3c) contain two doublets like for the 10:0 case (300 °C in Figure 5.2a): one at 161.3/ 162.4 eV, and the

other at 162.6/ 163.8 eV (green dotted lines, indicating NbS_3 growth, while only one doublet was observed for films deposited for the 5:5 case, confirming NbS_2 growth with some excess S. This is consistent with the RBS Nb/S ratio of 2.3 (see Table 5.1). Additionally, the XPS valence band spectra for 8:2 film show agreement with the 10:0 film, with four broad peaks centered around 2, 5, 11, and 16 eV (Figure 5.3d). For the 5:5 film, three broad peaks centered around 1, 4, and 13 eV were observed, indicating the deposition of NbS_2.

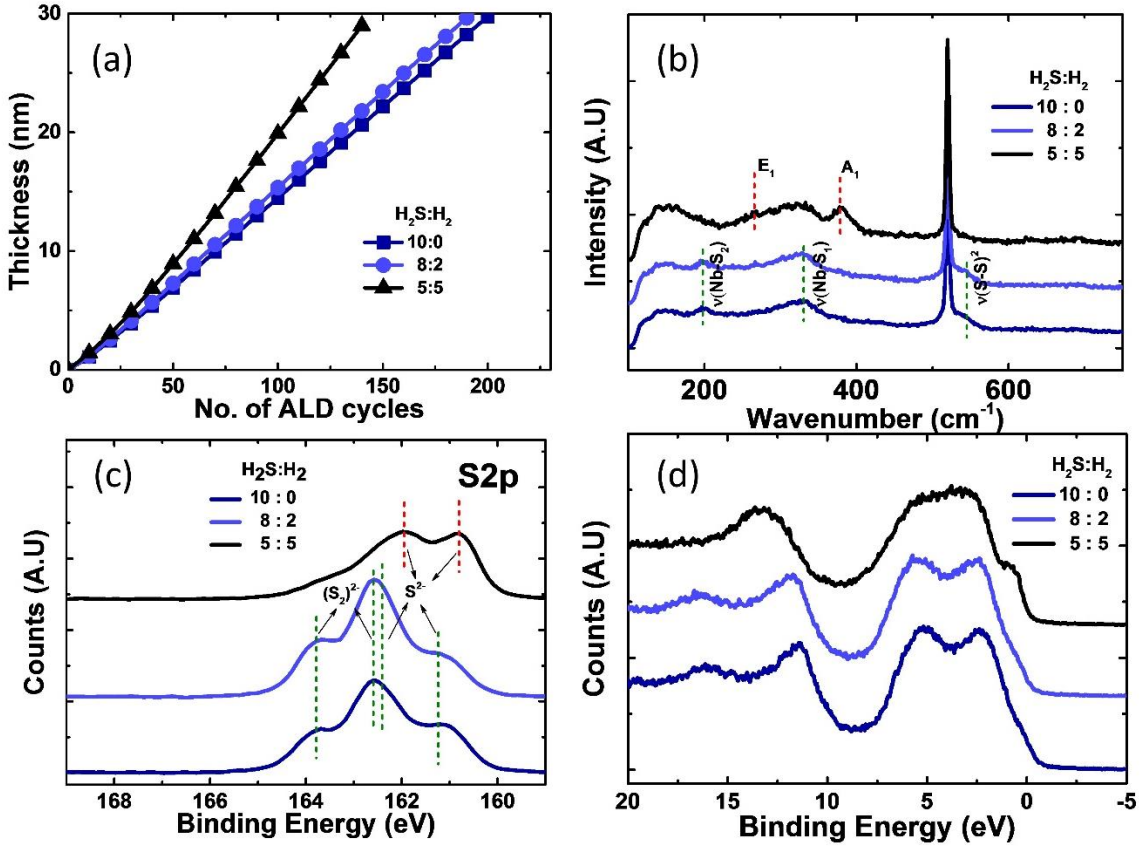

Figure 5.3 The coreactant plasma composition study with three H_2S:H_2 flow mixtures (type 2 ALD process) of 10:0 (blue), 8:2 (light blue) and 5:5 (black) at a deposition temperature of 300 °C. (a) Film thickness as a function of the number of ALD cycles for the three H_2S:H_2 plasma coreactant flow mixtures. The corresponding (b) Raman spectra, (c) S2p XPS spectra, and (e) XPS valence band spectra. Dotted lines in (b) indicate the Raman vibration modes of NbS_2 (red) and NbS_3 (green), and in (c) indicate the fitted peak position of the doublets corresponding to S^{2-} and $(S_2)^{2-}$ species.

To get more insights into the role of the coreactant plasma composition on the phase-control between NbS_3 and NbS_2, OES was performed to investigate the composition of S and H species in the various plasmas. The OES spectrum was measured for all three H_2S:H_2:Ar flow ratios, see Figure A5.2a. In the OES spectra, as expected, the intensity of the

S-containing species (mainly S_2, with peaks between 280 and 610 nm) decreases with the decrease in the flow of H_2S in the H_2S:H_2 mixture, while the intensity of the excited H-containing species such as H_β (at around 486 nm) and H_α (at around 566 nm) increases with respect to Ar. There is a clear correlation between the ratio of S:H species present in the plasma and the transformation from NbS_3 to NbS_2. However, the transformation might be due to a decrease in the concentration of S species or an increase in H species. Therefore, to get more insight into the independent roles of S and H species in obtaining NbS_2 growth, an additional film deposition was performed. For the additional deposition, H_2S flow of 5 sccm was used (like for the 5:5 case), but without the flow of H_2 to the flow mixture. So, to sustain a total flow of 50 sccm, the Ar flow was maintained at 45 sccm. The resulting film was NbS_3, as concluded by Raman spectroscopy and XPS (data not shown). This indicates that in the case of the 5:5 film, the addition of 5 sccm of H_2 to the flow mixture contributed to form a reduction atmosphere, which led to the synthesis of NbS_2 at 300 °C. Thus, the addition of H_2 plays a significant role in the phase change from NbS_3 to NbS_2 at a constant deposition temperature of 300 °C.

5.3.3 Structural and Electrical Properties of the Two Phases

The crystallinity and morphology of the deposited NbS_x films were examined by GI-XRD and SEM, respectively, see Figure 5.4a. In both temperature and coreactant plasma composition variation studies, no distinct peaks were observed in the GI-XRD pattern for all the films deposited with the stoichiometry and XPS and Raman response of a NbS_3 phase, indicating the formation of amorphous films. In the case of films with the NbS_2 phase, a strong peak around 15° 2θ was observed, indicating a crystalline and textured film. The peak corresponds to the (003) reflection of 3R-NbS_2 (green dotted line). Top-view SEM images from Figure 5.4(c-e) show that the NbS_3 film deposited at 300 °C (10:0 case) has no significant surface topography, while the NbS_2 films deposited at 300 °C (5:5 case) and 450 °C (10:0 case) shows the rough surface structure of a polycrystalline film, which is consistent with the GI-XRD pattern indicating the crystalline nature of the NbS_2 films. In addition to the phase transition from NbS_3 to NbS_2, the change in the crystallinity and morphology of the films could also play a role in the observed increase in GPC during both the temperature variation and plasma coreactant composition studies, as shown in Table 5.1. A similar correlation between the crystallinity, surface morphology, and increasing GPC with deposition temperature was previously observed for PE-ALD of MoO_3, where an increased GPC was associated with crystallinity and an increase in precursor adsorption caused by increased surface roughness and/or surface reactivity[43]. Thus, the transition from

amorphous NbS_3 to polycrystalline NbS_2 growth by the appearance of grains with the rough surface could lead to an increment in surface area, leading to an increase in GPC.

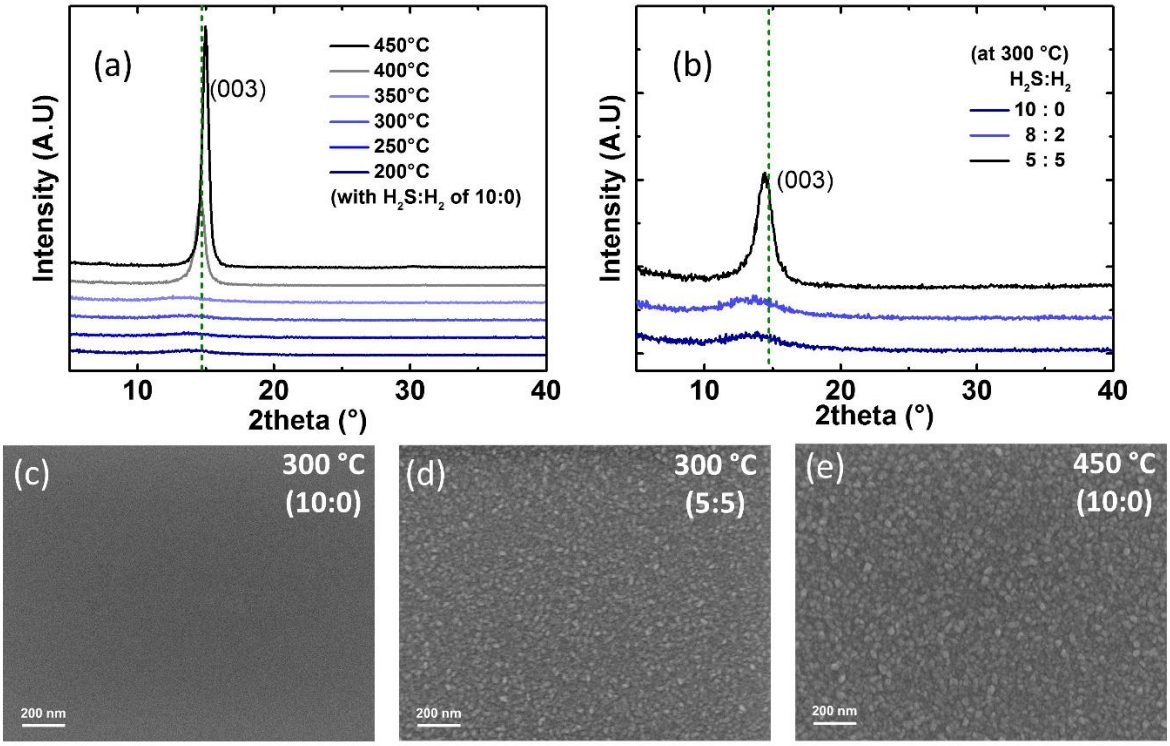

Figure 5.4 GI-XRD patterns of NbS_x films grown (a) at various temperatures between 200 °C and 450 °C, (b) at different plasma coreactant composition at a deposition temperature of 300 °C. The peaks position corresponding to (003) plane is mentioned by a green dotted line. Top-view SEM images of NbS_x films deposited at (c) 300 °C with H_2S:H_2 flow mixture of 10:0, (d) 300 °C with 5:5 flow mixture, and (e) 450 °C with 10:0 flow mixture, respectively.

The influence of the material phase (NbS_3 *vs*. NbS_2) on electrical properties such as resistivity, mobility, and carrier concentration were also studied. At room temperature, the resistivity was measured using the four-point probe method, whereas the charge carrier mobility and carrier concentration were measured using the Hall-effect method, see Table 5.1. The resistivities of the NbS_3 films were above 10^8 μΩ-cm, while the resistivities of the NbS_2 films were around 1-3x10^3 μΩ-cm. This difference in resistivity is consistent with values reported in the literature, for 3R-NbS_2: ~3x10^3 μΩ-cm[44] and for semiconducting NbS_3: ~10^9 μΩ-cm[31]. Hall-effect measurements were conducted only on the NbS_2 films as the NbS_3 films were too resistive. The NbS_2 films were all p-type with hole mobilities between 0.2–1.4 $cm^2V^{-1}s^{-1}$ depending on the deposition temperature and coreactant composition, see Table 5.1. The measured carrier concentrations of the films were around 5–10x10^{21} cm^{-3}.

Similarly, in the literature, NbS_2 has also been observed to have p-type carriers with a hole mobility of 1–3 $cm^2V^{-1}s^{-1}$ [45,46].

5.3.4 NbS_2-NbS_3 Heterostructure Formation

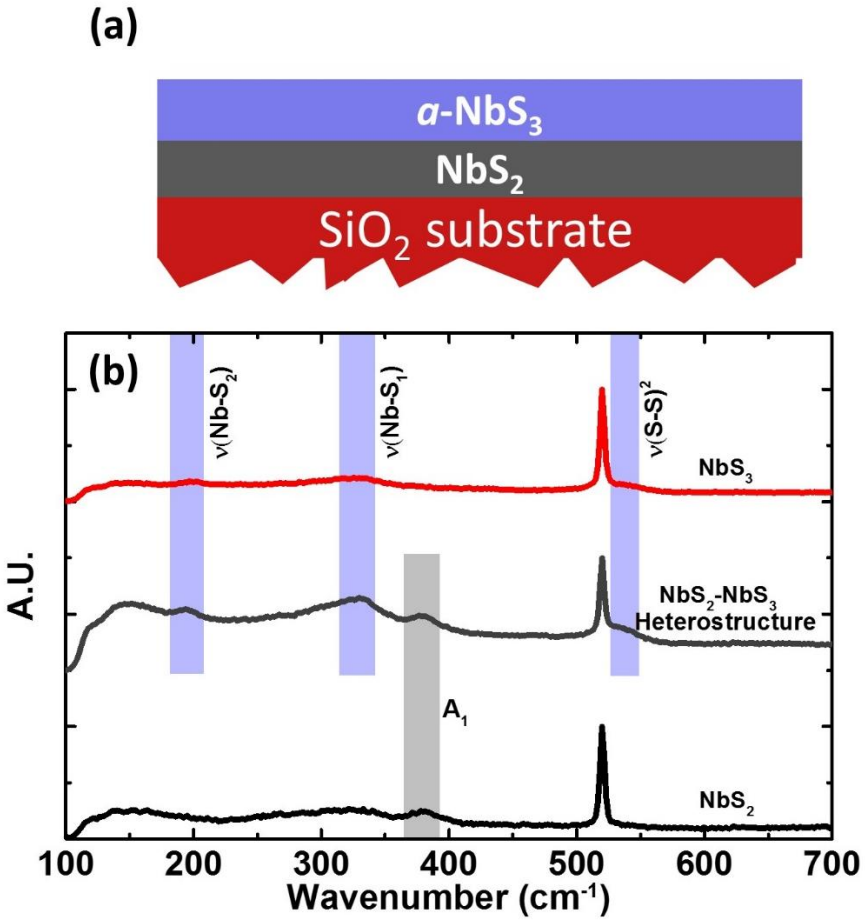

Figure 5.5 (a) Illustration of the NbS_2-NbS_3 heterostructure deposited at 300 °C. (b) Comparison of the Raman spectra of NbS_2 (black), and NbS_3 (red) films with the deposited NbS_2-NbS_3 heterostructure (grey).

A NbS_2-NbS_3 vertical heterostructure was synthesized *in-situ* at 300 °C, as shown in Figure 5.5a to demonstrate the phase control that can be achieved with our ALD process. First, NbS_2 was deposited on the substrate using the 5:5 (H_2S:H_2) type 2 ALD process, as described above. After the NbS_2 deposition for 100 ALD cycles, the coreactant plasma composition was switched to 10:0 (H_2S:H_2) flow mixture to deposit NbS_3 on top of the deposited NbS_2. The NbS_3 was deposited for 400 ALD cycles. The Raman spectrum of the as-deposited film shown in Figure 5.5b (grey) has four broad vibrational peaks at 195, 320, 380, and 530 cm^{-1}. The three peaks at 195, 320, and 530 cm^{-1} correspond to the v(Nb-S_2), v(Nb-S_1), and v(S-

S)[2] Raman modes of NbS_3, while the fourth peak at 380 cm^{-1} corresponds to the A_1 Raman mode of 3R-NbS_2. Thus, indicating the presence of both the NbS_2 and NbS_3 phase in the heterostructure.

A cross-section transmission electron microscopy (TEM) study was performed to confirm the NbS_2-NbS_3 heterostructure formation. The cross-section HAADF-STEM image in Figure 5.6a reveals a clear difference in contrast between NbS_2 and NbS_3 layers in the synthesized heterostructure. The corresponding EDX elemental mappings of Nb, S, and O are shown in Figure 5.6(b-d). The Nb and O EDX mappings show the surface oxidation of the top NbS_3 layer, which could be due to post-deposition exposure to the ambient environment or the deposition of the protective SiO_2 layer on the top prior to FIB sample preparation of the TEM sample. The EDX mapping of both Nb and S shows a clear difference in their elemental counts between NbS_2 and NbS_3 layers with a sharp interface. From the structural formula, it follows that NbS_2 has a larger Nb:S ratio than NbS_3. The EDX mapping shows relatively more Nb counts in the bottom NbS_2 layer, and relatively more S content in the top NbS_3 layer, confirming the synthesis of the NbS_2-NbS_3 vertical heterostructure by ALD at a constant deposition temperature of 300 °C. In conclusion, by modulating the H_2S:H_2 flow mixture at a constant temperature, the NbS_2-NbS_3 vertical heterostructure has been successfully synthesized.

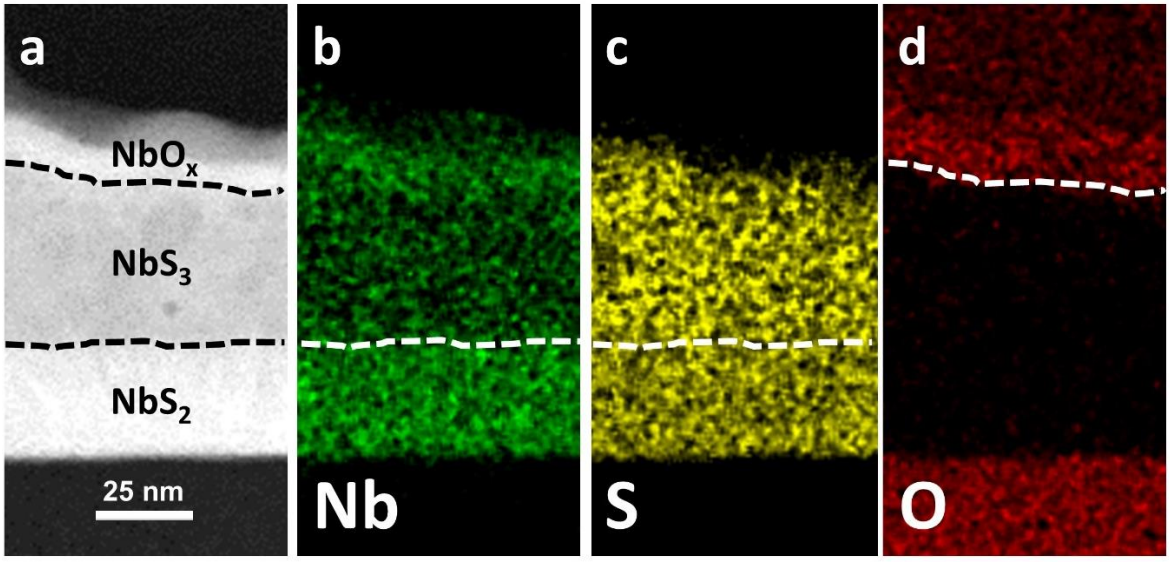

Figure 5.6 (a) HAADF-STEM image showing a cross-section of the deposited NbS_2-NbS_3 heterostructure with corresponding EDX elemental mappings of (b-d) Nb, S, and O, respectively.

5.4 Conclusions and Outlook

The phase-controlled synthesis of NbS_2 and NbS_3 was successfully achieved by PE-ALD at low-temperature. The phase-control between the two material phases was obtained by varying the deposition temperature and the coreactant plasma composition. When the temperature was varied, amorphous NbS_3 growth was observed below 350 °C, while above this temperature, polycrystalline NbS_2 was obtained. When the coreactant plasma composition was varied at 300 °C, a phase transition from NbS_3 to NbS_2 was achieved by adding H_2 to the plasma, which contributed to a reducing atmosphere. Using this coreactant modulation at 300 °C, NbS_2-NbS_3 vertical heterostructures were successfully prepared.

For the successful application of these heterostructures in devices, the amorphous NbS_3 phase could be annealed in an excess sulfur atmosphere wherein the film can undergo crystallization. While doing so, to obtain well defined interfaces, care should be taken to prevent intermixing at the interface. The ability to grow (poly)crystalline metal-semiconductor heterostructures with analogous elements could enable further improvement of the device performance. This work could open new avenues for the synthesis of other TMDCs, TMTCs, and their heterostructures for (opto)electronic applications.

Acknowledgments

The authors acknowledge Jeroen van Gerwen, Martijn G. Dijstelbloem, and Cristian van Helvoirt for their technical assistance and valuable suggestions. Dr. Beatriz Barcones is acknowledged for the FIB preparation of the TEM sample. Solliance and the Dutch province of Noord-Brabant are acknowledged for funding the TEM facility. This work was supported by the European Research Council (Grant Agreement No. 648787).

References

[1] S. Das, J.A. Robinson, M. Dubey, H. Terrones, and M. Terrones, Annu. Rev. Mater. Res. **45**, 1 (2015).

[2] M. Chhowalla, H.S. Shin, G. Eda, L. Li, K.P. Loh, and H. Zhang, Nat. Chem. **5**, 263 (2013).

[3] J.O. Island, A.J. Molina-Mendoza, M. Barawi, R. Biele, E. Flores, J.M. Clamagirand, J.R. Ares, C. Sánchez, H.S.J. van der Zant, R. D'Agosta, I.J. Ferrer, and A. Castellanos-Gomez, 2D Mater. **4**, 022003 (2017).

[4] A. Khatibi, R.H. Godiksen, S.B. Basuvalingam, D. Pellegrino, A.A. Bol, B. Shokri, and A.G. Curto, 2D Mater. **7**, 015022 (2019).

[5] J. Dai, M. Li, and X.C. Zeng, Wiley Interdiscip. Rev. Comput. Mol. Sci. **6**, 211 (2016).

[6] R. Kappera, D. Voiry, S.E. Yalcin, B. Branch, G. Gupta, A.D. Mohite, and M. Chhowalla, Nat. Mater. **13**, 1128 (2014).

[7] Y. Liu, P. Stradins, and S.-H. Wei, Sci. Adv. **2**, e1600069 (2016).

[8] Y. Liu, N.O. Weiss, X. Duan, H.-C. Cheng, Y. Huang, and X. Duan, Nat. Rev. Mater. **1**, 16042 (2016).

[9] J. Liu, Y. Guo, F.Q. Wang, and Q. Wang, Nanoscale **10**, 807 (2018).

[10] Z.-L. Liu, L.-C. Cai, and X.-L. Zhang, J. Alloys Compd. **610**, 472 (2014).

[11] Y. Wang, J.C. Kim, R.J. Wu, J. Martinez, X. Song, J. Yang, F. Zhao, A. Mkhoyan, H.Y. Jeong, and M. Chhowalla, Nature **568**, 70 (2019).

[12] Y. Choi, H. Bark, B. Kang, M. Lee, B. Kim, S. Lee, C. Lee, and J.H. Cho, J. Mater. Chem. C **7**, 8599 (2019).

[13] H. Bark, Y. Choi, J. Jung, J.H. Kim, H. Kwon, J. Lee, Z. Lee, J.H. Cho, and C. Lee, Nanoscale **10**, 1056 (2018).

[14] Y. Liu, J. Wu, K.P. Hackenberg, J. Zhang, Y.M. Wang, Y. Yang, K. Keyshar, J. Gu, T. Ogitsu, R. Vajtai, J. Lou, P.M. Ajayan, B.C. Wood, and B.I. Yakobson, Nat. Energy **2**, 17127 (2017).

[15] J. Zhang, J. Wu, X. Zou, K. Hackenberg, W. Zhou, W. Chen, J. Yuan, K. Keyshar, G. Gupta, A. Mohite, P.M. Ajayan, and J. Lou, Mater. Today **25**, 28 (2019).

[16] J. Yang, A.R. Mohmad, Y. Wang, R. Fullon, X. Song, F. Zhao, I. Bozkurt, M. Augustin, E.J.G. Santos, H.S. Shin, W. Zhang, D. Voiry, H.Y. Jeong, and M. Chhowalla, Nat. Mater. (2019).

[17] C.J. Carmalt, T.D. Manning, I.P. Parkin, E.S. Peters, and A.L. Hector, J. Mater. Chem. **14**, 290 (2004).

[18] C. Carmalt, E. Peters, I. Parkin, T. Manning, and A. Hector, Eur. J. Inorg. Chem. **2004**, 4470 (2004).

[19] W. Ge, K. Kawahara, M. Tsuji, and H. Ago, Nanoscale **5**, 5773 (2013).

[20] X. Wang, J. Lin, Y. Zhu, C. Luo, K. Suenaga, C. Cai, and L. Xie, Nanoscale **9**, 16607 (2017).

[21] Y.-P. Chang, A.L. Hector, W. Levason, and G. Reid, Dalt. Trans. **46**, 9824 (2017).

[22] Z. Li, W. Yang, Y. Losovyj, J. Chen, E. Xu, H. Liu, M. Werbianskyj, H.A. Fertig, X. Ye, and S. Zhang, Nano Res. **11**, 5978 (2018).

[23] A. Kozhakhmetov, T.H. Choudhury, Z.Y. Al Balushi, M. Chubarov, and J.M. Redwing, J. Cryst. Growth **486**, 137 (2018).

[24] W.G. Fisher and M.J. Sienko, Inorg. Chem. **19**, 39 (1980).

[25] M.A. Sriram, K.S. Weil, and P.N. Kumta, Appl. Organomet. Chem. **11**, 163 (1997).

[26] J. Kwak, S. Jung, N. Lee, K. Thiyagarajan, J.K. Kim, A. Giri, and U. Jeong, J. Mater. Chem. C **6**, 11303 (2018).

[27] S.G. Zybtsev, V.Y. Pokrovskii, V.F. Nasretdinova, S. V. Zaitsev-Zotov, V. V. Pavlovskiy, A.B. Odobesco, W.W. Pai, M.-W. Chu, Y.G. Lin, E. Zupanič, H.J.P. van Midden, S. Šturm, E. Tchernychova, A. Prodan, J.C. Bennett, I.R. Mukhamedshin, O. V. Chernysheva, A.P. Menushenkov, V.B. Loginov, B.A. Loginov, A.N. Titov, and M. Abdel-Hafiez, Phys. Rev. B **95**, 035110 (2017).

[28] V.E. Fedorov, S.B. Artemkina, E.D. Grayfer, N.G. Naumov, Y. V. Mironov, A.I. Bulavchenko, V.I. Zaikovskii, I. V. Antonova, A.I. Komonov, and M. V. Medvedev, J. Mater. Chem. C **2**, 5479 (2014).

[29] M.A. Bloodgood, P. Wei, E. Aytan, K.N. Bozhilov, A.A. Balandin, and T.T. Salguero, APL Mater. **6**, 026602 (2018).

[30] S.G. Zybtsev, V.Y. Pokrovskii, V.F. Nasretdinova, and S. V. Zaitsev-Zotov, Phys. B Condens. Matter **407**, 1696 (2012).

[31] S. Kikkawa, N. Ogawa, M. Koizumi, and Y. Onuki, J. Solid State Chem. **41**, 315 (1982).

[32] E. TRONG and M. Huber, COMPTES RENDUS Hebd. DES SEANCES L Acad. DES Sci. Ser. C **268**, 1771 (1969).

[33] S.B. Basuvalingam, Y. Zhang, M.A. Bloodgood, R.H. Godiksen, A.G. Curto, J.P. Hofmann, M.A. Verheijen, W.M.M. Kessels, and A.A. Bol, Chem. Mater. **31**, 9354 (2019).

[34] J.P. Perdew, K. Burke, and M. Ernzerhof, Phys. Rev. Lett. **77**, 3865 (1996).

[35] B. Morosin, Acta Crystallogr. Sect. B Struct. Crystallogr. Cryst. Chem. **30**, 551 (1974).

[36] S. Grimme, J. Antony, S. Ehrlich, and H. Krieg, J. Chem. Phys. **132**, 154104 (2010).

[37] P.E. Blöchl, O. Jepsen, and O.K. Andersen, Phys. Rev. B **49**, 16223 (1994).

[38] S.J. Denholme, P.S. Dobson, J.M.R. Weaver, I. MacLaren, and D.H. Gregory, Int. J. Nanotechnol. **9**, 23 (2012).

[39] A. Sharma, M.A. Verheijen, L. Wu, S. Karwal, V. Vandalon, H.C.M. Knoops, R.S. Sundaram, J.P. Hofmann, W.M.M. (Erwin) Kessels, and A.A. Bol, Nanoscale **10**, 8615 (2018).

[40] C. Sourisseau, R. Cavagnat, M. Fouassier, and P. Maraval, J. Raman Spectrosc. **21**, 337 (1990).

[41] S. Onari, T. Arai, R. Aoki, and S. Nakamura, Solid State Commun. **31**, 577 (1979).

[42] K. Endo, H. Ihara, K. Watanabe, and S. Gonda, J. Solid State Chem. **44**, 268 (1982).

[43] M.F.J. Vos, B. Macco, N.F.W. Thissen, A.A. Bol, and W.M.M. (Erwin) Kessels, J. Vac. Sci. Technol. A Vacuum, Surfaces, Film. **34**, 01A103 (2016).

[44] A. Niazi and A.K. Rastogi, J. Phys. Condens. Matter **13**, 6787 (2001).

[45] M. Naito and S. Tanaka, J. Phys. Soc. Japan **51**, 219 (1982).

[46] R. Yan, G. Khalsa, B.T. Schaefer, A. Jarjour, S. Rouvimov, K.C. Nowack, H.G. Xing, and D. Jena, Appl. Phys. Express **12**, 023008 (2019).

Appendix 5

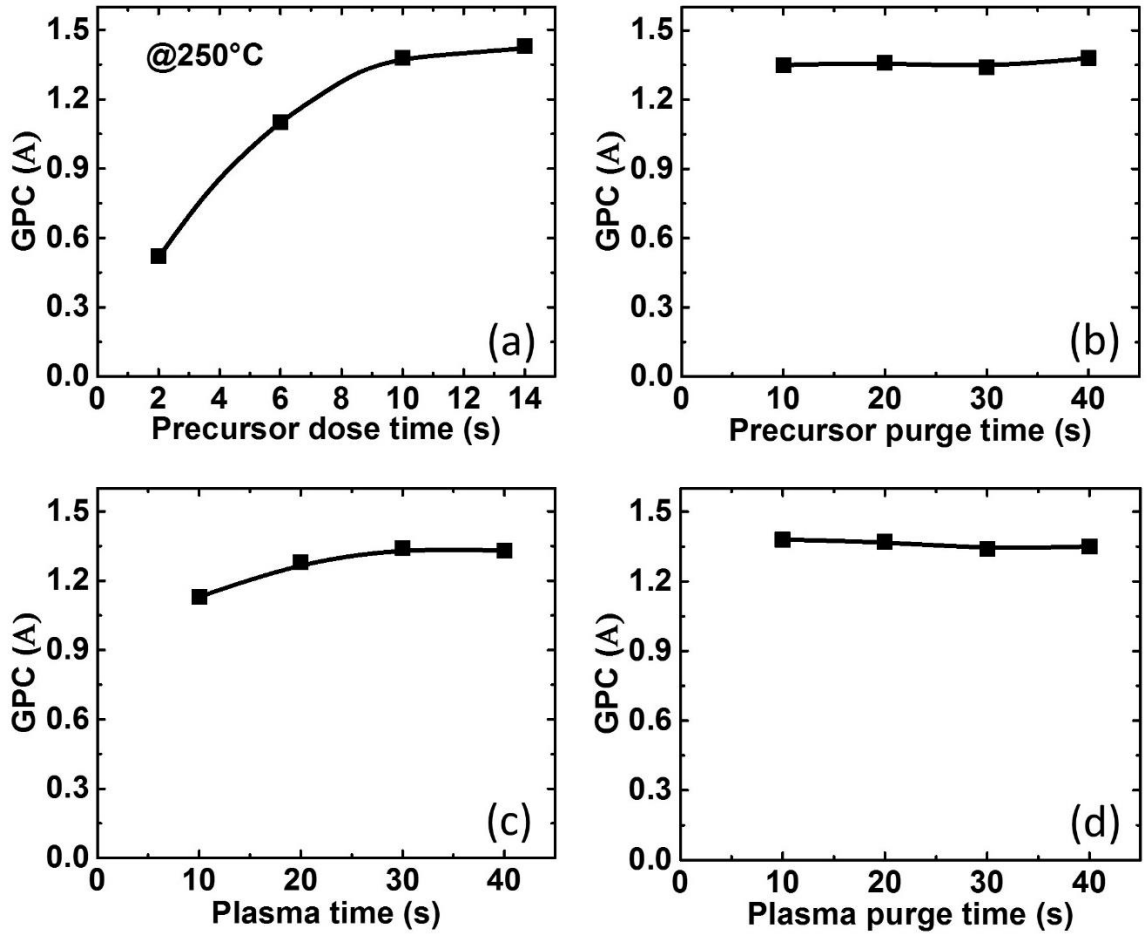

Figure A5.1 Saturation curves: GPC as a function of (a) precursor, (b) precursor purge, (c) plasma, and (d) plasma purge exposure time for PE-ALD type 1 process at 250 °C deposition temperature.

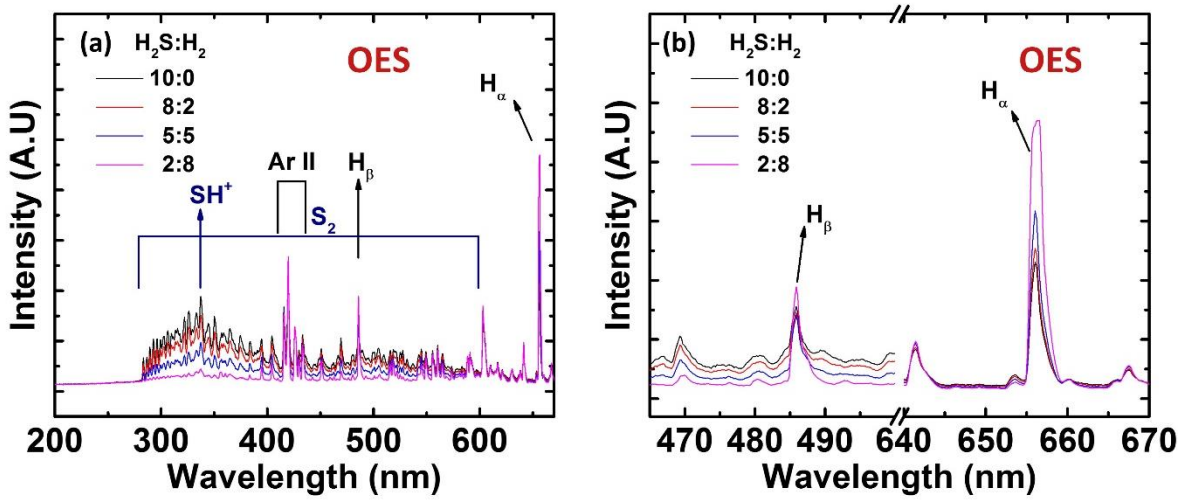

Figure A5.2 (a) OES spectra of the H_2S:H_2:Ar plasma with different H_2S:H_2 flow mixtures while the Ar flow was kept constant at 40 sccm. The spectra were normalized to the Ar II peak at 420 nm. (b) Magnified OES spectra of (a), with magnification to the wavelength range of 465-500 nm and 640-670 nm.

Activity and Stability of NbS_2 Hydrogen Evolution Electrocatalyst Synthesized by Atomic Layer Deposition

6

Recently, metallic group V based transition metal dichalcogenides (TMDCs), such as NbS_2 and TaS_2, have been introduced as new promising alternatives for non-noble metal catalysts to drive the electrocatalytic hydrogen evolution reaction (HER). However, the observed high HER activity was obtained only after an activation process, wherein the TMDC layers were depleted/ exfoliated, thus casting doubts over the long-term stability of the metallic TMDCs. Here, for the first time, NbS_2 fabricated by atomic layer deposition (ALD) is explored as an electrocatalyst for hydrogen evolution. The initial HER performance of the ALD-derived NbS_2 (overpotential of ~500 mV at η_{10}) was comparable to NbS_2 prepared by CVD (chemical vapor deposition) or SSR (solid state reaction) as reported before in the literature. Superior long-term stability over 24 hours (and 10000 LSV cycles) was observed for direct ALD-derived NbS_2 electrodes on glassy carbon and carbon fiber paper substrates, which was caused by strong adhesion of the direct ALD-grown NbS_2 film. Furthermore, direct ALD-derived NbS_2 was introduced as an adhesive buffer layer for sulfurization-derived NbS_2 (from ALD-grown Nb_2O_5) that suffer from preliminary delamination during HER. The adhesive buffer layer mitigated the delamination issue and improving the long-term stability of sulfurization-derived NbS_2. This work shows that ALD is a suitable method to fabricate high-performing NbS_2 electrocatalyst for HER with long-term stability.

Saravana Balaji Basuvalingam, Yue Zhang*, Emiel J. M. Hensen, Wilhelmus M. M. Kessels, Jan P. Hofmann, and Ageeth A. Bol, (to be submitted)*

6.1 Introduction

In the future, renewable energy will play a major role in the transition to a CO_2 neutral energy system. Nevertheless, there are big challenges to efficiently use renewable energy due to the intermittent availability of solar and wind energy, making large scale, efficient storage options indispensable[1,2]. Electrocatalytic water splitting is one of the promising pathways for storing renewable energy. The hydrogen evolution reaction (HER) is the cathodic half-reaction of water splitting, and traditionally noble metals (like platinum) are regarded as a benchmark electrocatalyst for this reaction[3]. However, the amount of noble metal available in nature is insufficient for an industrial scale terawatt level energy conversion. Recently, layered two-dimensional (2D) transition metal dichalcogenides (TMDCs) have gained momentum as alternative electrocatalysts for HER applications[4,5]. Among them, semiconducting TMDCs such as MoS_2 and WS_2 have been the most intensively studied materials, nevertheless, only the metallic edge sites have been found active, while their (00*l*) basal planes are inert[6]. Activating the basal planes could further enhance the HER activity. In the literature, two strategies are generally followed to enable the basal planes. One is the conversion from the semiconducting phase (*e.g.,* 2*H*-MoS_2) to a metallic phase (*e.g.,* 1*T*-MoS_2)[7], and the other is by creating defects on the basal plane known as defect engineering[8]. However, both methods lead or might lead to stability issues due to progressive oxidation and/or unsaturated sulfur species[9,10]. Therefore, significant interest has recently been directed towards the group V metallic TMDCs such as NbS_2[11–13], TaS_2[14,15] and VS_2[16]. In contrast to the semiconducting MoS_2 and WS_2, the key benefits of these metallic TMDCs are easier electron transfer kinetics and intrinsic catalytic activity of the basal planes. According to predictions from DFT calculations, the basal planes of group V metallic TMDCs possess close to thermoneutral Gibbs free energy for H atom adsorption[11–13,15,17].

Lately, among the group V metallic TMDCs, NbS_2 has spurred interest because of its high HER activity. NbS_2 exists in multiple stable metallic phases such as 2*H*, 3*R* and 1*T*[18]. Among those, 3*R* has been the most popular phase for HER studies, see Table 1. In most studies, NbS_2 required an overpotential of ≥500 mV to reach a current density of 10 mA cm^{-2} (η_{10}) during the initial HER cycle, except for non-stoichiometric $Nb_{1+x}S_2$ as well as Li or Pd intercalated NbS_2, which needed only an overpotential between 140 to 240 mV for reaching η_{10}[12,19,20]. With respect to pristine NbS_2, Lou *et al.* reported continuous improvement (decrease) of the overpotential from ~500 mV to as low as 60 mV over 10000 HER cycles to

reach η_{10}[13]. Such superior HER performance was only observed after an activation (so-called self-optimization) process in which the generated H_2 depletes or exfoliates the pristine NbS_2 by breaking the weak van der Waals interaction between the interlayers and as such exposing new active sites for electrocatalytic reaction. On the other hand, the overpotential of pristine NbS_2 has also been reported to decay (increase) over time[20]. This change in overpotential either way indicates poor long-term HER stability of the pristine NbS_2. This stability and the depletion or exfoliation issues of the NbS_2 catalyst cast doubt over their use for practical applications. Therefore, to further explore NbS_2 for HER electrocatalysis, it is vital to address and overcome the poor stability problem.

Table 6.1 HER performance of 3*R*-NbS_2 reported in the literature.

Material	**η_{10} (mV vs. RHE)**	**Tafel slope (mV dec^{-1})**	**Mass loading**	**Ref.**
3R-NbS_2	>500 (initial) / 60 (after 20000 cycles)	211 / 38	10 µg cm^{-2}	13
3R-NbS_2	459*	119	-	20
3R-NbS_2	>>500*	168	-	12
3R-NbS_2	550*	103	-	21
3R-NbS_2	442*	162	0.8 mg cm^{-2}	22
3R-NbS_2	420 (initial) / 200 (after 1000 cycles)	-	-	19
3R-$Nb_{1+x}S_2$	~240*	76	-	12
Li- 3R-NbS_2	140	-	-	19
3R-Pd_xNbS_2	157	50	-	20

η_{10} Overpotential at an HER current density of -10 mA cm^{-2}.
** The cycle number was not mentioned.*

Interestingly, in the literature, the above-mentioned HER stability issues were primarily observed for poorly covered electrodes, synthesized by solid state reaction (SSR) or chemical vapor deposition (CVD) methods (*i.e.,* non-uniform, island-like NbS_2 films) or by exfoliation (*i.e.,* NbS_2 flakes). On the contrary, Zhou *et al.* reported excellent HER stability for direct CVD-grown NbS_2 on glassy carbon substrates with polycrystalline nature and 100% coverage; there, only a 4% decay of the overpotential over 12 hours was observed[23]. Here, we synthesized NbS_2 on glassy carbon and carbon fiber paper substrates using atomic layer deposition (ALD) and investigated it's HER activity and stability. ALD is a variant of CVD, and it is a surface-controlled cyclic process based on self-limiting chemical reactions and can thus form intimate bonding between the deposited film/layers and the substrate. Furthermore, ALD provides benefits such as large-scale coverage with excellent uniformity, conformality, and atomic-level thickness control at relatively low processing temperatures[24]. In addition to the synthesis benefits, in terms of catalysis research, previously, ALD coatings have been shown to suppress leaching or depletion of the catalyst and impart long-term stability[25,26]. So far, to the best of our knowledge, HER activity and stability of ALD-grown group V TMDCs, specifically NbS_2, have yet to be investigated.

In this work, we investigate the HER performance of NbS_2 films synthesized by various (three) ALD-based methods. One of the three reported methods being the indirect ALD-based synthesis process, where the NbS_2 film is prepared by the sulfurization of ALD-prepared Nb_2O_5 films (see Chapter 7) in the H_2S atmosphere at high processing temperature (900 °C). The other two ALD-based methods being the direct growth of NbS_2 films by ALD (direct ALD) at low deposition temperatures (see Chapter 5) and post-deposition annealing of these direct ALD-grown NbS_2 films at high processing temperature (900 °C). The film and material properties of the NbS_2 films fabricated by all three methods are studied and compared, using an array of characterization techniques. Then, the HER performance, such as activity and long-term stability of various NbS_2 electrocatalysts prepared on glassy carbon and carbon fiber paper substrates, is studied. Finally, we investigate the adhesive strength of direct ALD grown NbS_2 film on the glassy carbon substrate using the scotch tape method and demonstrate its impact on long-term HER stability using a stack approach.

6.2 Experimental Section

6.2.1 Film Synthesis

6.2.1.1 Atomic Layer Deposition

Atomic layer deposition (ALD) was employed to deposit both NbS_2 and Nb_2O_5 thin films using an Oxford Instruments Plasma Technology FlexAL ALD reactor. The base pressure of the reactor chamber was 10^{-6} Torr, and the reactor was equipped with a remote inductively coupled plasma source (ICP, 13.56 MHz). The reactor acted as a warm wall reactor as the wall temperature was maintained at 150 °C, while the table temperature was varied according to the requirement between 200, 300 and 450 °C. The metal-organic precursor (tert-butylimido)-tris-(diethylamino)-niobium (TBTDEN) (STREM Chemical, Inc., 98%) was used for both NbS_2 and Nb_2O_5 depositions. The precursor was kept in a stainless-steel bubbler at 65 °C and was bubbled using Ar as the carrier gas. For the NbS_2 deposition, a plasma coreactant using a H_2S:H_2:A_r gas mixture of 5:5:40 or 10:0:40 sccm was employed, while for the Nb_2O_5 deposition, O_2 plasma with a gas flow of 100 sccm was utilized. The NbS_2 by direct ALD was deposited at 300 °C or 450 °C. All the Nb_2O_5 films were deposited at 200 °C. In both processes, the pressure during the precursor and coreactant exposure steps was maintained at 80 and 10 mTorr, respectively. All plasmas were struck with an ICP RF power of 200 W.

Both ALD processes consisted of a TBTDEN precursor dose step followed by a plasma coreactant step, with purge steps between both precursor and coreactant steps to avoid parasitic gas phase CVD reactions. For NbS_2 deposition, the precursor was dosed for 10 s, while the plasma coreactant H_2S:H_2:Ar was dosed for 20 s for both deposition temperatures. In the Nb_2O_5 ALD process, the TBTDEN precursor was dosed for 6 s, while the O_2 plasma coreactant was dosed for 4 s. For more details on ALD process optimization and ALD saturation data for both NbS_2 and Nb_2O_5, see Chapter 5 and 7, respectively[27]. For film and material characterization studies, the thin films were deposited on Si with thermally grown 450 nm of SiO_2. For HER related studies, the films were deposited on polished glassy carbon or carbon fiber paper substrates.

6.2.1.2 Post-annealing and Sulfurization Treatment

Post-annealing of NbS_2 and sulfurization of the ALD-grown Nb_2O_5 (indirect ALD) were performed under similar conditions in a tube furnace using a H_2S:Ar gas mixture with 10% H_2S concentration for 45 min at 900 °C. The substrate with the NbS_2 or Nb_2O_5 film was placed at the center of the tube furnace. The tube was sealed, pumped, and refilled with N_2, and it was repeated for three times to remove O_2 and water from the system. Then, a H_2S:Ar gas mixture (10% H_2S) at a flow of 100 sccm was led into the tube. Meanwhile, the furnace was heated up at a heating rate of 10 °C min^{-1} and kept for 45 min at the target temperature (900 °C). Subsequently, the system was let to cool down naturally to room temperature in an Ar atmosphere at the end of the treatment. Then, the samples were transferred to the glovebox immediately for later characterization and electrochemical measurements.

6.2.2 Material Characterization

Raman spectroscopy was performed with a Renishaw inVia system using a 514 nm excitation laser in ambient conditions. Scanning electron microscopy (SEM) was employed to investigate the surface morphology and grain size of the NbS_2 films. A Zeiss Sigma SEM with an in-lens detector operating at an accelerating voltage of 3 kV was used for SEM studies. X-ray photoelectron spectroscopy (XPS) data were collected on a Thermo Scientific KA1066 spectrometer with monochromatic Al Kα (hv = 1486.6 eV) X-ray radiation to determine the binding environment for the NbS_2 films. Resistivity measurements were performed ex-situ at ambient conditions using a Signatone four-point probe combined with a Keithley 2400 sourcemeter acting both as the current source and voltmeter. The resistivity of the NbS_2 films was determined from the slope of the obtained I-V curves. Inductively Coupled Plasma Optical Emission Spectrometry (ICP-OES) measurements were performed on a SPECTROBLUE EOP spectrometer equipped with an axial plasma source (Ar) to determine the amount of dissolved Nb in the electrolyte. The sample uptake rate was set to 2 ml/min. The emission intensity of Nb ions was measured at 309.4, 269.7 and 295.1 nm.

6.2.3 Electrochemical Measurements

Electrochemical measurements were performed in a three-electrode electrochemical cell with a saturated calomel electrode (SCE) (0.265 V vs. reversible hydrogen electrode (RHE)) as the reference electrode, glassy carbon rod as the counter electrode, and 0.5 M

H_2SO_4 (99.999%, Sigma-Aldrich) as the electrolyte. The electrolyte was prepared with 18 MΩ cm deionized Milli-Q water and purged with N_2 for 30 min to remove O_2 in the solution prior to the measurements. Linear sweep voltammetry (LSV) curves were recorded on a Metrohm Autolab PGSTAT302N potentiostat, and current density values were normalized by geometric area with a rotating rate of 1600 rounds per minutes (rpm). iR-correction (Ohmic drop compensation) (100%) has been done before normalizing the geometric area (geo). AC electrochemical impedance spectroscopy (EIS) (amplitude: 10 mV) was recorded at open circuit potential (OCP) in the frequency range of 10 kHz to 0.1 Hz. Stability tests were conducted by acquiring for 1000 and 10000 LSV cycles at 100 mV/s scan rate with a cathodic voltage limit set to attain a maximum current density of 10 mA/cm^2_{geo} (η_{10}), with a rotating rate of 800 rpm. The total duration of both the dynamic stability test, including activity assessment and other electrochemical measurements, was 1 and 14 hours, respectively. Similarly, chronopotentiometry tests with a current density of 10 mA/cm^2_{geo} were also performed for 24 hours using carbon fiber paper as the substrate. The carbon fiber paper was applied over glassy carbon substrate due to the better hydrophobicity. Also, the parallel-aligned design configuration of the glassy carbon substrate is not suitable to hold for 24 hours at 10 mA/cm^2_{geo} due to its high current and a relatively large amount of H_2 bubble generation. The electrochemical surface area (ECSA) was calculated based on the electrochemical double-layer capacitance (C_{dl}) measurement. For measuring C_{dl} of the samples, the potential was swept with a span of 100 mV and repeated five times at each of six different scan rates (10, 20, 30, 40, 50 and 60 mV/s). The specific capacitance (C_s) was chosen as C_s= 0.015 mF/cm^2 in 0.5 M H_2SO_4 based on reported values[28]. The number of replicates for each experiment was three to five.

6.3 Results and Discussion

6.3.1 Synthesis and Functional Characterization of NbS_2

We fabricated NbS_2 thin films for HER analysis using three ALD-based methods, as shown in Figure 6.1. Different synthesis methods were chosen to study and compare the role of synthesis approach, film and material properties on the HER performance, and to compare with the reported HER performances of the NbS_2 prepared by other synthesis methods in the literature. The thickness of all ALD deposited NbS_2 and Nb_2O_5 films was ~30 nm. In the first method (Figure 6.1a), the NbS_2 film was deposited directly by ALD at 300 °C or 450 °C, using TBTDEN as the niobium precursor and a H_2S:H_2:Ar plasma as the coreactant with a

flow ratio of 10:0:40 or 5:5:40 sccm, respectively. In the second method (Figure 6.1b), NbS_2 films deposited by ALD at 300 or 450 °C (method 1) were annealed at 900 °C for 45 min using 10% H_2S in carrier Ar gas. In the third method, a Nb_2O_5 film was deposited at 200 °C using TBTDEN as the niobium precursor and O_2 plasma as coreactant. This is followed by a sulfurization treatment (see Figure 6.1c) at 900 °C for 45 min using 10% H_2S in Ar to form NbS_2. From now on, NbS_2 films synthesized by method 1, 2 and 3 will be addressed as LT-NbS_2, HT-NbS_2 and Sulfox-NbS_2, respectively.

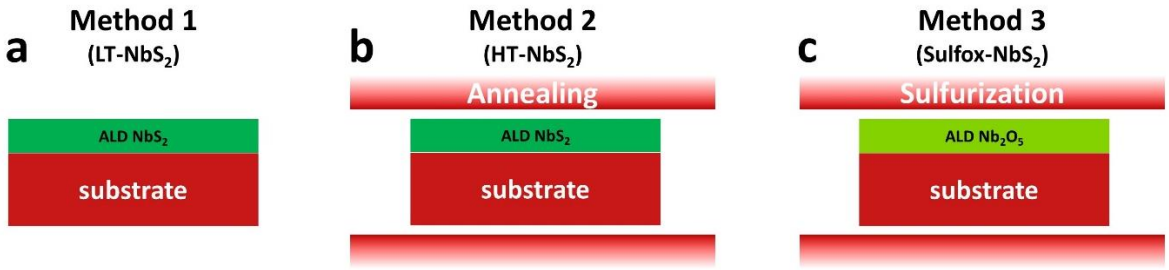

Figure 6.1 Schematic illustration of the three different methods used to synthesize NbS_2 films. (a) Method 1: direct ALD (LT-NbS_2) film growth using TBTDEN niobium precursor and H_2S (or H_2S + H_2) plasma coreactant at a deposition temperature of 300 °C or 450 °C. (b) Method 2: post-annealing (HT-NbS_2) of samples from the method 1 (a) in the tube furnace (red) at 900 °C using 10 % H_2S gas in Ar for 45 min. (c) Method 3: sulfurization (Sulfox-NbS_2) of the ALD grown Nb_2O_5 film (using TBTDEN niobium precursor and O_2 plasma at 150 °C) in the tube furnace (red) at 900 °C using 10% H_2S in Ar for 45 min.

As expected for ALD grown films, the films fabricated by all three methods have excellent areal coverage as shown by SEM top-view images in Figure 6.2(a-e). Due to high-temperature processing, the HT-NbS_2 (300°C), HT-NbS_2 (450°C) and Sulfox-NbS_2 films synthesized by methods 2 and 3 have larger grain size compared to films synthesized by method 1. The average grain size was determined from multiple grain measurements on SEM images. For both the LT-NbS_2 (300°C) and LT-NbS_2 (450°C) films deposited by method 1, the grain size was measured to be ~30-35 nm, while it increases more than 6-9 fold after the post-annealing treatment (method 2). Significantly larger grain size of ~300 nm was observed for the Sulfox-Nbs_2 film. This indicates that high temperature processed films were relatively more crystalline than the low temperature processed direct ALD-grown films. This is similar to NbS_2 synthesized by the CVD method at high temperatures in the literature.

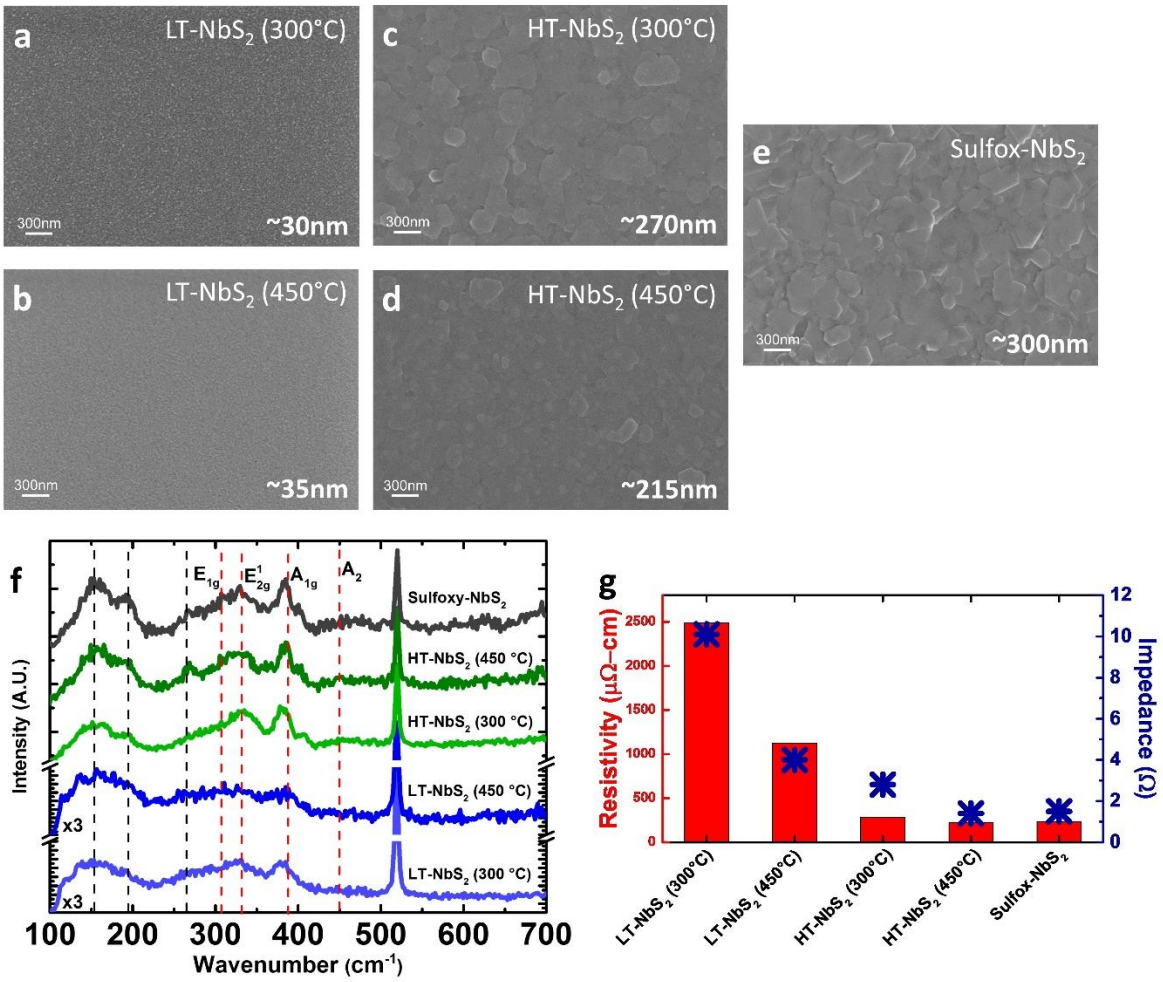

Figure 6.2 (a-e) Top-view SEM image of NbS_2 films obtained by various synthesis methods. The sample names are mentioned in the top right corner, and the average grain sizes are specified in the bottom right corner of the SEM image. (f) Raman spectra (λ_{ex} = 514 nm, both 300 °C and 450 °C spectra of method 1 have been magnified 3 times) and (g) measured film resistivity and electrochemical impedance for all the NbS_2 films.

Raman spectroscopy revealed that the NbS_2 films in all cases are in the 3*R* phase, showing the characteristic vibrational peaks at 307, 328, 385 and 449 cm-1 (Figure 6.2f), which correspond to the E_{1g}, $E^1{}_{2g}$, A_{1g} and A_2 Raman vibration modes, respectively[29]. The peaks located at 153, 195 and 267 cm^{-1} may correspond to impurities or defect modes[30]. For both LT-NbS_2 (300°C) and LT-NbS_2 (450°C), the A_2 mode was very weak, while the peaks of the other three Raman modes have broad FWHM and show low intensity. All four characteristic Raman modes were clearly visible for all three high temperature processed films with narrow FWHM, indicating relatively better crystallinity for these samples. This trend also confirms the observations made by SEM. The resistivity of the films was determined using four-point-probe measurements, revealing a decreasing trend in resistivity, as the processing temperature of the film increases from 300 °C to 900 °C, see Figure 6.2g. Such a

decreasing trend can be explained by the increasing film crystallinity. Interestingly, all three films processed at 900 °C by both method 2 and 3 showed comparable resistivity values around ~230 μΩ-cm, which is in good agreement with the reported bulk resistivity of NbS_2[31]. A similar trend was observed using EIS for all these five NbS_2 films on glassy carbon substrates. The films processed at 900 °C were measured to have a low impedance of ~2 Ω. Direct ALD-made LT-NbS_2 (300°C) and LT-NbS_2 (450°C) films showed a little higher systematic resistance in the electrochemical cell, while no value exceeded 10 Ω. From the above characterization methods, it is clear that the NbS_2 electrodes fabricated at higher temperature by method 2 and method 3 have similar properties.

6.3.2 HER Performance

The HER activity of the as-prepared NbS_2 electrodes was evaluated in N_2-purged 0.5 M H_2SO_4 electrolyte at room temperature. The iR-corrected (Ohmic drop compensation) Linear Sweep Voltammetry (LSV) curves and relevant Tafel slopes for electrodes with films deposited by all three synthesis methods are presented in Figure 6.3(a and b), where their performances are also compared to the reference bare glassy carbon substrate. We observed similar HER performance for electrodes from method 1 and 2, irrespective of the ALD deposition temperatures (300 °C and 450 °C, see appendix 6 Figure A6.1). Therefore, only the activity of the 450 °C samples will be discussed further. The LT-NbS_2 (450°C) and HT-NbS_2 (450°C) NbS_2 electrodes will be addressed as LT-NbS_2 and HT-NbS_2, respectively. The LT-NbS_2, HT-NbS_2 and Sulfox-NbS_2 electrodes exhibited similar initial HER performance, as shown in Figure 6.3a (initial LSV cycle) with an overpotential of 0.54 V, 0.53 V and 0.52 V, respectively at η_{10}. According to the literature, this HER performance at η_{10} is comparable to the reported initial activity of around 0.50 V for SSR/CVD grown NbS_2[11,13,20]. Furthermore, the Tafel slope for LT-NbS_2, HT-NbS_2 and Sulfox-NbS_2 electrodes were 114, 124 and 107 mV/dec, respectively. These values fall within the broad range of values reported in the literature for SSR/CVD grown NbS_2 spanning from 103 to 211 mV/dec (Table 6.1). This shows that regardless of the ALD-based synthesis method and material properties such as resistivity, crystallinity and grain size of the NbS_2, the initial electrochemical activity is similar and comparable to the activity reported in the literature for the high temperature grown NbS_2.

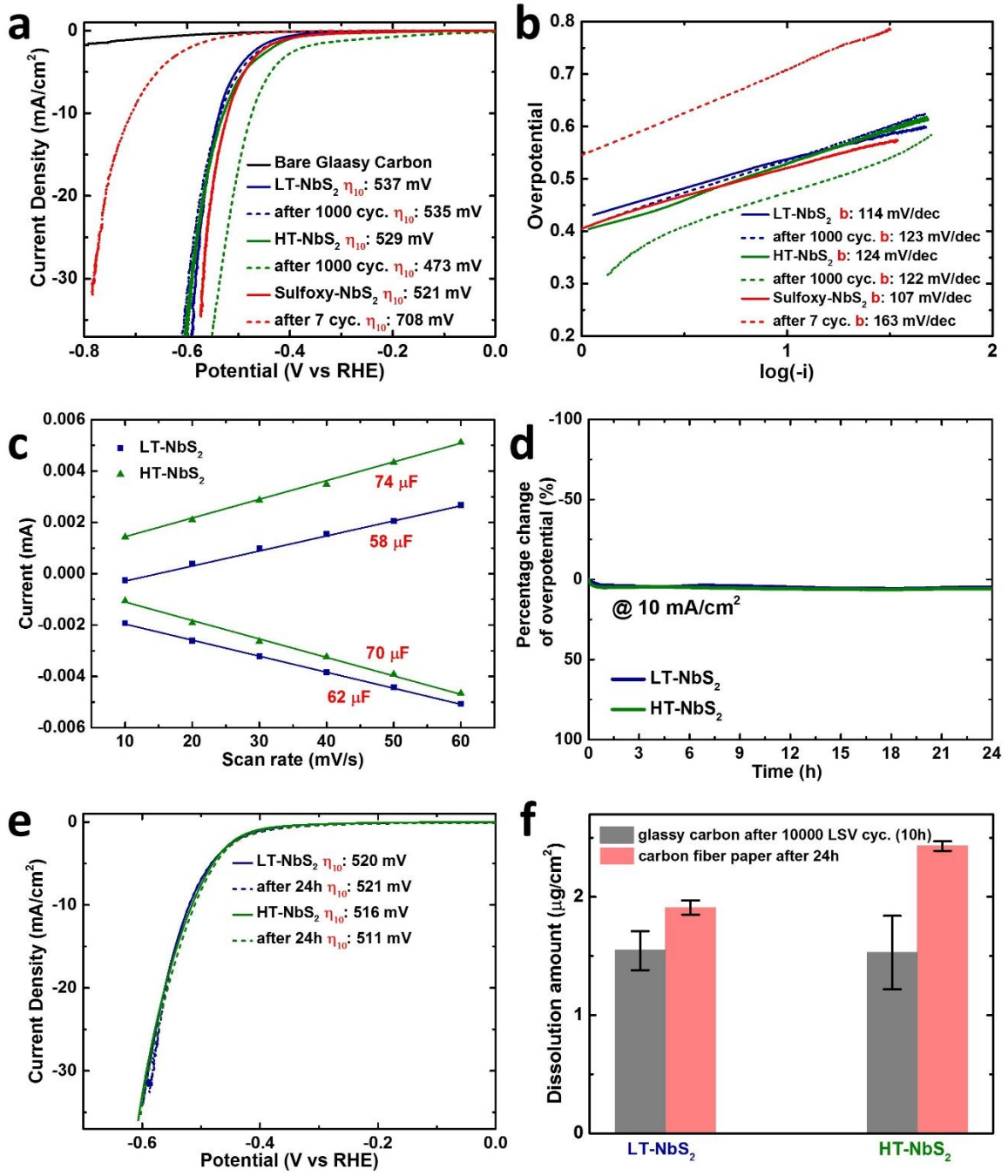

Figure 6.3 a) HER polarization curves of the NbS_2 electrodes synthesized by different methods. b) Corresponding Tafel plots of the NbS_2 electrodes in (a). (c) Double-layer capacitance measurement for determining the electrochemical active surface area (ECSA) for LT-NbS_2 and HT-NbS_2. (d) Chronopotentiometry HER performance of the NbS_2 electrodes synthesized by method 1 and 2. (e) Corresponding HER polarization curves before and after 24 hours. (f) Nb dissolution amount for NbS_2 electrodes on both glassy carbon and carbon fiber paper.

To investigate the similar initial HER performance observed for the various electrodes in more detail, LT-NbS_2 and HT-NbS_2 films were further studied by double-layer capacitance (C_{dl}) measurement. Here, as HT-NbS_2 and Sulfox-NbS_2 films have similar film properties, only HT-NbS_2 films were compared with LT-NbS_2 films. Cyclic voltammetry was applied with various scan rates to determine C_{dl} (Figure 6.3c). The C_{dl} was used to estimate the electrochemical surface area (ECSA) and to compare the exposed active sites between LT-NbS_2 and HT-NbS_2 films. The ECSA C_{dl} (Figure 6.3c) for LT-NbS_2 and HT-NbS_2 films were 60 and 72 µF, respectively. The ECSA per cm^2 was calculated to be 4.0 and 4.8 using C_s=0.015 mF/cm^2 as the specific capacitance value of NbS_2[28]. This indicates a similar number of active sites for NbS_2 prepared by both method 1 and 2, which matches with their similar initial HER performance (Figure 6.3a).

Furthermore, the long-term stability of all three electrodes was first investigated over 1000 LSV cycles. Both the LT-NbS_2 and HT-NbS_2 films showed stability over 1000 LSV cycles, while the Sulfox-NbS_2 activity decayed within 10 LSV cycles indicating poor stability (see Figure 6.3a). Next, the stability test of the LT-NbS_2 and HT-NbS_2 films were further extended to 10000 LSV cycles, and a drop in overpotential was observed from 525 and 520 mV in the initial LSV cycle to 489 and 435 mV at η_{10} (see appendix 6 Figure A6.3). The LT-NbS_2 film demonstrated a very low decrease in overpotential of 36 mV, while HT-NbS_2 showed a slightly larger decrease of 85 mV. In comparison, Lou *et al.*[13] (by SSR method) and Yakobson & Wood *et al.*[11] (by CVD method) reported a more substantial decline in overpotential of 500 mV and 450 mV, respectively, at η_{10} over 10000 LSV cycles as a result of a continuous delamination process. Thus, indicating that both direct LT- and HT-NbS_2 (method 1 and 2) are significantly more stable over 10000 LSV cycles compared to literature. Additionally, in comparison to the work of Lou *et al.*[13], smaller ECSA changes were observed after 10000 LSV cycles (see Figure A6.4), as C_{dl} only increased to less than 5 times the initial value in comparison to 100 times reported by Lou *et al.*, further confirming the stability of the direct ALD-derived NbS_2 electrodes. The 10000 LSV cycles data indicate that among the two ALD-derived NbS_2 films (method 1 and 2), the HT-NbS_2 film with larger crystal size (~300 nm) is relatively less stable and more prone to delamination than its counterpart synthesized directly by ALD at low temperature (LT-NbS_2).

Nowadays, applying a certain current density on the studied electrocatalyst over a long period is commonly regarded as a metric to determine its stability. Therefore, besides the dynamic long-term stability test by repeated LSV scans over 10000 cycles, we also measured the chronopotentiometric response at a constant current density of 10 mA/cm^2, see Figure

6.3d. Both LT- and HT-NbS_2 electrodes (prepared on carbon fiber paper) showed excellent stability over 24 h (Figure 6.3d). The amount of Nb dissolution in the electrolyte after both dynamic (~10h) and static (24h) stability tests were studied for LT-NbS_2 and HT-NbS_2 films using ICP-OES measurements, see Figure 6.3e. In the dynamic test case, for both the films, the Nb dissolution was similar around 1.5 µg/cm^2 (or 0.15 µg/cm^2 per h), which is around 10% of the initial mass loading (~13 µg/cm^2). In the static test case, the Nb dissolution was 0.08 and 0.1 µg/cm^2 per h, respectively, for LT-NbS_2 and HT-NbS_2 films deposited on carbon fiber paper substrates with a complex surface topography (larger surface area). This indicates relatively more Nb dissolution for HT-NbS_2 than for the LT-NbS_2 film. This is consistent with the dynamic 10000 LSV cycle study, where a larger difference in overpotential of 85 mV was observed for HT-NbS_2. This study shows the excellent durability of the direct ALD-grown NbS_2 prepared at low-temperature for HER application.

Turning to the Sulfox-NbS_2 electrode case, the dramatic increment in the HER overpotential during LSV measurements from 521 mV at the initial cycle to 708 mV within less than 10 cycles (Figure 6.3a) could be related to the observed visible delamination of this NbS_2 film from the glassy carbon substrate. This phenomenon has also been reported previously[12,32]. Such delamination of the NbS_2 film from the substrate resulted in sediments consisting of delaminated flakes at the bottom of the electrochemical cell. Even though HT-NbS_2 and Sulfox-NbS_2 films were synthesized in a similar condition of 10% H_2S at 900 °C for 45 min, and have comparable film and material properties, they show deviating HER performance. This dramatic difference in HER activity could be related to the ALD process, as HT-NbS_2 was directly deposited by ALD and only underwent diffusion and recrystallization during the high-temperature treatment. However, in the case of the Sulfox-NbS_2 film, the amorphous Nb_2O_5 film was deposited by ALD, and during the sulfurization treatment, O to S exchange reactions take place to form highly crystalline layered NbS_2. ALD is a technique in which precursors are adsorbed to the surface chemically, forming a chemical bond at the interface between the substrate and the initial layer(s) of the film. Previously, Shirazi *et al.*, using DFT simulations, reported a surface reaction mechanism during the early stage of the MoS_2 direct-ALD process[33,34]. In this work, when Mo precursor (containing tert-butylimido type ligands) was exposed to the SiO_2 substrate (with dangling bonds on the surface), strong chemical adsorption of the precursor was observed. This chemisorption process led to the formation of a covalently bonded initial MoS_2 layer on the growth substrate. A similar chemisorption process can be speculated for both ALD of NbS_2 and Nb_2O_5 on SiO_2, as the Nb precursor (TBTDEN) used here has tert-butylimido type ligands, similar to the Mo precursor used in the work of Shirazi *et al.*. The above speculation can be

extended for ALD of NbS_2 and Nb_2O_5 films on the glassy carbon substrates, as glassy carbon also has dangling bonds with which the precursor molecules react. Also, note that the

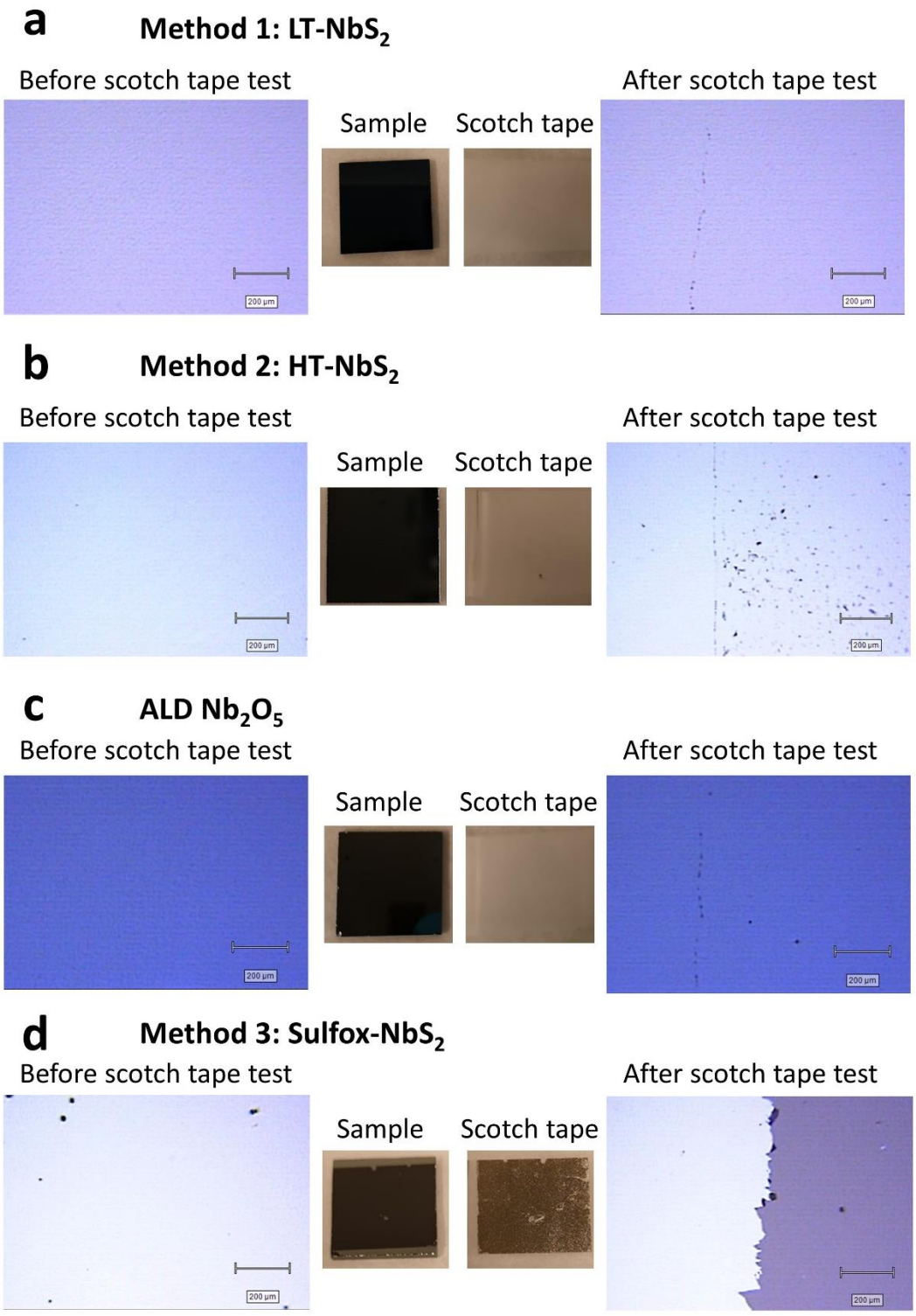

Figure 6.4 Shows the microscopy image of the NbS_2 (a, b and d) and Nb_2O_5 (c) films on glassy carbon substrate both before and after the adhesion test using the scotch tape. The pictures of both the sample and scotch tape are also shown.

material/film properties of both NbS_2 and Nb_2O_5 films grown on SiO_2 and glassy carbon substrate were examined to be similar. The as-formed strong chemical bonds between the ALD grown film and the substrate are not likely to be affected during the post-annealing treatment. Hence, stronger adhesion of ALD-grown NbS_2 films on the glassy carbon substrate could explain the stability of direct ALD-derived HT-NbS_2 films and the absence of visible exfoliation/ delamination during the LSV measurements.[35] However, in the case of the Nb_2O_5 sulfurization, the O to S exchange reaction, which transforms the three-dimensional (3D) Nb_2O_5 into the 2D NbS_2, could affect the strong chemical bond between the film and the substrate, and might create a weak interaction at the glassy carbon-NbS_2 interface. Such a newly created weak interaction could allow for easy delamination of the Sulfox-NbS_2 film during HER.

To test the above hypothesis, adhesion tests were conducted using scotch tape on all synthesized NbS_2 films on glassy carbon substrates. Figure 6.4(a, b and d) show the microscopy images of the NbS_2 films both before and after the adhesion test. The test shows that LT-NbS_2 and HT-NbS_2 films synthesized by method 1 and 2 were not delaminated from the substrate by the scotch tape, as both the microscope image and the pictures of the film and scotch tape appear fresh. Only tape residues were observed on the film. On the contrary, the Sulfox-NbS_2 film prepared by method 3 was delaminated entirely from the substrate as >90 % of material transferred to the scotch tape, see Figure 6.4d. Importantly, the ALD grown Nb_2O_5 film before sulfurization (Figure 6.4c) did not delaminate. Thus, the scotch tape adhesion test confirms the hypothesis on the formation of weak interaction between the NbS_2 film and the substate following the sulfurization treatment (Sulfox-NbS_2, method 3), leading to the complete exfoliation/ delamination of the film.

Inspired by the adhesion test results, the direct ALD-grown NbS_2 (LT-NbS_2) was introduced as an adhesive buffer layer between the glassy carbon substrate and the ALD-grown Nb_2O_5 layer before high-temperature annealing/sulfurization treatment, see Figure 6.5a. After higher temperature treatment, the LT-NbS_2 + ALD-grown Nb_2O_5 stack layer on glassy carbon substrate will become HT-NbS_2 + Sulfox-NbS_2 stack layer. We expected that the introduction of this new direct ALD-grown adhesive layer would prevent the electrochemical delamination and simultaneously improve the stability of the stack film.

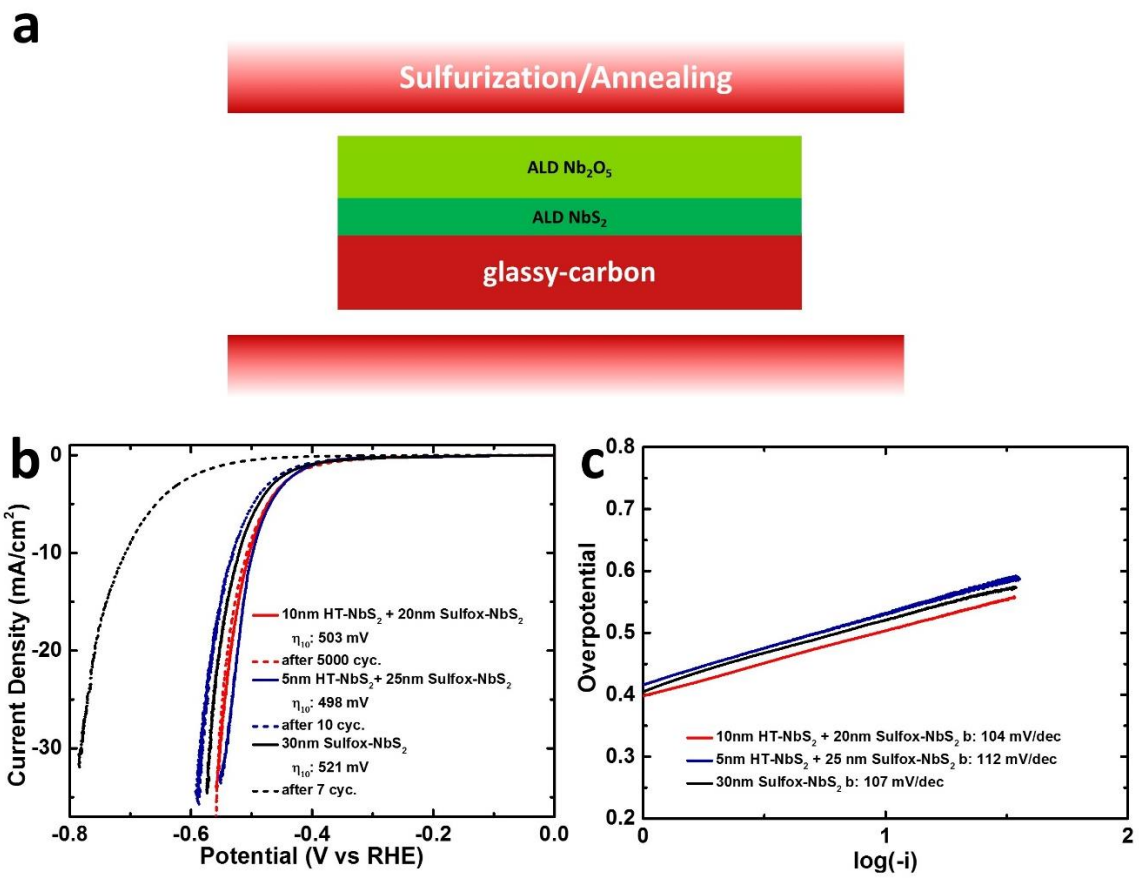

Figure 6.5 (a) Schematic illustration of sulfurization/ annealing of stack samples with ALD grown NbS_2 as the buffer layer between ALD grown Nb_2O_5 and the glassy carbon substrate in the tube furnace (red) at 900 °C using 10 % H_2S gas in Ar for 45 min. (b) HER polarization curves of all three samples. (c) Corresponding Tafel plots of the samples in (c).

To test this hypothesis, three electrodes were fabricated by ALD: a) 30 nm Sulfox-NbS_2 ; b) stack: 5 nm HT-NbS_2 (buffer layer)+ 25 nm Sulfox-NbS_2 and c) stack: 10 nm HT-NbS_2 (buffer layer) + 20 nm Sulfox-NbS_2. Following the ALD deposition, all three samples were post-annealed/sulfurized at 900 °C under 10% H_2S/Ar atmosphere. HER electrochemical LSV measurements were conducted on all three electrodes. As expected, all of them showed similar HER performance with an overpotential around 500 mV to reach η_{10} during the initial cycle (Figure 6.5b), and the Tafel slope values were in a narrow range of 104 to 112 (Figure 6.5c). Additionally, as hypothesized, the stack sample with 10 nm HT-NbS_2 + 20 nm Sulfox-NbS_2 showed good stability over 5000 LSV cycles with no significant variation in HER activity along with no visible exfoliation. On the other hand, both 30 nm Sulfox-NbS_2 and 5 nm HT-NbS_2 + 25 nm Sulfox-NbS_2 samples showed a decreasing trend in HER activity. While the 30 nm Sulfox-NbS_2 sample as anticipated showed a complete exfoliation of the NbS_2 film, the latter showed only a small decay in HER activity from 498 mV in the initial cycle to 530 mV

after 10 cycles with only partial exfoliation. This shows that with increasing thickness of the direct ALD-grown NbS_2 buffer layer from 0 nm to 10 nm, the HER stability improves, demonstrating that the HT-NbS2 can act as the adhesive layer between the Sulfox-NbS_2 and the glassy carbon substrate. Additionally, XPS spectra of all three electrodes were analyzed before and after the electrochemical measurements to obtain additional information on this delamination.

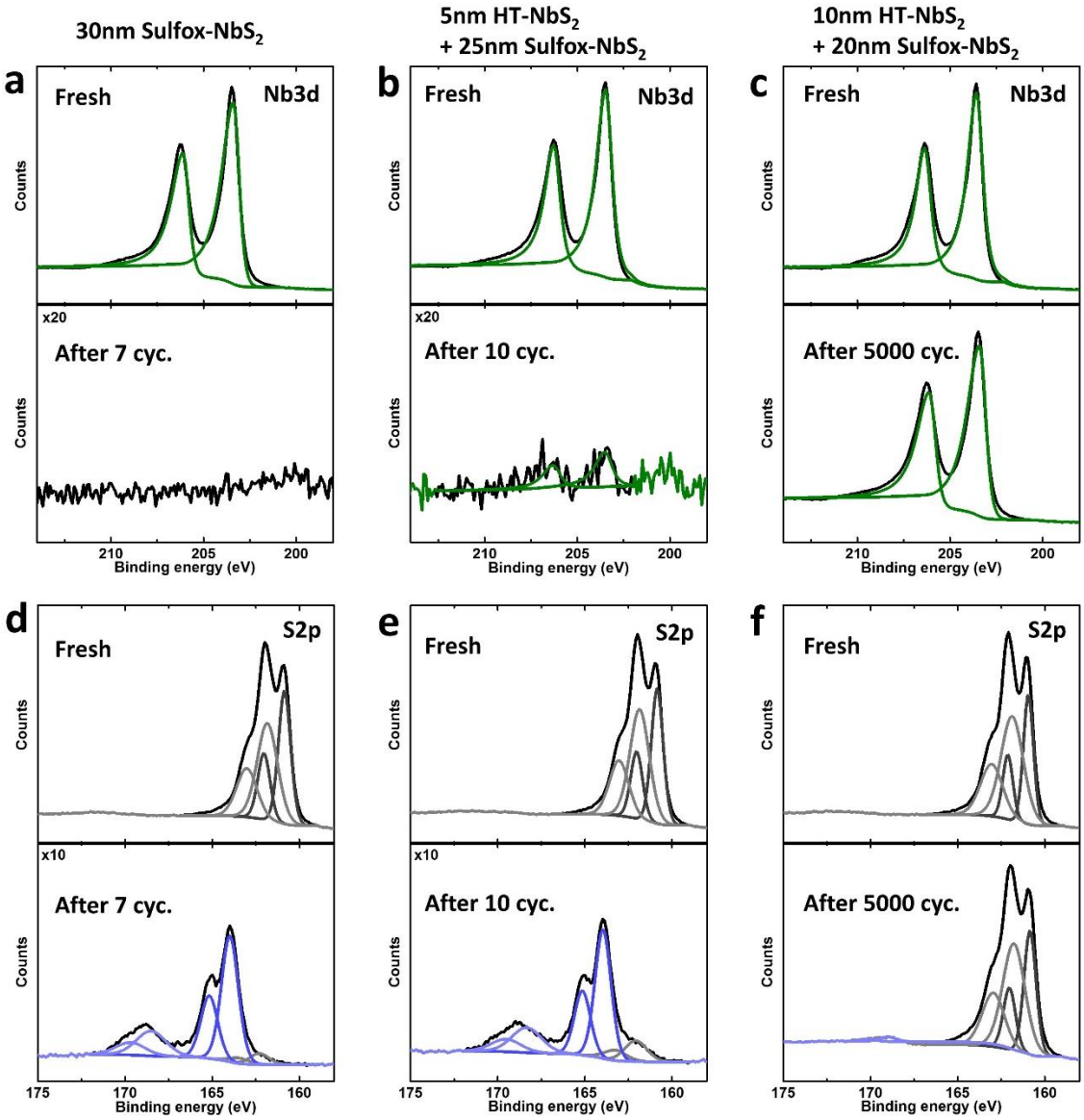

Figure 6.6 (a-c) Nb3d XPS spectra of all three stack samples before (fresh) and after LSV measurement cycles. (d-f) S2p XPS spectra of all three samples before (fresh) and after LSV measurement cycles.

The S2p and Nb3d XPS spectra of all three electrodes before undergoing HER measurements showed a similar spectral profile, indicating that they share the same surface species (Figure 6.6, fresh), which (partly) explains the similar initial HER performance. The peaks at 203.5 eV (Nb $3d_{5/2}$) and 206.3 eV (Nb $3d_{3/2}$) were assigned to the binding energies of Nb(+4) of NbS_2 and have split spin-orbit components of Δ=2.78 eV[30,36]. Also, the peaks at 160.9 eV (S $2p_{3/2}$) and 162.1 eV (S $2p_{1/2}$); 161.9 eV (S $2p_{3/2}$) and 163.1 eV (S $2p_{1/2}$) were assigned to the sulfur species in NbS_2[37,19].

In contrast, after the HER LSV measurements, the XPS spectra for the 30 nm Sulfox-NbS_2 electrode did not show any trace of Nb species (see Figure 6.6a). This confirms the complete delamination of the NbS_2 layer during HER measurement. In the case of the 5 nm HT-NbS_2 + 25 nm Sulfox-NbS_2 electrode, the XPS measurement was conducted on the delaminated area, and a significant drop in Nb signal was observed, indicating almost complete removal of the NbS_2 film as only some traces of Nb left on the surface (see Figure 6.6b). In the case of the 10 nm HT-NbS_2 + 20 nm Sulfox-NbS_2 electrode (see Figure 6.6c), no visible exfoliation of the film was observed, and the XPS profile after 5000 LSV cycles matches the fresh profiles. With respect to the S_2p spectra, for both delaminated electrodes, the presence of S_8 as the majority S species was observed at 164.0 (S $2p_{3/2}$) and 165.2 eV (S $2p_{1/2}$) which could be due to remaining S residues (see Figure 6.6d and e). Meanwhile, the electrodes with thicker-buffer-layer of ALD-grown NbS_2 (10 nm HT-NbS_2 + 20 nm Sulfox-NbS_2) remained stable in its sulfur (see Figure 6.6a) and niobium speciation (see Figure 6.6f) even after 5000 electrochemical cycles. This difference indicates the strong bonding of ALD-grown NbS_2 (HT-NbS_2) film on the glassy carbon substrates, while the bonding between Sulfox-NbS_2 and glassy carbon substrate is weakened or vanishes following the O to S exchange reaction during sulfurization treatment. This confirms that the strong adhesion of ALD-grown NbS_2 to be the reason for the excellent long-term stability of the NbS_2 electrode synthesized by method 1 and 2. Thus, in comparison to other synthesis methods, direct ALD synthesis of NbS_2 offers comparable HER performance with improved long-term stability along with the fabrication benefit for large area scalable synthesis, inherent to ALD.

6.4 Conclusions

In this work, we applied ALD grown NbS_2 for the first time for the hydrogen evolution reaction and demonstrated an overpotential of ~500 mV at η_{10} with excellent long-term stability over 24 hours (and for 10000 LSV cycles). NbS_2 films synthesized using direct ALD methods exhibited superior long-term stability over NbS_2 films synthesized through the

sulfurization of ALD-grown Nb_2O_5. The poor stability of sulfurization-derived NbS_2 was caused by electrochemical exfoliation/ delamination during HER LSV measurements. Variation in the adhesion strength between the film and the substrate was identified to be the reason for the observed difference in the stability between the direct ALD-derived and indirect ALD-derived (sulfurization) NbS_2 films. The sulfurization process, involving the exchange reaction between O and S to form 2D NbS_2 (from ALD-grown Nb_2O_5), was speculated to weaken the interface between the NbS_2 film and the substrate. As a result, complete delamination of the sulfurization-derived NbS_2 film occurred during HER. The long-term stability of the sulfurization-derived NbS_2 was drastically improved by adding a 10 nm thick direct ALD-grown NbS_2 film as an adhesive buffer layer between the sulfurization-derived (from ALD-grown Nb_2O_5) and the glassy carbon substrate, exploiting the strong adhesion of the ALD-grown NbS_2 to the glassy carbon. This enables the study of the intrinsic HER performance of the top 2D TMDC layer, independent of exfoliation/ delamination processes. The adhesive strength at the interface between the catalyst layer and the electrode substrate is a prerequisite to investigate the long-term stability of the 2D TMDC for HER. This work also shows that ALD could potentially provide a synthesize route for stable and active electrocatalysts based on other metallic 2D transition metal chalcogenides.

Acknowledgments

The authors acknowledge Martijn G. Dijstelbloem and Cristian van Helvoirt for their technical assistance and Dr. Matthew A. Bloodgood and Dr. Vincent Vandalon for valuable suggestions. Adelheid M. Elemans-Mehring is thanked for the assistance with ICP-OES measurements. Yue Zhang acknowledges financial support from the China Scholarship Council (CSC). Emiel J. M. Hensen acknowledges funding by an NWO Vici grant. This work was supported by the European Research Council (Grant Agreement No. 648787).

References

[1] S. Chu and A. Majumdar, Nature **488**, 294 (2012).

[2] M. Carmo, D.L. Fritz, J. Mergel, and D. Stolten, Int. J. Hydrogen Energy **38**, 4901 (2013).

[3] Z.W. Seh, J. Kibsgaard, C.F. Dickens, I. Chorkendorff, J.K. Nørskov, and T.F. Jaramillo, Science (80-.). **355**, eaad4998 (2017).

[4] X. Chia, A. Ambrosi, P. Lazar, Z. Sofer, and M. Pumera, J. Mater. Chem. A **4**, 14241 (2016).

[5] H. Pan, Sci. Rep. **4**, 5348 (2015).

[6] T.F. Jaramillo, K.P. Jørgensen, J. Bonde, J.H. Nielsen, S. Horch, and I. Chorkendorff, Science (80-.). **317**, 100 (2007).

[7] D. Voiry, M. Salehi, R. Silva, T. Fujita, M. Chen, T. Asefa, V.B. Shenoy, G. Eda, and M. Chhowalla, Nano Lett. **13**, 6222 (2013).

[8] H. Li, C. Tsai, A.L. Koh, L. Cai, A.W. Contryman, A.H. Fragapane, J. Zhao, H.S. Han, H.C. Manoharan, F. Abild-Pedersen, J.K. Nørskov, and X. Zheng, Nat. Mater. **15**, 48 (2016).

[9] T.W. Lee, C.C. Chen, and C. Chen, Environ. Sci. Technol. **53**, 6282 (2019).

[10] D. Escalera-López, Z. Lou, and N. V. Rees, Adv. Energy Mater. **9**, 1802614 (2019).

[11] Y. Liu, J. Wu, K.P. Hackenberg, J. Zhang, Y.M. Wang, Y. Yang, K. Keyshar, J. Gu, T. Ogitsu, R. Vajtai, J. Lou, P.M. Ajayan, B.C. Wood, and B.I. Yakobson, Nat. Energy **2**, 17127 (2017).

[12] J. Yang, A.R. Mohmad, Y. Wang, R. Fullon, X. Song, F. Zhao, I. Bozkurt, M. Augustin, E.J.G. Santos, H.S. Shin, W. Zhang, D. Voiry, H.Y. Jeong, and M. Chhowalla, Nat. Mater. (2019).

[13] J. Zhang, J. Wu, X. Zou, K. Hackenberg, W. Zhou, W. Chen, J. Yuan, K. Keyshar, G. Gupta, A. Mohite, P.M. Ajayan, and J. Lou, Mater. Today **25**, 28 (2019).

[14] J. Shi, X. Wang, S. Zhang, L. Xiao, Y. Huan, Y. Gong, Z. Zhang, Y. Li, X. Zhou, M. Hong, Q. Fang, Q. Zhang, X. Liu, L. Gu, Z. Liu, and Y. Zhang, Nat. Commun. **8**, 1 (2017).

[15] Y. Huan, J. Shi, X. Zou, Y. Gong, Z. Zhang, M. Li, L. Zhao, R. Xu, S. Jiang, X. Zhou, M. Hong, C. Xie, H. Li, X. Lang, Q. Zhang, L. Gu, X. Yan, and Y. Zhang, Adv. Mater. **30**, 1705916 (2018).

[16] J. Yuan, J. Wu, W.J. Hardy, P. Loya, M. Lou, Y. Yang, S. Najmaei, M. Jiang, F. Qin, K. Keyshar, H. Ji, W. Gao, J. Bao, J. Kono, D. Natelson, P.M. Ajayan, and J. Lou, Adv. Mater. **27**, 5605 (2015).

[17] S.H. Noh, J. Hwang, J. Kang, M.H. Seo, D. Choi, and B. Han, J. Mater. Chem. A **6**, 20005 (2018).

[18] Z.-L. Liu, L.-C. Cai, and X.-L. Zhang, J. Alloys Compd. **610**, 472 (2014).

[19] L. Najafi, S. Bellani, R. Oropesa-Nuñez, B. Martín-García, M. Prato, V. Mazánek, D. Debellis, S. Lauciello, R. Brescia, Z. Sofer, and F. Bonaccorso, J. Mater. Chem. A **7**, 25593 (2019).

[20] C. Huang, X. Wang, D. Wang, W. Zhao, K. Bu, J. Xu, X. Huang, Q. Bi, J. Huang, and F. Huang, Chem. Mater. **31**, 4726 (2019).

[21] D. Gopalakrishnan, A. Lee, N.K. Thangavel, and L.M. Reddy Arava, Sustain. Energy Fuels **2**, 96 (2018).

[22] X. Zhou, S.H. Lin, X. Yang, H. Li, M.N. Hedhili, L.J. Li, W. Zhang, and Y. Shi, Nanoscale **10**, 3444 (2018).

[23] X. Zhou, S.-H. Lin, X. Yang, H. Li, M.N. Hedhili, L.-J. Li, W. Zhang, and Y. Shi, Nanoscale **10**, 3444 (2018).

[24] H.C.M. Knoops, S.E. Potts, A.A. Bol, and W.M.M. Kessels, in *Handb. Cryst. Growth*, Second Edi (Elsevier, Amsterdam, 2015), pp. 1101–1134.

[25] J.A. Singh, N. Yang, and S.F. Bent, Annu. Rev. Chem. Biomol. Eng. **8**, 41 (2017).

[26] A.E. Settle, N.S. Cleveland, C.A. Farberow, D.R. Conklin, X. Huo, A.A. Dameron, R.W. Tracy, R. Sarkar, E.J. Kautz, A. Devaraj, K.K. Ramasamy, M.J. Watson, A.M. York, R.M. Richards, K.A. Unocic, G.T. Beckham, M.B. Griffin, K.E. Hurst, E.C.D. Tan, S.T. Christensen, and D.R. Vardon, Joule **3**, 2219 (2019).

[27] S.B. Basuvalingam, B. Macco, H.C.M. Knoops, J. Melskens, W.M.M. (Erwin) Kessels, and A.A. Bol, J. Vac. Sci. Technol. A **36**, 041503 (2018).

[28] C.C.L. McCrory, S. Jung, J.C. Peters, and T.F. Jaramillo, J. Am. Chem. Soc. **135**, 16977 (2013).

[29] S. Onari, T. Arai, R. Aoki, and S. Nakamura, Solid State Commun. **31**, 577 (1979).

[30] J.K. Dash, L. Chen, P.H. Dinolfo, T.-M. Lu, and G.-C. Wang, J. Phys. Chem. C **119**, 19763 (2015).

[31] A. Niazi and A.K. Rastogi, J. Phys. Condens. Matter **13**, 6787 (2001).

[32] L. Najafi, S. Bellani, R. Oropesa-Nuñez, B. Martín-García, M. Prato, V. Mazánek, D. Debellis, S. Lauciello, R. Brescia, Z. Sofer, and F. Bonaccorso, J. Mater. Chem. A **7**, 25593 (2019).

[33] M. Shirazi, W.M.M. Kessels, and A.A. Bol, APL Mater. **6**, 111107 (2018).

[34] M. Shirazi, W.M.M. Kessels, and A.A. Bol, Phys. Chem. Chem. Phys. **20**, 16861 (2018).

[35] Y. Huang and L. Liu, Sci. China Mater. **62**, 913 (2019).

[36] H. Bark, Y. Choi, J. Jung, J.H. Kim, H. Kwon, J. Lee, Z. Lee, J.H. Cho, and C. Lee, Nanoscale **10**, 1056 (2018).

[37] X. Song, Y. Wang, F. Zhao, Q. Li, H.Q. Ta, M.H. Rümmeli, C.G. Tully, Z. Li, W.-J. Yin, L. Yang, K.-B. Lee, J. Yang, I. Bozkurt, S. Liu, W. Zhang, and M. Chhowalla, ACS Nano **13**, 8312 (2019).

Appendix 6

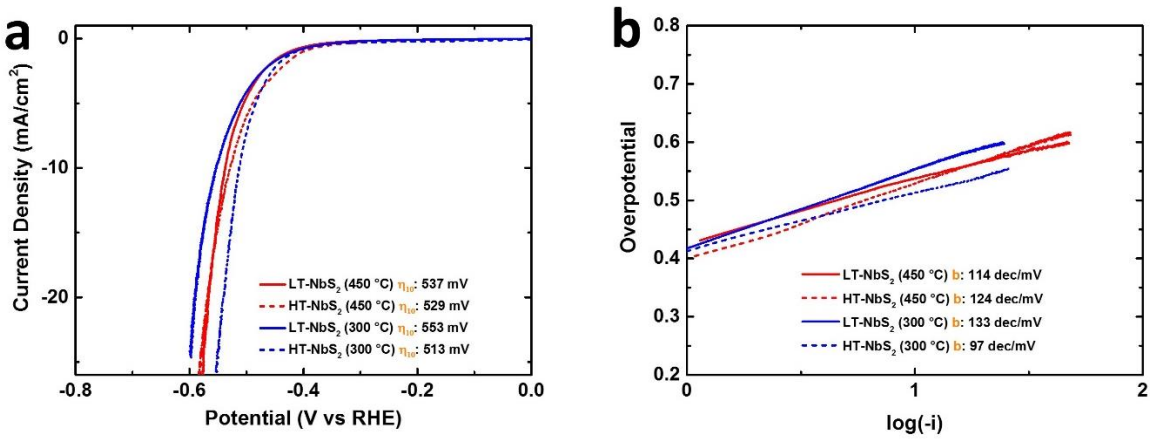

Figure A6.1 The HER polarization curves of method 1 and 2 NbS_2 electrodes deposited by direct ALD at 300 °C (blue) and 450 °C (red). b) Corresponding Tafel plots of the samples in (a).

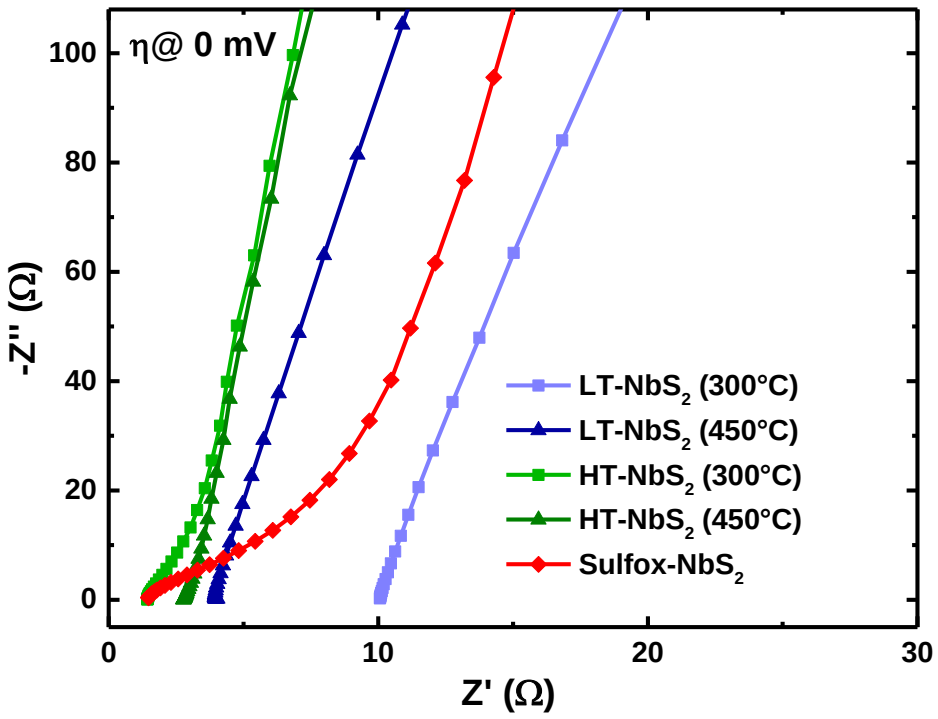

Figure A6.2 EIS of NbS_2 electrodes prepared by method 1, 2 and 3. Solid lines are fit to the equivalent circuit model.

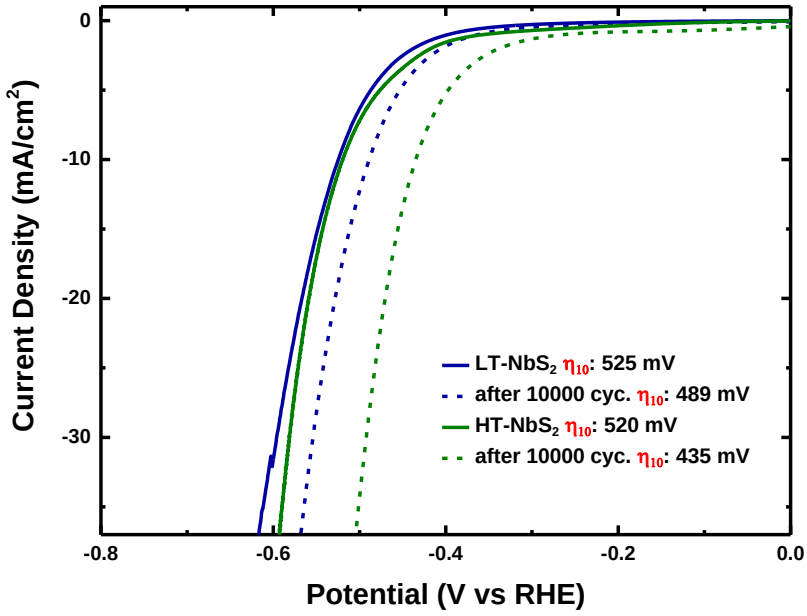

Figure A6.3 The HER performance of NbS_2 electrodes prepared by method 1 and 2 before and after long-term stability tests (10000 LSV cycles).

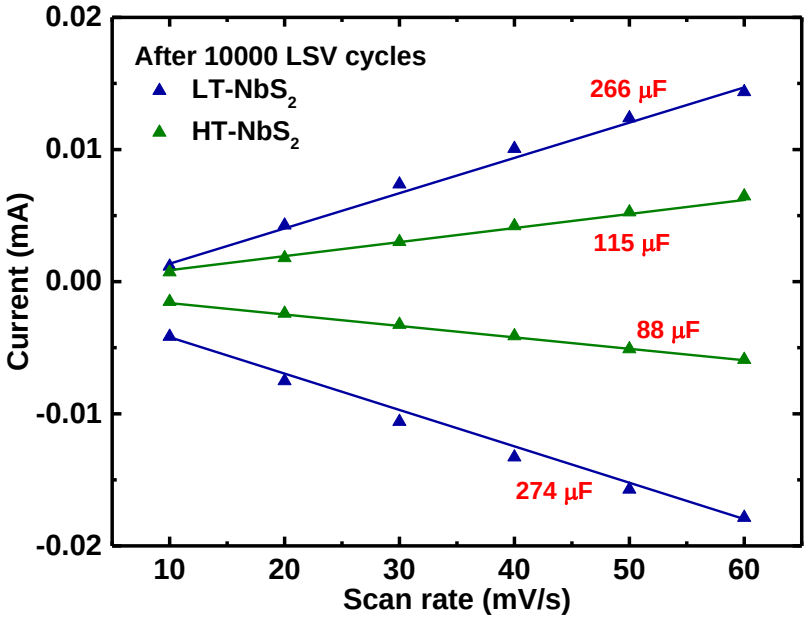

Figure A6.4 Double-layer capacitance measurement for determining the electrochemical active surface area (ECSA) for NbS_2 synthesized by method 1 and 2 after 10000 LSV cycles. Cyclic voltammograms were measured in a non-Faradaic region of the voltammogram at the following scan rates: 10-60 mV/s. Cathodic and anodic charging currents measured at OCP vs. RHE plotted as a function of scan rate.

Comparison of Thermal and Plasma-Enhanced Atomic Layer Deposition of Niobium Oxide Thin Films

7

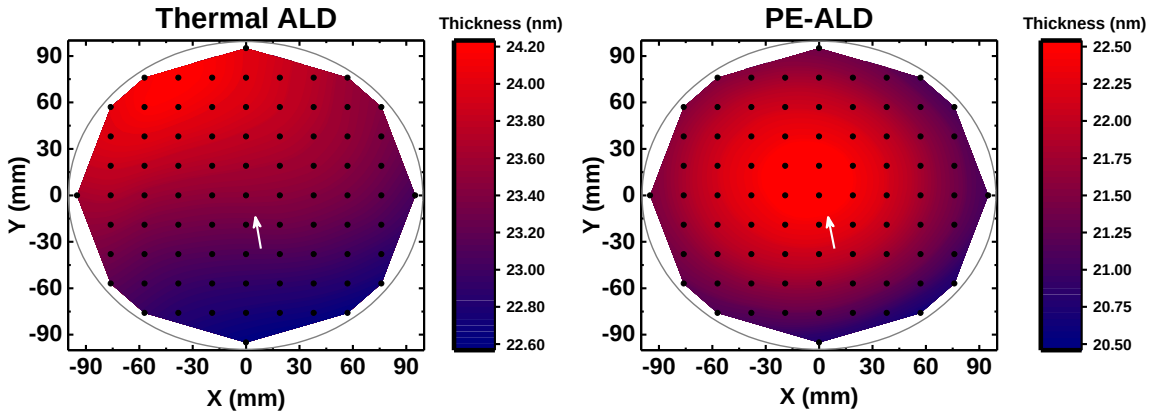

Niobium pentoxide was deposited using $^{t}BuN=Nb(NEt_2)_3$ as niobium precursor by both thermal atomic layer deposition (thermal ALD) and plasma-enhanced atomic layer deposition (PE-ALD) with H_2O and O_2 plasma as coreactants, respectively. The deposition temperature was varied between 150 and 350 °C in both ALD processes. Amorphous films were obtained in all cases. Self-limiting saturated growth was confirmed for both ALD processes along with high uniformity over a 200 mm Si wafer. The PE-ALD process enabled a higher growth per cycle (GPC) than the thermal ALD process (0.56 Å *Vs.* 0.38 Å at 200 °C, respectively), while the GPC decreases with increasing temperature in both cases. The high purity of the film was confirmed using Rutherford backscattering spectrometry (RBS), elastic recoil detection (ERD), and X-ray photoelectron spectroscopy (XPS), while the latter technique also confirmed the Nb^{+5} oxidation state of the niobium oxide films. The thermal ALD deposited films were sub-stoichiometric due to the presence of oxygen vacancies (V_O), of which a more dominant presence was observed with increasing deposition temperature. The PE-ALD deposited films were found to be near stoichiometric for all investigated deposition temperatures.

Saravana Balaji Basuvalingam, Bart Macco, Harm C. M. Knoops, Jimmy Melskens, Wilhelmus M. M. Kessels, and Ageeth A. Bol, *J. Vac. Sci. Technol., A*, **36**, 4 (2018)

7.1 Introduction

Niobium oxide has more than 15 polymorphs, making it a complex and an interesting material to investigate as the phase and stoichiometry of the material are directly dependent on the deposition technique and temperature[1,2]. The phase and stoichiometry of niobium oxide strongly influence its material properties. Stoichiometric niobium oxide (Nb_2O_5) has a high-k dielectric (insulating) behaviour that has been used in various applications such as capacitors[3,4], insulators[5], and sensors[6,7]. The slight deficiency in oxygen content (sub-stoichiometric) causes a transition from insulating to n-type semiconducting behaviour. This sub-stoichiometric conducting oxide can be used as an electron transport or passivating layer in solar cells[8], and also as a catalysts[9]. Additionally, Nb_2O_5 can be sulfurized into 2D-NbS_2 at high temperature (as discussed in chapter 6), which has both semiconducting and superconducting properties[10,11].

Nb_2O_5 has been synthesized adopting various techniques, such as sol-gel[12], sputtering[13], e-beam evaporation[14], pyrolysis[15–17], chemical vapour deposition (CVD)[18], pulsed laser deposition (PLD)[6], and atomic layer deposition (ALD)[3,19,28,29,20–27]. Of aforesaid techniques, ALD has the advantage of achieving precise thickness control, conformality, and uniformity over a large area, which are valuable assets for most of the above-mentioned applications[30]. ALD is a cyclic process where in the first half-cycle the precursor is dosed into the reaction chamber and followed by a purge step, and in the second half-cycle the co-reactant is dosed which is followed by a second purging step. The purge steps are there to avoid CVD reactions in the gas phase and on the surface. ALD of Nb_2O_5 has previously been demonstrated employing various precursors with either H_2O or O_3 as coreactant. ALD of Nb_2O_5 was first demonstrated using $Nb(OEt)_5$ as the precursor with H_2O as coreactant[19]. In this process, Kukli *et al.*[19] observed stoichiometric growth of Nb_2O_5 film with a growth per cycle (GPC) of 0.30 Å. Later, for this process more literature has appeared reporting similar low GPC[21,25]. Furthermore, this precursor has low volatility and decomposes when maintained above 100 °C. In the case of halide based precursors, NbI_5 with O_2 plasma was successfully demonstrated to result in Nb_2O_5[26], and also NbF_5 with H_2O was demonstrated, but in the latter case Nb_2O_5 film started to etch at higher temperatures resulting in no growth or non-uniform growth[3]. Also in the case of $NbCl_5$ with H_2O reproducibility problems were reported due to non-uniform growth[27]. Recently, Lee *et al.*[24] demonstrated a niobium oxide ALD process using NbF_5 as a precursor with H_2 plasma as coreactant to form niobium metal, which was followed by a super-cycle with O_3

as coreactant to form sub-stoichiometric niobium oxide. In this process, the stoichiometry of the oxide film was controlled by varying the number of super cycles. Blanquart *et al.*[20] demonstrated that ALD processes involving the amino-based precursors $^{t}BuN=Nb(NEt_2)_3$ and $^{t}BuN=Nb(NMeEt)_3$ attained a GPC of ~0.45 Å when used with either H_2O or O_3 as coreactants. While $^{t}BuN=Nb(NEt_2)_3$ appears to be the more commonly used ALD precursor in recent times, sub-stoichiometric growth of Nb_2O_5 with this precursor has been reported by using both H_2O and O_3 as coreactants individually[4,8]. It was also observed that films deposited with O_3 as coreactant had higher contamination levels compared to the case where H_2O was used as coreactant.

Although sub-stoichiometric growth of Nb_2O_5 has been reported, it has not been studied in detail. More specifically, a direct ALD process for Nb_2O_5 with both high GPC and good film quality along with stoichiometric film growth has not been reported in the literature. O_2 plasma is a well-known coreactant with a higher reactivity than H_2O and often gives rise to a higher GPC along with improved film quality and also reduced reactant purge times[31]. Therefore, in this work plasma-enhanced ALD (PE-ALD) of Nb_2O_5 using $^{t}BuN=Nb(NEt_2)_3$ with O_2 plasma and thermal ALD of Nb_2O_5 using H_2O as coreactants are investigated and both processes are compared. From here on, the thermal process with H_2O as coreactant will be referred to as thermal ALD, whereas the plasma process with O_2 plasma as coreactant will be referred to as PE-ALD. The GPC along with film properties, such as stoichiometry, purity, and optical constants are determined by employing various analysis techniques on the films deposited by both processes and are discussed and compared in detail.

7.2 Experimental Details

7.2.1 Atomic Layer Deposition

An Oxford Instruments Plasma Technology FlexAL ALD reactor was used for both thermal ALD and PE-ALD. This reactor was equipped with a remote inductively-coupled plasma source (ICP, 13.56 MHz) and the base pressure of the system was 10^{-6} Torr. The reactor was a warm wall reactor where wall temperature can be regulated between room temperature and a maximum temperature of 145 °C, independently. The warm wall temperature lead to longer residence time for reactant and product in the reactor so needed longer purge time in comparison to hot wall reactor (wall and table temperature are same) to avoid parasitic CVD reaction[32]. The similar system has been used for

depositing Al_2O_3 by both thermal ALD and PE-ALD[33]. More details about the reactor can be found in the literature.[34] The metal-organic precursor (tert-butylimido)-tris (diethylamino)-niobium "$^{t}BuN=Nb(NEt_2)_3$" (TBTDEN, 98% pure) was obtained from STREM chemical, Inc. The precursor was held in a stainless steel bubbler at 65 °C and was bubbled with Ar (99.999%, 100 sccm). The precursor supply line was maintained at 80 °C to avoid precursor condensation. The chamber wall was maintained at 145 °C for all investigated table temperatures. In the first half-cycle $^{t}BuN=Nb(NEt_2)_3$ was used as precursor, and the pressure was maintained at 80 mTorr for both the thermal ALD and PE-ALD processes using an automated pressure controller (APC). Ar (150-300 sccm) was employed as purge as well as carrier gas in both processes. The pressure was maintained at 80 mTorr in the second half-cycle of the thermal ALD process, using H_2O in the vapour phase as coreactant. In the PE-ALD process, O_2 plasma (100 sccm) was used as coreactant and the pressure during the second half-cycle was maintained at 10 mTorr. The ICP RF power was set to 200 W. The films were deposited at various table temperatures between 150 and 350 °C in both thermal ALD and PE-ALD processes. All depositions were conducted on Si substrates with a native oxide (SiO_2, ~2 nm).

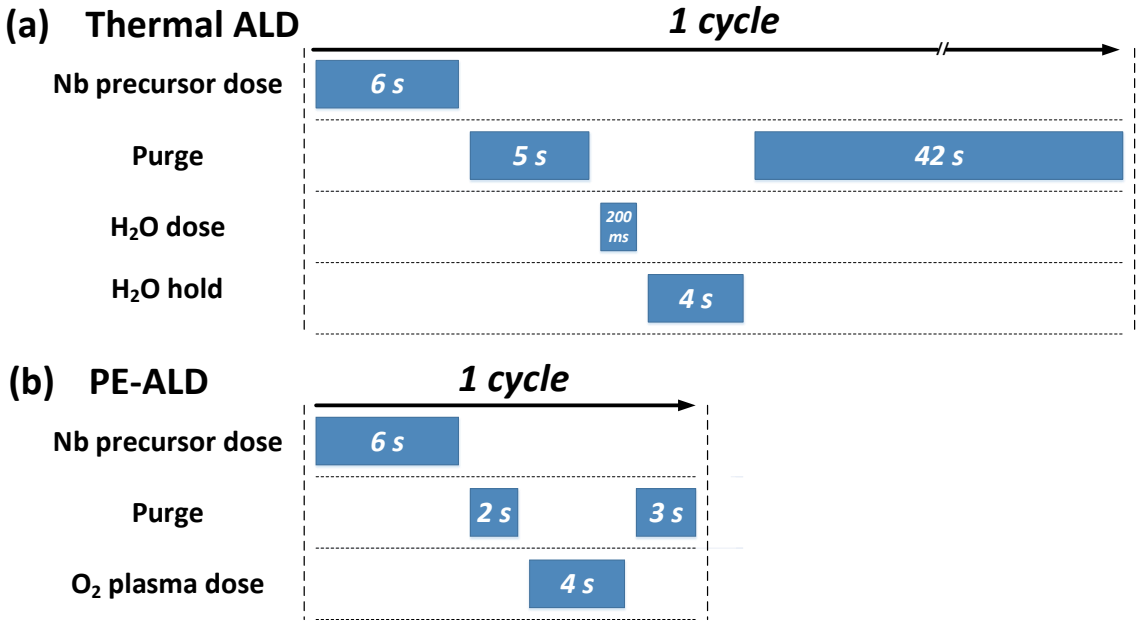

Figure 7.1 Schematic sketch of the standard recipe used for a) thermal ALD and b) PE-ALD of niobium oxide.

The optimized ALD recipes used are shown in Figure 7.1. They have a precursor dose time of 6 s, whereas the precursor purge time is 5 s in the thermal ALD process and 2 s in the PE-ALD process. The coreactant, H_2O in thermal ALD is dosed for 200 ms, while O_2

plasma in PE-ALD is dosed for 4s. Here, thermal ALD has an additional step to hold H_2O for 4 s. The coreactants purge time is 42 s in the former and is 3 s in the latter process. Note that the coreactant O_2 gas in PE-ALD is switched off before the purge step and only Ar is flown. The optimization of both ALD processes are discussed in detail in the Sec. 7.3.1.

7.2.2 Analysis Techniques

The film growth was monitored *in*-situ using a J.A. Woollam Co., Inc. M2000U rotating compensator spectroscopic ellipsometer (SE), over a photo energy range of 1.2 to 5 eV. CompleteEASE software was used to model the optical constants of the deposited film. The model consisted of a Si substrate, native oxide SiO_2, and Nb_2O_5 layers. The latter layer was modelled by employing two Tauc-Lorentz oscillators. More details on the SE technique and SE modelling can be found in the literature[35].

The elemental composition and valence band (VB) spectra were determined by X-ray photoelectron spectroscopy (XPS) using a Thermo Scientific KA1066 spectrometer employing monochromatic Al Kα (hν = 1486.6 eV) X-ray radiation. Rutherford backscattering spectrometry (RBS) and elastic recoil detection (ERD) measurements with a 1.9 MeV He^+ beam source were conducted by Detect 99 B.V. Eindhoven, The Netherlands to determine the composition and the mass density of the films. RBS was performed with two detectors at scattering angles of 150° and 170°. The hydrogen content was obtained in the same setup using ERD with the detector at a recoil angle of 30°. Grazing incidence X-ray diffraction (GI-XRD) measurements were performed to study the crystallinity of the film with a PANalytical X'Pert Pro MRD analyser, using a Cu Kα (λ = 1.54 Å) X-ray source.

7.3 Results and Discussion

7.3.1 ALD Film Growth

Films with a target thickness of ~30 nm were deposited on the starting substrate for both ALD processes at various deposition temperatures between 150 and 350 °C using the optimized ALD recipe shown in Figure 7.1. The film thickness for the initial 500 ALD cycles as-determined by *in-situ* SE is shown in Figure 7.2 as a function of the number of ALD cycles for all investigated deposition temperatures in both ALD processes. As clear from the Figure 7.2, a linear ALD growth behaviour is observed without any nucleation delay at

all deposition temperatures for both processes. The GPC was observed to decrease with increasing deposition temperature in both cases.

The self-limiting saturated growth behaviour was confirmed for both the thermal ALD and the PE-ALD processes at a deposition temperature of 200 °C, as shown in Figure 7.3. In thermal ALD, as seen in Figure 7.3(a-d), $^{t}BuN=Nb(NEt_2)_3$ precursor saturation was observed at 6 s exposure time when the H_2O exposure was fixed at 200 ms. The precursor purge with Ar (300 sccm) was observed to saturate at 5 s. The second half-cycle by using H_2O as coreactant saturated at 200 ms of exposure time. In the subsequent step, the APC valve was closed, to make sure that H_2O reacts with all adsorbed precursor sites uniformly. Reducing the duration of this step to less than 4 s resulted in poor thickness uniformity over an area of 200 mm diameter (as discussed later). In the following step, by fully opening the APC valve, Ar (300 sccm) was used to purge away remaining coreactants and by-products. This purge step saturated at 35 s. In comparison to the literature (where hot wall reactor was used)[20], the coreactant purge step needed longer time to reach saturation due to slow desorption of H_2O from the reaction walls (warm wall at 145 °C), which would otherwise result in parasitic CVD reactions.

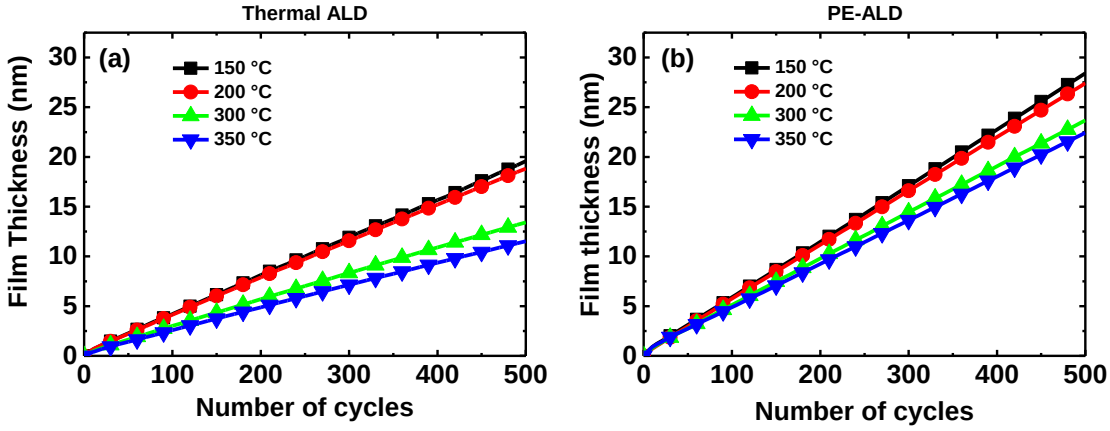

Figure 7.2 Thickness of Nb_2O_5 films as a function of the number of ALD cycles measured using *in-situ* SE for deposition temperatures between 150 °C and 350 °C, for both thermal ALD (a) and PE-ALD (b) processes.

In PE-ALD, as shown in Figure 7.3(e-h), precursor saturation was observed at 6 s exposure time similar to thermal ALD, when the coreactant O_2 plasma exposure time was fixed at 6 s. The Ar precursor purge (300 sccm) saturated at 1 s. In the next step, O_2 plasma (100 sccm) was used as coreactant and saturation occurred at 2 s. The following coreactant purge step saturated at 3 s. Note that this step was much shorter compared to the purge step in the thermal ALD process, because O_2 molecules are purged away rapidly

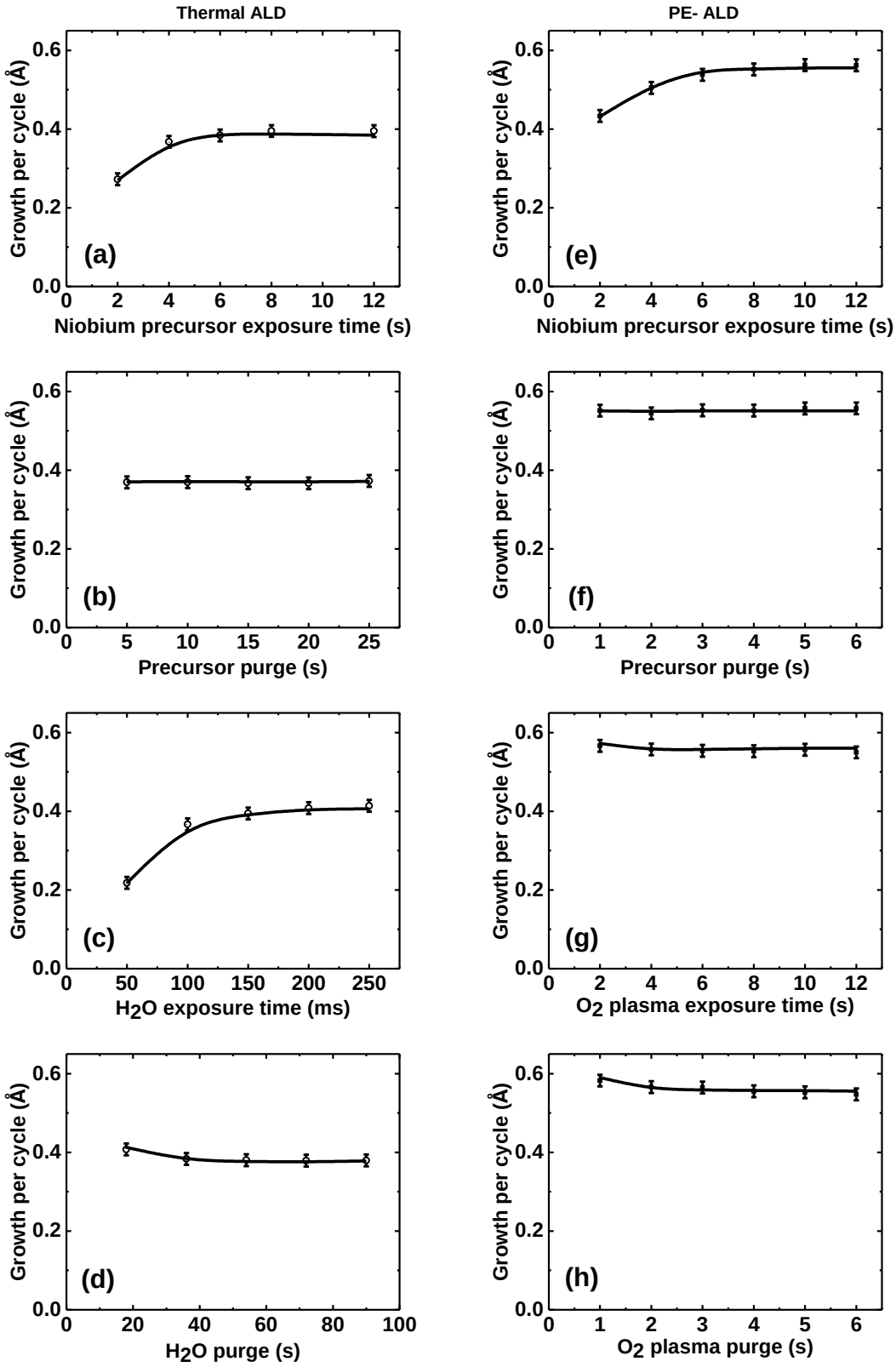

Figure 7.3 Saturation curves: GPC as a function of precursor (TBTDEN as Nb precursor), purge (Ar) and co-reactant flow time at 200 °C for both thermal ALD (a-d) and PE-ALD (e-h) processes with H_2O and O_2 plasma as co-reactants, respectively. The error bars indicate the fitting error in the SE measurements.

in comparison to the slow desorption of H_2O in the thermal ALD process. At 200 °C, the GPC was ~0.56 Å, which is higher in comparison to the thermal ALD process (~0.38 Å). Therefore, PE-ALD with O_2 plasma as coreactant enables a significantly shorter process time through both an enhanced GPC and a strongly reduced purge time.

In both thermal ALD and PE-ALD processes, the effect of deposition temperature on the film growth was studied by varying the deposition temperature between 150 and 350 °C. The growth per cycle (GPC_{SE}) was determined by calculating the slope for the last 100 cycles of the *in-situ* SE data shown in Figure 7.2. In both processes, the GPC_{SE} was observed to decrease with increasing deposition temperature, as shown in Figure 7.4. In thermal ALD, the GPC_{SE} decreases from 0.38 to 0.20 Å for temperatures ranging from 150 to 350 °C, whereas in PE-ALD the GPC_{SE} lowers from 0.58 to 0.45 Å. The growth per cycle (GPC_{RBS}) in terms of number of Nb atoms deposited per nm^2 per ALD cycle was calculated from RBS data by dividing the measured Nb atoms/nm^2 by the number of ALD cycles, see Figure 7.4 (right vertical axis). GPC_{RBS} decreases from 0.75 to 0.5 Nb atoms/nm^2 in the case of thermal ALD and from 1.1 to 0.8 Nb atoms/nm^2 in the case of PE-ALD when increasing the deposition temperature from 200 to 350 °C, which yields a similar trend when compared to GPC_{SE}. This evidently indicates that a decrease in GPC with increasing deposition temperature can be traced to reduced adsorption of Nb precursor per cycle at higher deposition temperatures. Similar behaviour has been previously observed in both thermal ALD as well as PE-ALD of Al_2O_3[33,36], where a decrease in GPC with increasing deposition temperature has been associated with thermally activated dehydroxylation reaction that reduce the concentration of surface –OH reactive sites. As the niobium oxide ALD processes are likely similar to that of Al_2O_3, the decrease in GPC with increasing deposition temperature is probably also due to thermally activated dehydroxylation reaction of surface –OH reactive sites.

For deposition temperatures of 200 °C and below, we observed a GPC of ~0.55 Å in our PE-ALD process, which is higher than previously reported values. Kulki *et al.*[19] and Liu *et al.*[25] reported a GPC of ~0.3 Å using $Nb(OEt)_5$ precursor with H_2O as co-reactant, while Blanquart *et al.*[20] reported a GPC of ~0.4 Å and ~0.45 Å with H_2O and O_3 as co-reactants, respectively using the same precursor $^tBuN{=}Nb(NEt_2)_3$. Generally, it appears that the GPC of the PE-ALD process is higher than the thermal ALD process for all investigated deposition temperatures. Therefore, it appears that an O_2 plasma is a more effective oxidant than H_2O as co-reactant such that it allows more Nb precursor molecules to adsorb on the surface per cycle. An extension of the Blanquart *et al.* work was reported by

Tomczak *et al.*[22] on the reaction mechanism using *in-situ* analysis techniques for the same precursor $^{t}BuN=Nb(NEt_2)_3$ with D_2O and O_3 as co-reactants. In case of the D_2O process, it was observed that -NEt_2 ligands reacted with the surface –OH reactive sites during the first half cycle, while the remaining ligands were exchanged during the second half cycle. The above mentioned reaction mechanism could also be speculated here for the thermal ALD of Nb_2O_5 with H_2O. In case of the O_3 process, it was speculated by Tomczak *et al.* that no –OH reactive sites were formed and all ligands were exchanged during the second half cycle. The above reaction mechanism could also be speculated here for the PE-ALD of Nb_2O_5 with O_2 plasma. However, in this case, the enhanced GPC observed with O_2 plasma could not be explained with this mechanism, as a lower GPC of ~0.45 Å was observed with O_3. Similar to other material systems, surface –OH reactive sites could be formed in an O_2 plasma, which could explain the enhanced GPC observed for PE-ALD of Nb_2O_5[37]. Similar behaviour was also observed for Al_2O_3 where PE-ALD with O_2 plasma shows higher GPC than thermal ALD with H_2O[33,36]. Thus, alternatively, similar to the reaction mechanism of Al_2O_3 with O_2 plasma[38]. It could also be hypothesized that a ligand reacts with surface –OH reactive site in the first half cycle, while the remaining ligands react with O_2 plasma species forming –OH surface groups, and H_2O, CO_x, NO_x by-products.

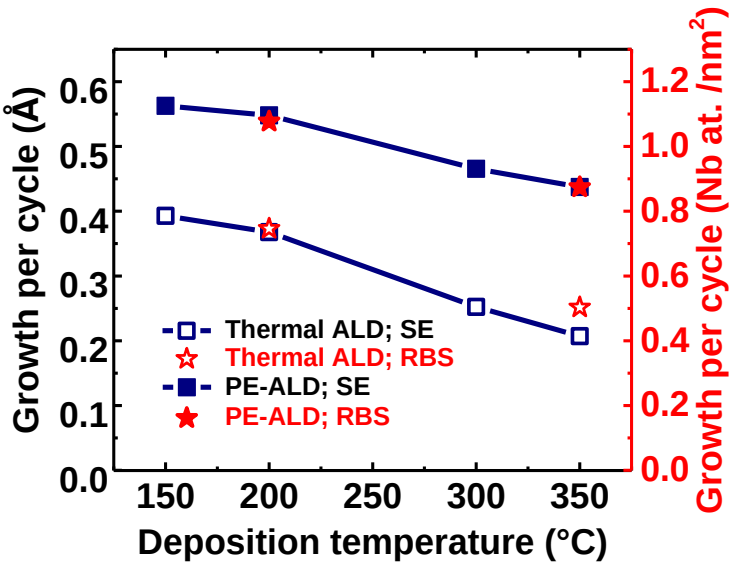

Figure 7.4 Growth per cycle (GPC_{SE}) measured using *in-situ* SE (left vertical axis) and deposited Nb atoms per nm^2 (GPC_{RBS}) measured using RBS (right vertical axis) for both the thermal ALD (open symbols) and the PE-ALD (close symbols) processes at various deposition temperatures between 150 °C and 350 °C.

The uniformity of both thermal ALD and PE-ALD films were determined using *ex-situ* SE by mapping a ~20 nm thick film over a 200 mm diameter Si wafer, see Figure 7.5. The

thickness non-uniformity was calculated by dividing the difference between the maximum and the minimum thickness by the average thickness. The non-uniformity in the thermal ALD grown film was around ±3.3%, whereas in the PE-ALD grown film it was around ±4.4%. In case of thermal ALD (Figure 7.5a), the decline in thickness was observed from the upper left to the bottom right. This non-uniformity in thickness was considered to originate from both the precursor and H_2O flow direction. In case of PE-ALD (Figure 7.5b), the higher thickness was observed in the middle of the wafer. Here, the non-uniformity was attributed to a non-uniform distribution of O_2 plasma over a 200 mm diameter substrate[39] as well as the precursor flow direction. Although the uniformity is fair for both processes, it may be further improved by increasing the H_2O dose or hold time in case of thermal ALD and by increasing the O_2 plasma dose time in case of PE-ALD process, and also by further optimizing precursor does time in both the cases.

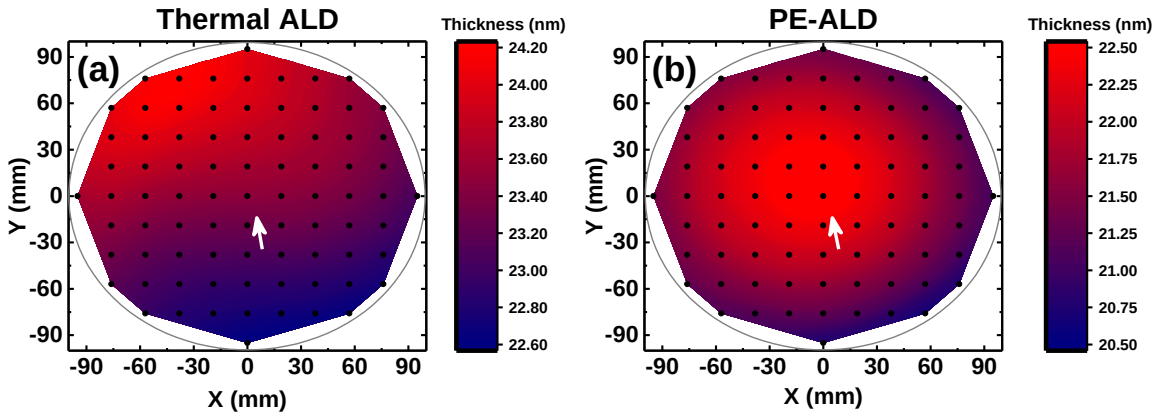

Figure 7.5 Thickness uniformity contour plot obtained using *ex-situ* SE mapping on (a) the thermal ALD and (b) the PE-ALD grown film over a 200 mm Si wafer at 200 °C. The white arrow shows the position of the precursor inlet as well as the flow direction above the wafer in the reactor. The exhaust is directly below the wafer stage in the reactor.

7.3.2 Film Characterization

Self-limiting growth of Nb_2O_5 was shown for both thermal ALD and PE-ALD in the Sec. 7.3.1. In this section, the material properties of the Nb_2O_5 films of ~30 nm thickness are discussed, utilizing various analytical techniques, to study their composition, density, and optical properties.

The effect of the temperature on the composition and quality of the films was determined using RBS. The RBS measurements were performed on both thermal ALD and PE-ALD deposited films at 200 and 350 °C. The O/Nb ratio in Table 7.1 shows that the

thermal ALD deposited films are sub-stoichiometric with all values being below 2.5 and the O/Nb ratio decreases when raising the deposition temperature from 200 to 350 °C. The sub-stoichiometric (Nb_2O_{5-X}) nature of the films can be linked to oxygen vacancies[1], and the further decline in O/Nb ratio at 350 °C indicates an increase in the number of oxygen vacancies with increasing deposition temperature. In the case of PE-ALD deposited films, the O/Nb ratio was ~2.5 illustrating the near stoichiometry of the films. All the deposited films show no traces of impurities in the films other than hydrogen. The carbon detection limit was relatively high at 10 at.% and it was detected only on the surface due to exposure to atmosphere. Around 3 at.% of H was detected using ERD in all the films and it was observed to decrease with temperature for both ALD processes.

XPS measurements were performed to determine the composition and also to further assess the quality of the films. Depth profiling of the films by means of sputtering with Ar^+ ions was performed to avoid surface impurities, but it resulted in preferential sputtering of O over Nb atoms and caused reduction of Nb^{+5} to lower oxidation state. Therefore, spectra acquired before sputtering were used to estimate the chemical states. Figure 7.6 shows the Nb3d and O1s core level XPS spectra of the films deposited at 200 and 350 °C for both the thermal ALD Figure 7.6(a and b) and the PE-ALD Figure 7.6(c and d) processes. All the XPS spectra shown in Figure 7.6 were calibrated by setting the carbon C-C bond peak to 248.8 eV in the C1s XPS spectra. In the Nb3d spectrum, as seen in Figure 7.6(a and c), the doublet $Nb3d_{5/2}$ and $Nb2d_{3/2}$ components are located at ~207.4 and ~210.2 eV, respectively. This corresponds to the Nb^{+5} oxidation state with the spin-split orbital components (between $Nb3d_{5/2}$ and $Nb3d_{3/2}$) of Δ~2.8 eV. An additional doublet at ~1.5 eV towards lower binding energy (BE) at ~205.9 eV is attributed to the Nb^{+4} oxidation state[40]. In the O1s spectrum, the peak centred around 530-531 eV corresponds to metal oxide O-Nb bonds and a second peak at ~532 eV to O-H bonds or other surface species originating from ambient exposure after deposition.

Table 7.1 Material properties of thermal ALD and PE-ALD deposited niobium oxide thin film at various temperatures between 150 °C and 350 °C, as determined from SE, RBS and ERD measurements. All films were ~30nm thick and the GPC was calculated from the last 100 cycles by *in-situ* SE. The refractive index (at 2.1 eV) and the Tauc band gap were also determined from SE. The number of deposited Nb atoms/nm^2 per ALD cycle and the O/Nb ratio were determined by RBS. The mass density was calculated using both RBS and thickness from SE. The H content was determined by ERD. The typical error range is indicated in the first row.

Process	T (°C)	GPC_{SE} (Å)	Refractive Index	E_g (eV)	GPC_{RBS} (at. nm^{-2} cycle^{-1})	Mass Density (g cm^{-3})	O/Nb ratio	H (at. %)
Error		*±0.03*	*±0.03*	*±0.03*	*±0.04*	*±0.1*	*±0.05*	*±0.1*
Thermal ALD	150	0.39	2.35	3.47	-	-	-	-
	200	0.37	2.37	3.45	0.75	4.35	2.36	3.38
	300	0.25	2.40	3.43	-	-	-	-
	350	0.21	2.46	3.36	0.50	4.98	2.22	1.97
PE-ALD	150	0.56	2.36	3.47	-	-	-	-
	200	0.55	2.36	3.47	1.08	4.11	2.48	2.9
	300	0.47	2.36	3.47	-	-	-	-
	350	0.44	2.36	3.47	0.87	4.10	2.49	2.37

"-" *no data*

In the case of PE-ALD films, the O1s spectrum in Figure 7.6d shows that the metal oxide peak centre is located at 530.3 eV for both temperatures. In the Nb3d spectrum, the $Nb3d_{5/2}$ component peak centre was observed at 207.3 eV (FWHM = 1.17 eV) for both temperatures, along with a negligible presence of the Nb^{+4} oxidation state. This confirms the near stoichiometry of the films with Nb_2O_5 composition. In the case of thermal ALD, for the 200 °C film the $Nb3d_{5/2}$ component peak centre shifts to 207.4 eV along with a further broadening (FWHM = 1.23 eV) and a similar shift in the metal oxide peak centre to 530.5 eV was observed. The broadening of the FWHM and shift in peak centre to higher binding energies have previously been associated with oxygen vacancies in the film[41]. For the 350 °C film, the $Nb3d_{5/2}$ peak FWHM further increases to 1.36 along with an additional 0.1 eV shift to 207.5 eV. The O1s metal oxide peak also further shifts to 530.8 eV indicating an increase in oxygen vacancies. Additionally, the second $Nb3d_{5/2}$ peak corresponding to the Nb^{+4} oxidation state is also significant at this temperature in the thermal ALD case, in contrast to the PE-ALD film. This confirms the presence of oxygen

vacancies and supports the RBS measurements with the suggested sub-stoichiometric nature of thermal ALD deposited Nb_2O_{5-X} films. From the deconvolution of the Nb3d peaks of the thermal ALD films, it is estimated that ~7% of the total Nb3d originates from the Nb^{+4} oxidation state for the 200 °C film, whereas at 350 °C this increases to ~12%. Carbon was only observed at the surface for all the deposited films, and its concentration was reduced to a negligible amount (identical to RBS measurements) after depth profiling. No other impurities were detected by XPS both before as well as after sputtering.

XPS valence band (VB) studies were performed on both the thermal ALD and the PE-ALD deposited films to further confirm oxygen vacancies observed in the films, see Figure 7.7. The Fermi level (BE = 0 eV) was calibrated by measuring the Fermi edge of gold. In thermal ALD films, trap states were observed between the valence band maximum (E_{VB}) and Fermi level (E_F), as seen in Figure 7.7b, whereas in the PE-ALD films no such trap states were observed. The localized trap states between E_{VB} and E_F have previously also been observed in various other materials, such as Ta_2O_5[41,42], and TiO_2[43] where it was attributed to the presence of oxygen vacancies. The number of trap states observed in the thermal ALD films increases with deposition temperature and could therefore be correlated with oxygen vacancies in the film, confirming observations from both the RBS and the XPS measurements. The trap states were not observed for films grown at temperatures below 300 °C contrary to the previous measurements. Presumably, the trap state density was too low to be detected by the XPS system used. The higher reactivity of the O_2 plasma compared to H_2O with the precursor can be speculated to be the reason for obtaining stoichiometric films with no significant amount of oxygen vacancies in the PE-ALD process.

The refractive index data (at 2.1 eV) shown in Table 7.1 were obtained from *ex-situ* SE mesurements. In case of PE-ALD films, the refractive index at 2.36 does not vary with the deposition temperature. Similarly, the mass density of both 200 and 350 °C films is 4.1 g/cm^3 around 90% of the Nb_2O_5 bulk density. Based on the literature, the bulk density is 4.5 g/cm^3 for Nb_2O_5 and 5.9 g/cm^3 for NbO_2[13]. This is typical for ALD grown amorphous films to have lower density than bulk density. In case of thermal ALD films, the refractive index increases from 2.35 to 2.46 with increasing deposition temperature.

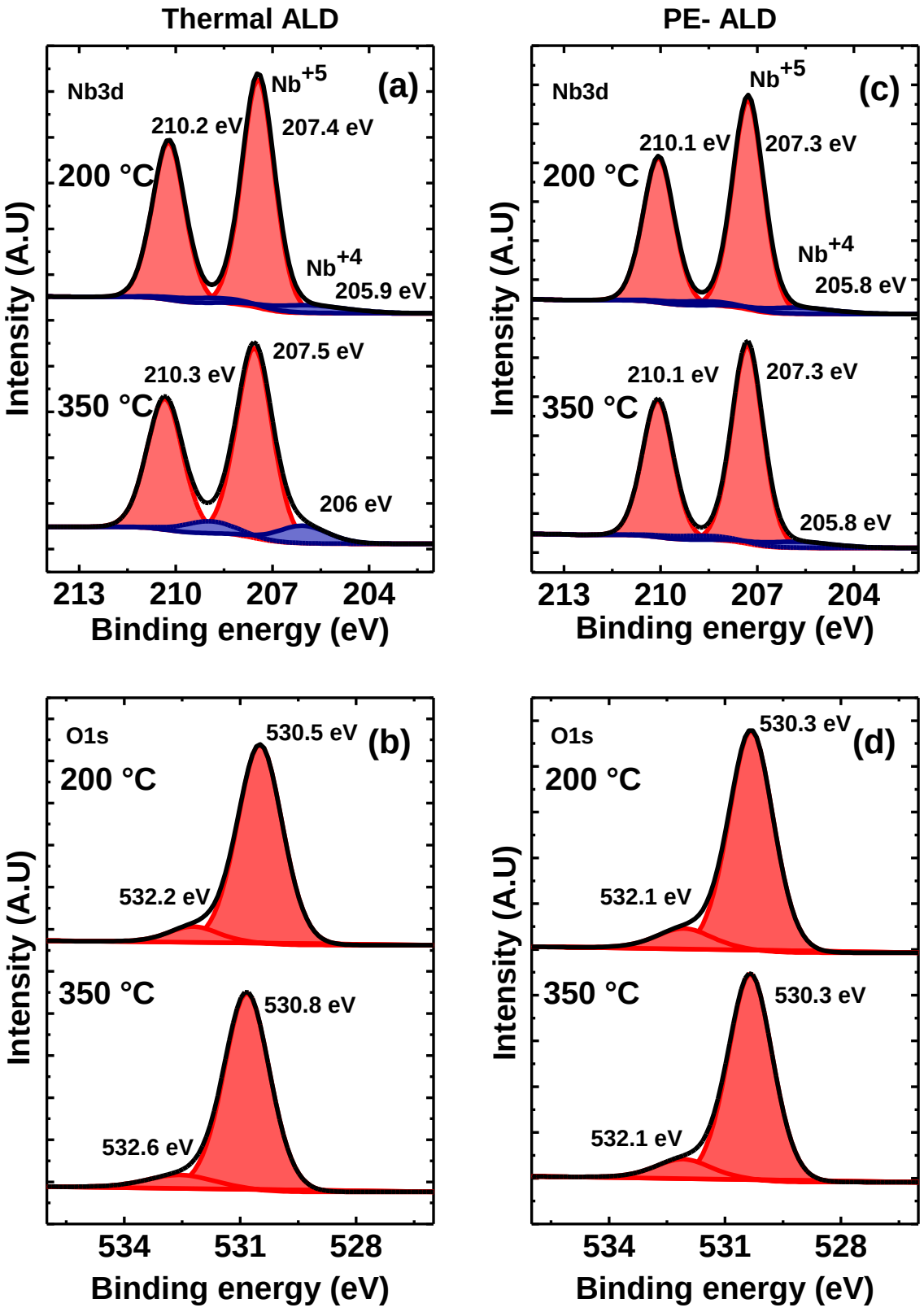

Figure 7.6 Nb3d and O1s XPS spectra for both the thermal ALD (a & b) and the PE-ALD (c & d) deposited films at 200 °C and 350 °C.

Likewise, the mass density increases from 4.35 g/cm^3 at 200 °C to 4.98 g/cm^3 at 350 °C. Interestingly thermal ALD films have higher density than PE-ALD films at all temperatures, and for 350 °C film the density was apparently higher than the bulk density of Nb_2O_5. This increase in density could potentially be explained by relating to the presence of oxygen vacancies in the form of Nb^{+4} oxidation states in the films. As the bulk density of niobium oxide at Nb^{+4} oxidation state (NbO_2) is higher than it is at the Nb^{+5} oxidation state (Nb_2O_5) presences of small faction of Nb^{+4} oxidation state would increase the density of the films. This also explains the density of the 350 °C film above the bulk density as the oxygen vacancies in the film increases with deposition temperature, which is consistent to other observations.

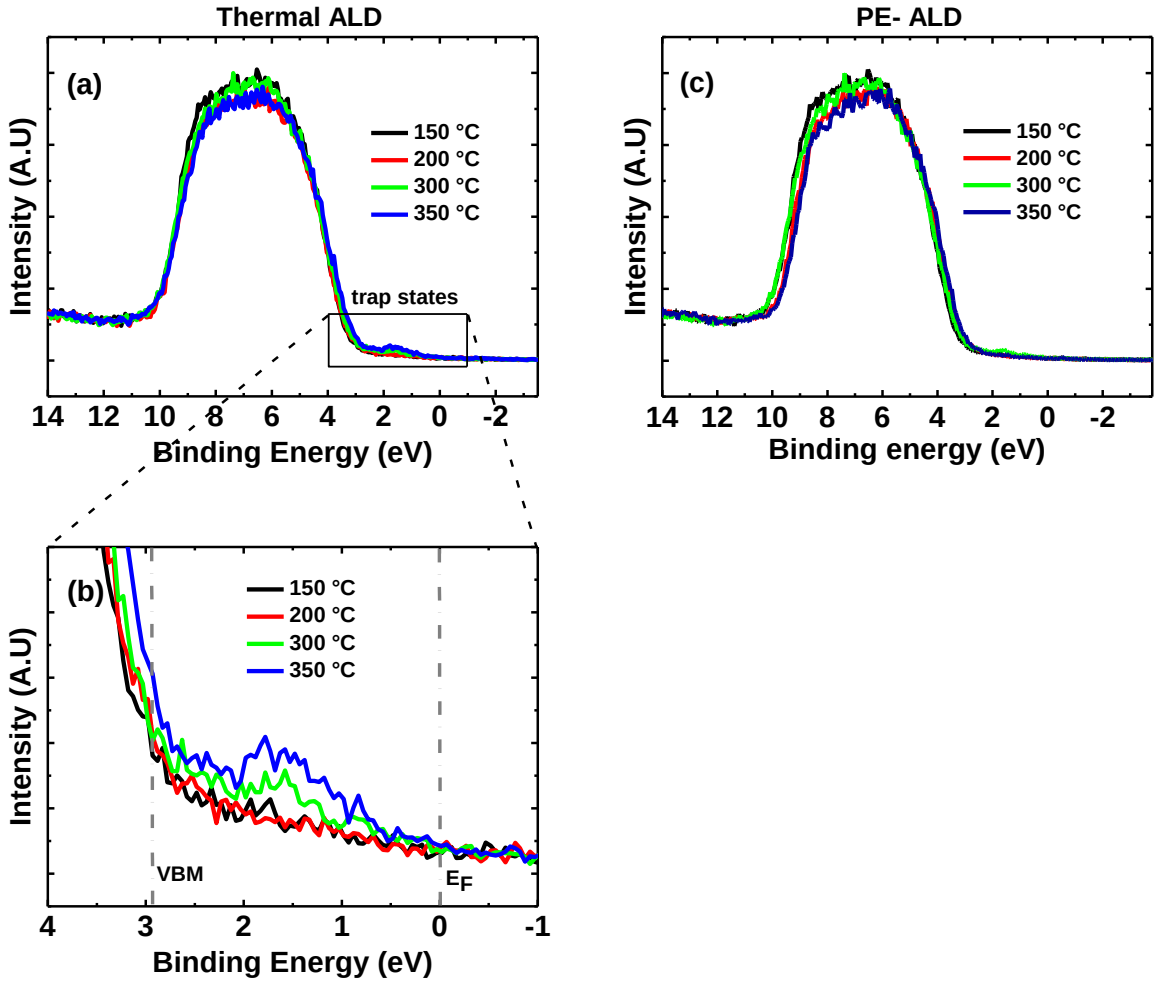

Figure 7.7 Valence band spectra for (a) thermal ALD and (c) PE-ALD films deposited at temperatures between 150 °C and 350 °C. Plot (b) shows a magnified part of the inset shown in (a).

The absorption co-efficient was obtained from *ex-situ* SE measurements. GI-XRD measurements revealed that all films deposited by thermal ALD and PE-ALD are amorphous regardless of the deposition temperature. Based on the absorption coefficient data, the optical band gap of the films can be determined using the Tauc equation: $(\alpha h\nu)^{1/2} \sim (h\nu - E_g)$, where α is the absorption coefficient, hν is the photon energy, E_g is the optical band gap, and the exponent '1/2' corresponds to the allowed indirect transition in the amorphous film[44,45]. The optical band gap from the Tauc plot ($(\alpha h\nu)^{1/2}$ vs hν) was estimated by extrapolating the linear region of the curve to zero absorption. The tail region below the optical band gap (linear region) in Figure 7.8 is most likely due to localized states and trap states (from defects) between the valence and conduction bands, as were also observed from XPS. In the case of thermal ALD films, the band gap was ~3.5 eV as shown in Table 7.1, but a small shift towards lower band gap was observed with increasing deposition temperature corresponding to oxygen vacancies present in the film. Lee *et al.*[24] also observed a similar reduction in band gap for niobium oxide films with increasing oxygen vacancies. Along with this reduction, the influence of oxygen vacancies in the films was further confirmed by a widening of the tail region towards the lower photon energy into the band gap. In case of PE-ALD films, the optical band gap was 3.5 eV, and the deposition temperature did not have any effect on the optical band gap of the films.

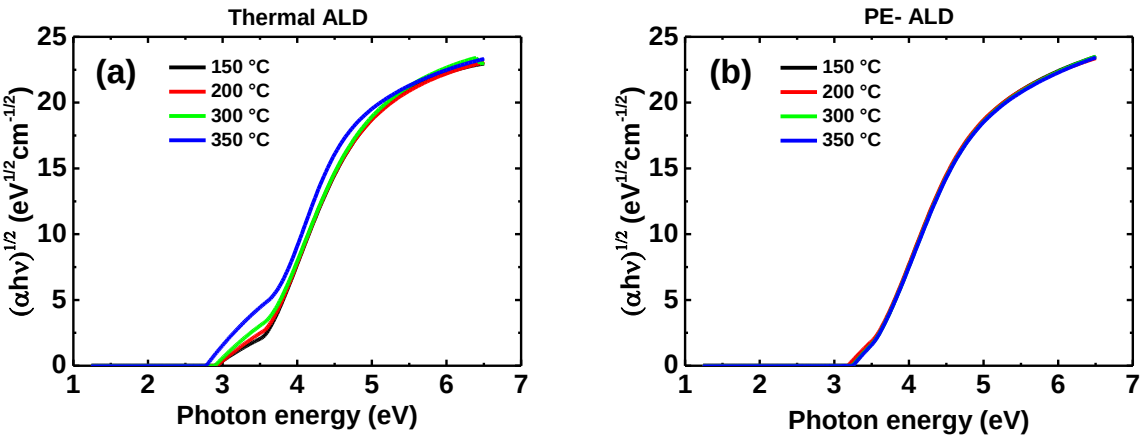

Figure 7.8 Tauc plot determined from the absorption coefficient measured by *ex-situ* SE for (a) thermal ALD and (b) PE-ALD films deposited at temperatures between 150 °C and 350 °C.

7.4 Conclusion

Nb_2O_5 thin films were deposited by both a thermal ALD and a PE-ALD process with H_2O and O_2 plasma as coreactants, respectively. The self-limiting saturated growth was confirmed for both processes at 200 °C and a high uniformity over a 200 mm Si wafer was obtained. All the films were of high quality with no detectable contamination apart from a H content of ~3 at.%. The PE-ALD process showed higher growth per cycle than the thermal ALD process due to enhanced Nb adsorption. The effects of deposition temperature were studied by varying the temperature between 150 and 350 °C in both processes. From RBS, XPS and SE the thermal ALD films were found to be sub-stoichiometric due to the presence of oxygen vacancies which observed to be more dominantly present in the film with increasing deposition temperature. The PE-ALD films were near stoichiometric in the entire investigated deposition temperature range. This work shows that the composition, density and sub-band gap states of Nb_2O_5 can be controlled by choosing the ALD process and processing temperature. This is advantageous for many applications in which Nb_2O_5 can be used, such as solar cells, microelectronic devices, and sensors.

Acknowledgments

The authors acknowledge Jeroen van Gerwen and Christian van Helvoirt for their technical assistance. Saurabh Karwal, Alfredo Mameli and Shashank Balasubramanyam for the valuable suggestions and Aileen O´Mahony from OIPT, UK for the assistance with uniformity measurements. The work of author J. Melskens was supported by the Netherlands Organisation for Scientific Research under the Dutch TTW-VENI Grant 15896. This work was supported by the European Research Council (grant agreement number: 648787).

References

[1] C. Nico, T. Monteiro, and M.P.F. Graça, Prog. Mater. Sci. **80**, 1 (2016).

[2] R.A. Rani, A.S. Zoolfakar, A.P. O'Mullane, M.W. Austin, and K. Kalantar-Zadeh, J. Mater. Chem. A **2**, 15683 (2014).

[3] T. Blomberg, C. Wenger, C. Baristiran Kaynak, G. Ruhl, and P. Baumann, Microelectron. Eng. **88**, 2447 (2011).

[4] H. García, H. Castán, E. Perez, S. Dueñas, L. Bailón, T. Blanquart, J. Niinistö, K. Kukli, M. Ritala, and M. Leskelä, Semicond. Sci. Technol. **28**, 055005 (2013).

[5] N. Alimardani, J.M. McGlone, J.F. Wager, and J.F. Conley, J. Vac. Sci. Technol. A Vacuum, Surfaces, Film. **32**, 01A122 (2014).

[6] M.E. Gimon-Kinsel and K.J. Balkus, Microporous Mesoporous Mater. **28**, 113 (1999).

[7] A. Kohli, C.. Wang, and S.. Akbar, Sensors Actuators B Chem. **56**, 121 (1999).

[8] W.L. Hoffeditz, M.J. Pellin, O.K. Farha, and J.T. Hupp, Langmuir **33**, 9298 (2017).

[9] H. Cui, G. Zhu, Y. Xie, W. Zhao, C. Yang, T. Lin, H. Gu, and F. Huang, J. Mater. Chem. A **3**, 11830 (2015).

[10] W. Hu, Y. Mi, D. Tian, Y. Zhao, Z. Liu, K. Yao, and Y. Zhu, Mater. Chem. Phys. **109**, 184 (2008).

[11] H. Simchi, T.N. Walter, T.H. Choudhury, L.Y. Kirkley, J.M. Redwing, and S.E. Mohney, J. Mater. Sci. **52**, 10127 (2017).

[12] N. Özer, D.-G. Chen, and C.M. Lampert, Thin Solid Films **277**, 162 (1996).

[13] E. Çetinörgü, B. Baloukas, O. Zabeida, J.E. Klemberg-Sapieha, and L. Martinu, Appl. Opt. **48**, 4536 (2009).

[14] D.-D. Zhao, Q.-Y. Cai, Y.-X. Zheng, J.-B. Zhang, S.-D. Yang, L. Yang, Z.-H. Liu, R.-J. Zhang, S.-Y. Wang, and L.-Y. Chen, J. Phys. D. Appl. Phys. **49**, 265304 (2016).

[15] M.T. Duffy, C.C. Wang, A. Waxman, and K.H. Zaininger, J. Electrochem. Soc. **116**, 234 (1969).

[16] R. Romero, J.R. Ramos-Barrado, F. Martin, and D. Leinen, Surf. Interface Anal. **36**, 888 (2004).

[17] R. Romero, E.A. Dalchiele, F. Martín, D. Leinen, and J.R. Ramos-Barrado, Sol. Energy Mater. Sol. Cells **93**, 222 (2009).

[18] J.-P. Masse, H. Szymanowski, O. Zabeida, A. Amassian, J.E. Klemberg-Sapieha, and L. Martinu, Thin Solid Films **515**, 1674 (2006).

[19] K. Kukli, M. Ritala, M. Leskelä, and R. Lappalainen, Chem. Vap. Depos. **04**, 29 (1998).

[20] T. Blanquart, J. Niinistö, M. Heikkilä, T. Sajavaara, K. Kukli, E. Puukilainen, C. Xu, W. Hunks, M. Ritala, and M. Leskelä, Chem. Mater. **24**, 975 (2012).

[21] A. Brodie, P. De Cecco, C. Bevis, J.R. Maldonado, R. Bhatia, E. Deguns, and G.M.

Sundaram, in *ECS Trans.* (2010), pp. 101–110.

[22] Y. Tomczak, K. Knapas, M. Sundberg, M. Leskelä, and M. Ritala, Chem. Mater. **24**, 1555 (2012).

[23] T. Blanquart, K. Kukli, J. Niinisto, V. Longo, M. Heikkila, M. Ritala, and M. Leskela, ECS Solid State Lett. **1**, N1 (2012).

[24] S.-H. Lee, J.-D. Kwon, J.-H. Ahn, and J.-S. Park, Ceram. Int. **43**, 6580 (2017).

[25] J. Liu, Y. Xu, Q. Sun, H. Lu, and D.W. Zhang, Mater. Lett. **65**, 2182 (2011).

[26] M. Rooth, K. Kukli, and A. Hårsta, in *Proc. - Electrochem. Soc.* (2005), pp. 598–604.

[27] K.-E. Elers, M. Ritala, M. Leskelä, and E. Rauhala, Appl. Surf. Sci. **82–83**, 468 (1994).

[28] J.P. Correa Baena, L. Steier, W. Tress, M. Saliba, S. Neutzner, T. Matsui, F. Giordano, T.J. Jacobsson, A.R. Srimath Kandada, S.M. Zakeeruddin, A. Petrozza, A. Abate, M.K. Nazeeruddin, M. Grätzel, and A. Hagfeldt, Energy Environ. Sci. **8**, 2928 (2015).

[29] A. Guerrero, G. Garcia-Belmonte, I. Mora-Sero, J. Bisquert, Y.S. Kang, T.J. Jacobsson, J.-P. Correa-Baena, and A. Hagfeldt, J. Phys. Chem. C **120**, 8023 (2016).

[30] H.C.M. Knoops, S.E. Potts, A.A. Bol, and W.M.M. Kessels, in *Handb. Cryst. Growth*, Second Edi (Elsevier, Amsterdam, 2015), pp. 1101–1134.

[31] H.B. Profijt, S.E. Potts, M.C.M. van de Sanden, and W.M.M. Kessels, J. Vac. Sci. Technol. A Vacuum, Surfaces, Film. **29**, 050801 (2011).

[32] G.B. Rayner and S.M. George, J. Vac. Sci. Technol. A Vacuum, Surfaces, Film. **27**, 716 (2009).

[33] J.L. van Hemmen, S.B.S. Heil, J.H. Klootwijk, F. Roozeboom, C.J. Hodson, M.C.M. van de Sanden, and W.M.M. Kessels, J. Electrochem. Soc. **154**, G165 (2007).

[34] S.B.S. Heil, J.L. van Hemmen, C.J. Hodson, N. Singh, J.H. Klootwijk, F. Roozeboom, M.C.M. van de Sanden, and W.M.M. Kessels, J. Vac. Sci. Technol. A Vacuum, Surfaces, Film. **25**, 1357 (2007).

[35] E. Langereis, S.B.S. Heil, H.C.M. Knoops, W. Keuning, M.C.M. van de Sanden, and W.M.M. Kessels, J. Phys. D. Appl. Phys. **42**, 073001 (2009).

[36] S.E. Potts, G. Dingemans, C. Lachaud, and W.M.M. Kessels, J. Vac. Sci. Technol. A Vacuum, Surfaces, Film. **30**, 021505 (2012).

[37] S.E. Potts, H.B. Profijt, R. Roelofs, and W.M.M. Kessels, Chem. Vap. Depos. **19**, 125 (2013).

[38] E. Langereis, M. Bouman, J. Keijmel, S. Heil, M.C. Van de Sanden, and W.M. Kessels, in *ECS Trans.* (ECS, 2008), pp. 247–255.

[39] K.-E. Elers, T. Blomberg, M. Peussa, B. Aitchison, S. Haukka, and S. Marcus, Chem. Vap. Depos. **12**, 13 (2006).

[40] Z. Weibin, W. Weidong, W. Xueming, C. Xinlu, Y. Dawei, S. Changle, P. Liping, W. Yuying, and B. Li, Surf. Interface Anal. **45**, 1206 (2013).

[41] K. V Egorov, D.S. Kuzmichev, P.S. Chizhov, Y.Y. Lebedinskii, C.S. Hwang, and A.M.

Markeev, ACS Appl. Mater. Interfaces **9**, 13286 (2017).

[42] M. V. Ivanov, T. V. Perevalov, V.S. Aliev, V.A. Gritsenko, and V. V. Kaichev, J. Appl. Phys. **110**, 024115 (2011).

[43] S. Wang, L. Zhao, L. Bai, J. Yan, Q. Jiang, and J. Lian, J. Mater. Chem. A **2**, 7439 (2014).

[44] J. Tauc, R. Grigorovici, and A. Vancu, Phys. Status Solidi **15**, 627 (1966).

[45] S. Balasubramanyam, A. Sharma, V. Vandalon, H.C.M. Knoops, W.M.M. (Erwin) Kessels, and A.A. Bol, J. Vac. Sci. Technol. A Vacuum, Surfaces, Film. **36**, 01B103 (2018).

Conclusions and Outlook

8

Beyond widely studied semiconducting group VI layered transition metal dichalcogenides (TMDCs), there are other relatively less explored layered transition metal chalcogenides (TMCs). These less explored TMCs also exhibit complementing or similar material properties such as metallic TMDCs and semiconducting transition metal trichalcogenides (TMTCs). The latter TMCs materials are recently starting to gain research interests for various applications such as (opto)electronics and electrocatalysis. In addition to TMCs in their primitive form, heterostructures of TMCs have become of relevance due to the improved device performance and novel properties they present. In terms of synthesis techniques, atomic layer deposition (ALD) is gaining momentum for TMC fabrication. ALD can offer benefits such as high quality, uniform, conformal, and scalable films with a high degree of thickness control over a large area at low processing temperatures.

This dissertation work has focused on the fabrication of lesser-known TMCs (disulfides and trisulfides of Ti and Nb) and oxides (for indirect TMDC growth through sulfurization of oxides) by ALD. This work also investigates the ability of ALD to control the TMC phase, and to form TMC based heterostructures on both planar and 3D substrates. This dissertation also targeted to investigate the catalytic performance of ALD grown metallic TMDCs for the hydrogen evolution reaction (HER). The following conclusions can be drawn from the research described in this thesis:

- New ALD processes were developed for TiS_x (group IV) and NbS_x (group V) using the metal-organic precursors tetrakis(dimethylamido)titanium (TDMAT) and (tert-butylimido)-tris(diethylamino)-niobium (TBTDEN), respectively. For both material systems, thermal ALD and plasma-enhanced ALD (PE-ALD) processes were developed using H_2S gas or H_2S plasma as coreactant. Control over the ALD process parameters such as deposition temperature, coreactant type, and coreactant chemistry offered opportunities to tune various properties. This includes film properties: stoichiometry, morphology, crystallinity and band structure, and material functionalities: resistivity and catalytic performance.

- Phase-engineering between TMDCs and TMTCs was achieved for both TiS_x and NbS_x systems. The phase-controlled synthesis was obtained by varying deposition temperature and coreactant type (H_2S gas or H_2S plasma). In both material systems, the TMTC phase (TiS_3 and NbS_3) was synthesized using H_2S plasma (PE-ALD), especially at lower deposition temperatures. At higher deposition temperature, the TMDC phase (TiS_2 and NbS_2) was grown. In the case of H_2S gas as co-reactant (thermal ALD), only the

TMDC phase (TiS_2 and NbS_2) was fabricated. From optical emission spectra (OES), it was speculated that the generation of S_2 species in the H_2S plasma (absent in H_2S gas) led to the TMTC growth during PE-ALD processes. As TMTC (both TiS_3 and NbS_3) crystal structures have two third of their S atoms in the form of S-S pairs (S_2), S_2 species promote their formation. The phase transition temperature between TMTC and TMDC was ~120 °C and ~ 350 °C for the TiS_x and NbS_x system, respectively. This transition temperature is lower than that observed using the CVT method for both material systems. In the NbS_x system, the phase-controlled synthesis between NbS_3 and NbS_2 was demonstrated at a constant deposition temperature of 300 °C by adding excess H_2 gas to the coreactant plasma composition. The excess H_2 in the coreactant composition contributes to the reduction reactions for NbS_2 growth and plays a significant role in the phase change from NbS_3 to NbS_2 at 300 °C. In this work, all TMTC (TiS_3 and NbS_3) films synthesized were amorphous, while TMDC (TiS_2 and NbS_2) films synthesized by both thermal ALD and PE-ALD were poly-crystalline in nature. The amorphous TiS_3 film was crystalized by a post-annealing treatment in S atmosphere. As a result, photoluminescence was detected for the post-annealed few layer TiS_3 film at ~0.9 eV, indicating the material´s direct semiconducting nature of the material.

- The impact of the deposition temperature on the material properties during thermal ALD of TMDCs (TiS_x and NbS_x) was investigated. In both material systems, stoichiometry and morphology of the films were greatly influenced as a function of the deposition temperature. The stoichiometry was observed to vary from close to stoichiometric (transition metal to sulfur ratio of 2) at lower deposition temperatures to sub-stoichiometric (ratio of < 1.5) at higher deposition temperatures. This reduction in stoichiometry caused the resistivity of the films to decrease with increasing deposition temperatures. In addition, the morphology of the film changed, as the density of out-of-plane-orientation (OoPO) structures was suppressed at higher deposition temperatures.

- The direct growth of a TMDC (NbS_x) on another TMDC (TiS_x) was achieved, resulting in the fabrication of 2D TMDC-TMDC heterostructures using ALD in the form of TiS_x-NbS_x heterostructures at low deposition temperatures ($\leq$ 300 °C). The precise control over the thickness of the individual material layer was demonstrated by fabricating a multilayer (5-layer) heterostructure with varying individual layer thickness. In addition to deposition on a planar substrate, high-quality uniform and conformal growth of

TMDC-TMDC heterostructures were demonstrated on a complex 3D structure by depositing the multilayer heterostructure on an array of nanowires.

- The deposition of metal-semiconductor heterostructures, through a TMDC-TMTC heterostructure consisting of analogous elements in the form of NbS_2-NbS_3, was demonstrated using PE-ALD at a constant deposition temperature of 300 °C. The heterostructure fabrication was achieved by modulating the coreactant plasma composition (H_2S:H_2 ratio) as a function of the thickness (number of ALD cycles)

- New thermal ALD and PE-ALD processes for Nb_2O_5 were developed using the metal-organic precursor (tert-butylimido)-tris(diethylamino)-niobium (TBTDEN) with H_2O and O_2 plasma as coreactant, respectively. Nb_2O_5 process was developed to combine with post-sulfurization treatment for the indirect synthesis of NbS_2 (TMDC) films. Growth and material properties were analyzed over a wide range of temperatures (150 – 350 °C). High uniformity was demonstrated over a 200 mm Si wafer for both thermal ALD and PE-ALD processes. Thermal ALD grown Nb_2O_5 films were sub-stoichiometric due to the presence of oxygen vacancies with a dominant presence at higher deposition temperatures. On the other hand, PE-ALD grown films were near stoichiometric over the entire investigated temperature window.

- The indirect approach to synthesize metallic TMDCs using ALD grown transition metal oxides together with a high temperature thermal sulfurization treatment was successfully developed to grow NbS_2 films. Then the film´s material properties were compared with the properties of direct ALD grown films. The high temperature synthesized films obtained through O to S exchange reactions were highly crystalline with grain sizes around ten times larger (~300 nm) than their direct ALD (~30 nm) counterparts. The resistivity of the high temperature processed film was measured to be an order of magnitude lower at ~0.2 KμΩ-cm than that of the direct ALD grown films. The measured resistivity was also in good agreement with the bulk resistivity reported in the literature.

- The hydrogen evolution reaction (HER) performance of the NbS_2 films synthesized by various ALD based methods was investigated. In all cases, an overpotential of ~500 mV was achieved at a current density of 10 mA/cm^2, which is comparable to the reported literature values for NbS_2 grown by other methods. The direct ALD-grown films were observed to offer better long-term stability with a small change in HER performance

(overpotential) of 36 mV after 10000 HER cycles. On the other hand, the NbS_2 film obtained through thermal sulfurization of Nb_2O_5 offered poor HER performance due to the film´s complete delamination within a few HER cycles. This significant difference in stability between the direct ALD and the sulfurization derived NbS_2 was caused by differences in the film adhesion to the substrate. For sulfurization-derived NbS_2, the formation of 2D NbS_2 following the O to S exchange reaction weakens the interaction between the film and the glassy carbon substrate at the interface. As a result, the NbS_2 film delaminated during HER. Thus, direct-ALD of NbS_2 offers superior HER stability.

- The delamination issue observed during the HER for the sulfurization-derived NbS_2 was overcome by using the direct ALD-grown NbS_2 as an adhesive buffer layer between the sulfurization-derived NbS_2 (from ALD-grown Nb_2O_5) and the glassy carbon substrate. A buffer layer with a thickness of 10nm was enough to avoid delamination. Furthermore, solving the delamination problem improved the long-term HER stability of the sulfurization-derived NbS_2. This study demonstrates the HER performance of the intrinsic material (metallic TMDC), independent of the delamination issue. Thus, the stability of the interface between the catalytic film and the electrode substrate is a prerequisite for testing the catalytic material's long-term stability. This study shows the added benefit offered by direct-ALD of TMDCs for electrochemical applications.

Based on the findings communicated in this dissertation, some recommendations for further research directions can be given:

- Thus far, most of the research interests have been primarily focused on synthesizing sulfur-based TMCs using ALD, with very few reports on synthesizing selenide based group VI TMCs, such as $MoSe_2$ and WSe_2. Regarding ALD of telluride based TMCs, no reports have been presented to the best of our knowledge. It would be interesting to expand the ALD toolbox further to synthesize both selenide and telluride based TMCs over a large area as they can offer property advantages such as better mobility, superconductivity, etc. However, it is important to consider the challenges associated with the choice of coreactant such as H_2Se, H_2Te, etc., as they are highly toxic.

- The TMTCs grown by ALD in this work are amorphous in nature. So, an additional annealing treatment was required to crystallize the deposited film. Such additional treatment involves sample transfer through the ambient condition, which causes surface oxidation. Next, to implement the synthesized TMTCs for device fabrication, an

etch step would be required to remove surface oxides, increase complexity. Therefore, the next research step in terms of process development could be to investigate the possibility of synthesizing crystalline TMTC directly by ALD. This could be possible through further optimization of process parameters and/or by looking for alternative transition metal precursors and/or chalcogenide coreactants.

- Inspired by the development of PE-ALD processes for TMTCs growth, a thermal ALD process for the deposition of TMTCs could be developed. S_2 (S-S pairs) species in the H_2S plasma coreactant were speculated to make a significant difference in achieving a phase-controlled synthesis of TMTCs over TMDCs. Similarly, in the literature, TiS_3 (TMTC) was obtained using CVD only by using organic coreactants containing S-S bond species, otherwise TiS_2 (TMDC) growth was observed[1]. In this regard, by using an alternative organic molecule containing S-S bond species (*e.g.,* dimethyl disulfide) as the co-reactant, it could be possible to develop a thermal ALD process for TMTC growth.

- The ability to deposit TMDCs and their heterostructures conformally over a complex 3D substrate by ALD could fastrack their implementation in industrial processes. One such possibility could be as a barrier and/or liner material layers at the BEOL of the semiconductor chip fabrication processes, where conformal coverage along with good thickness control offered by ALD would be of great advantage. It was recently reported that TaS_2 (TMDC) synthesized by the sulfurization of a Ta film can act both as liner and Cu barrier material layer. In comparison to conventional TaN/Ta bilayer used in the industry, TaS_2 was also reported to have superior properties[2]. In this regard, it would be ideal to combine the superior liner and barrier properties exhibited by TMDCs with the synthesis benefits of ALD.

- When NbO_x was grown by thermal ALD in this work, sub-stoichiometric films were obtained due to oxygen vacancies. The number of oxygen vacancies varied as a function of the deposition temperature. As reported for TaO_x[3], the stoichiometry of NbO_x can be further reduced by adding H_2 plasma as a C step to the existing AB thermal ALD process. So, an ABC process can be developed, where TBTDEN precursor and H_2O coreactant steps remain as A and B steps, respectively. Such control over the stoichiometry of NbO_x would be useful for resistive switching random access memory (ReRAM) applications as NbO_2 undergoes a metal-insulator transition at 800 °C[4].

- Increasing the H_2 content in the coreactant step contributed to the formation of a reduction atmosphere, which led to the formation of TMDC over TMTC at low deposition temperature. Such control over the phase through the modulation of the plasma coreactant composition as a function of thickness at a constant deposition temperature led to the fabrication of vertical TMDC-TMTC (metal-semiconductor) heterostructures. Similarly, by using H species as the reducing agent, a TMTC film could be reduced to TMDC. If such a reduction process can be performed area-selectively on the TMTC film using an H_2 plasma, lateral TMDC-TMTC (metal-semiconductor) heterostructure could be fabricated by locally reducing the TMTC (*e.g.,* TiS_3/NbS_3) into TMDC (*e.g.,* TiS_2/NbS_2). The selective reduction of TMTC to TMDC could be achieved using a plasma (H_2 plasma) printing tool or using lithography to expose only certain areas of the TMTC film to H_2 plasma.

- High catalytic activity is the primary requirement for HER. Currently, the HER activity of metallic TMDCs is restricted by the high resistivity of TMDCs perpendicular to the basal planes. Charge transfer from the TMDC to the glassy carbon substrate must overcome the van der Waals gaps in the TMDCs. Therefore, to benefit completely from the active basal sites in group V TMDCs the charge transfer kinetics between the layers needs to be improved. In literature, the charge transfer was reported to improve by intercalating the intrinsic van der Waals gap with Li[5] or with metals like Nb (self-intercalation)[6] or Pd[7], and as a result, higher HER activity was achieved. In this regard, by intercalating or by increasing the metal (including Nb or other metal dopants) content through further process optimization, the HER activity of the ALD grown HER stable NbS_2 film could be improved further.

- Metallic TMDC with good electrical properties were synthesized over a large area in this work. In the literature, the device performance of the FETs has been reported to improve by using metallic 2D TMDCs over 3D metals as the contact material to form 2D-2D metal-semiconductor heterostructure configuration. Such improvement was due to the reduction of the contact resistance and Schottky barrier height[8]. Hereof, the next step would be to integrate ALD growth 2D metallic TMDCs as the contact material (source and drain) with 2D TMDC semiconductors in scalable nanoelectronics devices and investigate their role on the device performance.

References

[1] C.J. Carmalt, I.P. Parkin, and E.S. Peters, Polyhedron **22**, 1263 (2003).

[2] C. Lo, M. Catalano, A. Khosravi, W. Ge, Y. Ji, D.Y. Zemlyanov, L. Wang, R. Addou, Y. Liu, R.M. Wallace, M.J. Kim, and Z. Chen, Adv. Mater. **31**, 1902397 (2019).

[3] K. V Egorov, D.S. Kuzmichev, P.S. Chizhov, Y.Y. Lebedinskii, C.S. Hwang, and A.M. Markeev, ACS Appl. Mater. Interfaces **9**, 13286 (2017).

[4] E. Cha, J. Woo, D. Lee, S. Lee, J. Song, Y. Koo, J. Lee, C.G. Park, M.Y. Yang, K. Kamiya, K. Shiraishi, B. Magyari-Kope, Y. Nishi, and H. Hwang, in *2013 IEEE Int. Electron Devices Meet.* (IEEE, 2013), pp. 10.5.1-10.5.4.

[5] L. Najafi, S. Bellani, R. Oropesa-Nuñez, B. Martín-García, M. Prato, V. Mazánek, D. Debellis, S. Lauciello, R. Brescia, Z. Sofer, and F. Bonaccorso, J. Mater. Chem. A **7**, 25593 (2019).

[6] J. Yang, A.R. Mohmad, Y. Wang, R. Fullon, X. Song, F. Zhao, I. Bozkurt, M. Augustin, E.J.G. Santos, H.S. Shin, W. Zhang, D. Voiry, H.Y. Jeong, and M. Chhowalla, Nat. Mater. (2019).

[7] C. Huang, X. Wang, D. Wang, W. Zhao, K. Bu, J. Xu, X. Huang, Q. Bi, J. Huang, and F. Huang, Chem. Mater. **31**, 4726 (2019).

[8] Y. Liu, P. Stradins, and S.-H. Wei, Sci. Adv. **2**, e1600069 (2016).

Summary

The impactful discovery of graphene kick-started an avalanche of research on layered two-dimensional (2D) van der Waals materials. Among various 2D materials, transition metal dichalcogenides (TMDCs, MX_2) such as MoS_2 and WS_2 with semiconducting properties have gained a lot of attention for their unique optoelectronic properties in combination with an ultrathin body. TMDCs are viewed as promising materials to enable further downscaling of (opto)electronic devices. But there are also other TMDCs with metallic properties, and a class of layered materials known as transition metal trichalcogenides (TMTCs, MX_3) involving similar elements as in TMDCs with semiconducting properties, which are less well studied. In terms of technology, atomic layer deposition (ALD) is playing a significant role in the continuous down-scaling of devices because of their low processing temperatures, precise thickness control, scalability, and conformality. Therefore, the synthesis of TMDCs by ALD has gained particular interest, albeit mostly for semiconducting TMDCs. ALD of both metallic TMDCs and TMTCs has not been explored to the best of our knowledge. Additionally, ALD could enable heterostructure formation over a large area at low temperatures. This dissertation is focused on investigating ALD as a technique to synthesize metallic TMDCs, as well as semiconducting TMTCs, and their heterostructure formation. Additionally, the role of ALD parameters in achieving phase-controlled growth between TMDCs and TMTCs has been investigated for next-generation optoelectronic devices as well as for electrochemical catalytic applications.

In the first part of this dissertation, a novel ALD process for the phase-controlled synthesis of titanium sulfide (TiS_x) was developed. TiS_2 is a metallic TMDC, while TiS_3 is a semiconducting TMTC. Both thermal ALD and plasma-enhanced ALD (PE-ALD) processes were realized using a metal-organic precursor tetrakis(dimethylamido)titanium (TDMAT) with H_2S plasma and H_2S gas as coreactants, respectively. The phase control between TiS_2 and TiS_3 by ALD was demonstrated by varying both the deposition temperature and sulfur-based coreactant. The presence of S_2 species in H_2S plasma was speculated to enable the formation of TiS_3 by PE-ALD, otherwise, TiS_2 was obtained. The present study is the first report on the synthesis and characterization of TMTCs using ALD. The crystallinity of PE-ALD grown TiS_3 was improved by post-deposition annealing to yield photoluminescence at ~0.9 eV, indicating the semiconducting nature of the material with a direct bandgap. This opens

up a new avenue for controlled thin-film deposition of TMDCs and TMTCs at low-temperature.

Next, the ability of ALD to fabricate TMDC heterostructures by ALD was demonstrated by synthesizing TiS_x-NbS_x heterostructures. Thermal ALD was preferred over PE-ALD for heterostructure formation, as plasma could cause interface damage and mixing between the layers, plus thermal ALD gives better conformality in a 3D structure. A new thermal ALD process for NbS_x thin films was developed using a metal-organic precursor (tert-butylimido)-tris(diethylamino)-niobium (TBTDEN) and H_2S gas as coreactant. This is the first work to report on the synthesis of both NbS_2 and a metallic TMDC by ALD. The TiS_x-NbS_x heterostructure consisting of multiple layers with various thickness was fabricated on both nanowires (3D structure) and flat substrates. The individual TiS_x and NbS_x layers were deposited at distinct deposition temperatures to demonstrate the flexibility provided by ALD. This work successfully shows the advantages of ALD for synthesizing TMDC heterostructure *in-situ* at low deposition temperatures with precise thickness control and conformality over a 3D structure.

Lately, the prospects of combining metal-semiconductor TMCs to form heterostructure have gained momentum. While various TMDC based heterostructure have been explored, metal-semiconductor heterostructure based on TMDC-TMTC have yet to be studied experimentally. In the next part of this work, a new process to synthesize metal-semiconductor (NbS_2-NbS_3) heterostructures by PE-ALD was demonstrated. The phase control between NbS_2 and NbS_3 was attained by two methods: first, by varying the deposition temperature similar to the TiS_x work, and second, by adding H_2 to the standard H_2S plasma coreactant step (at constant temperature) while maintaining a constant total flow. A high H_2S gas fraction led to NbS_3, otherwise, NbS_2 was deposited. Using the later method, the H_2S:H_2 ratio was modulated to obtain phase-controlled growth of NbS_3 on NbS_2 yielding NbS_2-NbS_3 heterostructures.

In the next part, NbS_2 films synthesized using various methods were investigated for the electrochemical hydrogen evolution reaction (HER). Both as-deposited and post-annealed PE-ALD NbS_2 films were observed to have superior HER activity in comparison to NbS_2 films synthesized by sulfurization of ALD grown Nb_2O_5 films (CVD sulfurization method). In comparison to CVD growth NbS_2 in the literature, this work shows that ALD grown NbS_2 films have better stability and equivalent HER activity. Thus, opening up new opportunities for ALD grown metallic TMDCs for electrocatalysis applications.

Finally, the high-k dielectric niobium oxide (Nb_2O_5) was synthesized using the TBTDEN precursor with both O_2 plasma (PE-ALD) and H_2O (thermal ALD) as coreactants, respectively. High uniformity over a 200 mm was obtained using both the ALD processes. The effect of deposition temperature on the film properties was investigated for both the ALD processes. Thermal ALD grown films were found to be sub-stoichiometric due to the presence of oxygen vacancies, which were observed to be more dominantly present in the film with increasing deposition temperature while all the PE-ALD films were near stoichiometric.

To conclude, this dissertation manifests the benefits associated with ALD to fabricate novel transition metal chalcogenides and their heterostructures. Specifically, ALD processes for TiS_x and NbS_x were developed, the phase control between TMDC and TMTC for both the materials thoroughly investigated and their heterostructures formation demonstrated. Furthermore, these findings on material processing could be expanded to other transition metal chalcogenides and their heterostructures, and various applications beyond optoelectronics and catalysis, such as quantum computing could also gain from this valuable addition to the ALD toolbox.

Contributions of the Author

This thesis presents the outcome of original work conducted by the author (Saravana Balaji Basuvalingam), except for the following contributions:

- Wim A. Bik (Detect 99) contributed to the RBS and ERD measurements in Chapter 3, 4, 5 and 7.
- Dr. Marcel A. Verheijen (Eurofins Materials Science) contributed to the TEM measurements in Chapter 3, 4 and 5.
- Aileen O´Mahony (Oxford Instruments Plasma Technology) contributed to the SE measurements on large-area 200 mm wafers in Chapter 7.
- Yue Zhang (TU/e) contributed to the post-annealing and sulfurization treatment in Chapter 3 and 7, and to the measurement of NbS_2 HER datasets in Chapter 7 (Yue Zhang and the author contributed equally to the Chapter 7).
- Jeff J.P.M. Schulpen (TU/e) contributed to the DFT calculations in Chapter 4 and 5.
- Dr. Beatriz Barcones (TU/e) contributed to the FIB preparation of the TEM samples in Chapter 3, 4 and 5.
- Elham M.T. Fadaly and Dr. Erick P.A.M. Bakkers (TU/e) provided the GaAs nanowire substrates in Chapter 4.
- Dr. Matthew A. Bloodgood (TU/e) assisted in the TEM image analysis in Chapter 3 and 4.
- Rasmus H. Godiksen and Dr. Alberto G. Curto (TU/e) contributed to the NIR PL measurements in Chapter 3.

List of Publications

Peer-reviewed articles

- W. J. H. Berghuis, J. Melskens, B. Macco, **S. B. Basuvalingam**, M. A. Verheijen, W. M. M. Kessels, "Atomic Layer Deposition of Nb-doped TiO_2: Dopant Incorporation and Effect of Annealing", Journal of Vacuum Science & Technology A 38, 2 (2020).

- A. Khatibi, R. H. Godiksen, **S. B. Basuvalingam**, D. Pellegrino, A. A. Bol, B. Shokri, A. G. Curto, "Anisotropic Infrared Light Emission from Quasi-1D Layered TiS_3", 2D Materials 7, 1 (2020).

- **S. B. Basuvalingam**, M. A. Bloodgood, M. A. Verheijen, W. M. M. Kessels, A. A. Bol, "Conformal Growth of Transition Metal Dichalcogenide TiS_x-NbS_x Heterostructures over 3D Substrates by Atomic Layer Deposition", *to be submitted*. **Chapter 4**

- **S. B. Basuvalingam**, M. A. Bloodgood, J. J. P. M. Schulpen, M. A. Verheijen, W. M. M. Kessels, A. A. Bol, "Vertical Heterostructures of NbS2 and NbS3 using Low Temperature, Phase-controlled Atomic Layer Deposition", *to be submitted*. **Chapter 5**

- **S. B. Basuvalingam**, Y. Zhang, W. M. M. Kessels, J. P. Hofmann, A. A. Bol, "Activity and Stability of NbS2 Hydrogen Evolution Electrocatalyst Synthesized by Atomic Layer Deposition", *to be submitted*. **Chapter 6**

- L. Ghorbani, A. Khatibi, **S. B. Basuvalingam**, B. Shokri, "Fabrication of Flexible Filter for Efficient Hot Oil/Water Separation Using Plasma Polymerization", *to be submitted*.

- **S. B. Basuvalingam**, Y. Zhang, M. A. Bloodgood, R. H. Godiksen, A. G. Curto, J. P. Hofmann, M. A. Verheijen, W. M. M. Kessels, A. A. Bol, "Low-Temperature Phase-Controlled Synthesis of Titanium Di- and Tri-Sulfide by Atomic Layer Deposition", Chemistry of Materials 31, 22 (2019). **Chapter 3**

- D. Visser, **S. B. Basuvalingam**, Y. Desieres, S. Anand, "Optical Properties and Fabrication of Dielectric Metasurfaces based on Amorphous Silicon Nanodisk Arrays", Optics Express 27, 4 (2019).

- **S. B. Basuvalingam**, B. Macco, H. C. M. Knoops, J. Melskens, W. M. M. Kessels, A. A. Bol, "Comparison of Thermal and Plasma-enhanced Atomic Layer Deposition of Niobium Oxide Thin Films", Journal of Vacuum Science & Technology A 36, 4 (2018). **Chapter 7**

- B. Macco, M. Bivour, J. H. Deijkers, **S. B. Basuvalingam**, L. E. Black, J. Melskens, B. W. H. van de Loo, E. J. H. Berghuis, M. Hermle, W. M. M. Kessels, "Effective Passivation of Silicon Surface by Ultrathin Atomic-Layer Deposited Niobium Oxide", Applied Physics Letters 112, 24 (2018).

Popular publications

- A. A. Bol, S. Balasubramanyam, **S. B. Basuvalingam**, J. J. P. M. Schulpen, V. Vandalon, "Tailoring the Properties of 2D Transition Metal Dichalcogenides by ALD", 58, special on ALD (2020).

Acknowledgments

Everything that has a beginning comes to an end. Here I am writing the last few pages of my PhD dissertation. This wonderful journey started four years ago, and I am happy to say that this ends with lots of great memories, which I will cherish. Although this journey was lonely at times, I was lucky to have lots of people for support and encouragement. Without whom these last four years wouldn't have been a wonderful experience, both personally and professionally. I would like to thank everyone who helped me through this journey to achieve this personal milestone.

First and foremost, I would like to thank my promoter **Ageeth** for offering me this wonderful opportunity four years ago by coming all the way to Stockholm for interviewing me during your busy schedule. I appreciate the support and freedom you granted to carry my research while also making sure I was not drifting too much from the research plan. The freedom you offered was one of the primary reasons for this dissertation to get the shape it has taken. I also thank you for constantly pushing me to look for more, so the pond of satisfaction/curiosity is always only half-full. Your comments and guidance have helped me improve my presentation and writing skills a lot. I always enjoyed our conversations about India and travel. Once more, thank you for keeping me focused and for offering the freedom to explore new things while also reminding me constantly to relax and enjoy.

Next, I would like to thank my second promoter **Erwin** for your valuable feedback and comments on my work whenever I needed it the most. I greatly appreciate your keen eye for details. I should thank you for your prompt and timely response and feedback on abstracts, manuscripts, and presentations, even if I approach you at the very last moment. I am particularly happy that you started to like my presentation style, which was a long journey from your comments on having too many colors in my slides during my first year. I admire your dedication to keeping us always on our toe, both in research and other group activities.

Another person I should thank next is **Marcel.** For not just the awesome TEM images you made (shown throughout this dissertation), but also for insightful and valuable suggestions on my work and manuscripts. I appreciate your interest to study MX_3 and also for taking the time to offer valuable feedback on the introduction chapter. I find your enthusiasm for 2D materials very motivating.

Next, I would like to thank my collaborators. **Jan Philippe**, I would like to thank you for the long and fruitful collaborations with the sulfurization and HER studies. **Yue**, I can always count on you to perform the experiments on time and to say yes to new ideas on future experiments. I greatly appreciate your 24X7 response. I wish you all the best for your PhD. **Ali**, I am happy that our research paths crossed in the name of TiS_3. I enjoyed discussing about TiS_3 and various other topics with you. I admire how you adapted to new surroundings and managed to publish two articles during your short stay in Eindhoven. **Rasmus**, I should thank you for taking over the collaboration and helping me get some nice results and all the best with your PhD. **Alberto**, I enjoyed our short discussions about various 2D materials and their interesting optical properties.

Harm, thanks for your guidance and support with the Nb_2O_5 work. I much appreciate your valuable suggestions regarding the ALD tool and process development throughout this journey. I learned a lot about ALD from you. **Adrie**, you always take a minute to ask about how I'm doing and how things are going with me. I thank you for all the kind and supporting words you said when I need it. **Adriana**, I thank you for the support during the ALD conference. Hope the TiS2 for perovskite work offers some nice results. I also thank **Richard**, **Fred** and **Daan** for feedback on my presentations during TuMos.

I cannot forget the incredible team of technicians who make our life as a PhD a lot easier by stepping in every time there is a problem in the lab. **Cristian**, I admire how you approach everything (problems) with a smile. I always enjoy our conversations, be it about work or life. I very much appreciate all the important life advice you gave. **Jeroen**, thanks for patiently fixing the reactor every time with a smile. I enjoyed discussing with you about 80's references and Indian culture. **Martijn**, in India, we have a term called Jugaad, which precisely describes your after 4pm fix. One moment I will always remember is the video call you made at 9 pm from your home to help me fix the problem, so I wouldn´t have to waste tool time. Thanks again for taking great care of the FlexAL2D. **Casper**, I always enjoy our conversations during the coffee break and lunch, and it was fun to hike and travel with you during our Seattle trip. Thanks for inviting me to the pizza parties at your place and for organizing the chocolate-making workshop. **Janneka** and **Joris**, I would like to thank (infinite times) both of you for being there during the worst day of this journey. I will not forget the support and concern you both showed on the day. **Barathi**, I always enjoy our small (Tamil) conversations, and thanks for reminding me about the Diwali and Pongal festivals. **Beatriz**, all the awesome cross-section TEM images in this thesis wouldn´t have been possible without your FIBing. Thank you for your valuable contribution.

The other face of the PMP support coin is **Jeanne** and **Lianne**. They made this journey easier with the support and help with administrative work. I much appreciate your prompt response to any questions and emails. *Jeanne*, thanks for informing and reminding me about the various deadline with forms and thesis.

I once more like to thank **Tamalika Banerjee**, **Jaap den Toonder**, **Peter Steeneken**, **Saurabh Lodha** and **Remco Tuinier** for accepting to be a part of my doctoral committee and for evaluating my thesis during your busy schedule.

Most of the week at PMP started with the group discussion with my subgroup members: **Rene**, **Nick**, **Akhil**, **Bora**, **Eldad**, **Vincent**, **Shashank**, **Reyhaneh**, **Bart**, **Mahdi**, **Mat t** and **Jeff**. I thank all of you for the valuable and wonderful discussions during every stage of this journey. Your suggestions and support mean a great deal and played a significant role in planning my experiments.

Golden God, *aka Martijn*, thanks for being there at countless moments to celebrate happy news or to vent about a problem. I enjoyed being your guide during your India trips hope you grasped the 2%. You were a pleasant and entertaining roommate during the ALD conference. **Shashank**, thank you for the company with dinner/lunch and movies. We had lots of fun during our post-conference adventure in Sweden and Norway. **Morteza**, I enjoyed having you as the office neighbor. Thank you for helping me with shifting houses and for the fantastic rice you make. *Guys*, I will always treasure the times we spent at parties and the road trip.

Dr. Biasing, *aka Tahsin*, we have had lots of "discussion" (trash talk), really a lot almost about anything and everything. It was a pleasure to share the office and our SPARing time with you. I greatly appreciate your suggestions and interests in my research, MX_3s, mobile shopping, etc. I can always count on your help when needed, and thanks for always looking out for me. **Saurabh**, you made our office fun (I think most of the time, you did it without knowing you are doing it). I greatly appreciate your valuable suggestions and constant blind critics. Looking forward to meeting you and your wife again in Leiden sometime.

Matt, thanks for being the other MX_3 guy in the group. I enjoyed our long never-ending discussions and debate about interesting and unusual MX_3s both in person and over WhatsApp. I greatly appreciate your speedy feedback on my work and writing. Your active feedback and comments have helped me to immensely improve my writing skills. **Nick**, I enjoy watching Formula 1 races and football matches at the center with you. We had lots

of fun at parties and the casino. It was a fun experience to guide you and *Martijn* during your trip to India. The part of you dealing with not having non-veg meals for a brief time during the trip was one to remember forever.

Claire, you were an awesome office neighbor and co-TuMo organizer. I will always cherish our intense philosophical discussions about science and life both at work and during WOKing. Thanks again for accompanying me to the cleanroom after 7 pm. **Maria**, I enjoyed our serious and not so serious conversation about life, food and our PhD, any day anywhere. We had lots of fun-partying, road-tripping and at the ALD conference. I wish you the best with your PhD.

Jeff, I always enjoy our discussion about 2D materials. I am fascinated by your interest in addressing the mystery from a theoretical point of view. I wish you all the best with your PhD. **Jun-Li**, even though we were office neighbors for only a short while, I enjoyed our conversations about ALD. Good luck with your new job at ASML.

Jimmy, I enjoyed our intense discussions about living abroad, Netherlands and academia. I enjoyed having you as a roommate during the MRS conference in Boston. Thanks for introducing me to cards against Humanity. **Bart Macco**, being unplugged during the Portland trip was the craziest day ever on the road. We had quite an adventurous day. I am still surprised about surviving the day while managing to do more than what we had planned.

Bora, thanks for introducing me to the world beyond TMDCs within the world of 2D materials. Your timely interest in brainstorming at the initial months of my PhD led me to MX_3s, so this dissertation. Thank you again. **Reyhaneh**, thanks for your interest and collaboration to implement metallic TMDCs I grew as contacts in your devices. I wish you the very best for your PhD.

Karsten, you are one of the most outgoing people in PMP. Thanks for the company during both virtual and in-person coffee breaks. **Marc**, I will always remember your persistence to celebrate the National Tequila day (the last day of the ALD conference). Guys (*Karsten*, *Marc* and ***Casper***), I had a wonderful time with you during the adventurous Seattle trip. I will cherish it more now as we have become the survivors. Thanks again for helping me to descend the peak of the Pinnacle Peak. *Karsten* and *Marc*, good luck with your PhD.

Lachlan, thanks for hosting the Christmas lunch for PMP orphans during my first Christmas in Eindhoven. **Valerio Di Palma**, we had a good pool rivalry during our La folie time.

However, scores are yet to be settled, looking forward to continuing our pool rivalry. I wish you all the best with your PostDoc in Italy. **Andrea**, it was always nice to discuss with you about TiS_2 and other topics. Hope our collaboration results in some nice results. Good luck with your PhD.

I should also thank **Lila** and **Daniel** for contributing to this thesis directly and indirectly as a part of your respective summer internship. Good luck with your studies and graduation.

I also like to thank the rest of the PMP (past and present) colleagues: **Sanne**, **Norah**, **Luca**, **Willem-Jan**, **Dibya**, **Farzad**, **Anna**, **Michel**, **Yinguan**, **Bas**, **Gerben**, **Damen**, **Valerio Zardetto**, **Alberto**, **Maik**, **Mark**, **Janne**, **Michelle**, **New Nick**, **David**, **Royue**, **Alfredo** and **Bart Klarenaar** for making the interaction during the lunch, borrel, coffee and vlaai breaks enjoyable.

I have moved to a new house five times within Eindhoven in my four years and so have had many housemates. But I should mention some of my ex-House mates: **Ervin**, **Olivia**, **Valliappan** and **Vivek** for their support and encouragement and for putting up with me. We have had some wonderful days BBQing and partying in the garden, and by watching the last season of GOT on our couch.

I must thank my friends here in Eindhoven, **the ABCD Dost gang**, for making the past year for me and my wife wonderful. We have had several wonderful times, partying and celebrating. Recently we have managed to find new ways to socialize in the current social-distancing era through online pub quiz and CSing, hope we can continue reaching the magic number.

I should mention the friends from my Bachelors: **Varun**, **Muthu**, **Nisha**, **VB**, **Rohit**, **Anbu**, **Dondu**, **Bandla**, **Sai**, **DB**, **Bar**, **Mahesh**, **Poorni**, **Siva** for continually supporting me for more than 7 years. Even though we live in different parts of the world and have moved to different phases of our lives. I am happy that we always make time for each other to support and help each other in every aspect of our lives. A special thank you to you guys for being there for me whenever I needed and for regularly checking on me.

Athe, **Mava**, **Nithya** and **Hema,** I thank you for the love and support you show since the day we have met. A special thanks to my **Bava** for always supporting me and for always looking out for me. **Soundarya**, I am lucky to have you as my sister, and I am sorry for not being there with you at home. Thanks for always (most of the time) taking my side and for always looking out for me. I am very excited to meet and play with the new handsome addition to our family. Looking forward to watching you and *Bava* raise the handsome little one.

Appa and **Amma**, I couldn't have reached this point in my life without your constant support and motivation. Your love and confidence in me have helped me to stay focused. I am grateful for all your sacrifice. I am happy that social networking apps have enabled us to stay connected and to see each other in the past few years. *Appa***,** you are my hero. I admire how you worked hard from a very early age and established yourself starting from nothing by countering all the hardships life has thrown at you.

Finally, I would like to thank my wife **Komala** for all the support and trust, and for continually believing in me. This dissertation wouldn´t be possible without your encouragement and constant support. I am very proud of you for the way you have handled yourself moving to Eindhoven and for making an awesome social circle for yourself by stepping out.

My sincere apology to anyone I forgot to mention in these last few pages of the dissertation. I would like to thank you for your part in helping me reach this personal milestone.

Sincerely,

Saravana Balaji Basuvalingam

October 2020

Curriculum Vitae

July 29, 1991	Born in Salem, India
2009 – 2013	Bachelor of Engineering Degree in Materials Science and Engineering, College of Engineering Guindy, Anna University, Chennai, India
2013 – 2015	Master of Science Degree in Nanotechnology with a major in Engineering Physics, KTH Royal Institute of Technology, Stockholm, Sweden
2015 – 2016	Research Engineer at Semiconductor Materials group, School of Information and Communication Technology, KTH Royal Institute of Technology, Stockholm, Sweden
2016 – 2020	PhD candidate in the group of Plasma and Materials Processing (PMP), Department of Applied Physics, Eindhoven, The Netherlands